CRANFIELD INSTITUTE OF TECHNOLOGY

DEPARTMENT OF MATERIALS

DOCTOR OF PHILOSOPHY THESIS

ACADEMIC YEAR 1976 - 78

GURNAM SINGH SOHAL

B.Sc (Hons), M.Sc

CAVITATION OF SUPERPLASTIC ALLOYS:

A STUDY USING A HOT MICROHARDNESS TECHNIQUE

SUPERVISOR: ROGER PEARCE

B.A, B.Sc, F.I.M

JANUARY 1980

Abstract

This thesis is concerned with the study of cavitation behaviour of two-phase superplastic alloys, using mainly a hot microhardness technique. Cavitation is a serious problem in copper and iron base alloys, it drastically limits the elongation to failure and may affect the service properties of superplastically formed components. There is some empirical evidence to suggest that, for cavitation to occur, the two phases involved must be 'incompatible' that is, they show marked differences in certain properties. Ideally, this phenomenon would be investigated directly by an in-situ study of the deformation behaviour of each phase separately in the microduplex alloy at the superplastic temperature and hence pinpointing the phase incompatibilities, but existing techniques do not allow for this. Here, a hot microhardness tester was commissioned and used to determine the hardness and activation energy of each phase in-situ in a duplex alloy in the superplastic temperature range.

Zn/Al eutectoid and 60/40 brass were here used as models to represent a non-cavitating and cavitating class of superplastic alloys. In addition, a series of alloys were produced of compositions corresponding to those of the individual phases in these systems over a superplastic temperature range. These alloys were hot tensile tested to find the ductility and tensile strength of each phase of superplastic alloy. The hot hardness data was correlated with the hot tensile data for the alloys over the whole temperature range from 0.4 to 0.84 T_m. Variation of Young's modulus with temperature was determined by a vibration technique and activation energy calculated form ℓnH versus T_m plots for all the alloys. In 60/40 brass, the amount $\bar{E}$ of $\bar{T}$ cavitation decreased with an increase in temperature and this alloy gave a maximum elongation of $\sim$ 110 pct at 250°C (0.45 T_m), but it still exhibited extensive cavitation. In the Zn/Al eutectoid, no cavitation was observed apart from that associated with a few large inclusions. The hardness values of the two phases in α/β brass were very different at the superplastic temperature, as were the load extension curves from the tensile tests and the calculated activation energies. In the Zn/Al eutectoid however, the mechanical properties of the two phases were similar, though the activation energies were different.

Finally, an attempt was made to explain the occurrence of cavitation in Supral 150 and certain steels, in some cases experimentally and in others from data available in the literature.

Acknowledgements

I am extremely grateful to my supervisor, Mr Roger Pearce, for his constant encouragement, invaluable guidance and assistance throughout this programme of research.

I am also grateful for the co-operation and help that has been extended to me by every member of the Department of Materials in some way or another throughout this work. My thanks are due to Miss Elizabeth Bellamy for typing this thesis and Mrs Sue Oxley for tracing the graphs.

This research project was sponsored by the Science Research Council and their financial support is gratefully acknowledged.

Finally, I must thank my wife, Narinder, for her encouragement and understanding throughout this work.

CONTENTS

			Page Number
Abstract			
Acknowledgements			
Symbols			
List of Figures			
List of Tables			
Chapter 1		Introduction	1
Chapter 2		Literature Survey Superplasticity	4
	2.1	Introduction	4
	2.2	Environmental Superplasticity	4
	2.3	Structural Superplasticity	5
	2.4	Strain-Rate-Sensitivity Index and Plastic Flow	6
	2.5	Activation Energy for Superplastic Flow	7
	2.6	Mechanisms of Superplasticity:	8
		2.6.1 Introduction	8
		2.6.2 Diffusion Creep	9
		2.6.3 Dislocation Creep	11
		2.6.4 Recrystallisation	12
		2.6.5 Grain Boundary Sliding	12
Chapter 3		Literature Survey Cavitation in Creep and Superplasticity	22
	3.1	Introduction	22
	3.2	Cavitation in Creep	22
		3.2.1 Introduction	22
		3.2.2 Nucleation	23
		3.2.3 Growth	24
		3.2.4 Final Fracture	25
	3.3	Cavitation in Superplasticity	26
		3.3.1 Introduction	26
		3.3.2 Sites for Cavity Nucleation	27
		3.3.3 Models for Cavity Nucleation	27
		3.3.4 Cavity Stability and Growth	28
		3.3.5 Fracture	36

Chapter 4		Literature Survey Hardness	39
	4.1	Introduction	39
	4.2	Microhardness and Macrohardness Testing	39
	4.3	Hot Hardness and Other Properties	40
	4.4	Indenter Materials	41
	4.5	Various Hot Hardness Machines	41
	4.6	Effect of Indenter Temperature on Hardness	42
	4.7	Use of a Hot Hardness Technique in the Study of Cavitation in Superplasticity	43
	4.8	Effect of Loading Time on Hardness	43
	4.9	Indentation Hardness and Creep	44
	4.10	Assessment of Superplastic Characteristics of an Alloy by a Simple Hardness Technique	45
	4.11	Short-Time Hardness and Temperature Relations	46
	4.12	Activation Energy for Creep from Hot-Hardness Data	48
	4.13	Hardness Softening Parameters and an Apparent Activation Energy for Indentation	50
Chapter 5		Experimental	51
	5.1	Introdution	51
	5.2	Hardness Testing	52
	5.3	Young's Modulus Testing	56
	5.4	Tensile Testing	59
Chapter 6			
	6.1	Results	60
	6.2	Discussion	66
	6.3	Conclusions	75
		References	78
		Figures	87
		Tables	164-195

Symbols

σ	True stress
ε	True strain
$\dot{\varepsilon}$	True strain-rate
σ_f	Flow stress
σ_o	Back stress
ε_t	Total strain
ε_{gb}	Strain due to grain boundary sliding
$\dot{\varepsilon}_s$	Steady state creep rate
$\dot{\varepsilon}_{tr}$	Transient creep rate
$\dot{\varepsilon}_{DAflow}$	Strain rate due to diffusion accommodation flow
$\dot{e}$	Engineering strain-rate
m	Strain-rate-sensitivity index
$\bar{m}$	True value of m = 1
k'	Constant
k	Boltzmann constant
R	Gas constant
N	Strain hardening index
n	Stress exponent ($=\frac{1}{m}$)
T	Temperature
RT	Room temperature
T_m	Melting temperature
T_t	Transition temperature
L	Grain size
Q	Activation energy
$Q_{(const.\sigma)}$	Activation energy at constant stress
$Q_{(const.\varepsilon)}$	Activation energy at constant strain rate
Q_c	Activation energy for creep
Q_L	Activation energy for lattice self-diffusion
Q'	Apparent activation energy for indentation
Ω	Atomic volume
w	Grain boundary width
D	Diffusion coefficient
D_L	Coefficient of lattice diffusion
D_{gb}	Coefficient of grain boundary diffusion

γ	Surface energy
d_o	Atomic jump distance
b	Burgers vector
b_n	Component of Burgers vector normal to boundary plane
G'	Constant
G	Shear modulus
τ	Shear stress
UTS	Ultimate tensile strength
E	Young's modulus
σ_y	Yield stress
λ	Distance between steps on grain boundary
Γ	Grain boundary free energy
δ	Thickness of the boundary
GBS	Grain boundary sliding
$\Delta\mu_i$	Interface potential
ρ	Density of dislocations
M	Mobility of boundary dislocation
H	Hardness
H_v	Vickers hardness number
W	Applied load
d	Diameter of indentation
t	Time of loading
h	Depth of indentation
f_o	Characteristic frequency of the first mode of vibration
α	Coefficient of linear thermal expansion

(Other symbols are defined as they appear in the text)

List Of Figures

1 Strain-rate dependence of (a) flow stress and (b) parameter $m=(\frac{\delta \ell n \sigma}{\delta \ell n \dot{\varepsilon}})$ for the Mg-Al eutectic alloy. Regions I, II, and III are delineated.

2 Relationship between tensile elongation and strain-rate sensitivity, m, for a number of materials.

3 Schematic diagrams summarising the important features of mechanical properties of superplastic materials.

4 A summary of the important metallographic and texture changes accompanying superplastic deformation, in different regions of the $\ell n\sigma$ - $\ell n\dot{\varepsilon}$ curve.

5 Typical relationship between measured strain rate and applied stress for superplastic materials. The effect of subtracting a constant-stress term is shown.

6 A schematic illustration of the grain-switching mechanism described by Ashby and Verral[20].

7 Diffusion accommodation at the intermediate stage of the switching event illustrated in fig 6.

8 A plot of equation (2 - 36), using the input data for lead. The microstructural and other characteristics of the model are listed.

9 Phase diagram of Zn-Al system.

10 Phase diagram of Cu-Zn system.

11 Optical micrograph of 60/40 brass. Annealed at 700°C for 118 hours and then quenched in water.

12(a) Optical micrograph of Zn/Al eutectoid. Homogenised at 380°C for 25 hours, quenched in iced-water. $FeAl_3$ type inclusions are ~ 2 - 3 μm in size.

(b-e) Optical micrograph of Zn/Al eutectoid. Homogenised at 380°C for 25 hours, quenched in iced-water. Then annealed at 260°C (0.7 Tm) for (b) 1 hour, (c) 2 hours, (d) 3 hours and (e) 5 hours.

13 High temperature microhardness tester (a) general view, (b) console front, (c) base plate assembly, (d) window, indenter beam assembly and dashpot and (e) indenter position inside its furnace.

14 Hardness specimen drawing.

15 Hardness specimen and its furnace.

16 Indenter furnace.

17 Parts of the indenter assembly.

18 Hardness vs load for leaded-brass using present machine and Vickers.

19 Hardness vs temperature curve for pure aluminium.

20 Schematic layout of a vibration technique.

21 ℓnH vs $\frac{1}{T^{o}K}$ graph for pure aluminium. Q = 33Kcal/mole.

22 $\ell n\frac{H}{E}$ vs $\frac{Tm}{T}$ graph for pure aluminium. Q = 31 Kcal/mole.

23 Hardness vs temperature curve for 60/40 brass. (A) as-extruded, (B) 3 hours at 800^{o}C, air cool (lamellar structure) and (C) 1 hour at 600-620^{o}C, anneal.

24 Hardness vs temperature curves for the in-situ α and β phases of the 60/40 brass.

25 The in-situ ratio $\frac{H\alpha}{H\beta}$ vs T^{o}C plot for 60/40 brass.

26 ℓnH vs $\frac{1}{T^{o}K}$ graph for in-situ α and β phases of the 60/40 brass. $Q\alpha$ = 48.2 Kcal/mole, $Q\beta$ = 53.6 and 25.8 Kcal/mole, below and above the order-disorder transition respectively.

27 $\ell n\frac{H}{E}$ vs $\frac{Tm}{T}$ graph for 60/40 brass. Q = 21.2 Kcal/mole.

28 Hardness vs temperature curve for 62Cu/38Zn alloy. (A) 1 hour at 600-620^{o}C anneal, L = 100 gm, (B) 19 hours at 630-670^{o}C anneal, L = 10 gm.

29 $\ell n\frac{H}{E}$ vs $\frac{Tm}{T}$ graph for 62/38 brass ($B\alpha$). Q = 42.2 Kcal/mole.

30 Hardness vs temperature curve for 55/45 brass ($B\beta$), (A) as-extruded, (B) 1 hour at 600-620^{o}C anneal, L = 100 gm and (C) 19 hours at 630-670^{o}C anneal, L = 10 gm.

31 $\ell n\frac{H}{E}$ vs $\frac{Tm}{T}$ graph for 55/45 brass. Q = 43 Kcal/mole and 22 Kcal/mole, below and above the order-disorder transition respectively.

32 Hardness vs temperature cruves for 55 Cu/45 Zn, 60 Cu/40 Zn and 62Cu/38Zn alloys. All three annealed at 600-620^{o}C for 1 hour.

33 The ratio $\frac{H\alpha}{H\beta}$ vs T^{o}C plot for 60/40 brass, (A) 19 hours at 630-670^{o}C, (B) 1 hour at 600-620^{o}C and (C) in-situ. In (A) and (B), α and β phases are represented by 62/38 and 55/45 brasses respectively.

34 Effect of loading time on the hardness of 60/40 brass at 300^{o}C, 450^{o}C and 600^{o}C.

35 Effect of loading time on the indentation diameter for 60/40 brass at 300^{o}C, 450^{o}C and 600^{o}C.

36 Shows the ductility and UTS of 60/40 , 62/38 and 55/45 brasses at different temperatures in the range 300-700^{o}C.

37 Shows the effect of strain-rate on the ductility and UTS of 60/40 brass at 250^{o}C.

38 Young's modulus vs temperature curves for 62/38, 60/40 and 55/45 brasses, (A) measured by vibration technique, (B) calculated from a simple empirical relation: $E_{AB} = \frac{x\ wt\%A \times E_A + (100 - x)wt\%B \times E_B}{100}$

39 Young's modulus vs temperature curve for 55/45 brass (B_β) is compared with those for β brass from ref 200.

40 Variation of hardness and Young's modulus with temperature for 55/45 brass.

41 Variation of hardness and Young's modulus with temperature for 60/40 and 62/38 brasses.

42 Hardness vs temperature curves for Zn-Al alloys. (A) 78Zn/22Al eutectoid, (B) 22Zn/78Al, (C) 99.5Zn/0.5Al, (D) 12.4Zn/87.6Al and (E) 5.6Zn/94.4Al.

43 Hardness vs temperature curves for the α and β phases of the Zn/Al eutectoid.

44 The ratio $\frac{H\alpha}{H\beta}$ vs T^oC plot for Zn/Al eutectoid.

45 Hardness vs temperature plot for Zn-Al eutectoid, (A) time of loading = 15 sec, (B) time of loading = 30 sec.

46 Hardness vs temperature curve for Zn-Al eutectoid. (A) homogenised at 375°C for 4 hours, furnace cooled (lamellar structure), (B) 4 hours at 380°C, quenched iced-water. Then 2 hours at 250°C anneal, (C) as-extruded and (D) 3 hours at 370°C, quenched water.

47 (a) Effect of loading time on the hardness of Zn/Al eutectoid at 100°C, 150°C, 200°C and 250°C. (A) L = 10 gm, (B) L = 100 gm. (b) Effect of loading time on the indentation diameter for Zn/Al eutectoid at 100°C, 150°C 200°C and 250°C.

48 Zn/Al eutectoid showing indentation creep at room temperature.

49 $\ell n\frac{H}{E}$ vs $\frac{Tm}{T}$ graph for Zn/Al eutectoid, homogenised at 390°C for 15 hours, quenched iced-water. Q = 11.3 Kcal/mole.

50 $\ell n\frac{H}{E}$ vs $\frac{Tm}{T}$ graph for Zn/Al eutectoid. Homogenised at 380°C for 4 hours, quenched iced-water. Then 2 hours at 250°C anneal. Q = 13.2 Kcal/mole.

51 $\ell n\frac{H}{E}$ vs $\frac{Tm}{T}$ graph for 99.5 Zn/0.5 Al alloy (A_β). Q = 19.5 Kcal/mole.

52 $\ell n\frac{H}{E}$ vs $\frac{Tm}{T}$ graph for 22 Zn/78 Al alloy ($A\alpha_3$). Q = 29.9 Kcal/mole.

53 $\ell n\frac{H}{E}$ vs $\frac{Tm}{T}$ graph for 12.4 Zn/87.6 Al alloy ($A\alpha_2$). Q = 29.5 Kcal/mole.

54 $\ell n\frac{H}{E}$ vs $\frac{Tm}{T}$ graph for 5.6 Zn/94.4 Al alloy ($A\alpha_1$). Q = 32,7 Kcal/mole.

55 Shows the ductility and UTS of Zn/Al eutectoid and its two phases at 120°C, 190°C and 250°C.

56 Young's modulus vs temperature curves for Zn-Al alloys.. (A) measured by vibration tehcnique, (B) calculated from a simple empirical relation as in fig 38.

57 Variation of hardness and Young's modulus with temperature for Zn/Al eutectoid.

58 Variation of hardness and Young's modulus with temperature for 99.5 Zn/0.5 Al, 22 Zn/78 Al, 12.4 Zn/87.6 Al and 5.6 Zn/94.4 Al alloys.

59 Mechanical properties (ie., H, UTS and % elongation) of Zn/Al alloys as a function of zinc content.

60 Shows that the ratio $\frac{H}{UTS} = 3 \pm 1$ for alloys in the temperature range 0.4 to 0.84 T_m.

61 Young's modulus vs T_m for alloys.

62 Hardness vs temperature curves for (A) $CuAl_2$, (B) Al-matrix and (C) Supral 150 (Al-6Cu-0.5Zn), 15 min at 450°C (superplastic condition).

63 ℓnH vs $\frac{1}{T^oK}$ graph for (A) $CuAl_2$, (B) Al-matrix and (C) Supral 150. Q = 50.8, 37.3 and 21.5 KCal/mole for A, B and C respectively.

64 Hardness vs temperature curves for different phases in steel.

65 ℓnH vs $\frac{1}{T^oK}$ graph for (A) cementite of white cast iron, (B) ferrite and austenite in steel (0.19C) and (C) nominally pure iron.

66 Optical micrograph of Zn/Al eutectoid deformed superplastically to 400 pct at 250°C, $\dot{\varepsilon} = 1.6 \times 10^{-3} sec^{-1}$. There is little cavitation. The $FeAl_3$ type inclusions are shown.

67 Optical micrograph of Zn/Al eutectoid in the as-received condition, showing the presence of $FeAl_3$ type inclusions.

68 Optical micrograph of Zn/Al eutectoid after 400 pct superplastic deformation at 250°C (0.7 T_m), showing that the $FeAl_3$ type inclusions neither changed in shape nor cracked during deformation.

69 (a,b) Optical micrographs of Zn/Al eutectoid after 400 % superplastic deformation at 250°C (0.7 T_m), showing that some of the cavities are associated with inclusions.

70 (a,b) Scanning electron micrographs of fracture surfaces of specimens of Zn/Al eutectoid deformed at (a) 250°C (0.7 T_m) and (b) 190°C (0.6 T_m), showing the decohesion of $FeAl_3$ type particles to form cavities.

71 Optical micrograph of lamellar Zn/Al eutectoid (not superplastic), after 70% deformation at 250°C (0.7 T_m), showing extensive cavitation.

72 Optical micrograph of duplex 60/40 brass after 170% superplastic deformation at 600°C (0.74 T_m), $\dot{\varepsilon} = 1.6 \times 10^{-3} sec^{-1}$, showing cavitation mainly at the α/β boundaries. Grain size ~ 40 μm, initial grain size was ~ 7 μm.

73 Optical micrographs of 60/40 brass deformed at (a) 500°C (0.66 T_m) (b) 600°C (0.74 T_m) and (c) 700°C (0.83 T_m), $\dot{\varepsilon} = 1.6 \times 10^{-3}sec^{-1}$, showing that the amount of cavitation decreases with an increase in temperature.

74 Optical micrograph of 60/40 brass deformed at 700°C, $\dot{\varepsilon} = 1.6 \times 10^{-3}sec^{-1}$, showing elongation of individual phases in the direction of the tensile axis.

75 (a) Scanning electron micrograph of the fracture surface and (b) optical micrograph of the 60/40 brass deformed at 600°C (0.74 T_m), $\dot{\varepsilon} = 1.6 \times 10^{-3}sec^{-1}$, showing interlinking of the cavities to cause final failure of the alloy.

76 Optical micrograph of 60/40 brass deformed at 250°C (0.45 T_m), $\dot{\varepsilon} = 1.6 \times 10^{-3}sec^{-1}$, showing cavitation at triple points. The individual phases are elongated in the direction of the tensile axis.

77 Optical micrograph of 62/38 brass deformed at 600°C (0.74 T_m), $\dot{\varepsilon} = 1.6 \times 10^{-3}sec^{-1}$, showing extensive amount of cavitation in the vicinity of the fractured tip.

78 Optical micrograph of 55/45 brass. Deformed at 600°C (0.75 T_m), $\dot{\varepsilon} = 1.6 \times 10^{-3}sec^{-1}$, showing very little cavitation in the vicinity of the fractured tip.

79 Optical micrograph of 55/45 brass, deformed to 170% at 600°C (0.75 T_m), $\dot{\varepsilon} = 1.6 \times 10^{-3}sec^{-1}$, showing small grains apparently forming within larger ones.

TABLES

1 Composition and proportion of α and β phases in the Zn/Al eutectoid at different temperatures.

2 Composition and proportion of α and β phases in the 60Cu/40Zn alloy at different temperatures.

3 Composition and room temperature hardness of all the alloys.

4 Alloys that represent the two phases of Zn/Al eutectoid ($A_{\alpha\beta}$).

5 Alloys that represent the two phases of 60Cu/40Zn alloy ($B_{\alpha\beta}$).

6 Composition and proportion of phases in $A_{\alpha 1}$, $A_{\alpha 2}$; $A_{\alpha 3}$ and A_{β} alloys.

7 Composition and proportion of phases in B_{α} and B_{β} alloys.

8 Hardness of fine-grained Zn/Al eutectoid measured by Reichert and present microhardness tester.

9 Ductility and UTS values of 60-40 brass at 250°C, $\dot{\varepsilon} = 1.6 \times 10^{-3} sec^{-1}$.

10 Ductility and UTS values of 60-40 brass at 600°C, $\dot{\varepsilon} = 1.6 \times 10^{-3} sec^{-1}$.

11 Ductility and UTS values of Zn/Al eutectoid at 250°C, $\dot{\varepsilon} = 1.6 \times 10^{-3} sec^{-1}$.

12 Activation energies for $A_{\alpha 1}$, $A_{\alpha 2}$, $A_{\alpha 3}$ and A_{β} alloys.

13 Ductility, hardness and UTS values of Zn/Al eutectoid ($A_{\alpha\beta}$) and its phases.

14 n values used for the alloys.

15 Ductility, hardness and UTS values of 60-40 brass ($B_{\alpha\beta}$) and its phases.

16 Hot hardness data on pure aluminium, on heating up and cooling down.

17 Hot hardness data on 60-40 brass. As-extruded; annealed at 800°C for 3 hours, air cooled (lamellar structure).

18 In-situ hot hardness data on α and β phases in 60-40 brass and hot hardness data on 60-40 brass, 1 hour at 600-620°C anneal.

19 Hot hardness data on 62/38 brass (B_{α}). Annealed at 600-620°C for 1 hour, indenter load = 100 gm; annealed at 630-670°C for 19 hours, indenter load = 10 gm.

20 Hot hardness data on 55/45 brass (B_{β}). As-extruded; annealed at 600-620°C for 1 hour, indenter load = 100 gm; annealed at 630-670°C for 19 hours, indenter load 10 gm.

21 Hardness data on 60/40 brass as a function of loading time at 300°C, 450°C and 600°C.

22 Young's modulus vs temperature data on 62/38 brass (B_α).

23 Young's modulus vs temperature data on 60/40 brass ($B_{\alpha\beta}$).

24 Young's modulus vs temperature data on 55/45 brass (B_β).

25 Hot hardness data on 99.5Zn/0.5Al (A_β) and 22Zn/78Al ($A_{\alpha 3}$) alloys.

26 Hot hardness data on 12.4Zn/87.6Al ($A_{\alpha 2}$) and 5.6Zn/94.4Al ($A_{\alpha 1}$) alloys.

27 Hot hardness data on Zn/Al eutectoid ($A_{\alpha\beta}$). Homogenised at 370°C for 3 hours, quenched in water. Loading time = 15 and 30 seconds.

28 Hot hardness data on Zn/Al eutectoid ($A_{\alpha\beta}$). Homogenised at 390°C for 15 hours, quenched iced-water, indenter load = 10 and 100 gm; homogenised at 380°C for 4 hours, quenched iced-water, then annealed at 250°C for 2 hours, indenter load 100 gm.

29 Hot hardness data on Zn/Al eutectoid ($A_{\alpha\beta}$). As-extruded; homogenised at 375°C for 4 hours, furnace cooled to get lamellar microstructure.

30 Hardness data on Zn/Al eutectoid ($A_{\alpha\beta}$) as a function of loading time at 100°C, 150°C, 200°C and 250°C.

31 Young's modulus vs temperature data on 99.5Zn/0.5Al alloy (A_β).

32 Young's modulus vs temperature data on 78Zn/22Al eutectoid ($A_{\alpha\beta}$).

33 Young's modulus vs temperature data on 22Zn/78Al alloy ($A_{\alpha 3}$).

34 Young's modulus vs temperature data on 12.4Zn/87.6Al alloy ($A_{\alpha 2}$).

35 Young's modulus vs temperature data on 5.6Zn/94.4Al alloy ($A_{\alpha 1}$).

36 Hot hardness data on Supral 150 (Al-6Cu-0.5Zr) and its Al-matrix.

CHAPTER 1

1. INTRODUCTION

Soon after the publication of Underwood's review[1] of superplasticity - a phenomenon whereby certain crystalline materials can be deformed to produce unusually high ductility at above 0.5 T_m - much research interest developed in this field. Since then a large number of alloys have been rendered superplastic and these are listed in recent reviews[2,3,4] of the subject. For a material to show superplasticity it must have a fine (< 10 μm) equiaxed grain size which remains stable at the temperature of deformation. The simplest way of obtaining the required stable grain structure is by producing a two-phase mixture in which the phases are present in approximately equal proportions. Because of this very high ductility, which is coupled with a low flow stress, these alloys can be formed almost as easily as hot glass or thermoplastics. Further, their service properties can be generally better than conventionally-formed materials because a fine, uniform grain size is obtained which leads to better strength, ductility and fatigue resistance.

From a large number of superplastic alloys, the following are among those commercially available, namely,

(a) variants of the Zn - Al eutectoid with minor additions

(b) a stainless steel, IN 744 (67.5% Fe - 26% Cr - 6.5% Ni)

(c) Ti - base alloy, Ti 318 with 6% Al and 4% V

(d) Ni - base alloy IN 100

(e) Supral 150 (Al - 6% Cu - 0.5 Zr).

The reason for this short list is that many superplastic alloys offer an unattractive property poor creep resistance because of fine grain size and so find limited engineering use.

For example, Zn - Al eutectoid is highly superplastic at 250°C and maintains complete microstructural integrity even at strains in excess of 1500 %, but its strength and creep resistance is inadequate for many engineering applications; it creeps even at room temperature. On the other hand, superplastic alloys based upon better-known alloys which have been used for many years in the engineering industry - brasses, steels - often fail at relatively low elongations - less than 400 % - due to extensive grain boundary cavitation.

The materials in which cavitation has been reported are α - β brasses[5], aluminium bronze[6], Al-Zn-Mg-Zr[7], Al-Cu-Zr alloys[8], a Mg-6 Zn - 0.5 Zr alloy[9], microduplex steels[10], and Fe-Ni-Mo alloys[11]. For cavitation to occur, the two phases involved

must be incompatible[3] that is, supposedly show marked differences in 'properties' and in this context, mechanical properties and diffusivities would appear to be the most important.

The aim of this research programme was to identify the basic reasons for cavitation in superplastic alloys and to do that it was necessary to find out the properties of each of the two phases of a superplastic alloy. In this work, two alloys were used, firstly 78 Zn - 22 Al which does not cavitate and secondly, 60 Cu - 40 Zn which does, as models of each classs of behaviour. The choice of Zn - Al eutectoid was based on the fact that it is a classic superplastic alloy which has been studied in detail and although quite a large volume of literature is available on this alloy there is little evidence that it cavitates. Whilst 60 Cu - 40 Zn is an important engineering material, it suffers from serious cavitation when superplastically formed.

Ideally, this phenomenon would be investigated directly, that is, by an in-situ study of the deformation behaviour of each phase separately in its true environment in the duplex alloy and hence pinpointing out the phase incompatibilities, but existing techniques do not allow for this. Therefore, a different approach was used to collect the critical data i.e. properties of individual phases in a duplex alloy at the superplastic temperature.

A series of alloys were produced of compositions corresponding to those of the individual phases in the Zn - Al eutectoid and 60 Cu - 40 Zn alloys over a range of temperatures in the superplastic range. These alloys were tested in tension to determine the flow characteristics of each phase of the superplastic alloy at the superplastic temperature. But it is the behaviour of these phases in a duplex alloy of fine grain size which is a matter of real importance. Therefore, a hot hardness technique was used to determine the flow stress and activation energy for each phase in-situ in a duplex alloy in the superplastic temperature range.

To study variations of hardness with temperature a high-temperature microhardness tester was commissioned from A.E.D. Rugby, which enabled the indentations to be made and measured accurately at the same temperature. It was not possible to measure hardness in the superplastic - sized grains and therefore, the duplex alloys were annealed until the grain size was large enough for indentations to be made well within each grain and reasonably away from grain boundaries. This was achieved in 60 Cu - 40 Zn duplex alloy but Zn - Al eutectoid was found to show little grain growth after a small initial increase. Therefore, in-situ results for Zn - Al eutectoid could not be produced from this work. Instead, alloys that represented alpha and beta phases in the eutectoid were hot hardness tested to give hardness vs temperature relationship for each phase.

Finally, the same approach was used in an attempt to study the cavitation behaviour of Al/Cu/Zr (Supral 150) and certain steels, in some cases experimentally and in others from data available in the literature.

CHAPTER 2

2. LITERATURE SURVEY
SUPERPLASTICITY

2.1 Introduction

This anomalous ductility phenomenon has been reported as early as 1928 (by Jenkin[12]); Pearson[13] (1934) while studying some mechanical characteristics of Pb - Sn and B_i - S_n systems was able to obtain neck-free elongations of up to ~ 2000 %. However, it was Bochvar[14] in 1945 who introduced the term 'superplasticity' in his work to describe the ductility of Al - Zn alloys near the eutectoid composition (80 wt % Zn - 20 wt % Al) and at a temperature of 275^{o}C. The phenomenon has since been studied extensively by Presnyakov and other Russian workers and their work is fully referenced in the first English review of the subject by Underwood[1] (1962).

During those days, the reason for superplasticity was not understood at all and the phenomenon was merely of continuum interest. However, following the pioneering work of Backofen et al[15] and others[16-20], the subject received considerable attention and nowadays superplasticity is no longer a scientific curiousity but is the basis of a viable forming technique that is already being used commercially to manufacture components in Ni-, Ti-, Cu-, Al-, and Zn- base alloys[21]. The necessary conditions for superplastic flow and the materials in which superplasticity has been reported are now well-documented in a number of reviews[2,3,4,22,23] of the subject. Here, it is worth mentioning that cavitation of superplastic alloys has been generally neglected throughout these reviews except one[4] which discusses it to some extent. Since the study of cavitation is important in the understanding of the mechanism/or mechanisms of superplasticity, in the following sections emphasis will be given to the reasons put forward for superplasticity.

On the basis of large numbers of papers published on superplasticity, this subject can be divided into two groups, i.e. (a) environmental and (b) structural superplasticity.

2.2 Environmental Superplasticity

This type of superplasticity occurs in a wide range of materials during (i) temperature cycling through a phase transformation, (ii) thermal cycling of an anisotropic material (e.g. Zinc and Uranium), and (iii) neutron irradiation. Large amounts of elongation can be obtained when a material in one of these conditions (environments) is subjected to a small tensile stress. This form of superplasticity is fully described in a number of reviews (Johnson[3], Davies et al[2], Edington et al[4]) and no attempt is made to discuss it any further here because our main interest lies in the cavitation of materials

consisting of two phases present approximately in equal proportions, and which exhibit structural superplasticity.

2.3 Structural Superplasticity

This type of superplasticity in materials is associated with fine (<10 μm) equiaxed grain size at temperatures above 0.5 Tm. Large elongations in tension are achieved under relatively low load conditions and the initial microstructure is maintained during superplastic deformation. The material can be single-phase but those exhibiting maximum superplasticity consist of two phases, each of quite different chemical composition to minimise coarsening of small grains at the superplastic temperature. There is an empirical evidence[2,3] to believe that the various phases should have comparable ductility and be present in approximately equal proportions at the temperature of deformation.

This group of materials obey the following relationship (Backofen et al[15]),

$$\sigma = K' \dot{\varepsilon}^{m} \qquad (2 - 1)$$

where σ is the applied stress, $\dot{\varepsilon}$ the strain rate, K' a constant and m the strain-rate sensitivity index defined as

$$m = \frac{\delta \ln \sigma}{\delta \ln \dot{\varepsilon}} \qquad (2 - 2)$$

which is the slope of line in Fig. 1 at any particular strain rate. The sigmoidal variation of $\ln \sigma$ with $\ln \dot{\varepsilon}$, which is usually observed in superplastic materials, can be conveniently divided into three regions. Regions I and III where $m \leq 0.3$ correspond to conventional plasticity and region II ($0.3 \leq m \leq 1$) defines the strain rate range over which superplasticity occurs. The parameter m is very important in superplasticity and represents the ability of a material to resist necking (see the following section).

In general, maximum elongations are obtained under conditions of maximum m. In fact, Woodford[24] has pointed out that there exists a general relationship between the value of m and elongation to failure and this is shown in Fig. 2. As m increases elongation to failure increases. However there are a number of anomalies[4] which probably arise from structural changes which alter m during the test. For example, the Zn - Al eutectoid alloy ($m = 0.5$) gives larger elongations than the Al - Cu eutectic ($m = 0.7$). Fig. 3 gives a summary of the influence of important parameters on the mechanical properties of superplastic materials and Fig. 4 summarises the important metallographic and texture changes accompanying superplastic deformation, in different regions of the $\ln \sigma - \ln \dot{\varepsilon}$ curve.

2.4 Strain-rate Sensitivity Index and Plastic Flow

At temperatures below 0.3 T_m , the plastic flow of metals during tensile deformation is stabilised by strain-hardening effects and instability occurs when the material has exhausted its ability for strain-hardening. In this case, the uniform plastic flow of metals can be described by the equation

$$\sigma = A \varepsilon^N \qquad (2 - 3)$$

where σ and ε are the true stress and true strain respectively, A a constant and N the strain hardening index. Usually N lies within the range 0.1 to 0.3.

It can be easily shown that at the point of instability, $\varepsilon = N$. Since $N < 0.3$, a uniforn elongation will not exceed about 30%. As temperature increases, N decreases and materials should exhibit small elongations because the strain-hardening effects are now of less significance, yet at temperatures above 0.5 T_m materials often undergo extensive plastic deformation without necking. At elevated temperatures the important parmeter is not N but m, the strain-rate sensitivity inded. In fact, it was demonstrated experimentally by Backofen et al[15] and analytically by Rossard[25] that the magnitude of strain-rate sensitivity is of considerable importance in most cases of superplastic deformation.

Analysis of plastic stability, when both strain-hardening and strain-rate effects are taken into account, was done by Rossard[25] and Hart[26]. It was assumed that a mechanical equation of state exists of the following form

$$\sigma = k' \varepsilon^N \dot{\varepsilon}^m \qquad (2 - 4)$$

where $\dot{\varepsilon}$ is the strain-rate and m the strain-rate sensitivity index and k' a constant. Then the general condition for plastic stability is

$$N + m > 1 \qquad (2 - 5)$$

For materials which are not strain-rate sensitive, Equation (2-4) reduces to Equation (2-3); and in the case of superplastic materials which show little (i.e. small N) or no (i.e. N = 0) work-hardening effects, Equation (2-4) reduces to Equation (2-1).

Now substituting σ in terms of load and area; and $\dot{\varepsilon} = -\frac{1}{A}\frac{dA}{dt}$, Equation (2-1) can be written as

$$-\frac{dA}{dt} = \left(\frac{W}{k'}\right)^{1/m} \cdot A^{\frac{m-1}{m}} \qquad (2 - 6)$$

The minus sign indicates that cross-sectional area of the specimen decreases as the test goes on.

Case 1. when m = 1 i.e. Newtonian flow
the rate at which cross-sectional area decreases is independent of area A (and hence stress) and therefore 'neck-free' uniform flow occurs.

Case 2. when m < 0.3 i.e. non-superplastic flow
$\frac{dA}{dt}$ is strongly dependent on A and smaller cross-sections are therefore rapidly reduced.

Case 3. when 0.3 < m < 1 i.e. superplastic flow
$\frac{dA}{dt}$ is very weakly dependent on A. Thus although plastic instability ('necking') does occur during superplastic flow, the material in the neck does not extend at a rate significantly faster than the rest of the specimen, because any stress increase in the necking region will produce only a small increase in strain rate and the result is as if 'neck-free' flow has taken place in the whole of the specimen gauge length. In fact, Morrison[10] and Wray[27] have shown the formation of a series of diffuse necks during superplastic flow.

2.5 Activation Energy for Superplastic Flow

In practice, most systems often do not exist in a state of minimum free energy which would correspond to their equilibrium position, but rather stay in a state called metastable equilibrium (e.g. the equilibrium state of most metals in the earth's crust is their oxide). It frequently happens that in order to reach its equilibrium state of minimum free energy, the system must pass through a higher energy state (called the activated state). Thus there is a barrier and until the system can temporarily acquire the necessary extra energy to carry it over this barrier, it must reamin in the metastable position. This minimum extra energy required to cross the barrier is called activation energy.

Consider for example the diffusion of atoms in a metallic system. For an atom or vacancy to move from one lattice point to the next it must possess the necessary energy to overcome the energy barrier, Q. Since the probability that an atom has sufficient energy to jump the barrier is proportional to $e^{-Q/kT}$ (using Maxwell-Boltzmann Law, see Smallman[28]), the rate of reaction is given by Arrhenius equation

$$\text{Rate} = A' \exp\left(-\frac{Q}{kT}\right) \qquad (2 - 7)$$

where A' is a constant that includes the number of atoms that possess the required energy Q and the frequency of vibration, k a Boltzmann constant.

The temperature-dependence of superplastic strain-rate is not well established at present. However, assuming a thermally activated mechanism for superplastic deformation, it can be described as follows[2]

$$\dot{\varepsilon} = \text{Constt} \ \frac{\sigma^n}{L^a} \ \exp\left(\frac{-Q}{kT}\right) \qquad (2 - 8)$$

where L is the grain size, a has values 2 or 3 and $n = \frac{1}{m}$ with m the strain-rate sensitivity index.

For a constant grain-size material, Equation (2-8) can be written as

$$\ln \dot{\varepsilon} = \text{Constt} + \frac{1}{m} \ \ln \sigma - \frac{Q}{kT} \qquad (2 - 9)$$

which can be used to find out the activation energy at constant stress or at constant strain-rate. In fact, Padmanabhan and Davies[29] has shown that

$$Q_{(\text{Const } \sigma)} = \frac{1}{m} \ Q_{(\text{Constt } \dot{\varepsilon})} \qquad (2 - 10)$$

holds good for superplastic flow.

However, on account of the temperature dependence of m, experimental determination of the activation energy from =n (8) involves approximations which leads to scatter of results[23]. Reported values of the activation energy for superplastic deformation, together with measured values for diffusional processes, are collected for a number of materials in reference[2]. Activation energy values generally fall into two categories: one where the same value is observed in conventional creep by dislocation climb (activation energy) for lattice self-diffusion), and the other where values are somewhat lower and can be identified with grain boundary diffusion energy.

2.6 Mechanisms of Superplasticity

2.6.1 Introduction

Some of the earliest theories of superplasticity, particularly those of Bochvar and Presnyakov are fully described in Underwood's review[1] of the subject. It was thought that superplasticity occurs under conditions associated with a phase change, or, more generally, with a temporary structural change involving breaking of atomic bonds in the crystalline lattice. According to Soviet theorists the application of a stress at high temperatures leads to profound changes in the structure of solid solutions and promotes a rearrangement of the atoms. A theory based on such concepts was put forward by Bochvar and is called the solution-precipitation

theory. An essential feature of this theory, which is based on the transfer of a solute through a solution, is that it occurs primarily at the interface between phases. On the other hand, Presnyakov is of the opinion that superplasticity occurs as a result of the breakdown of the initially metastable state.

As the number of alloys exhibiting superplasticity increased, these theories were shown to be inadequate by various workers and summarised by Chaudhari[30].

2.6.2 Diffusion Creep

Stress-directed vacancy migration process, which is the rate-controlling mechanism in creep deformation at low stresses and high temperatures, has been used by many workers[16,31,32] to explain superplasticity. In a tensile region, the energy to create a vacancy is aided by the stress whereas in a region under compression it is opposed by the stress. There will, therefore, be a concentration of vacancies above the equilibrium vacancy concentration in a tensile region and below the equilibrium value in a compression region. Consequently, there is a net flow of vacancies from one region (under tension) to the other (under compression) and the atom flow in the opposite direction. Grain boundaries are considered to be perfect sources and sinks for vacancies at high temperatures. Then, if the stress-directed flow of vacancies occurs through the lattic, Nabarro-Herring creep occurs with a strain-rate

$$\dot{\varepsilon} = \frac{B_1}{L^2} \frac{\Omega\sigma}{kT} D_L \qquad (2 - 11)$$

and if the stress-directed flow of vacancies occurs along the grain boundaries, Coble creep occurs with a strain-rate

$$\dot{\varepsilon} = \frac{B_2}{L^3} \frac{\Omega\sigma}{kT} w D_{g.b} \qquad (2 - 12)$$

where L is the grain size, Ω the atomic volume, and w the grain boundary width; B_1 and B_2 are constants; D_L and $D_{g.b}$ are the diffusion coefficients for lattice and grain boundary diffusion.

If both grain and grain boundary diffusion paths are taken into account, a complete diffusion equation is obtained[33] giving

$$\dot{\varepsilon} = \frac{20\ \Omega\sigma\ D_L}{kT\ L^2} \left(1 + \frac{\pi\ w\ D_{g.b}}{L\ D_L}\right) \qquad (2 - 13)$$

where the first term describes the contribution of bulk diffusion and the second that of grain boundary diffusion.

According to these theories, creep strain accumulates by the elongation of individual grains in the direction of the applied stress. But this is in contradiction to the experimental observations that, in general, during superplastic deformation very little grain elongation occurs. Also, it has been shown by Alden[17] and Hayden et al[34] that the calculated values of strain-rates based on these theories are too small, often by several orders of magnitude. From Equation (2-11, 12, 13), $m = 1$ is predicted, but the measured values of m are usually <1 and fall within the range 0.3 - 0.8. However, if a σ_o term is introduced which might reflect the difficulty of interfaces in acting as sources and sinks for vacancies, Karim[35,36] has shown this problem may be overcome and the measured value of m is given by

$$m = \left(\frac{\sigma - \sigma_o}{\sigma_o}\right) \bar{m} \qquad (2 - 14)$$

where $\bar{m}$ is the true value of $m = 1$.

Furthermore, these theories predict that texture existing prior to deformation is maintained, which is again in conflict with the experimental observations that texture is destroyed by the superplastic deformation.

Avery and Backofen[16] proposed that the strain-rate in a superplastic deformation can be expressed in the form

$$\dot{\varepsilon} = \frac{A'\sigma}{L^2} + B \operatorname{Sinh} \beta\sigma \qquad (2 - 15)$$

where A', B and β are constants at a given temperature. The first term in the above equation describes the contribution of Nabarro-Herring creep which dominates over the dislocation climb (second term) at low values of strain-rates and leads to $m = 1$ at very small stresses. But, in general, m reaches a maximum of <1 as the strain rate falls and then decreases again. However, it has been suggested[37,38] that the fall in m at low strain rates may be only an apparent effect arising out of the presence of a back stress, σ_o. Therefore, the operative stress is now $(\sigma - \sigma_o)$ and at low stress the region of apparent low m is changed to one of high m (see Fig. 5).

Sherby and Packer[39] used Weertman's expression as the second term in Eqn (15) to describe non-superplastic high strain-rate beahviour and substituted $\frac{A'' \sigma^2}{L^3}$ for the first term to get

$$\dot{\varepsilon} = \frac{A'' \sigma^2}{L^3} + B' \sigma^2 \operatorname{Sinh} \beta' \sigma^{2.5} \qquad (2 - 16)$$

which was shown to be satisfactory for the Pb-Sn data of Avery and Backofen[16].

2.6.3 Dislocation Creep

One of the earliest models was that due to Chaudhari[30], who proposed that superplastic deformation occurs entirely by the motion of dislocations within the grains. This model requires an internal stress which opposes dislocation motion and is supposed to arise from the accumulation of $\sim 10^{11}$ dislocations within the grains. But in practice no dislocations or cells are observed after superplastic deformation. Secondly,his mechanism does not explain how the grains can remain equiaxed during deformation.

In another dislocation model for superplasticity, Hayden et al[34] suggested that the square root dependence of stress on strain-rate may be an important feature of superplastic flow and point out that a similar stress dependence is predicted in the recovery creep analysis of Mott[40] and Friedel[41] . According to this model

$$\dot{\varepsilon} = \text{Constt} \frac{\sigma^2}{L} \exp\left(\frac{-Q}{kT}\right) \qquad (2 - 17)$$

It was predicted by Hayden et al[34] that the leading dislocation in a pile-up will be an appreciable distance from the grain boundary so that its climb-rate would be controlled by volume diffusion in agreement with their measured activation energies. However, the activation energy for the process should be that of grain boundary diffusion, because in the Mott and Fridel model the dislocations pile up against the grain boundary and the leading dislocation escapes from the pile-up at a rate determined by grain boundary diffusion.

From Equation (2-17), $\dot{\varepsilon} \alpha \frac{1}{L}$ which is not generally observed.

Secondly, the absence of dislocations and cells in grains after the superplastic deformation makes a justification of this model difficult.

Hayden and Brophy[42] proposed a new dislocation model for superplasticity based on Weertman's[43] climb theory. According to this model, there is only one dislocation source in each grain and that the back stress of a gliding dislocation prevents the further operation of source until the dislocation has climbed out of the slip plane. If a constant density of sources is assumed, the strain-rate can be described[44] as

$$\dot{\varepsilon} = \text{Constt} \quad \sigma^2 L^2 \exp\left(\frac{-Q}{kT}\right) \qquad (2 - 18).$$

Although this model predicted no dislocation pile-ups and tangles after the superplastic deformation, it is in contradiction to the observed relationship between strain-rate and grain size (i.e. $\dot{\varepsilon} \alpha L^2$).

2.6.4 Recrystallisation

Models involving dynamic recrystallisation [45,46], which have some similarity to mechanisms of hot working[47] have been proposed for superplasticity. For example, a model for superplasticity in two phase alloys involving crystallographic slip and continuous recovery by grain boundary migration or recrystallisation has been put forward by Packer, Johnson and Sherby[45] . However, some doubts on this model have been expressed by Davies et al[2] on the basis that (a) there is no periodic fluctuation in the flow stress during superplastic flow, as would be expected if repeated recrystallisation occurred[17], (b) in high temperature creep under thermal and mechanical conditions similar to those required for superplastic deformation no recrystallisation takes place[48], (c) no recrystallisation is seen during direct observation of superplastic flow[49]. However, it has been suggested[50] that recrystallisation occurs in the commerical Al - 6wt % Cu - 0.5 Zr, Al - Zn - 0.5 Zr, Al - Zn - 1 wt% Mg - 0.5 Zr alloys during at least the initial stages of superplastic deformation. On the basis of present evidence it appears that dynamic recrystallisation is not an important component in the superplastic deformationof most materials.

2.6.5 Grain Boundary Sliding

It is generally observed that the grain structure remains essentially equiaxed and very little grain growth occurs during superplastic deformation. These observations lend support to the suggestion that a major part of the total strain is due to grain boundary sliding[37,51]. In fact, a number of workers[17,31, 45, 52-55] have shown its importance during superplastic deformation since offsets have been observed where polishing scratches cross grain boundaries. Such offsets were used by Holt[19] to determine the importance of sliding in an aluminium-zinc entectoid alloy. It was found that

$$\gamma_o = 100 \times \frac{\varepsilon_{g.b} \text{ (Strain due to grain boundary sliding)}}{\varepsilon t \quad \text{(Total strain)}} \qquad (2 - 19)$$

reached values up to 60% at intermediate rates of strain.

The theoretical limit of the contribution of grain boundary sliding to the total strain has been estimated[56] to be 60-65%. This upper limit of 60-65% contribution from sliding is a consequence of the assumption that both diffusion and grain boundary sliding are present as separate steps and that the latter accommodates diffusional flow.

Very recently a new model based on a viscous boundary approach for superplasticity is presented by Padmanabhan[23] which under suitable conditions can account for 100% contribution from grain boundary sliding. The important features of this model are:

(a) ideal superplastic deformation occurs as a result of 'pure' grain boundary sliding which requires no accommodation,

(b) The relative movement of grains is considered to arise from the accumulation of localised and atomic scale displacement in the grain boundary region,

(c) the localised movements are caused by atom-vacancy exchanges,

(d) the entire deformation is concentrated in the grain boundary region,

(e) the activation energy for the process is that for grain boundary diffusion in the alloy,

(f) the model is similar to the $\hat{\nu}_e$ model[47] in that it involves only a few atoms at a time and an accumulation of localised flow leads to unlimited deformation.

According to this model

$$\dot{\varepsilon} = \frac{c' d_o}{L^2} \sigma^n \exp\left(\frac{-Q}{kT}\right) \qquad (2 - 20)$$

where c' is a constant, d_o the atomic jump distance which for metallic materials is approximately the same ($\sim$ interatomic distance, i.e. $2\text{-}3A^o$), and n given as

$$n = \left[\frac{1}{L} + Po\left(1 + \frac{1}{\ell n\ Z^*}\right)\right] (A + B\ \ell n\ L)\left(b_1 + \frac{b_2}{T}\right) \qquad (2 - 21)$$

with po, A, B, b_1 and b_2 as constants, Z^* the shear stress, L the grain size and T the temperature.

When n is identified as stress sensitivity ($= 1/m$), Eqn (20) simplifies to

$$\dot{\varepsilon} \alpha \frac{\sigma^{1/m}}{L^2} \exp\left(\frac{-Q}{kT}\right) \qquad (2 - 22)$$

which is the empirical equation for superplastic flow.

The model, however, is valid only for low stresses where no other mechanism is operating and since the entire deformation is occurring in the grain boundary region, it is applicable only to materials with an ultra-fine grain size. Furthermore, the mobilities of all types of boundaries are considered to be comparable and this model cannot be used when the mobilities of the different types of boundaries are dissimilar.

Other models for superplasticity involving grain boundary sliding [20,48] consider sliding as a unit process involving the entire boundary which requires subsequent accommodation. Local accommodation may take place by the motion of run-in dislocations in or near the grain boundary. Such a model, based on grain boundary sliding in terms of motion of dislocations along or adjacent to the boundary by a combination of climb and glide, was used by Langdon[50] to obtain the following rate equation

$$\dot{\varepsilon} = \frac{\beta' b^2 \sigma^2 D_L}{L G k T} \qquad (2 - 23)$$

where β' is a constant close to unity and D_L the coefficient of lattice diffusion. The use of D_L in Equation (2-23) was based on the limited experimental evidence that the activation energy for grain boundary sliding corresponded to volume diffusion. However, a more recent study[59] has concluded that sliding is controlled by grain boundary diffusion, so that $D_{g.b}$ should be used in place of D_L in the above equation.

Grain boundary sliding may also be accommodated by plastic flow in which case dislocations are generated at ledges[51] and then travel either along the grain boundaries, or through the lattice, or both. Accommodation by diffusion of atoms from part of the boundary under compression to another region under tension was considered by Raj and Ashby[33]. In this model sliding is considered to be controlled by the rates of diffusion around steps on the boundary. The strain-rate is given by

$$\dot{\varepsilon} = \frac{C Z_a \Omega}{kT} \cdot \frac{D_L}{L^2} \left[1 + \frac{\pi w}{\lambda} \times \frac{D_{g.b}}{D_L} \right] \qquad (2 - 24)$$

where Z_a is shear stress, C a constant, λ the wavelength or distance between steps. The first term in the bracket is the contribution from a lattice diffusion path and the second along the grain boundaries. Since the diffusion path is now decreased, the strain-rate would be faster and the process would therefore be expected to have a high strain-rate sensitivity.

Ball and Hutchinson[60] proposed that groups of grains slide as units during superplastic deformation. The shear stress on a group becomes concentrated on any grain or protrusion that obstructs the motion of group. The resultant stress concentration is relieved by the generation of dislocations in the blocking grain that pile-up at the opposite grain boundary until their back stress prevents further generation of dislocations and thus further sliding by the group. However, the dislocation at the head of the pile-up can climb into and along the grain boundary. The continuous removal of these dislocations permits grain boundary sliding at a rate governed by the kinetics of dislocation climb along grain boundaries to annihiliation sites. This model leads to the following expression for strain-rate

$$\dot{\varepsilon} = \text{Constt.}\ D_{g.b.}\ \frac{\sigma^2\ b^2}{G\ kT\ L^2} \qquad (2 - 25)$$

However, it was pointed out by Mohammed et al[61] that the postulate of Ball and Hutchinson that a group of grains slide as a unit is not supported by the direct observations of superplasticity in the scanning electron microscope.

A mechanism similar to Ball and Hutchinson's except that individual grains rather than groups of grains slide, was proposed by Mukherjee [62]. According to this model sliding is accommodated by the generation of dislocations at ledges or protrusions in the grain boundary surface. These dislocations traverse the blocked grain and pile up at the opposite grain boundary. The rate of sliding is then determined by the rate of climb of dislocations from the head of the pile up to the appropriate annihiliation sites along the grain boundary. The strain-rate is

$$\dot{\varepsilon} = \text{Constt.}\ (b)\ D_{g.b.}\ \frac{\sigma^2\ b^2}{G\ kT\ L^2} \qquad (2 - 26)$$

which is very similar to Equation (2-25). Using this model, a reasonable correlation between the experimental and theoretical $\ell n\ \sigma$ vs $\ell n\ \dot{\varepsilon}$ relationship was obtained for a Zn - Al eutectoid.

Both these mechanisms suffer from the same criticism that pile-ups of dislocations are not observed after superplastic deformation. Further, in any case the existence of pile-ups in most materials is unlikely, because at such high deformation temperatures and low stresses dislocations would be expected to climb/cross-slip out of their slip plane while transversing the grain[4].

According to a recent model proposed by Gifkins[63], sliding takes place by the motion of grain boundary dislocations that pile up at triple points. The stress concentration thus set up at a triple point is relieved by dissociation of the leading dislocation in the pile up into grain boundary dislocations capable of moving in the remaining two boundaries and/or into crystal dislocations which accommodate sliding. These new dislocations then climb/glide in or near the boundaries until they meet others, when they may annihiliate or combine with them to form different grain boundary dislocations. The rate equation is

$$\dot{\varepsilon} = \text{Constt.}'\ (b)\ D_{g.b.}\ \frac{\sigma^2\ b^2}{G\ kT\ L^2} \qquad (2 - 27)$$

which is the same as eq (26) except that the constants in the two equations are different. However, direct evidence for this mechanism is not available at present. Furthermore, from Equation (2-25, 26, 27) $\dot{\varepsilon} \alpha \sigma^2$ i.e. maximum value of m = 0.5 but

in practice m >0.5 have been reported in many cases of superplastic deformation.

A new mechanism based on grain boundary sliding with diffusional accomodation was proposed by Ashby and Verral[20]. They identified a grain switching event, shown schematically in Fig. 6, which was first recognised by Rachinger[64] and has been observed by Naziri, Pearce, Henderson-Brown, and Hale[65] during in situ deformation of the Zn - Al eutectoid alloy in the high voltage electron microscope. The model differs fundamentally from Nabarro-Herring and Coble creep in the sense that grains switch their neighbours and do not elongate significantly.

Ashby and Verral model the unit step of the process by considering the relative motion of a group of four grains as shown in Fig. 6. This relative motion causes the cluster as a whole to change shape. Meanwhile the grains themselves suffer accommodation strains which permit them to remain stuck together. In their model, these accommodation strains are accomplished by diffusion - both lattice and grain boundary. It can be seen from Fig. 6 that the shapes of individual grains in the initial and final states are identical, but the shape of the group has changed (by a true strain of 0.55) allowing the external stress to do work.

This work drives four irreversible processes:

(1) The diffusive process by which the grains temporarily change shape, suffering accommodation strains. (Fig. 7).

(2) The interface reaction: i.e. grain or phase boundaries may be imperfect sinks or sources for point defects.

(3) Grain boundary sliding: as well as the normal displacements which diffusion produces, shear displacements occur in the boundary plane.

(4) Fluctuations of boundary area: the grain boundary area increases as the cluster of four grains moves from the initial to the intermediate state, storing free energy in the system; as the cluster moves from the intermediate to the final position the boundary area decreases again, releasing the energy.

At steady state, the rate at which work is done by the applied stress is equal to the power dissipated internally by the above four irreversible processes. Assuming no interface barrier - that is, that boundaries act as perfect sinks and sources of vacancies, the constitutive equation for diffusion-accommodation flow is

$$\dot{\varepsilon}_{\text{D.A flow}} = \frac{100\ \Omega}{kT\ L^2}\left[\sigma - \frac{0.72\Gamma}{L}\right] D_L \left(1 + \frac{3.3\ \delta}{L}\ \frac{D_{g.b}}{D_L}\right) \qquad (2 - 28)$$

where Γ is the grain boundary free energy, δ is the thickness of the boundary as a high diffusivity path.

Equation (2-28) resembles that for combined Nabarro-Herring and Coble creep (Equation 2-13) from a mechanical point of view though it predicts strain-rates about an order of magnitude faster, because less diffusion is needed for a given strain. But from a topological point of view, it is quite different: grains change their neighbours and do not show extensive elongation.

The model predicts a small threshold stress below which no flow is possible. The reason is that unless the external stress does enough work to supply the energy stored temporarily as new boundary, flow cannot occur.

Ashby and Verral also considered the case when grain boundaries are not perfect sources and sinks for point defects. The ability of a boundary to act as a source or sink for point defects can be described by an interface potential $\Delta\mu_i$ required to drive the boundary as a sink or source. A boundary with a low $\Delta\mu_i$ is a good sink or source and vice versa. In this case, the constitutive equation becomes

$$\dot{\varepsilon} = \frac{100\ \Omega}{kT\ L^2}\left[\sigma - \frac{0.72\Gamma}{L} - 0.84\ \Delta\mu_i\right] D_L \left\{1 + \frac{3.3\delta}{L}\ \frac{D_{g.b}}{D_L}\right\} \qquad (2 - 29)$$

If grain boundary dislocations are the actual sources and sinks for point defects and are also responsible for sliding,

$$\Delta\mu_i = \frac{\dot{\varepsilon}\ \Omega\ L}{\rho\ b_n^2 M} \qquad (2 - 30)$$

and Equation (2-29) becomes

$$\dot{\varepsilon} = \frac{100\ \left(\sigma - \frac{0.72\Gamma}{L}\right)}{kT\ L^3}\ \text{Deff.}\ \frac{\rho\ b_n^2\ M}{0.84}\left\{\frac{1}{\frac{\rho\ b_n^2 M}{0.84\ \Omega\ L} + \frac{100\ \Omega}{kT\ L^2}\ \text{Deff}}\right\}$$

where $\text{Deff} = D_L\left[1 + \frac{3.3\ \delta}{L} \times \frac{D_{g.b}}{D_L}\right]$ (2 - 31)

with ρ the density of dislocations in the boundary plane, M the mobility of the boundary dislocation and b_n the component of its Burgers vector which is normal to the boundary plane.

When the mobility M and density ρ of the dislocations are large, Equation (2-31) reduces to Equation (2-28) and deformation is diffusion controlled. But when M and ρ are small the deformation is interface-reaction controlled.

For an interface-reaction controlled deformation, Ashby and Verral suggested

$$\rho = \beta \left(\frac{\sigma}{G\, b_n}\right) \qquad (2 - 32)$$

that is, a dislocation density that increases linearly with stress. β is a constant of order unity. Using Equation (2-32) and when M and ρ are small equation (2-31) becomes

$$\dot{\varepsilon} = \frac{1}{0.84} \cdot \frac{\sigma}{G} \left(\sigma - \frac{0.72\Gamma}{L}\right) \frac{\beta b M}{\Omega L} \qquad (2 - 33)$$

Thus $\dot{\varepsilon} \alpha \sigma^2$ except near the threshold limit ($\frac{0.72\Gamma}{L}$ is the threshold stress due to fluctuations in boundary area), which gives m = 0.5 and may account for the common observation of m = 0.5 in certain superplastic alloys.

When L is sufficiently small, Equation (2-31) reduces to Equation (2-33) and therefore the fine grain size favours interface-reaction control according to this model. Neglecting the threshold stress $\frac{0.72}{L}$ in Equation (2-33),

$$\dot{\varepsilon} = \frac{\beta b M}{0.84\, \Omega G} \left(\frac{\sigma 2}{L}\right) \qquad (2 - 34)$$

Thus this model predicts, $\dot{\varepsilon} \propto \frac{\sigma^2}{L}$ for a fine-grain size materials.

When the two components of an alloy have different diffusivities, the components redistribute themselves under stress, leading to concentration gradients in the alloy. In deriving Equation (2-28), this additional energy-storing and energy-dissipating process has been ignored.

There has been general agreement for quite some time that in the region beyond peak m (region III in Fig.1) where the strain rate sensitivity is graudally decreasing, the dominant mechanism is climb-controlled motion of dislocations. The constitutive equation describing this sort of flow is (see Mukherjee et al [66])

$$\dot{\varepsilon} = A_1 \frac{Gb}{kT} \left(\frac{\sigma}{G}\right)^n \exp\left(\frac{-Q_c}{kT}\right) \qquad (2 - 35)$$

where A_1 and n are empirical constants and Q_c is the activation energy for dislocation creep.

The overall description of superplasticity based on the Ashby and Verral model is then obtained to a sufficient approximation by adding Equations (2-28) and (2-35):

$$\dot{\varepsilon} = \frac{100\ \Omega}{kT\ L^2}\left(\sigma - \frac{0.72\Gamma}{L}\right) D_L \left\{1 + \frac{3.3\ \delta}{L}\ \frac{D_{g.b}}{D_L}\right\} + A_1 \frac{Gb}{kT}\left(\frac{\sigma}{G}\right)^n \exp\frac{-Q_c}{kT}$$

(2 - 36)

Using input data for lead in Equation (2-36), the general form of $\ell n\sigma/\ell n\ \dot{\epsilon}$ relationship is shown in Fig. 8. Clearly the overall form of the relationship is correct. In the low-stress regime, diffusion-accommodated flow is dominant; it accounts for 99 per cent or more of the total strain-rate. In the high stress regime, dislocation creep is dominant; it accounts for 99 percent or more of the total strain rate. In the intermediate stress regime, the two mechanisms each contribute more than 1 per cent of the total strain-rate. However, the elongation caused by the dislocation creep component will interfere with the grain-switching mechanism and as a result the intermediate stress regime becomes narrower.

Padmanabhan[23] combines dislocation-creep Equation (2-35) and boundary flow Equation (2-20) mechanisms to obtain an overall description of superplasticity:

$$\dot{\varepsilon} = \frac{c'd_o}{L^2}\ \sigma^n\ \exp\left(\frac{-Q}{kT}\right) + A_1 \frac{Gb}{kT}\left(\frac{\sigma}{G}\right)^n\ \exp\left(\frac{-Q_c}{kT}\right)$$

(2 - 37)

At low stresses, only the boundary flow mechanism operates. Once the stress is sufficient to activate dislocation sources there will be a zone where both the viscous flow and dislocation mechanisms are important. However, climb-controlled dislocation motion absorbs vacancies[67] and this will reduce the number of vacancies available for viscous flow process. Thus the region in which both the mechanisms are important becomes narrower. Beyond this, dislocation motion (= n 35) is predominant.

Recently Gifkins[68] has developed his earlier model[69] which was based on the divison of grains into their central 'cores' and peripheral 'mantles'. According to this model, grain boundary sliding and its accommodation (i.e. by fold formation, dislocation motion in the mantle or pure diffusion) is limited to the 'mantles' of grain while the 'cores' remain practically undeformed except at high enough stresses. Grain boundary sliding is produced by the motion of grain boundary dislocations that pile-up at triple edge. Under the stress concentration thus generated they dissociate into crystal dislocations in the sliding grains and then glide and climb in the mantle along adjacent grain boundaries giving grain rotation; eventually they are annihiliated or recombine to form new grain boundary dislocations.

In region III, deformation occurs by grain boundary sliding accommodated by dislocation generation at triple point folds. There is a general dislocation motion in the core. In region II, grain boundary sliding occurs with accommodation in a narrow mantle in the vicinity of the grain boundary, very few dislocations being present in the core. In region I, grain boundary sliding occurs with accommodation in a very narrow mantle, there being no dislocations present in the core, as is the case for diffusion-creep via grain boundaries. The model is consistent with the observed lack of recrystallisation and limited grain growth. However, direct evedience for this mechanism is not available at present.

A theory of superplastic flow in two-phase materials is proposed by Gittus [70]. In this theory, the unit process is assumed to be the grain-switching event observed during superplastic flow [65]. The geometry of this process has been idealised by Ashby and Verral[20] and their values for diffusion distances and for the relationship between sliding and strain are adopted.

It is based on a model process in which dislocations from the head of the pile-up climb in a boundary - the interphase boundary. As dislocations are rarely seen inside the grains during superplastic flow, it is postulated that the pile-ups occur on dislocation interphase boundaries and that dislocations climb away from the head of the pile-up into adjacent disordered segments of the interphase boundary. Sliding then occurs at an interphase boundary as dislocations glide toward the head of the pile-up to replace those which have climbed into disordered regions of the boundary. Sliding at a dislocation interphase boundary by the glide of a single dislocation is theoretically resisted by large energy barriers due to the disorder which its passage creates. It is postulated therefore that dislocations glide in pairs, as interphase boundary super-dislocations. The first of a pair of boundary dislocations creates disorder, but the second dislocation, when it passes along the same path, restores order once more.

The strain rate is given by

$$\dot{\varepsilon} = 53.4 \frac{D_B}{k} \frac{\mu b}{T} \left(\frac{\sigma - \sigma_o}{\mu}\right)^2 \left(\frac{b}{L}\right)^2 \qquad (2 - 38)$$

where μ is an effective shear modulus defined as a function of the two moduli μ_α and μ_β.

$$\mu = f(\mu_\alpha, \mu_\beta) \qquad (2 - 39)$$

D_B, the coefficient of interphase boundary diffusion, and σ_o, the dislocation friction-stress.

The threshold stress for superplastic flow is identified with the stress which pins interphase boundary super-dislocations to the boundary ledges.

It was found by Baudelet et al [71], in their studies of Cu-P alloys, that the activation energy for superplastic flow, calculated with no care to correct for change in structure, was close to that for grain boundary diffusion in copper. When, however, corrected for change in structure, it corresponded to that for volume self-diffusion in copper. This high value of activation energy in two-phase materials can now be explained, since recent measurements[72a] has shown that the activation energy for self-diffusion in interphase boundaries can itself be high, and is much nearer to the value for volume self-diffusion than to that for grain boundary diffusion. On the basis of these studies, Gittus has pointed out that the high value of activation energy may be a general feature of superplastic flow in two-phase materials.

However, the suggestion that the formation of super-dislocations during deformation may be a quite general phenomenon in interface boundaries is based on a single investigation of interphase boundary structure by Nakagawa and Weatherley[72b] and actually observed pairs of dislocations in the interface between the lattices of Ni_3 Al and Ni_3 Nb in a directionally solidified eutecticalloy. More evidence of super-dislocations in inter-phase boundaries of the two-phase superplastic materials is necessary.

CHAPTER 3

3. LITERATURE SURVEY

CAVITATION IN CREEP AND SUPERPLASTICITY

3.1 Introduction

It is clear from the foregoing that grain boundary sliding (GBS) is an important mode of superplastic deformation. GBS also plays in important role in creep deformation at high temperatures and low stresses and gives rise to cavitation in creep [73]. Thus GBS should lead to cavitation in superplastic deformation as well, because there is a close similarity between deformation processes of creep and superplasticity. Until 1970, except for a few reports [9,10] of cavitation, it was generally thought that superplastic deformation occurred with little void formation [2,3]. Since that time, a number of alloys i.e., α - β brasses [5], aluminium bronze [6], Al - Zn - Mg - Zr [7], Al - Cu - Zr alloys [8], a Mg - 6 Zn - 0.5 Zr alloy [9], microduplex steels[10], and Fe - Ni - Mo alloys , have been shown to cavitate during superplastic deformation. The phenomenon of cavitation was largely neglected and the various ideas put forward to explain it, accurately dealt with cavitation in creep. Edington[21] is of the opinion that, if a material cavitates during creep, it is likely to do so at certain combinations of temperature and strain-rate in superplastic deformation. Consequently, many Cu-, Fe-, Al-, and Ni- base alloys may in fact cavitate generally in superplastic tensile deformation, although others, notably Ti-, Zr-, and Pb- base alloys, will probably not because they do not do so in creep.

The subject of cavitation in creep has been reviewed by Greenwood[74] (1969) and recently by Perry[75] (1974), so only the important points will be presented here, while the progress made so far in the field of cavitation behaviour of superplastic alloys will be discussed in detail.

3.2 Cavitation in Creep

3.2.1 Introduction

A number of metals when tested in tension at temperatures in the range 0.3 to 0.9 T_m often fail after a relatively limited extension due to either cracking at grain boundary triple points or the formation of cavities on boundaries. It is the development of this latter type leading to premature failure with limited ductility which is termed creep cavitation and this is favoured by lower stresses as compared to the triple-point cracking which occurs at higher stresses.

The general features[75] of creep cavitation include the nucleation and growth of cavities on grain boundaries which are approximately normal to the applied stress. They only form if the temperature is sufficiently high and the rate of deformation

is sufficiently low. The formation of cavities is usually associated with grain boundary sliding[76] which contributes a constant fraction of the overall strain in a given test[77] and this contribution becomes greater as the grain size is reduced[76,78].

3.2.2 Nucleation

It was first propsed by Greenwood[79,80] that the nucleation of cavities might arise from the condensation of vacancies at the grain boundaries, but it has been shown that the super-saturation of vacancies required to nucleate a cavity by their spontaneous agglomeration is too high to be plausible[81]. In order to form cavities, it is then necessary to consider mechanisms which allow large stress concentrations to be developed on grain boundaries and these are based on a combination of stress and grain boundary sliding.

Chen and Machlin[82] found no cavities formed when bicrystals of copper were loaded at elevated temperature simply in tension, whereas cavities did appear when the bicrystals were loaded to produce grain boundary sliding. Nucleation of cavities is then considered to be a result of grain boundary sliding causing a high stress concentration at either ledges[82,83], impurity particles[84,85], precipitates or other irregularities at the grain boundaries.

Evidence for cavity nucleation at ledges was obtained by Interater and Machlin[88]. Copper bicrystals were deformed at room temperature to produce slip intersecting the boundary and then let sliding take place at elevated temperature. The incidence of cavities in the predeformed specimens were many times higher than in specimens which were not deformed prior to creep. Chen and Machlin[81] found that the void spacing was less than the slip line spacing. These results indicate that, whilst grain deformation increases cavity incidence, presumably by forming ledges, cavities may be nucleated at other sites, such as inclusions, on the grain boundary.

Increasing thepurity of metals reduces the incidence of cavities and improves ductility[89-91]. These observations support the view that cavity nucleation occurs at second-phase particles because inclusions would have acted as cavity nuclei[85,90]. However, several studies [89-92] suggest that this improvement in ductility is a consequence of the enhanced grain boundary migration with the purer metals which destroys the boundary jogs (or ledges) and thereby prevents nucleation of cavities. Also [93], some impurities can markedly decrease the surface energy, γ, of a metal and hence reduce the critical cavity size, given as $2\gamma/\sigma$. This effect may account for the observation that even very small amounts of impurities can sometimes seriously reduce the creep lives and ductilities[94,95].

A number of workers [96-98], using density measurements, have shown that cavity nucleation begins very early in the creep life of materials even though these cavities may not become

visible under an optical microscope until a later stage of creep. However, if the cavity radius is less than a critical value (i.e. $2\gamma/\sigma$) the cavity should shrink by the loss of vacancies[99] to the surrounding lattice or grain boundary. Greenwood[100] has shown that all the data were in agreement with a model in which the number of cavities depends linearly on creep-strain.

Perry[75] has pointed out that grain boundary sliding will cause cavities to develop at irregularities whenever plastic flow or diffusion is not fast enough to prevent it. The role of the applied stress is to cause sliding and the development of local stress concentrations.

3.2.3 Growth

There is no general agreement as to whether the growth of cavities is vacancy or deformation - controlled since experimental support exists for both of them. When cavities are above the critical size, they can grow by absorption of vacancies from the surrounding lattice or grain boundary. Originally, Greenwood[79,80,101] thought that at high temperatures and low strain rates, the nucleation and growth of cavities was occurringby vacancy condensation. A model for cavity growth by vacancy accretion was put forward by Balluffi and Siegel[99]. According to this model, vacancies are originated in transverse grain boundaries under the action of the tensile stress and flow to voids to cause their growth. But it was found by Nield and Quarrel[89] that the volume fraction of voids was not consistent with this type of growth.

Hull and Rimmer[102] suggest that cavities grow by grain boundary diffusion and that fracture occurs when the growing cavities overlap. They studied creep in copper by applying both tensile and hydrostatic stresses, σ and P respectively and showed that, for the condition where failure was controlled by diffusional growth of a fixed number of cavities, the creep life is related to the difference $(\sigma - P)$. They found that no cavitation in copper occurred when $\sigma = P$, and this was confirmed for magnesium by Ratcliffe and Greenwood[98].

However, in view of the evidence that the number of voids is not constant during creep, the theory of Hull and Rimmer was extended subsequently by Greenwood[103]to allow for the situation that cavities may be nucleated continuously throughout the creep test.

A number of workers[90,104] supported the vacancy growth model and experimental support came from Boettner and Robertson[97], who found that void growth in copper began near the specimen surface and worked its way inwards. The hydrostatic stress experiments are strong support for the vacancy mechanism since the presence of hydrostatic stress doe not change the deformation processes. On the other hand, Machlin[105] remarks that these

experiments only show that a net stress difference across the boundaries is necessary to prevent re-cohesion and do not provide a critical evidence for vacancy growth. Further, it was found by Krammer and Machlin[106] that creep strain and void area are linearly related in nickel, which rules out vacancy-controlled growth.

In fact, the evidence in favour of deformation controlled growth is far stronger. Thus, Intrater and Machlin[107] found that the area of visible voids was independent of temperature. Bowring et al[96] reported a linear relation between void volume and strain in dilute alloys. Cavities were found to be angular in magnesium by Presland and Hutchinson[108,109] and in Magnox by Harris et al[110]. Gittins[111] has observed that the largest cavities on the surface of a magnesium specimen were on the boundaries which slid the most. Taplin and Barker[112], using a shadowgraphic technique in the electron microscope, found the cavities to be irregular in shape in α - brass and copper samples, and remark that diffusional processes are not responsible. They proposed some other mechanisms for cavity growth, such as crack propagation from void apices, tearing and grain boundary sliding. Spark and Taplin[113] concluded that grain boundary sliding is the dominant mode of cavity growth in their brass samples and propose that grain boundary area occupied by voids is proportional to the degree of sliding.

A further support[93] to deformation-controlled growth comes from the observation that the rate of cavity growth is markedly lower for an alloy than for the pure metal under the same creep conditions, even though the alloy additions do not change the diffusion parameters substantially.

All of these observations favour deformation-controlled growth of cavities. Taplin[114] gives support to the possible role of vacancies at low strain rates and suggest that several types of deformation-controlled growth are possible. Taplin and Wingrove[115], and Taplin and Barker[112] are of the opinion that several modes of growth are possible, of which one or more may dominate under a given set of conditions.

3.2.4 Final Fracture

Final fracture occurs when the cavities interlink to form a critical Griffith crack length. The propagation of such cracks was attributed to stress concentration at the crack tip by Greenwood[78, 80, 116]. From the observation that cracks present in fractured specimens have wavy outlines, Chen and Machlin[81] suggest that cavities grow until they link together. Hull and Rimmer[102] assume that fracture occurs when the growing cavities link together by merging. Seigel[117] has proposed that cavities link-up occurs by a tearing process between the cavities. He provides evidence that the cracks in deoxidised copper matched edge to edge with little grain boundary sliding.

The mechanism of cavitation failure due to Rogers[118,119] is void sheeting by necking of the material between voids. Taplin and Barker[112], in their studies on brass and copper, concluded that tearing due to the concentration of stress at cavity apices and concomitant grain boundary sliding, control crack propagation. Cocks and Taplin[120] studied the effect of grain size on crack propagation by cavity linkage. If the grain size is smaller than the Griffith crack length, then an interaction between cavities on different boundaries is necessary for crack propagation.

At very small grain sizes, a critical crack length cannot be reached because cavity linkage appears to be arrested at triple points. In this case ductile sheet effect occurs where failure is dominantly related to loss in specimen cross-section rather than to cavity linkage. In coarse grained materials[121], failure is a question of critical crack length.

It was pointed out by Taplin and Barker[112] that a vacancy condensation process will blunt the crack tip and thereby possibly increasing ductility. Taplin[114] remarked that the propagating crack was stopped at the triple junctions. According to Taplin[122] the final mode of fracture may not be unique and he attributes the onset of failure to the ease with which voids are able to link to form a crack capable of spontaneous propagation.

3.3 Cavitation in Superplasticity

3.3.1 Introduction

On the basis of metallographic evidence, it is now firmly established that superplastic deformation in tension can be accompanied by cavitation on grain or phase boundaries. In a discussion on superplastic forming operations, Ridley[123] expressed his view that all systems can be made to cavitate if the appropriate conditions are selected and Edington[21] has pointed out that cavitation may be a more general phenomenon than is realised at present. Cavities can be easily seen using conventional metallography and form throughout the gauge length but not in the shoulders of the tensile specimen. Cavitation does not occur in compression tests performed on the same material at the same temperature and strain rate[4].

The importance of cavitation during superplastic forming depends upon the tensile strains involved to make a component, provided the strain rate and temperature are carefully selected. Thus, Grimes[124] reported that cavitation occurs in Al - Cu - Zr alloys in the vicinity of the fractured tip, but is not significant at the normal sorts of superplastic strain involved in manufacturing a component. Although superplasticity has been observed in Cu- and Fe- base alloys, here cavitation is a serious problem in their commercial exploitation for it drastically limits the elongation to failure and may affect the room temperature properties of superplastically deformed components.

3.3.2 Sites for Cavity Nucleation

Preferential nucleation sites have been identified to be α/β interfaces and triple points in 60/40 brass;[5,125-128] coarse Fe- particles and α/β boundaries in ternary brass[129] of composition 58.5 wt% Cu - 38.5 wt% Zn - 3.0 wt% Fe; α/β interfaces and triple junctions involving both phases in aluminium bronze[6] (Cu - 9.5 wt% Al - 4 wt%Fe) particles and twin boundary/grain boundary intersections in Cu alloy[130] (Cu - 2.3 wt% Al - 1.8 wt% Si - 0.4 wt% Co); α/β interfaces and Ti(C,N) particles in α/γ stainless steel[126,131] (25Cr/6Ni); α/γ interfaces and $Cr_{23}C_6$ particles in 26Cr/9Ni steel[132] α/Fe_3C interfaces in α + Fe_3C steel;[133,134] crabide particles in Fe - 4 wt% Ni - 3 wt% Mo - 1.6 wt% Ti alloy[11] and at α/β interfaces in nickel - silver (48 wt% Cu - 37 wt% Zn - 15 wt% Ni) alloy.[126]

Recently, Humphries and Ridley[135] have shown that cavitation can be induced in microduplex Pb - Sn eutectic during superplastic flow, by introducing the relatively hard intermetallic phase based on Ag_3Sn. Cavitation was shown to occur at Ag_3Sn/matrix interfaces in Sn - Pb - Ag alloys. This was confirmed in a further work[136] on ternary alloys based on Pb - Sn eutectic where the presence of relatively hard particles (based on SbSn, Ag_3Sn, Cu_6Sn_5 phases) induced cavitation at particle/matrix interfaces during deformation in an otherwise non-cavitating system.

3.3.3 Models for Cavity Nucleation

Although most models of cavitation that have been developed actually deal with creep, they can be related to superplasticity as well because the deformation mechanisms for creep and superplasticity are similar. The Stroh[137] condition for cavity nucleation is:

$$z^2 > \frac{12\gamma G}{\pi L_o} \qquad (3.3 - 1)$$

where z is the shear stress, γ is the surface energy and L_o represents either the length of the boundary or the separation of points of blockage on grain boundaries. For superplastic materials, this condition for cavity nucleation at triple junctions is not satisfied because here L_o is small and the applied stress is low. Nucleation on the boundary will be still more difficult than at the triple junction because the spacing between the ledges or precipitates or inclusions is less than that of triple junctions and the stress that must be reached is correspondingly higher (3.3 - 1). But, in practice, cavities do form at triple junctions and on grain boundaries during superplastic deformation. An important factor here may then be the segregation of trace impurities to grain boundaries[138]. It is also possible that[139] particles near the triple junction may aid void formation as the surface energy term γ may be considerably lower at the precipitate/matrix interface.

In general, cavities will be nucleated[128] whenever the rate of accommodation at triple points, grain boundary irregularies etc., is exceeded by the rate of grain boundary sliding. The incomplete accommodation results in stress concentrations which exceed the critical stress for cavity formation.

For cavity nucleation at particles in the boundary, grain boundary sliding is necessary to induce the initial breakdown of the particle/matrix interface, and this is consistent with the observation that cavitation is a maximum in region II where grain boundary sliding is also a maximum[140] . A model for cavitation at particles was proposed by Smith and Barnby[141]. The model is based on fracture of the particles which does not occur in practice during superplastic deformation. The model also predicts that small particles are preferential sites for cavity nucleation, whereas the opposite is found in practice. Recently, a model combining the Smith-Barnby and Stroh criteria and based on decohesion of the particle rather than its fracture, has been developed by Fleck et al[142]. This model predicts nucleation preferentially at large particles and is generally consistent with experimental observations.

3.3.4 Cavity Stability and Growth

Thermodynamic stability of a cavity against shrinkage by diffusion occurs where the radius r is given by[85]

$$r = \frac{2\gamma}{\sigma} \qquad (3.3 - 2)$$

where σ is the applied stress. Thus there is a minimum radius at which a cavity nucleus is stable against shrinkage, and this implies that there is a minimum effective particle size. In superplastic deformation, grain boundary sliding is likely to be the dominant factor in cavity stabilisation, whereas vacancy absorption is probably more important in creep[143].

The growth of cavities greater than the critical size defined by (3.3 - 2) can occur by either diffusion or deformation. Holes may grow by the action of the applied stress alone producing strains at the surface of the hole which cause it to grow. This mechanism does not involve a vacancy flux to the hole. Hancock[144] has studied the conditions under which hole growth without vacancy condensation should be faster than diffusion.

Low values of the ratio $\sigma/\dot{\varepsilon}$, where σ is the stress and $\dot{\varepsilon}$ is the strain rate, as well as large voids favour the strain process. For example, in a 1 % Cr - ½% Mo ferritic steel, for $\sigma/\dot{\varepsilon} = 9 MNmm^{-2}$ the diffusion hole-growth becomes the slower mechanism for hole radii > 0.7 μm. Typical values of $\sigma/\dot{\varepsilon}$ used in the work on Al - Mg alloys[143] range from 6.8×10^{-2} to 2.8×10^{-4} $MNmm^{-4}$, so that void growth should be deformation-controlled almost throughout, assuming that there are no order-of-magnitude differences in the relevant material parameters between ferritic steel and Al - Mg

alloys. Because of the extensive grain boundary sliding associated with the large deformation in superplastic flow, the strain contribution to growth is probably more than that of diffusion, which is consistent with the irregular shapes of cavities observed during superplastic deformation[5,113,143].

One of the earliest reports on cavitation in superplasticity came from the work of Morrison[10](1968) on various low-alloy steels. The microstructure of the steels at the optimum testing temperature was characterised by a fine mixture of ferrite and austenite with an interparticle spacing of a few microns. The pores were most numerous in a 2% Al steel (Fe - 0.34 wt% C - 0.47 wt% Al) but were also present to a much lesser extent in the 2% P steel (0.16 C - 1.54 Mn - 1.98 P) and the 2% Si steel (0.12 C - 1.97 Si). They were found to be evident in Al steel after about 100% elongation and it was thought that the pores probably originated as a result of incompatible deformation of the material on either side of an interface.

A number of workers[5,125-129]have studied cavitation behaviour in brasses during superplastic deformation. Thus, Sagat et al[5](1972) noted that the cavities were present along the whole gauge length of the 60/40 brass specimen; the average cavity size increased when the strain rate decreased; the volume fraction of voids generally increased as the strain rate was increased and the cavities did not readily interlink. In this material the optimum ductilities were observed at ~600°C where the ratio of the volume fraction of the constituent α and β phases was equal. The mechanism of cavity nucleation at $\alpha/\beta/\alpha$ triple junctions was not given. The cavities were found to be rounded rather than sharp and wedge-like.

Dunlop et al[6](1973) observed cavities to form at grain and phase boundaries during high temperature tensile deformation of a superplastic commercial aluminium bronze, CDA 619 (9.5 pct Al - 4 pct Fe) and the process of cavitation they deduced was most likely to be associated with grain/phase- boundary sliding and that the nucleation of cavities probably occurred at stress concentrations in the sliding interfaces. It was found that significant cavitation occurred only in material strained at rates higher than that corresponding to maximum m while at lower strain rates, cavitation was not detected in this alloy, unlike the observation that cavities appeared under $\overline{\text{al}}^{1}$ conditions, in α/β brass, by Humphries and Ridley[128]. Dunlop et al found that the cavities increased in frequency as the strain rate was increased above that for maximum m and the extent of cavitation increased both in size and frequency with increasing strain for a given strain above 1.67×10^{-3} sec^{-1}. However, cavity interlinkage was slow even at strain rates as fast as 6.5×10^{-2} sec^{-1}. The slow rate of cavity growth and interlinkage was attributed to the high m value of the material which minimized the rate of internal necking between cavities, in a manner analogous to the way in which the rate of external necking is reduced[2].

The gradual development of cavitation with increasing strain observed during superplastic deformation is consistent with nucleation by grain boundary sliding as observed in creep[73]. Since the high strain-rate sensitivity range (Region II) occurs between a slow strain-rate range where sliding is accommodated by diffusion, and a fast range, where accommodation occurs by dislocation movement[145], the change in accommodation mechanism with strain rate was considered to be responsible for the dependence of cavitation on strain rate.

Firstly, it was anticipated that the resistance to sliding would be greater at α-α and β-β boundaries compared to α-β boundaries as a result of the strong crystallographic texture present in CDA alloy 619[146]. This was found to be true for α/β brass, where chandra et al[127] actually measured the grain and phase boundary sliding at various interfaces and showed that sliding occurred on α/βboundaries more readily than on α/α and β/β interfaces . Secondly, the high temperature flow stress of β phase is much lower than that of α phase, resulting in a disproportionately greater accommodation of grain boundary sliding by the beta phase. The predominance of α-β phase boundary cavitation in aluminium bronze was thus deduced to be either the result of greater sliding at this boundary, or to a decreased ability to accommodate sliding adjacent to this type of boundary.

Dunlop et al[6](1973) defined an acceptable level of cavitation as that which left the subsequent room temperature properties nearly unaffected. Thus 'useful' elongation was determined as a function of engineering strain-rate at 1073^{o}K for CDA alloy 619 as:

800 pct elongation - 0.08 min^{-1}

300 pct elongation - 1.0 min^{-1}

100 pct elongation - 4.0 min^{-1}

which is sufficient at reasonably high strain-rates to make it an attractive candidate material for superplastic forming by commercial methods.

After Morrison[10], a number of other workers[11,126,131-134,147-148]investigated, in detail, the occurrence of cavitation in steels. Thus Naziri[132](1974) used high voltage electron microscopy to study cavitation in fine-grained (3 - 4μm) 26Cr/9Ni duplex stainless steel which exhibited superplastic behaviour at 925^{o}C. Extensive cavitation was observed at the austenite-ferrite interphase boundaries, although the carbon level was less than 0.03 %. $Cr_{23}C_6$ particles also formed and the formation of cavities was associated with these carbide particles. Hayden et al[149] while working on a similar type of steel, suggested that a dislocation mechanism involving recovery creep/grain boundary sliding was operating and that the rate of grain boundary sliding was controlled by the rate of intragranular creep. Since the number of carbide particles present was small and did not seem to account for the observation of the very high volume fraction of cavities, it was suggested that the cavity nucleation at the interphase boundaries was the result of the high number of discontinuities/

dislocation pile-ups developed at the boundaries during grain boundary sliding.

Since cavitation is not obtained in other fine-grained duplex superplastic alloys which deform predominantly by a diffusion creep/grain boundary sliding mechanism[65,149], it was suggested that, in alloys prone to cavitation, the high ductility obtained was due to the difficulty of cavity growth and interlinkage to form a cavity of a critical size.

Smith and Ridley[11](1974) designed an iron K1970 alloy of composition Fe - 4% Ni - 3% Mo - 1.6% Ti, which showed good superplastic behaviour in the temperature range 900 - 960°C, where it exists as an α/γ structure containing approximately equal proportions of the two phases. Cavitation still occurs during tensile straining and as the deformation proceeds, the voids grow in size until interlinkage leads to failure. In an attempt to reduce the extent of cavitation in this alloy, an addition of boron was made. Boron is known to reduce microcracking[150] during creep of austenitic stainless steels.

Thus, if the mechanism of cavitation during both creep and superplasticity were similar, then boron might reduce its occurrence in iron K1970 alloy. It was found that trace additions of boron (40 ppm) to the alloy of lower titanium content led to a marked decrease in the extent of cavitation. As compared to boron-free, the alloy containing boron had a larger reduction in area at the fracture surface and contained a lower volume fraction of cavities. The inhibiting effect of boron on cavitation was also observed in the K1970 alloy by Humphries[151]However, both the mechanism of cavity formation and the way in which cavitation was inhibited by trace additions of boron, were not understood.

Chandra et al[125](1975), working on three binary α/β brasses (B_1 Cu - 38.7 Zn, B_2 Cu - 40.5 Zn, B_3 Cu - 40.5 Zn) of stable grains size ~32 μm , found cavitation to be dependent upon alpha/beta phase ratio. On the basis of quantitative metallographic measurements they showed that the extent of cavitation and the volume fraction of voids increased with decreasing beta phase proportion. The high temperature flow stress of a binary brass was found to decrease considerably as the beta phase content in the alloy increased. It was also observed that both the number n and the volume fraction V_f of voids increased with increasing deformation, while the aspect ratio (defined as average length parallel to the stress axis/average length perpendicular to the stress axis) of grain boundary voids at 600°C was mich higher for the B_1 alloy (α/β ratio = 70/30) compared with B_2 (α/β = 62/38) and B_3 alloy (α/β = 48/52). It was suggested that the decreased cavitation in alloys containing higher beta phase was associated with the lower flow stress and relative ease of recovery at β/β boundaries which are present in higher proportion in B_3 alloys compared to B_1 and B_2 alloys. Cavities were nucleated at various grain and phase boundaries and the larger voids were not formed simply by growth of a single void but by the interlinking of several smaller voids through internal necking.

Ridley et al[126](1976) and later Humphries and Ridley (1978)[128] investigated intergranular cavitation during superplastic tensile flow of 60/40 brass. They reported that cavities were uniformly distributed and found to be nucleated most frequently at β/α/β triple points while their growth tended to occur along boundaries between like phases rather than unlike phases. The cavity nucleation was also frequently associated with small inclusions of sub-micron dimensions. The type of particle was not known, but were thought to be oxides or sulphides.

Their experimental results showed that the volume fraction of voids increased as strain, strain-rate, and grain size were increased and as the deformation temperature was decreased. The influence of these variables was interpreted in terms of their effects on cavity nucleation and/or cavity growth rates. Increasing strain-rate and decreasing temperature are accompanied by increasing flow stress. If the external stress level reflects the magnitude of the stress concentrations which can develop in the material, then the threshold stress for cavity nucleation will be exceeded at more potential nucleation sites as the stress level rises, so increasing the cavity nucleation rate. Alternatively, Humphries[152] has pointed out that behaviour in this system is qualitatively consistent with incomplete diffusional accommodation of cavity growth, by a process similar to that which leads to complete accommodation of grain bourdary sliding in a non-cavitating system. Thus, if cavity growth is controlled by lack of diffusional accommodation, then increasing strain-rate reduces the time available for diffusion, increasing grain size increases the length of the diffusion path, and decreasing temperature leads to lower diffusivities.

Sagat and Taplin[129](1976) studied the flow and fracture behaviour in a strain-rate-sensitive ternary brass (58.5 Cu - 38.5 Zn - 3.0 Fe) at 400 - 800°C over a range of strain rates. Plastic flow in tension was shown to accompany a continuous development of intergranular and interphase cavities. However, cavitation was not observed in compression.

Cavities could be detected at a strain of 0.03 and were abundant at a strain of 0.40. They found that at low strains, most of the cavities were associated with coarse Fe- particles whereas at higher strains cavity nucleation at α/β boundaries became almost equally abundant. The number of cavities per unit area increased approximately linearly with strain but the area fraction of cavities increased more rapidly with strain, due to their rapid growth.

It was found that at (~~higher and~~) ~~lower~~ strain-rates the extent of cavitation decreased at 600°C, which is opposite to the general observation[5,126,128] that volume fraction of voids increases with increasing strain rate. However, this was explained on the basis that a balance between stress and sliding is necessary for cavity necleation. At low strain-rates the stress is low and at high strain-rates the contribution from sliding is reduced. These results are in accord with a recent model presented.[153-154] Further, the effect of increasing temperature was to reduce the extent of cavitation. Based on the observation that growth of cavities occurred concomitantly with large plastic flow, it

was suggested that most of the growth occurs by plastic deformation rather than vacancy condensation and grain/phase boundary sliding.

Smith et al[131](1976) examined the superplastic characteristics of a microduplex IN 744 (26 Cr/6.5 Ni) stainless steel over the temperature range 700 - 1020°C. The alloy has a duplex α/γ microstructure from room temperature to 1080°C, when it becomes ferrite. The formation of cavities during superplastic deformation of steels in the α/γ region has been reported previously.[30,17,35,36] During deformation of IN 744 alloy, cavities formed at α/γ boundaries and at Ti (c,Ni) particles. The growth and coalescence of cavities led to premature failure, although this failure was frequently associated with large elongations.

Density measurements showed that the total volume of cavities increased with increasing strain, decreasing strain rate (unlike in aluminium bronze[6] and 60/40 brass[5,128]), increasing temperature (unlike in α/β brass[128,129]) and increasing grain size, although the latter effect was relatively small. The observation that the maximum elongation at 960°C tended to be associated with higher initial strain-rate than that corresponding to maximum m is consistent with the way in which void volume varies with strain rate in this alloy. The lower strain rate gives the larger volume fraction of voids and consequently this leads to premature failure more rapidly than deformation at the higher rate.

However, the variation of void volume with strain rate, temperature and grain size does not appear to be consistent with incomplete diffusional accommodation at sliding grain boundaries. Thus, increasing deformation temperature causes diffusional accommodation to occur more rapidly and decreasing strain rate increases the time for accommodation to occur, and both of these lead to decrease in cavitation. This is the reverse of the behaviour obtained in IN 744 alloy and in work on a steel of lower alloy content[148]. If lack of grain boundary accommodation was important then cavitation should increase markedly with increasing grain size, because of the increasing distance over which diffusion had to occur. Their results show that although void volume did increase with increasing grain size, the effect was very small.

In studies of cavitation during creep it has been observed[98,103] that the relationship between void volume, v, and the time of deformation, t, is $v \alpha t^n$, where n is an exponent having values in the range 1.5 - 2.5. Assuming that during superplastic deformation a similar relationship existed between v and t, a time-dependence of overall void volume of 1.6 - 2.0 was observed. The time exponent of void volume increase was interpreted in terms of the Avrami equation[155] and suggested that many of the voids were growing from pre-existing nuclei and these were probably provided by the Ti (C,N)/matrix interfaces.

From their study of superplastic IN 744 alloy, it was apparent that at least a substantial proportion of the cavities observed were associated with Ti(C,N) particles, although it was not clear why higher temperatures and lower strain rates should lead to larger volumes of voids for a given strain.

Ridley et al[126](1976) examined cavitation behaviour during superplastic deformation of an α/γ stainless steel (25Cr/6Ni) at 960°C as a function of strain and strain-rate. They found that the volume fraction of cavities increased as the strain was increased, but was almost constant with strain rate, for a given strain. Cavities were thought to be nucleated by decohesion of the particle/matrix interface, or by particle cracking, due to stress concentrations resulting from grain boundary sliding. It seems likely also that many of Ti(C,N) cuboids were cracked during mechanical processing of the steel prior to testing so that only growth was involved in the cavitation process. A nucleation and growth study of cavitation in a low alloy steel containing Ti(C,N) showed that the material contained many pre-existing nuclei[148].

Ridley et al[126] were not certain about the mechanism of cavity growth since their results were consistent with both growth by sliding and by vacancy condensation. Thus it is possible that for the range of strain rates involved, the stress concentrations arising during grain boundary sliding are in excess of those required to nucleate voids at the large Ti(C,N) particles. If these nuclei and any pre-existing nuclei, grow by sliding then the total void volume will be determined by strain and not by strain rate. On the other hand the results could represent a situation where a smaller number of voids are nucleated by the lower stresses associated with slower strain rates and is compensated for by the longer times available for void growth to occur by vacancy condensation.

The same authors[126] also found cavitation to occur at 580°C during superplastic deformation of a nickel - silver of nominal composition 48 wt% Cu - 37 wt% Zn - 15 wt% Ni. The alloy had a microduplex structure consisting of α grains (2 - 3μm diameter) with about 10% volume fraction of β particles (~1μm diameter) located on the α boundaries. The cavitation behaviour ofα/β Cu - Zn - Ni alloy more closely resembles that of the α/γ stainless steel than the brass. Nucleation of cavities occurred at β particles and these were playing a similar role to the uncracked Ti (C,N) cuboids in the steel.

As in the case of α/γ steel, the density studies showed that during superplastic flow the volume fraction of cavities increased with increasing strain but, for a constant strain, was almost independent of strain rate. Growth of cavities occurred along α/α boundaries but, as in the case of steel, it could not be established whether growth was due to sliding or to vacancy condensation. The observation that strain rate was not an important variable in either system led these authors to suggest

that the simpler explanation of void growth by grain boundary sliding was the more likely.

Recently, Taplin and Smith[143](1977) have reported their results from a study of cavitation and superplastic flow in Al - Mg alloys. These alloys are moderately superplastic, exhibiting maximum elongations up to 500%. It was found that the area fraction of cavities at fracture is a maximum at the conditions for maximum elongation and there is roughly a linear relationship between the two. These results are in agreement with the previously reported[5,126,151] ones and show that the extent of cavitation increases with increasing strain. No significant effect of strain rate upon the degree of cavitation, for a given strain was apparent which confirmed similar results obtained by Ridley et al[126] on α/γ stainless steel and nickel - silver alloy.

Cavities nucleate at particles, in grains or phase boundaries by sliding, and their growth is thought to be deformation controlled, although there may be some initial contribution to growth by vacancy condensation. The alloys fail by the growth and interlinkage of cavities without the formation of an external crack.

Recently, Humphries and Ridley[135](1977) have shown that cavitation can be induced in microduplex Pb - Sn eutectic during superplastic flow, by introducing a relatively hard intermetallic phase based on Ag_3Sn. Lead-tin eutectic is superplastic at room temperature and does not appear to under go cavitation[156]. The Sn - 38.1 wt% - Pb eutectic alloy had a microduplex structure with an average grain size of $\sim$ 2 μm while the Sn - 36 wt% Pb - 5.6 wt% Ag alloy had a similar matrix structure but also contained ~5% by volume of silver-rich particles based on Ag_3Sn of rectangular or rounded shape with average dimensions of 3 μm. Vickers microhardness results obtained from a coarsened microstructure were as follows: Ag_3Sn 77 VPN, Sn-rich phase 3VPN, Pb-rich phase 2VPN. Cavitation occurred at the Ag_3Sn/matrix interfaces, a situation which was analogous to that in steels containing Ti(C,N) particles.[131,148]

Levesey and Ridley[136](1978) studied the effect of a range of phases of different hardnesses based on Bi, SbSn, Ag_3Sn and Cu_6Sn_5 on superplastic behaviour and cavitation by making additions of Bi, Sb, Ag or Cu to the Pb - Sn eutectic. Although the m values for all the alloys (excluding Pb - Sn - Bi alloy) were very similar ($m = 0.425 \pm 0.025$), the superplastic behaviour was greatly influenced by the third element addition. The presence of hard internetallic phases caused cavitation to occur in an otherwise non-cavitating Pb - Sn eutectic and the cavities were found to be assocated with intermetallic phase/matrix interfaces. No cavitation was detected in either Pb - Sn or Pb - Sn - Bi eutectics. Bismuth appears as a relatively soft Bi - rich solid solution in the microstructure, and increases the superplasticity of the material unlike Sb, Ag or Cu which occur as relatively-hard intermetallic phases in the microstructure and reduce the superplasticy of the material.

In general, cavities nucleate whenever the sliding generates stress concentrations at triple points or boundary irregularities faster than they can be relieved by either diffusion or slip, and the stress builds up until the cavity forms. Accommodation at any potential nucleation site will occur more readily if all the phases at this point can contribute to the accommodation process, whether this involves diffusion or dislocation glide. Thus, cavitation does not occur in the Pb - Sn and Pb - Sn - Bi eutectics because accommodation can keep pace with the rate of grain boundary sliding in these alloys. In others, cavitation is due to the incomplete accommodation at the interfaces due to restricted accommodation within the intermetallic phase. The level of cavitation increased as the volume fraction, hardness and size of the intermetallic particles increased. An increase in strain-rate, or decrease in deformation temperature, also resulted in an increased level of cavitation.

Chandra et al's[127](1978) results of the extent of sliding at α-α , β-β and α-β boundaries showed that the maximum sliding occurred at the α-β interfaces while the β-β boundaries exhibited very little sliding. In fact, the sliding rate at α-β interfaces was found to be about $1\frac{1}{2}$ times that at α-α and about $2\frac{1}{2}$ times that at β-β boundaries. Since the maximum amount of cavitation is associated with the maximum amount of sliding[157], the results of their investigation are consistent with the predominance of α-β interface cavitation and very small amount of cavitation at β-β boundaries.

They pointed out that the preferential sites of cavitation can also result from the mismatch in recovery rate between α and β phases across the interfaces, because the β phase is softer (lower flow stress) than α phase at high temperatures. Further, it was shown that the energy required to nucleate a cavity at α-α, β-β andα-β interfaces is almost the same. Thus, although the surface energy term may be important, it does not explain why cavities form at α-β interfaces perferentially. Therefore, the predominance of α-β interface cavitation is believed to be as a result of greater sliding at the α-β boundary and of an unbalanced accommodation of sliding adjacent to this type of boundary.

3.3.5 Fracture

According to the Hart criterion[26] the onset of plastic instability occurs when:

$$\gamma' + m = 1 \qquad (3.3 - 3)$$

where $\gamma' \equiv \left(\frac{\delta\sigma}{\delta\varepsilon}\right)\frac{1}{\sigma}$ and $m \equiv \left(\frac{\delta\sigma}{\delta\dot{\varepsilon}}\right)\frac{\dot{\varepsilon}}{\sigma}$

and σ, ε and $\dot{\varepsilon}$ are true stress, true strain, and true strain-rate respectively. This is in agreement with the Considere criterion for strain hardening materials with negligible rate dependence. In strain-rate-sensitive materials the rate of strain hardening is very low (< 0.1) and this reduces to:

$$m = \left(\frac{\delta\sigma}{\delta\dot{\varepsilon}}\right)\frac{\dot{\varepsilon}}{\sigma} = 1 \qquad (3.3 - 4)$$

so that necking will not occur at all. (Newtonian Viscosity). Because $m < 1$ for superplastic materials, necking would be expected to occur in a tensile test.

Sagat and Taplin[158] studied the stability of plastic flow in a non-cavitating superplastic alloy (wrought Pb - Cd eutectic) and showed that its behaviour may be described in terms of two instabilities. Instability I corresponds to the development of measurable external necks at a strain somewhat higher than the point of maximum pulling force. After Instability I, several very shallow necks are formed which grow simultaneously at comparable rates. The flow stress remains approximately constant and this mode of deformation persists for several hundred percent deformation in a fairly stable fashion without causing rupture. Instability II is associated with the onset of preferential and rapid growth of one neck accompanied by a marked increase in the flow stress until the alloy fails by intrinsic plastic rupture at a point.

It is suggested that Hart's model[26] may be adequate to explain Instability I, but Instability II cannot be explained at present by any model.

The same authors[129] also studied the plastic flow stability in a cavitating superplastic alloy. For this investigation they chose ternary brass (58.5 Cu - 38.5 Zn - 3.0 Fe) because it cavitates extensively during superplastic flow and yet exhibits no external necking prior to failure at 600°C, which avoids the problem of the interaction of external instabilities (necks) with internal instabilities (cavities). They suggested that the process of fracture may be analysed in an analogous way to flow instability in non-cavitating superplastic alloys. Thus the onset of cavitation (an internal, diffuse bifurcation) is analogous to the onset of external, diffuse necks (Instability I). The onset of cavity linkage of rapid internal necking between cavities is analogous to the preferential rapid growth of a single external neck (Instability II).

It was suggested that the high value of strain-rate-sensitivity index minimises the rate of growth of internal necks between individual cavities in a manner analogous to the way the rate of external necks is reduced.[158] A characteristic feature of the fracture of the alloy is the increase of load-carrying ability in the final stage of deformation despite the fact that the material is very heavily cavitated at this stage of deformation. This is caused by the formation of internal necks between cavities, which eventually deform in a non-superplastic manner and strain-hardens.

Two potential failure mechanisms may be distinguished[143]. Firstly, sufficient cavities may coalesce to constitute a crack,

which then propagates by tearing. This may be likened to low-temperature ductile fracture, where cavities nucleate on second phase particles and grow and move together by plastic flow until coalescence by shear causes failure. Secondly, the reduction in effective cross-section by cavity growth may be such that failure effectively occurs simultaneously over the whole section, which is catagorised as void sheeting. Failure in Al - Mg alloys[143] is reported to occur by the first mechanism. Void interlinkage has also been observed in aluminium-bronze [6], ternary brass[129] and steels[11,148]. At very small grain sizes, a critical crack length cannot be reached because cavity linkage appears to be arrested at triple points. In this case the void sheeting effect occurs where failure is dominantly related to the loss in specimen cross-section rather than to cavity linkage.

Fleck et al[153] studied the hot-fracture characteristics of an industrial copper-base alloy (CDA 638; 95.0% Cu - 2.8% Al - 1.8% Si - 0.4% Co) as a function of grain size. For grain sizes < 100 μm, fracture is a result of void formation. The voids are suggested to grow as a result of plastic strain concentrations in the region of the void. Fracture results from the interlinkage of these voids by the fracture of internal necks. This mode of fracture is referred to as the Intergranular Void Sheet (IVS) mechanism. The important factors that control the onset of fracture by IVS are the value of m, and the void size, spacing and geometry. For a given void size, spacing and geometry fracture by the IVS mechanism will occur at higher strains if m is increased.

CHAPTER 4

4. HARDNESS

4.1 Introduction

Hardness is a measure of the resistance of a material to plastic deformation. Since correlations exist between hardness and yield strength and ultimate tensile strength, UTS, the hardness test is widely used in the engineering industry. It is a quick and simple test to make and requires a small specimen with a flat, polished surface, as compared to the tensile test which requires relatively-large, specially-shaped specimens and an expensive and complex apparatus. The general definition of indentation hardness, which relates to the various forms of indenter is the ratio of the load applied to the surface area of the indentation and is usually expressed in kg/mm^2. In a Vickers hardness test, a square-based pyramid is used, for which the angle included between opposite faces is ideally 136^0. Then, from the general definition of hardness, for a given diagonal, d mm, we have:

$$\text{Vickers hardness number} \quad Hv = \frac{1.8544w}{d^2} \quad (kg/mm^2) \qquad (4 - 1)$$

where w is the load applied.

4.2 Microhardness and Macrohardness Testing

The term 'microhardness testing' has no real significance, although it is generally accepted as implying the measurement of hardness at low loads. The precise range of loading considered varies markedly with different workers and some consider that no test involving a load of more than 100 gms should be referred to as microhardness test, while others accept loads of 1 kg as being in this category. The term 'microindentation hardness testing' relating the type of test to that involving small dimensions of the indentation obtained, was adopted by Mott[159]. Although no attempt was made to define precisely what is meant by 'microindentation', a load of less than 1 kg was generally implied. Then the macrohardness testing would be one which utilises loads in excess of 1kg.

The factors that are important in the measurement of hardness are: the value of applied load, the angle ($\bar{\alpha}$) subtended by opposite faces of the indenter, the indentation diameter and the area of the specimen chosen. Thus the applied load must be known accurately. This depends upon the calibration of the instrument used. For an incorrect value of α the standard tables (based on $\bar{\alpha} = 136^0$) no longer apply, clearly. Measurement of the indentation diameter introduces an error due to incorrect calibration of the measuring device or to a personal factor depending on the operator. If the specimen is non-uniform in composition and deformation, then variations in hardness can be expected. The most common source

of error in low-load testing is probably that due to vibration, which can arise from motors driving equipment in the vicinity of the tester or shocks, such as those due to the slamming of a door. An increase in hardness of a copper specimen for L = 25 gm, when the whole apparatus was placed on a thick rubber mat, has been reported[160].

At low loads, the indentations made are small both in relation to surface area and depth. This defines two types of test piece, viz., those which have a small surface area perpendicular to the axis of the indenter and those which have limited depth parallel to the axis of the indenter. Thus, microhardness testing is useful for small components which cannot be tested at higher loads, and small areas such as constituents in a multiphase alloy where the maximum dimension may only be a few microns; and also for surface coatings and thin sheets where the thickness is less than the depth of indentation made at higher loads.

4.3 Hot hardness and other properties

The indentation hardness of a metal is related to its flow stress. Thus, Tabor[161] has shown that a Vickers indentation formed at room temperature can be considered to have an average strain of 8 ~ 10% associated with it and that the hardness value is approximately three times the flow stress at this strain. Work at elevated temperatures indicates that although creep may complicate the picture a general correlation between hot hardness and flow stress exists also in this range[162-63]. Thus it seems possible to determine at least qualitatively the temperature dependence of the flow stress via a determination of the much more easily measured hot hardness variation. Since the flow stress of a metal is a function of strain-rate and temperature, the hardness might be expected to vary in an analogous way.

A number of workers[164-171] have attempted to correlate the hot hardness data of metals and alloys with their known creep characteristics. Hot hardness testing is now generally considered to be a very useful method of sorting out quickly the higher temperature strength and creep characteristics of dissimilar solids. Thus, from 1949 onwards, hot hardness tests have been used at Renault Laboratories as a simple means of sorting out new creep-resistant alloys[171]. Some authors[164,169-171] have attempted to determine activation energies from such studies. A simple method of assessing the superplastic characteristics of an alloy, based on[172] Rockwell indentation hardness test has been reported . Belk[173] has pointed out the experimental difficulties associated with such a test and proposed an alternative simple ball-indentation test for superplastic materials which allows a value for the strain-rate-sensitivity to be determined.

4.4 Indenter Materials

In conventional hardness testing, it is assumed that the indenter remains undeformed during the indentation process and this is justified only if the indenter is at least twice as hard as the material being indented[174] . This raises the problem of choosing a very hard material for the indenter, particularly at high temperatures, where indenter softening might occur. Interaction between indenter and specimen may be another serious problem at elevated temperatures. Diamond is the natural choice of indenter material for low temperature use because of its great hardness value and chemical stability and diamond is suitable at temperatures up to 1000^{o}C, above which graphitisation becomes[175] serious. Garofalo et al[166], when making indentations on steel at temperatures above 815^{o}C, found that the tip of the indenter deteriorated due to solution of carbon into the steel. These observations were confirmed by Gove[176], who also reported that no deterioration in a sapphire indenter occurred at temperatures up to 1000^{o}C.

4.5 Various hot hardness machines

Several reviews[175,177-180] of work on hot hardness have appeared, the most recent being that by Geach[17]. In these reviews are described the various hot hardness measuring techniques that have been used by various workers to collect hot hardness data. The Bens tester[165] is designed to operate in vacuo on a Vickers hardness machine at temperatures up to about 930^{o}C. The same furnace is used to heat both the specimen and indenter, and the indentation measurements are made after cooling to room temperature. A vacuum tester made by Geach and Hartee[181] can be used up to 1200^{o}C. More recently indenting machines have been offered on the market by Nikon[182], by Satec Corporation of Grove City, Pennsylvania and by Marshall Products Company of Columbus, Ohio.

However, these techniques have only been able to measure the hardness of the bulk material and not to select and measure the hardness of individual phases within a duplex microstructure. The main reasons being that either a very small indenter load connot be used in such machines or they are not equipped with a measuring microscope to select an area for indentation. The poor positional accuracy for indentation coupled with the use of the same heating furnace for both specimen and indenter are the other major difficulties in obtaining accurate hot hardness data on the individual phases of a duplex alloy.

Landingham[183] obtained some data on dispersion-hardened tungsten by the use of lightly-loaded, unheated indenter with a heated specimen. The method of heating the indenter was to hold it close to the specimen surface for $\sim$ 5 minutes before making an indentation. Although it was possible to make, observe and photograph the indentations at the same test temperature,

the data is of limited value since it has been demonstrated[184] that localised chilling of the specimen occurs unless the indenter is at the same temperature as the specimen. Bens[165] and later Petty and O'Neill[168] appreciated the importance of heating the indenter to prevent the localised chilling of specimen. They made sure that both the specimen and the indenter were situated within the uniform temperature zone of their furnace.

4.6 Effect of indenter temperature on hardness

In order to determine the dependence of measured hardness on the indenter temperature, Gove[176] determined the hardness of nominally pure iron (0.14%C, 0.008%N) over a range of temperatures up to 800^{o}C, under three different conditions:

(a) with an indenter heated by means of its own furnace to the same temperature (± 3^{o}C) as the specimen,

(b) using an atmosphere of argon (which has low thermal conductivity) and preheating the indenter by holding for 5 minutes at a distance of about 0.1 mm from the specimen surface, and

(c) using an atmosphere of helium (which has high thermal conductivity) and preheating by holding it at the same distance from the specimen surface.

The results clearly indicated that with the indenter furnace not in use, the hardness measurement was markedly dependent on the thermal conductivity of the gas used, the greater error occurring with the gas of lower thermal conductivity. The magnitude of this error was estimated to indicate that a localised chilling of approximately 150^{o}C was occurring at the higher temperatures using an atmosphere of argon, and of approximately 100^{o}C in the case of helium. The localised chilling of the specimen was predicted to be greater in vacuo. With the indenter heated by its own furnace, the nature of the gas had no detectable effect.

In order to measure the high temperature hardness of various phases present in steel, including non-metallic inclusions, a high temperature microhardness tester was designed and constructed. The instrument, in its original form, described fully elsewhere[176,184] was capable of operating at temperatures slightly above 1000^{o}C. The specimen and indenter were both heated by their individual furnaces. Indenter loadings from 3 gm to 500 gm were available, although it was not possible to change the indenter load during operation. The high temperature microhardness tester used for the present work was commissioned from AED Rugby and is an improved design of the above instrument. This will be described later in chapter 5.

4.7 Use of a hot hardness technique in the study of cavitation in superplasticity

It has already been stated that for cavitation to occur in a microduplex superplastic alloy consisting of two phases in approximately equal proportions at the superplastic temperature the two phases involved must be 'incompatible' that is, supposedly show marked differences in properties such as flow stress, ductility and diffusivity. Now, ideally this phenomenon could be investigated by an in situ study of the deformation behaviour of each phase separately in its true environment in the duplex alloy and pinpointing the phase incompatibilities. Existing techniques do not allow for this, but a hot hardness technique could determine the flow stress and activation energy for each phase in situ in the duplex alloy in the superplastic temperature range.

4.8 Effect of loading time on hardness

In determining the hardness of a material, it is assumed that the size of the indentation depends solely on the applied load and the results are not affected significantly by the time of loading. This is true at temperatures < 0.3 Tm above which the effect of increasing loading time is to increase the size of indentation due to creep. In hardness tests, even at room temperatures, the loading time is kept to a minimum (usually 15 seconds) because the longer the time of loading the greater the chance of a heavy vibration effect. For most materials, loading time does not affect hardness significantly below ~ 0.5 Tm, but above, hardness decreases with increase in time of loading

Earlier observations of this phenomenon were of an empirical nature. The effect of loading time, t, on the hardness, H, of lead measured by using a ball indenter, was studied by Hargreaves[185] who proposed the following relationship at constant temperature and load;

$$\log H = a - b \log t \qquad (4 - 2)$$

The constants a and b depend upon composition of the sample and b increases as the grain size reduces. Work by Shishokin[186] led to;

$$\log H = A - BT - CT \log t \qquad (4 - 3)$$

Where A, B and C are constants, and this relationship describes the effect of both temperature and loading time on hardness.

4.9 Indentation hardness and creep

The possibility that change in hardness with time of loading may have a useful relationship with creep properties has attracted considerable interest[165,166,168,171].

Thus Mulhearn and Tabor[169] studied the hardness and creep of single crystals of indium and lead. Using a spherical indenter, they found that a linear relationship exists between log H and log t for temperatures above ~ 0.6 Tm and for times of loading exceeding a few seconds. Assuming that temperatures above 0.6 Tm lie in the viscous or steady-state creep range, they obtained the following relationship;

$$H^{-(n+\frac{1}{2})} = K\left(\frac{D^2}{W}\right) e^{-Q/RT} t \qquad (4-4)$$

where steady-state creep rate, $\dot{\varepsilon}_s = A\sigma^n \exp\left(\frac{-Q}{RT}\right)$ (4 - 5)

and n and K are constants, D the diameter of spherical indenter, W the load applied, R the gas constant and Q is the activation energy. Thus, plot of log H against log t should be linear. At any two temperatures T_1 and T_2 the interval on the log t scale between the two log H/log t lines is given by

$$\log t_1 - \log t_2 = Q/R\left|\frac{1}{T_2} - \frac{1}{T_1}\right| \qquad (4-6)$$

and provides a measure of the activation energy for the flow process. The values of Q obtained were 16 KCal/mole for indium and 28 KCal/mole for lead, which were close to the activation energies for self-diffusion.

Later it was pointed out[171] that a viscous or steady-state creep equation was not the most appropriate type of creep relation to apply for an indentation process. A non-steady-state creep relation was implicitly used by Pomey and his colleagues[187] in their study of the variation in hardness with loading time.

Atkins et al[171] used the following transient creep equation due to Mott[188];

$$\dot{\varepsilon}_{tr} = A_2 \dot{\varepsilon}_s^{1/3} t^{-2/3} \qquad (4-7)$$

where A_2 is independent of both stress and temperature, and $\dot{\varepsilon}_s$ is the strain rate of the steady, second-stage or viscous creep under the same constant stress σ.

The use of a transient creep equation was considered to be more reasonable than a viscous creep relation, since during an indentation process the plastic zone is continuously increasing with time. Assuming that the indentation process corresponds to the plastic movement of a series of shells concentric with the contact region, into the undeformed material ahead, they arrived at the following relationship;

$$H^{-n/3} - H_o^{-n/3} = A_4 \exp\left(\frac{-Q}{3RT}\right)\left(t^{1/3} - t_o^{1/3}\right) \qquad (4 - 8)$$

where H is the hardness at time, t, and H_o is the hardness immediately after attaining the full load, W, at to and n = 10. This relationship predicts linear log plots of

$$(H^{-n/3} - H_o^{-n/3}) \text{ vs } (t^{1/3} - t_o^{1/3})$$

and the interval between two lines for different temperatures T_1 and T_2 giving an estimate of the activation energy of the process.[2] The activation energies derived from such hardness measurements for a number of materials eg., indium, lead, tin, aluminium and magnesium oxide were close to the activation energies for self-diffusion.

4.10 Assessment of superplastic characteristics of an alloy by a simple hardness technique

A simple test of assessing the superplastic characteristics of an alloy has been reported[172] . It is based on the Rockwell test and defines a superplasticity index I as the difference in dial readings after 30 and 60 seconds, respectively, of application of the major load. It was shown for aluminium-zinc alloys that the elongation at failure was linearly proportional to this index. The superplasticity index of one alloy varied from 2.5 to 17 as the grain size was reduced. All measurements of the superplasticity index were made at room temperature.

Belk[173] has shown why such a test should work and proposed his own simple ball indentation test for superplastic materials. He extended an analysis of ball indentations in work-hardening metal (ie., relations such as $H = 2.8\sigma_{y,\varepsilon} = 0.2\ d/D$ and $\dot{\varepsilon} = 0.2/D\ dd/dt$) to cover the case of strain-rate sensitive materials (ie., $\sigma = K\dot{\varepsilon}^m$) and obtained the following relation;

$$d^{\frac{2+m}{m}} = 5D\left(\frac{2+m}{m}\right) \times \left(\frac{4W}{2.8\pi K}\right)^{1/m} t \qquad (4 - 9)$$

where m is the strain-rate-sensitivity index, d the diameter of indentation, D the diameter of indenter, k the flow stress at unit strain rate, W applied load and t is the time of loading. It was assumed that m and k are constants in (4 - 9) over the range of strain rates occurring in the indentation test.

Since indentation is spherical,

$$d^2 = 4Dh\ (1 - h/D) \qquad (4 - 10)$$

and using (4 - 10) in (4 - 9) gives

$$h\ (1 - h/D) = \frac{1}{4D} \left|\frac{5D}{m}\ (2 + m)\right|^{\frac{2m}{2+m}} \times \left(\frac{4W}{2.8\pi k}\right)^{\frac{2}{2+m}} \times t^{\frac{2m}{2+m}} \qquad (4 - 11)$$

where h is the depth of penetration.

Most indentations are shallow ie., h << D, so the term h/D is small and can be neglected. Thus we have a relationship between depth of penetration and time which depends primarily on m. By means of this the Rockwell ball hardness can be related to the time, and the proposed superplasticity index I can be related to m.

If a ball indenter is applied for times differing by a factor of ten and the measured diameters are d_1 and d_{10}, then (4 - 9) gives

$$\log_{10}\left(\frac{d_{10}}{d_1}\right) = \frac{m}{2 + m} \qquad (4 - 12)$$

Hence m can be found. Once m is known, k can be calculated from (4 - 9).

Room temperature tests were done on three zinc-aluminium eutectoid-based alloys, and the m and k values obtained from the indentation tests were found to be similar to those obtained from room-temperature tensile tests. Since the overall strain rate varies considerably during an indentation test, the value of m obtained can only be a mean value.

4.11 Short time hardness and temperature relations

In order to compare strictly the hot hardness data with the corresponding creep data one must define the stress, strain and strain rate associated with the indentation and be able to vary them at will, which is not the case in practice. Usually, the hot hardness data is obtained by using a constant load and a constant time of loading at different temperatures. In a hardness test, the indentation stress decreases and the strain rate increases somewhat as the metal softens with increased temperature. The effect of this deviation from constancy will be

minimised if the time of loading is kept short and this approach was considered to be the best one by Larsen-Badse[164]. This also implies that for short times of loading, the hardness measurements may be interpreted in terms of a steady-state creep equation.

Westbrook[180] (in 1957) has reviewed the literature on temperature dependence of hardness of pure metals and considers that it can be well represented by the following Ito-Shishokin relation;

$$H = A\, e^{-BT} \qquad (4 - 13)$$

where T is the absolute temperature. The constant, A, is extrapolated 'intrinsic hardness' ie., hardness at T = 0 and constant, B, is the softening coefficient of hardness. The constants A and B have one set of values (A_1, B_1) at low temperatures and another set (A_2, B_2) at higher temperatures, suggesting a change of mechanism. In most metals and alloys, the transition temperature (Tt) is about half the melting temperature.Later, Merchant[189] confirmed the Ito-Shishokin relation below 0.55 Tm and at temperatures above Tt he proposed a relation

$$H = A' \exp(-B'/RT) \qquad (4 - 14)$$

Where A' and B' are constants and R is a gas constant. The nature of the equation (4 - 14) suggests the possibility of a thermally activated mechanism of deformation above T_t and therefore, he defined B' as the 'apparent activation energy of indentation'.

The strain rate associated with the formation of a hardness indentation is not well known. It has been proposed that[197,189] it is proportional to $\dot{d}$, the rate of change of the indentation diagonal. According to Larsen-Badse [6], for Vickers hot hardness data obtained at a constant time of loading, an average value of $\dot{d}$ can be given as;

$$\dot{d} = \frac{d}{\Delta t} = \frac{1}{\Delta t}\left(\frac{W}{1.8554\ H}\right)^{\frac{1}{2}} = C_1 \frac{1}{\sqrt{H}} \qquad (4 - 15)$$

where Δt is the time of loading and W is the load. Substituting H from the relation

$$\ln H = A_2 + B_2 Tm/T \qquad (4 - 16)$$

(similar to equation (4 - 14) and therefore suggesting a thermally activated deformation) into (4 - 15) gives

$$\dot{d} = C \exp\left(\frac{-B_2 T_m}{2T}\right) \qquad (4 - 17)$$

By comparison with expressions for thermally activated phenomenon eg.,

$$\{\dot{\varepsilon} \propto \exp\left(\frac{-Q'}{RT}\right)\} .$$

an apparent activation energy may be obtained from

$$Q' = B_2 T_m R/2 \simeq B_2 T_m \text{Cal/mole} \qquad (4 - 18)$$

where R, the gas constant is equal to 2 calories per mole per degree.

It was then remarked on the basis that the strain rate assignable to thermal activation is only a part of $\dot{d}$, that Q' will be proportional to, but not equal to the activation energy for steady-state creep (Qc) or for self-diffusion (Q_L). This was found to be true for twenty-three pure metals for which Larsen-Badse determined Q' from hot hardness data obtained under conditions of constant time of loading. The relation used by Larsen-Badse[164] can now be written as;

$$H = A \exp\left(\frac{Q'}{T}\right) \qquad (4 - 19)$$

4.12 Activation energy for creep from hot-hardness data

Later, Sherby and Armstrong[190] showed why a correlation exists between Q' and Q_L or Q_c, and how to determine activation energy for creep for pure metals directly from hot hardness data obtained under constant load time conditions. On the assumption that elastic modulus is not a function of temperature, the following equation for steady-state creep rate, $\dot{\varepsilon}_s$, at temperatures above 0.6 T_m, was used:

$$\dot{\varepsilon}_s = B\sigma^n \exp\left(\frac{-Q_c}{RT}\right) \qquad (4 - 20)$$

where n is the stress exponent and equals 5 or 7 for most pure metals, and B is a material constant. It has been shown elsewhere[191,192] that the same functional relation can be used to describe tensile data by replacing σ with the ultimate tensile

strength, UTS, and $\dot{\varepsilon}_s$ by the engineering tensile rate $\dot{e}$. Thus, the temperature dependence of UTS at constant engineering strain rate is given by

$$UTS = C \exp\left(\frac{Q_c}{nRT}\right) \qquad (4 - 21)$$

where $C = \left(\dot{e}/B\right)^{1/n}$

Some authors[166,168] have observed a direct proportionality between UTS of a given material and its hot hardness value H, either as a function of temperature or as a function of composition. Therefore, (4 - 21) can be written as

$$H = F \exp\left(\frac{Q_c}{nRT}\right) \qquad (4 - 22)$$

where F and C are related by a constant of proportionality comparing (4 - 19) with (4 - 22) gives

$$Q' = \frac{Q_c}{nR} \qquad \text{or} \qquad Q_c = nRQ' \qquad (4 - 23)$$

Since n equals 5 or 7 for most pure metals, Qc equals about 10 to 14 times Q' which agreed fairly well with the results of Larsen-Badse[164] who found Q' to be about one-tenth to one-twentieth of the value for Qc, the activation energy for steady-state creep.

From (4 - 22), a plot of natural logarithm of H against reciprocal absolute temperature is a straight line with slope equal to $\frac{Q_c}{nR}$. Thus activation energy for creep can be found directly from hot hardness data. Since it has been shown[193,194] that the temperature variation of Young's modulus, E, can lead to an erroneous activation energy for creep, Sherby and Armstrong[190] introduced this as a variable to rewrite (4 - 22) as

$$H/E = G' \exp\left(\frac{Q_c}{nRT}\right) \qquad (2 - 24)$$

and used this equation to plot modulus-compensated hot hardness versus reciprocal temperature for aluminium and copper. With n = 5, activation energies of Q = 48 Kcal/mole for copper and Q = 38 Kcal/mole for aluminium were obtained which are close to the activation energies for self-diffusion.

4.13 Hardness softening parameters and an apparent activation energy for indentation

Merchant et al[195] collected hot hardness data from published literature for thirty-seven metals and analysed it in view of equations (4 - 13) ie., $H = A \exp(-BT)$, (4 - 19) ie., $H = A' \exp(Q'/T)$ and (4 - 23) ie., $Qc = nRQ'$ to calculate the softening parameter B and the apparent activation energy for indentation Q'. The plots of lnH against 1/T and lnH against T were described by two straight lines with a break occurring over a range of temperatures, giving one set of values for the parameters (B_1,Q'_1) below and another(B_2,Q_2') above the transition.

These parameters were related to the melting temperature and found that the softening parameters decreased whereas the activation energies increased with an increase in the melting temperature. It was suggested that the value of Q' at low temperature (< $0.75T_m$, Q'_1) may be correlated with the activation energy for the dislocation pipe diffusion, Qd, and that at the higher temperature (< $0.75T_m$, Q'_2) with the activation energy for lattice self-diffusion, Q_L, as pointed out by Sherby and Armstrong[190]. Assuming that for T/Tm = 0.5 to 0.7 $Qc \approx 2/3\ Q_L$, for T/Tm = 0.7 to 0.95, $Qc \approx Q_L$ and for T/Tm = 0.5 to 0.95, $Qc \approx \frac{1}{2}(Qd + Q_L) \approx 5/6 Q_L$, the values of Q' were compared with Qc to obtain an estimate of the stress co-efficient, n, for creep, approximately close to 5. There was a considerable deviation from n = 5 characteristic of the 'five' power law, even in the case of data above 0.75 Tm, where power law relation was expected to be valid.

Merchant et al[195] calculated $B_1(E)$ and $B_2(E)$ values from lnE against T plots (the way B_1 and B_2 parameters were calculated from lnH against T plots) using data from Lozinski[196] and correlated with the hardness softening parameters B_1 and B_2 respectively.

It was found that the low melting metals, which soften rapidly, also decrease their elastic modulus rapidly with temperature, indicating a close relationship between H and E. It was reported that by taking into account the effect of elastic modulus variation with temperature on the hardness variation with temperature, the values of n and Q' were improved.

CHAPTER 5

5. EXPERIMENTAL

5.1 Introduction

In this work, to understand cavitation during superplastic deformation, two alloys were used; firstly zinc-aluminium eutectoid which normally does not cavitate and secondly, a microduplex Cu - 40wt. Zn brass which does, as models of each class of behaviour. The phase diagram of Al - Zn system is shown in Figure 9, and that of Cu - Zn system in Figure 10. From Figure 9 and 10 it can be seen that the composition and proportion of individual phases in the two systems vary with temperature and this is also shown in Table 1 and Table 2. Initially, it was hoped to study the flow characteristics and activation energies of each phase, in situ, using hot-microhardness technique, in the two model systems. Whilst, this was possible in Cu - 40% Zn brass with coarsened microstructure (Figure 11) the in situ results for each phase in the Zn - Al eutectoid could not be obtained because of its limited propensity for grain growth (see Figure 12).

A series of alloys was produced of compositions corresponding to those of the individual phases in Zn - Al eutectoid and Cu - 40 wt% Zn alloy over a range of temperatures in the superplastic range. These alloys were in the form of extruded bars of $\frac{5}{8}$" diameter for tensile specimens and 1" diameter for hardness specimens. The composition and room-temperature hardness of all the alloys is given in Table 3. Throughout the present work, these alloys were used to represent α and β phases in each model system (see Table 4 and Table 5).

In Zn - Al eutectoid, the α phase varies in composition from 5.6 to 22wt% Zn whereas the β phase is almost the same - ~99.5wt% Zn - over the whole of the temperature range 120 - 250^{o}C. Therefore, a single alloy of composition 99.5 Zn - 0.5 Al was used to represent the β phase and three alloys of composition 5.6 Zn - 94.4 Al, 12.4 Zn - 87.6 Al and 22Zn - 78 Al to represent the α phase. In Cu - 40wt% Zn brass, the α phase varies in composition from 36 - 39% Zn and the β phase from 41 - 46.5% Zn over the temperature range 300 - 700^{o}C. The α and β phases in this system were represented by 62Cu-38Zn and 55 Cu - 45 Zn alloy respectively.

It was realised that these alloys represented the phases correctly only at one temperature at which the composition of a phase in the duplex was exactly the composition of the alloy that represented it. At other temperatures, although the representation was only approximate, it can be seen from Table 6 and Table 7 that these alloys represented quite well the phases of the duplex alloys, over the superplastic temperature range. Apart from the in situ hot-microhardness results for each phase in

Cu - 40% Zn brass, all the remaining data, for the two phases in the two model systems, was obtained by hot hardness, modulus and tensile testing of such representative alloys.

5.2 Hardness Testing

A major part of the present work was done on a high temperature microhardness tester, commissioned from AED Rugby, in order that the hardness of the individual phases in a duplex alloy could be measured.

The instrument shown in Figure 13, consists of a sealed vessel made from nickel-plated brass that contains the specimen, indenter, furnaces and other associated components. The sealed vessel comprises the main body, lower and upper box together with the window assembly and base plate. It may be evacuated or filled with an inert gas or gas can flow through it. In some cases, especially at very high temperatures, to prevent atmospheric oxidation of the specimen and indenter, the gas was flowed in continuously and sucked away by a vacuum pump. A gas flow rate of ~ 5 ft^3/hr was found to be sufficient to give a constant bubbling rate through a wash bottle. The vacuum pump was used throughout the test, except, when making and measuring the indentation (< 2 minutes).

The specimen , its drawing shown in Figure 14, is retained within its furnace by two 8BA x $\frac{5}{8}$" cap screws. The specimen furnace (Figure 15) consists of four pieces of pyrophyllite, two of which are concentric sleeves between which the winding is held. The furnace is wound with a 0.025 mm nichrome wire for 1000^{o}C operation or 0.020 mm tungsten wire for 1200^{o}C. Initially, the specimen furnaces (tungsten/nichrome wound) did not last long, due either to an excessive current through its outer leads or short circuiting of the successive turns in the winding itself. Subsequently, all the furnaces used had their winding leads doubly wound and the threads on the two pyrophyllite sleeves were deepened. These furnaces gave a satisfactory performance. Further, since tungsten becomes very brittle after high temperature use and the maximum test temperature (up to 700^{o}C) was well below 1000^{o}C, only the nichrome wound furnaces were used. The specimen heater had 80 turns/inch.

The furnace assembly is contained within a water-cooled copper jacket. Because of the small size of furnace, temperature gradients may be severe and therefore, a chromel/alumel thermocouple was spot-welded on to the specimen surface for an accurate measurement and control of its temperature. The thermocouple leads are connected to terminals machined from the nickel/chromium and nickel/aluminium alloys, so that the cold junction is removed from the vicinity of the furnace to a part of the apparatus where negligible temperature rise occurs during operation. The expected

variation in temperature was less than ± 2.5°C.

The specimen furnace is mounted on a table that can be traversed in longitudinal and transverse directions. The drive knobs have counting dials such that 1 division (001) corresponds to a movement of 0.005 mm (5 μm). The specimen itself can be moved from the observation position to the indenting position by means of a sliding handle operating through a spring loaded device which also accommodates the longitudinal traverse. The ability to locate the indentations accurately on the specimen surface depends on this distance of movement being constant. This is achieved by using a spring loaded device which holds the position of the assembly accurately at the end position of its travel (ie., under the indenter).

A window of optically flat quartz is provided through which the specimen can be observed by means of a Zeiss Epignost microscope mounted above the window on an adjustable bracket. The microscope is fitted with a x15 screw micrometer eyepiece to measure the indentations made. Two objective lenses with magnification of x10 and x32 are provided, but the former was most frequently used unless the size of indentation was very small. The specimen thickness was more critical (between 10.0 - 10.5 mm) for focussing with a x32 objective than x10 because its downward motion was restricted by the water cooling fittings on the window assembly. The window was then modified to move the water cooling fittings out of the way of the x32 objective movement. Although, this helped to focus with x32 lens, but now the sideways movement of the microscope, required to align the indentation with the cross-wires of the eyepiece, was restricted.

When the specimen thickness was more than 10.5 mm and the thermocouple spot-welded on its surface, it tended to touch the inside top of the sealed vessel, during its motion from a position under the window to a position under the indenter and vice-versa. As a result, the temperature dropped suddenly or the thermocouple separated from the specimen surface, leading ultimately to the failure of the furnace. Further, on moving a thicker specimen to the far end position under the indenter it may hit the indenter tip and hence damage it. Thus, in all cases the specimen thickness was kept below 10.5 mm.

The instrument was calibrated for use with both x10 and x32 objective lenses. When x10 objective is in position, 1 ocular reading (O.R) = 1 μm and 1 O.R = 0.3125 μm in the case of x32 objective. The positioning of the indentation was accurate to ± 5 μm although, under favourable conditions it was possible to make indentation with an accuracy of ± 1 μm.

The indenter is heated by means of its own furnace (shown in Fig 16) which is constructed in a similar way to the

specimen furnace. The indenter heater had 48 turns/inch. The indenter heater is surrounded by two concentric pieces of pyrophyllite and the whole assembly is contained in a water cooled jacket.. After using it for about a month, heavy leaking developed in the water cooling jacket which had to be suitably modified for further use . When the specimen assembly is moved by means of a sliding handle to the far end of its travel, the indenter furnace is situated directly above the specimen furnace with a clearance of approximately 0.5 mm.

Furnace controllers, ammeters and indenter beam position indicating lights are mounted in a control console, which is connected to the microhardness tester by means of a cable harness and water pipes. The main cooling water supply was connected to a fitting at the back of the console. Using a harness of flexible nylon pipe connections were made between the three connections labelled I, S and W on the console and the indenter furnace, specimen furnace and window cooling connections on the instrument. The two control valves mounted inside the rear console panel were used to obtain an approximately equal flow in the three circuits. The return of water was made via a manifold in the side of the main body to the connection labelled R on the rear of console and then to the drain.

The indenter, either diamond or sapphire, is mounted at the end of a shaft which passes down through the indenter furnace. A fine wire chromel/alumel thermocouple is inserted through a bore in the indenter shaft and it touches the backof indenter tip. The various parts of the indenter assembly are shown in Fig 17. This thermocouple not only measures the temperature of the indenter but also controls it, as is the case with specimen thermocouple. The indenter assembly is carried by means of two parallel beams which are mounted on miniature precision ball bearings. Before applying any load to the indenter assembly, the beams are balanced by sliding a counter balance weight on the top beam.

Two types of weight-holders were available, one with weights of 10, 20, 50 and 100 gm, and the other with 100, 200, 500 and 1000 gm. The former was the one mainly used in this work. The weight holder carrying the required weight range is inserted in its position and the load is applied by rotation of the holder. It was possible to change the load within a given range during operation at high temperature. The indenter is lowered or raised by means of a cam controlled by an external oil-filled dashpot. The piston rod passes freely through a hole in the top of the dashpot. This free movement is necessary to achieve a constant rate of lowering of the indenter, determined by the rate of flow of oil through a hole in the bottom of the piston. Another hole was drilled through the top of dashpot to facilitate oil filling with the help of an ordinary plastic syringe. The dashpot was always checked to be full with oil before starting a hardness test and the drilled hole closed with a brass screw.

Specimens of the required geometry (as shown in Fig 14) were machined from 1" diameter rods of the material. In the case of sheet material (eg., Supral) a spacer was used to made the composite thickness 10 - 10.5 mm. The specimen was polished and etched with a suitable reagent to reveal the microstructure and a chromel/alumel thermocouple spot welded on its surface. It was then fixed within its furnace by two 8BA x $\frac{5}{8}$" cap screws and the thermocouple leads connected to the terminal blocks, ensuring correct polarity. The base plate with the specimen assembly on it, was inserted into the main body of the vessel and its end secured by using wing nuts.

The weight holder carrying the weight range required was put in position and rotated to apply the correct load. The dashpot was checked to be full with oil. Firstly, an indentation was made at room temperature which was then aligned with the cross-wires of the eyepiece by moving the microscope on its adjustable base.

The instrument was sealed by using 'O' rings and vacuum grease. However, because of wear of the main body at the entrance of the base plate, there was ome leaking from atmosphere into the vessel. Consequently, the vessle was either evacuated, or flushed with argon for about 30 minutes before switching on the furnaces. Switching on of the mains and a green light on the console front indicated that the indenter was raised. With the sliding handle fully out, the specimen was in the observation position under the window. By using the specimen traverse knobs a selected area for indentation was aligned with the cross-wires of the eyepiece. The specimen was then moved to the indenting position (handle fully in).

The cooling water supply was turned on and the amber neon light appeared. In the absence of this light no furnace could be switched on. The cooling water returning to the drain was checked to be sufficient to ensure an adequate cooling of various components of the instrument. Occassionally the flow of cooling water was increased during operation if the nylon pipes carrying the return water became very hot.

Ensuring that the specimen furnace was under the indenter furnace and that the current adjustment knobs were fully anti-clockwise, both furnaces were switched on. Using the current and maximum power controls provided temperature was slowly raised to the set temperature. Although a heating and cooling rate of $50^{o}C$/minute was recommended by the manufacturer of instrument, a heating rate of 10 - $20^{o}C$/minute was employed above which the furnace tended to draw excessive current (> 2 amp) resulting in its failure. However, a cooling rate of $50^{o}C$/minute could be safely used.

The specimen and indenter were held at the test temperature for about 15 minutes before the first indentation was made. Ensuring that the temperature had reached equilibrium and that the weight holder was in a position to apply the correct load, the dashpot actuating lever was released. The green light disappeared indicating that the load was fully applied to the specimen. After a fixed period of time (15 sec unless otherwise stated) the indenter was raised by means of a dashpot knob and the green light appeared again. The specimen was brought back to the observation position and by using a micrometer eyepiece the indentation was measured to give the hardness of the specimen at the set temperature.

Because of some leaking in the main body at the entrance of base plate, vacuum pump or argon gas were continuously used during operation, except when making an indentation to avoid the effect of vibrations on applied load arising from working of the vacuum pump. The temperature was increased to a higher set temperature and the hardness measured in a similar manner. Errors in hardness can arise from the following causes. Inaccuracy of the applied load due to friction in the bearings, an inaccurate measurement of the temperature and personal error in measuring the indentation diameter. Errors will also arise due to a difference between the temperature of the cold junctions (thermocouple metal/copper) and the temperature at the terminals of the furnace control untis. The possible errors in measuring the hardness of various alloys is likely to be the same however, and, since we are interested in comparing the hardness of two alloys or phases, it is hoped that the absolute values of the hardness will not affect the results to any significant extent.

The absolute accuracy of the present machine was, however, checked by measuring hardness of a number of materials (eg., Zn - Al eutectoid, Cu - 40 wt% Zn and leaded brass) at room temperature using it, the Reichert and a Vickers hardness machine. The results are compared in Table 8 and Figure 18. The hardness numbers obtained with Reichert machine at small loads $\leq$ 100 gm agreed fairly well with those of this machine. From Figure 18, the hardness measured by using this machine at different loads tended to approach that of Vickers hardness at higher loads eg., 20 kg. Surprisingly, the Vickers machine was very much in error at a load of 1 kg. The results were reproduced quite accurately as can be seen from Figure 19 which plots the variation of hardness of pure aluminium, on heating up and cooling down temperature.

5.3 Young's Modulus Testing

In order to determine the variation of Young's modulus with temperature, a vibration technique described elsewhere[197] was used. It was based on the Rayleigh principle, when a long

thin cylindrical rod is subjected to flexural vibration in a freely supported position, the characteristic frequency of the first mode of vibration (fo) is related to the dimensions and Young's modulus (E) of the rod by the following equation,

$$fo^2 = \frac{(4.73)^4 \, E \, a^4}{16\pi m l^3} \qquad (5.3 - 1)$$

where a, l and m are the radius, length and mass of the rod. A schematic layout of the technique is shown in Figure 20.

All materials were centreless ground to the form of cylindrical rods of 0.2 inches diameter which dimension was constant along the length to within ± 0.0002 inches. The specimens were annealed to relieve any residual stresses. The length of each specimen was close to 4.25 inches. Specimens were cleaned ultrasonically in a solution of 'Grammosol', washed with alcohol and dried, before carefully weighing. The dimensions of each specimen were accurately recorded before the test.

A specimen was suspended from the vibrators (see Fig 20) by means of asbestos string swabbed with acetone to make it stiff. The specimen was lowered into the furnace and the latter switched on. A Pt/Pt - Rh thermocouple welded to a small rod was suspended close to the specimen centre to measure its temperature accurately. The specimen was agitated by an excitor (a vibrator) driven by an oscillator.

A range of frequencies was scanned and the frequency of the vibrating specimen was sensed by a pick-up vibrator. The pick-up signal was amplified before feeding it into the resonance sensor. At resonance, the frequency of the applied alternating force (ie., oscillator) was equal to the first natural frequency of the rod. At this point, the amplitude of the vibrating rod was maximum and was indicated by the maximum deflection of the galvanometer incorporated in the resonance sensor.

In all cases, the effect of change in dimensions due to thermal expansion on the measured resonance frequency was neglected. This seems justified on the basis of a following argument.

From equation (5.3 - 1)

$$fo^2 \propto a_o^4 / l_o^3 \qquad (5.3 - 2)$$

where ao, lo are the radius and length of the specimen at room

temperature. If f_T is the resonance frequency at room temperature corresponding to dimensions of the specimens at T^oC above the room temperature, then

$$f_T^2 \alpha \frac{ao^4(1 + \alpha T)^4}{lo^3(1 + \alpha T)^3}$$

or

$$f_T^2 \alpha \frac{ao^4}{lo^3}(1 + \alpha T) \qquad (5.3 - 3)$$

where α is the coefficient of linear thermal expansion of the alloy.

From equations (2) and (3),

$$(\frac{f_T}{f_o})^2 = 1 + \alpha T \qquad (5.3 - 4)$$

or

$$(\frac{fo + \Delta fT}{f_o})^2 = 1 + \alpha T \qquad (5.3 - 5)$$

Therefore, fraction change

$$\frac{\Delta f_T}{fo} = \frac{\alpha T}{2} \qquad (5.3 - 6)$$

where ΔfT is the change in resonance frequency due to thermal expansion of the specimen and the square term $(\Delta fT/fo)^2$ has been neglected in comparison to $2\Delta fT/fo$.

From equation (5.3 - 6) the fraction change in frequency due to thermal expansion can be estimated. Taking maximum temperature $T = 680^oC$ and $\alpha \simeq 25 \times 10^{-6}/^oC$ for both Al - Zn alloys and Cu - Zn alloys, $\% \frac{\Delta fT}{fo} = 1\%$. However, there was an uncertainty of ± 10 Hz in finding fo the resonance frequency and since for the present alloys fo lies in the range 1.150 - 1830 kHz, $\% \frac{\Delta fT}{fo} \simeq 1\%$. Thus the total error in determining modulus by the vibration technique was in the region of ~ 2%.

5.4 Tensile Testing

Round tensile specimens of 0.178" diameter and 1" gauge length with ⅜" BSF thread on the ends were machined from the extruded rods of each alloy. All the eight alloy specimens were annealed at different temperatures and the tests carried out on a standard Instron 4536 kg tensile testing machine at various temperatures from 100 - 700°C at a fixed corsshead speed of 0.1 in/min. An air circulating oven furnace with a uniform hot zone of 7" was used for tests on Al - Zn alloys between 100 - 270°C. The specimen temeperature was measured by a mercury thermometer inserted through a hole in the centre of the furnace front and was constant to within ± 1.5°C. For tests on Cu - Zn alloys at higher temperatures between 300 - 700°C a three zone furnace with a uniform hot zone 6" long was used. The temperature was accurate to within ± 2.5°C and measured by using a Chromel/alumel thermocouple. In all cases, the top grip end was water cooled to prevent heating of the load cell. Each specimen was soaked for about 30 minutes at the test temperature before pulling it to failure.

CHAPTER 6

6.1 Results

Hot hardness tests were conducted on pure aluminium. The results are shown in Figure 19 where it can be seen that the hardness/temperature curve is almost unaltered whether the specimen is tested during heating up or whilst cooling down. The same graph also shows the good reproducibility of results which are obtained with the present machine. A ℓn H vs $1/T^{o}K$ plot in Figure 21 gives a value of 33 Kcal/mole for the activation energy of deformation of aluminium above 0.5 Tm. Using modulus data from Fine[198], a modulus-compensated hardness, H/E vs Tm/T is plotted in Figure 22 and the value of activation energy is now found to be 31 Kcal/mole.

The hot hardness results for 60/40 brass ($B_{\alpha\beta}$) under different microstructural conditions are given in Figure 23. These tests were important to understand the effect of grain size on cavitation behaviour of this alloy. The as-extruded, fine-grain-size material had a lower hardness value than the annealed one above $350^{o}C$ ($\sim$0.5 Tm) whereas the lamellar structure was harder than both above $250^{o}C$.

$B_{\alpha\beta}$ was annealed at $700^{o}C$ for 118 hours and then quenched in water to retain the highest possible proportion of β phase in large crystals. This was necessary because, in another experiment, the β phase was found to be very soft and the indentation tended to distort the adjacent grain boundaries. Indentations were made in each phase, in-situ, in the alloy with a coarsened microstructure (Figure 11) at different temperatures and the results so obtained are shown in Figure 24. At low temperatures, the β phase is harder than the α phase, the two phases are equal in hardness at $250^{o}C$ and above this the β phase is much softer than the α phase. The ratio of the hardness of the two phases versus temperature is plotted in Figure 25; at the superplastic temperature ($\sim 600^{o}$), $\frac{H(\alpha)}{H(\beta)} = 6.3$.

Ignoring the effect of temperature on Young's modulus (it is not possible to determine the modulus of each phase in-situ of the alloy $B_{\alpha\beta}$ at the superplastic temperature), a graph of ℓn H vs $1/T^{o}K$ for each phase in-situ in $B_{\alpha\beta}$ is shown in Figure 26. At high temperatures, the slope of the graph is almost constant for the α phase, but for the β phase it increases up to $600^{o}C$ and then decreases. The calculated activation energy for the α phase near $600^{o}C$ is 48.2 Kcal/mole whereas it has a value of 53.6 Kcal/mole and 25.8 Kcal/mole for the β phase below and above $600^{o}C$.

Plotting ℓn H/E vs Tm/T (Figure 27), activation energy of 21.2 Kcal/mole was found for the annealed condition of $B_{\alpha\beta}$ alloy near its superplastic temperature ($\sim 600^{o}C$).

Hardness results for 62/38 brass (B_{α}) used to represent the α phase in $B_{\alpha\beta}$ alloy are shown in Figure 28. At elevated temperatures, the hardness is higher when the indentation falls within a grain than if the grain boundaries were included. A plot of the ℓn H/E vs $Tm/T^{o}K$ relationship in Figure 29 gave an activation energy of 42.2 Kcal/mole.

Results for 55/45 brass (B_β) which represents the β phase in $B_{\alpha\beta}$ alloy over a range of temperatures are shown in Figure 30 where it can be seen that the annealing treatment had very little effect on the hardness of this alloy above 0.5Tm. The change in hardness with load was also negligibly small above 0.5 Tm. The alloy is very soft above 500°C and at 600°C, its H = 1.6 kg/mm^2. A plot of ℓn H/E vs Tm/T in Figure 31, gave Q = 43 Kcal/mole and Q = 22 Kcal/mole respectively below and above the order/disorder transition (458°C).

The hardness of the separate α and β phases together with that of $B_{\alpha\beta}$ is compared in Figure 32. The β phase is harder than α phase below 250°C above which the β phase becomes much softer than the α phase, the two phases are about equally hard at 250°C. Above 250°C, $B_{\alpha\beta}$ is harder and softer than B_β and B_α alloys whereas below this temperature it is softer and harder than Bβ and B_α alloys respectively. Beyond 600°C, the hardness of $B_{\alpha\beta}$ approaches that of B_β alloy. The ratio H(α)/H(β) vs T plot in Figure 33 follows a similar pattern to the in-situ results. The ratio H(α)/H(β) = 12.6 and 7.7 for an indenter load of 10 gm and 100 gm respectively while the in-situ ratio is 6.3 for a load of 10 gm at the superplastic temperature of 600°C.

The effect of loading time on the hardness of $B_{\alpha\beta}$ at different temperatures is indicated in Figure 34. Figure 35 shows that indentation creep is absent at room temperature, but becomes more and more important as the temperature is increased.

In order to determine the ductility and strength of these alloys, tensile tests were done in the temperature range 300 - 700°C at a constant cross-head speed of 0.1 in/min. The results are illustrated in Figure 36. This shows that ductility of $B_{\alpha\beta}$ is a maximum at 600°C and then decreases with further increase in temperature. B_β was highly ductile (172% elongation) at 600°C whereas in the B_α alloy an elongation of only 54% could be obtained at the same temperature. The two alloys B_α and B_β were about equally ductile at 700°C.

Earlier it was noted that the hardness of both phases in the $B_{\alpha\beta}$ alloy was nearly the same at 250°C. Then it was found that the alloy had more ductility at this temperature than at any other temperature up to 500°C. Further tests at 250°C at different strain rates gave a maximum elongation of 109 pct at a strain rate of $1.6 \times 10^{-3} sec^{-1}$ where the UTS of the alloy was also maximum (Figure 37). Table 9 shows that the various annealing treatments used, confer less ductility than is found in the as-extruded fine-grained condition of the material.

The UTS of all three Cu-Zn alloys decreases with increase in temperature. At 600°C, the ratio UTS(α)/UTS(β) ≃ 7.2 and the ratio of the hardness, H(α)/H(β) ≃ 7.6 at the same temperature. The tensile strength of $B_{\alpha\beta}$ (Figure 36) is less than and, more than that of B_α and B_β respectively (at all temperatures between 300 - 700°C), as is the case with hardness of these alloys (Figure 32). In the case of $B_{\alpha\beta}$, Table 10 shows that the lamellar structure

gives lower ductility and higher UTS than the material in the annealed or the as-extruded condition.

Variation of Young's modulus of Cu-Zn alloys with temperature, determined by a vibration technique, is shown in Figure 38 along with the calculated values of the modulus according to a simple empirical relation:-

$$E_{AB} = \frac{(x\text{wt\%A}) \times E_A + (100 - x)\ \text{wt\%B} \times E_B}{100}$$

where E_{AB}, E_A and E_B are the moduli at a certain temperature of the alloy and of its constituents A and B respectively. In order to calculate the modulus of alloy at a temperature higher than the melting point of one of its constituents, a value of the modulus near the melting point of the constituent was used. Modulus data on pure elements, Cu and Zn, was taken from Köster[199]. Although the calculated values are close to the experimental ones in some cases (ie., below 450°C in B_α alloy and at all temperatures but between 250 - 400°C in $B_{\alpha\beta}$ alloy) in general, the above relationship cannot be used safely to predict accurately the modulus of an alloy at a given temperature. The experimental and predicted moduli are completely different for B_β alloy, in which a change in structure (ie., the order-disorder transition) occurs.

The modulus decreases linearly with increasing temperature, with a change in slope at about 0.6 Tm. The results on B_β alloy are compared with those of Sherby[200] in Figure 39. It can be seen that the modulus decreases rapidly as the temperature approaches the order-disorder transition temperature, above which it falls only slowly with increasing temperature. Figure 40 shows that a similar trend is followed in the hardness decrease with temperature in this alloy, except that at low temperatures the fall in hardness is more rapid than that of modulus. Figure 41 compares the hardness and modulus decrease with temperature for B_α and $B_{\alpha\beta}$ alloys. At low temperatures the decrease is similar, at intermediate temperatures the hardness decreases more rapidly than the modulus and then less rapidly at higher temperatures.

The hot hardness results for all the Al-Zn alloys used in the present work are shown in Figure 42. It can be seen, except for the case of the eutectoid ($A_{\alpha\beta}$), that the various hardness curves tend to converge at 250 - 270°C. The hardness of the eutectoid is lower than that of any other Al-Zn alloy between 120 - 270°C.

The α and β phases of the eutectoid near its superplastic temperature 250°C, are represented by 22Zn - 78Al ($A_{\alpha 3}$) and 99.5Zn - 0.5Al (A_β) respectively. At this temperature, the alloys $A_{\alpha 3}$, A_β and $A_{\alpha\beta}$ have hardness values of 18, 15 and 2 kg/mm^2 respectively. The relevant parts of the curves which represent the hardness of the α phase in the eutectoid $A_{\alpha\beta}$, over different ranges of temperature, together with the full curve for β phase as represented by a single

alloy over the whole temperature range, are shown in Figure 43.

Figure 44 plots the ratio of the hardness of the two phases from 20°C to 270°C and at 250°C; the ratio $H(\alpha)/H(\beta) = 1.2$.

The superplastic eutectoid has a minimum hardness, dependent on time of loading (Figure 45), between 250 - 270°C, above which it increases and then slowly falls to a value at 400°C about twice the hardness at 270°C. At 280°C, the H-value is about five times its value at 270°C, ie., just below the transformation temperature, ~ 275°C of $A_{\alpha\beta}$ alloy above which it is similar to that of the other Al - Zn alloys.

Figure 46 shows that the hardness of the eutectoid, homogenised at between 370 - 380°C for several hours and then quenched into iced-water to obtain an equiaxed fine-grain-size superplastic microstructure or in quenched-annealed or as-extruded condition is much lower at all temperatures up to 270°C than if the alloy is furnace-cooled from the same temperature to yield a lamellar microstructure. Table 11 shows that the lamellar eutectoid is not superplastic,it gives lower ductility (75 pct elongation) and higher UTS than the superplastic condition of the quenched-annealed or as-extruded material. The importance of grain size is indicated in that the hardness of the quenched-annealed material is more than the as-quenched condition.

The effect of applying a longer time of loading (Figure 47a,b) is to decrease the hardness value of the material at all temperatures. Figure 48 shows that the superplastic $A_{\alpha\beta}$ creeps even at room temperature, under a load of 10 gm, whereas $B_{\alpha\beta}$ does not.

As in Cu-Zn alloys, an activation energy for plastic deformation was calculated from the ℓn H/E vs Tm/T plots for each of Al-Zn alloys. The as-quenched and quenched-annealed superplastic conditions of the eutectoid showed activation energies of 11.3 Kcal/mole and 13.2 Kcal/mole respectively (Figures 49 and 50). There is some error in the determination of Q from ℓn H/E vs Tm/T plots. It was mentioned in Chapter 5 that $\Delta T \sim \pm 2.5$°C and $\Delta E \sim \pm 2\%$. Further the error in measuring the hardness values for a typical metal (aluminium) was about ± 2% in the temperature range of 0.6 - 0.9 Tm. Apart from these experimental errors involved in the measurement of H, E and T, there is an error in drawing a straight line through the data points. Since it is the variation of H and E with T which is important in calculating the Q values from ℓn H/E vs Tm/T plots, the total error in Q-values is about ± 2 Kcal/mole.

Similarly, the Q-values were found for A_β which represents the βphase and also for $A_{\alpha 1}$, $A_{\alpha 2}$ and $A_{\alpha 3}$ representing the α phase in Aαβ alloy over a wide range of temperatures (Figures 51 - 54). The results are listed in Table 12. At the superplastic temperature ~250°C, the activation energies were found to be 29.9 Kcal/mole and 19.5 Kcal/mole for the α and β phase respectively.

Figure 55 shows the ductility and ultimate tensile strength of $A_{\alpha\beta}$ alloy and its α and β phases as represented by ($A_{\alpha 1}$, $A_{\alpha 2}$, $A_{\alpha 3}$) and A_β alloys respectively over a range of temperatures, 120 - 250°C. At 250°C, elongations of 30 pct and 33 pct and UTS values 6.6 x 10^3psi and 8 x 10^3psi were obtained for α and β phases respectively. At all temperatures between 120 - 250°C, the eutectoid was much more ductile and its UTS value less than either of its phases. It has already been noted that at these temperatures the hardness of $A_{\alpha\beta}$ alloy is considerably lower than that of its individual UTS(α)/UTS(β) = 6.6 x 10^3psi/8 x 10^3psi ≃ 0.8 whereas the ratio of the hardness of α and β phases, H(α)/H(β) = 18kg/mm^2/15kg/mm^2 = 1.2.

Young's modulus, E, was determined in a similar way as for the Cu-Zn alloys by the vibration technique and the results for each alloy are shown in Figure 56, together with the values predicted from an empirical relation, using modulus data on pure elements Al and Zn from Köster[199]. The variation of E and H with temperature for the eutectoid $A_{\alpha\beta}$ and those of $A_{\alpha 1}$, $A_{\alpha 2}$, $A_{\alpha 3}$ and A_β alloys is shown in Figure 57 and Figure 58 respectively. The predicted moduli of $A\alpha_1$, $A\alpha_2$ and $A\alpha_3$ alloys are higher than the experimental ones, but the shape of the modulus graph is similar in each case. The modulus decrease with temperature is relatively slow in these alloys as compared to A_β and $A_{\alpha\beta}$ alloys. In general, the predicted values of the modulus are not close to the experimental moduli of Al-Zn alloys. A similar observation was made in Cu-Zn alloys. It can be seen from Figure 57 that the modulus decreases sharply in the vicinity of 250°C, where the hardness of the eutectoid $A_{\alpha\beta}$ is a minimum. Figure 58 shows that the decrease in modulus of $A\alpha_1$, $A\alpha_2$, $A\alpha_3$ and $A\beta$ alloys with temperature is similar to the decrease in hardness of these alloys with temperature.

The variation of mechanical properties at 250°C as a function of zinc content in the Al-Zn alloys is shown in Figure 59. The eutectoid has the minimum hardness and UTS and the maximum ductility, as compared to all the other alloys studied in this system. The hardness and UTS increases, while the ductility decreases with an increase in zinc content up to 22 wt pct. The properties of $A_\alpha 3$ (ie.,α phase) and A_β (ie β phase) are comparable, and the difference between the two is small.

The UTS and hardness values of all the alloys investigated in the present work were correlated in the temperature range 0.4 to 0.84 Tm and the results are given in Figure 60. It is clear that the majority of the data points can be expressed as, H/UTS = 3 ± 1. Since some of the alloys, eg., $A_{\alpha\beta}$, $B_{\alpha\beta}$ and B_β are more strain rate sensitive than others, the scatter could probably arise from the difference in true strain rate in the tensile test and the fact that in the hardness test, the strain rate is not known.

The Young's modulus at room temperature is plotted against Tm in Figure 61 for all the eight alloys in the annealed and as-extruded conditions. Except in the B_β alloy, the annealing treatment does not seem to alter the modulus value significantly. Figure 61 shows that the linear increase in modulus with Tm is only a rough approximation and the scatter in the results is considerable.

In-situ hot hardness tests between 20°C and 500°C were carried out on the aluminium matrix in the coarsened microstructure of an Al-6Cu-0.5Zn alloy. Hot hardness tests were also done on the alloy in the superplastic state. Unfortunately, the $CuAl_2$ particles were too small to be indented, even using the smallest load provided with the present machine. However, hot hardness data on $CuAl_2$ was available from Petty[201]. The alloy, in its superplastic condition, is softer than either of its phases at all temperatures. It is also clear from Figure 62 that $CuAl_2$ is considerably harder than the Al - matrix at all temperatures. At the superplastic temperature ($\sim$ 450°C), the ratio of the hardness of $CuAl_2$ and Al-matrix, $H(CuAl_2)/H(Al\text{-matrix} = 80/6 \tilde{-} 13$. Ignoring the effect of temperature on modulus, a plot of $\ell n\ H$ vs $1/T^{o}K$ (Figure 63) gives an activation energy of 50.8 Kcal/mole and 37.3 Kcal/mole for $CuAl_2$ and the Al-matrix respectively. An activation energy for the alloy itself near its superplastic temperature was found to be 21.6 Kcal/mole (Figure 63). A slight increase in hardness of the alloy between 450°C and 500°C was noted.

In-situ hot hardness data on ferrite and austenite phases of 0.19C steel and on moninally pure iron and cementite of white cast iron has been obtained by Gove[176]. Figure 64 shows that cementite is considerably harder than ferrite at all temperatures, and at 700°C,

$\frac{H(\text{cementite})}{H(\text{ferrite})} = \frac{97}{22} \simeq 4.$ Similarly, at 890°C,

$\frac{H(\text{austenite})}{H(Fe)} = \frac{20}{6} \simeq 3.$ Using, a plot of $\ell n\ H$ vs $1/T^{o}K$

activation energies of 60.2, 62.1, 83.4 and 28.7 Kcal/mole were found for pure iron, ferrite, cementite and austenite respectively (Figure 65).

Hot-hardness data and Young's modulus versus temperature data on all the alloys is given in Tables 16-36.

6.2 Discussion

In the present investigation of cavitation behaviour of superplastic alloys, the Zn-Al eutectoid is a model that represents a non-cavitating system. It consists of two phases which are very fine (< 1 μm, Figure 12) with a hardness, at the superplastic temperature 250°C, considerably lower than either of its constituent phases (Figure 13).

Figure 66 confirms that little cavitation occurs in this alloy. A number of inclusions were present in the as-received alloy (Figure 67) and it is clear from Figure 68 that these impurities have not changed their shape nor are cracked after deformation. An analysis in the SEM showed that these impurities are rich in iron. Woodthorpe and Pearce[202], while studying the fatigue behaviour of this alloy, also encountered these regularly-shaped inclusions and identified tham as $FeAl_3$ type.

The observation that these inclusions do not change in shape after deformation means that they are hard compared with their surroundings and remain practically undeformed during superplastic flow. The size of the inclusions was too small to allow measurement of their hardness variation with temperature using the present machine; however, Petty[201] has measured the hot hardness of $FeAl_3$ and gives 750 Hv at 20°C falling to 650 Hv at 250°C. He showed also that the inflection temperature of $FeAl_3$ was ~ 450°C, below which its hardness did not alter appreciably. In the low temperature regime, cracking of the $FeAl_3$ sample occurred under an indenter load of 5 kg, and so it was inferred that slip processes were difficult and that the atoms were very tightly bound.

Figure 69 shows that there are a few cavities associated with such inclusions; although much work has been done on this alloy there is little evidence of serious void formation (Ball and Hutchison[60]). The association of cavities with inclusions was confirmed by a SEM study and Figure 70 shows a cavity formed from an $FeAl_3$-type inclusion.

The likely explanation for the fact that other workers have not reported cavitation in this alloy could be that they used high-purity Al and Zn in their alloy preparation. Recently, Humphries and Ridley[128], have shown that the introduction of a hard intermetallic phase in the otherwise non-cavitating superplastic alloy Pb-Sn induces cavitation in this system. The Pb-Sn eutectic was a microduplex structure with an average grain size of ~2 μm while the ternary Sn-3.6%Pb-5.6%Ag alloy had a similar matrix structure but also contained ~5% by volume of silver-rich particles based on Ag_3Sn. The alloy is superplastic at room temperature and Vickers microhardness results obtained from a coarsened microstructure were as follows: Ag_3Sn 77 Hv, Sn-rich phase 3 Hv and Pb-rich phase 2 Hv.

Table 13 shows that the hardness, tensile strength and ductility values of the two phases at 250°C in the eutectoid, represented by $A_{\alpha 3}$ and A_β alloys are quite similar. It is widely considered that

accommodation of boundary sliding at any potential nucleation site will occur more readily if all phases present can contribute to the accommodation process, whether this involves diffusion or dislocation glide. The activation energies for deformation of $A_{\alpha 3}$, A_{β} and $A_{\alpha\beta}$ alloys at 250°C are 29.9 Kcal/mole, 19.5 Kcal/mole and 11.3 Kcal/mole respectively, which indicates that the β phase is more 'active' than α phase. The accommodation in the α phase may occur predominantly by dislocation glide whereas in the β phase the diffusion of atoms may be more important. Higher diffusivity of the β phase has been indicated in the work of Naziri and Pearce[203] and Naziri et al[65], in their in-situ experiments on the eutectoid at 100°C observed no dislocation activity in the β grains while some dislocation activity was observed in the α grains.

In calculating the activation energy for deformation from hot hardness data, the equation (4-24) ie., $H/E = G'\exp(Q/nRT)$ has been used. With $n = 5$, an activation energy value of $Q = 31$ Kcal/mole was obtained near 450°C (0.78 Tm) for commercial purity aluminium, which agrees reasonably with $Q = 34$ Kcal/mole determined from diffsuion studies by Lundy and Murdock[204].

At sufficiently high temperatures (> 0.5 Tm) the creep of solid-solution alloys can be described by a viscous glide of dislocations or a dislocation-climb mechanism. Weertman[205] showed that, whenever viscous glide of dislocations is the rate-controlling process, in solid-solution alloys, (the microcreep theory of Weertman) the creep rate should be proportional to the third power of stress ($n = 3$), in contrast to the fifth power law dependence observed for pure metals. For dislocation-climb-controlled creep of pure metals and alloys n lies in the range 4 to 7 which suggests an average value of $n = 5$. (Sherby and Burke[206]).

Sherby and Burke[206] collected data on power-law denendence for creep of solid-solution alloys and separated them into two categories. They list beta brass with $n = 3.5$ in class I alloys which follow the microcreep law, the alpha brasses, with $n = 5$ were in class II, which follows a dislocation-climb law ($n = 5$).

In superplasticity, the stress dependence of the strain rate (Ball and Hutchison[60]) has a value of $n = 2$ and Hayden et al[34] have observed that the $n = 2$ power dependence often extends over four orders of magnitude of strain rates. Assuming that an average of about 8 - 10 pct strain occurs during the hardness indentation process the approximate strain rate in a hardness test is $\dot{\varepsilon}_H \approx 10\text{pct}/15\text{sec} \approx 0.67 \times 10^{-3}\text{sec}^{-1}$, (15 seconds was the time of loading used).

The initial strain rate used in the present tensile tests was $1.6 \times 10^{-3}\text{sec}^{-1}$. Thus, although the strain rate in a hardness test is not accurately known, it would be reasonable to use $n = 2$ for the superplastic alloys here employed and to describe the activation energies calculated from hot hardness data as that for superplastic deformation. Further, since the strain-rate-sensitivity index, $m(=1/n)$ varies with temperature and grain size, $n = 2$ should <u>only</u> be

used for alloys in the fine-grained condition and at the superplastic temperature.

It has been pointed out (Sherby and Burke[206]) that the five-power law for steady-state creep breaks down when $\dot{\varepsilon}/D \geq 10^9$ and at $\sim$ 0.6 Tm for a pure polycrystalline metal. In view of this, it was for hot hardness data > 0.5 Tm only that n = 5 was used to calculate the activation energy for creep.

The shape of the hardness/temperature curves of intermetallic compounds is similar to those of pure metals (Petty[201]). There is no data available on the n values of $CuAl_2$ and Fe_3C; a value of n = 5 is assumed for these materials. The n-values used are shown in Table 14.

A number of workers have determined the activation energy for superplastic flow in the Zn-Al eutectoid. The results are summarised by Mohammed et al[61]. An activation energy of 15.4 Kcal/mole was obtained by Ball and Hutchison[6] and 13 - 20 Kcal/mole by Naziri et al[65]. It was pointed out that these workers did not correct their Q-values for the temperature dependence of the shear modulus and by doing so Mohammed et al obtained Q = 17.9 Kcal/mole for the Zn-Al eutectoid. In addition, they used an empirical relation of the type, $G = N_{Zn}G_{Zn} + N_{Al}G_{Al}$ to calculate the shear modulus of the alloy. This relationship is not correct for the eutectoid for, as Figure 56 shows, the calculated Young's modulus of the eutectoid from such a relationship is markedly different from the actual modulus values experimentally determined around 250°C.

In the present study, the variation of modulus with temperature was taken into account and a Q-value of 11.3 Kcal/mole and 13.2 Kcal/mole found for the as-quenched and quenched-annealed condition of the eutectoid respectively. This value is close to the activation energy of grain boundary diffusion in zinc, and indicates the important role played by the β phase, as suggested by Naziri et al[65].

Livesey and Ridley[136] reported that the degree of cavitation increased with the volume fraction, hardness and size of the intermetallic phase particles and attributed the cavitation phenomenon to the incomplete accommodation at the interfaces due to the restricted accommodation within the intermetallic phase. Thus, $FeAl_3$-type inclusions could produce cavitation in the normally non-cavitating Zn/Al eutectoid.

It was found that the lamellar structure of Zn/Al eutectoid gave a relatively low ductility, a high flow stress and cavitated extensively (Figure 71). This indicates the importance of a very fine equiaxed microstructure because the large grain boundary area associated with such a microstructure makes grain boundary diffusion the rate-controlling process.

At low temperatures (ie., 120°C and 190°C), the mechanical (eg., hardness, tensile strength and ductility) and diffusion (eg., activation energy) properties of the two phases

of the eutectoid are quite different, but, because of the small strains arising from grain-boundary sliding in a very fine-grained structure and the diffusion of the low melting point β phase, the alloy shows superplasticity without any significant amount of cavitation.

The H-value of the phases is important: firstly, because it gives a measure of the ease or difficulty of plastic deformation by dislocation glide in the individual phases and secondly, the variation of hardness with temperature provides information about the rate of diffusion in each phase. This two-fold information from the hardness measurements is important in explaining cavitation during superplasticity. The relative difference in H-value of the phases becomes less significant as the grain size is decreased since the strains developed in the individual grains as a result of greater grain boundary sliding become small and less accommodation over the grain or phase boundary area is needed. Moreover, because a larger grain boundary area is now available the contribution to accommodation processes from grain-boundary diffusion will be increased. This is probably the case in the deformation of the very fine grained Zn-Al eutectoid.

The other alloy studied is 60 Cu - 40 Zn brass ($B_{\alpha\beta}$) and this represents a cavitating superplastic alloy. Figure 72 shows the extent of cavitation in this alloy after superplastic deformation at 600°C. The cavity sites were mainly in α/β boundaries although some cavities were also situated at α/α, β/β and inside of β grains. The cavities were found not to interlink readily. The amount of cavitation decreased with increasing temperature at a fixed strain rate. The final failure is due to interlinking of the cavities.

The alloy shows maximum ductility at ~ 600°C where the two phases are present approximately in equal proportions and then decreases at 700°C. Sagat et al[5] showed that the grains were free of dislocation sub-structures after superplastic deformation and it was inferred that grain and phase boundary sliding contributed significantly to flow under superplastic conditions. The lower ductility at 700°C could be due to the large proportion of soft β phase and the small amount of hard α phase and a rapid increase in grain size at this temperature.

Figure 23 shows the influence of grain size on the H-value of $B_{\alpha\beta}$ alloy. At high temperatures, this is the reverse of the Hall-Petch relationship and is claimed to be due to an increased contribution of grain boundary diffusion and grain boundary sliding to flow with decreasing grain size, ie., with an increase in specific grain boundary area (Sagat et al[5], 1972).

In order to explain extensive cavitation at α/β boundaries, a surface energy term may be an important parameter, since different phase boundaries may require different energies to nucleate a cavity. However, Chandra et al[127](1978) made calculations on the energy required to nucleate a cavity at a given phase boundary and showed that if similar stress concentrations arise at different interfaces

then cavity formation will not be greatly favoured on any one type of boundary. They also measured the extent of sliding at α-α , β - β and α - β boundaries and showed that maximum sliding occurred at the α/β interfaces while the β -β boundaries exhibited very little sliding. This led them to believe that the predominance of α -β interface cavitation is either a result of greater sliding at the α/β boundary, or of a different ease of accommodation of sliding to each type of boundary.

Table 15 records the values of H, UTS, ductility and activation energy for the two phases at 600°C in $B_{\alpha\beta}$ alloy. The corresponding values of these properties for the superplastic $B_{\alpha\beta}$ are also shown in the same table 15, for comparison. The two phases are clearly 'incompatible', that is, they have different activation energies and mechanical properties.

An activation energy value of 21.2 Kcal/mole for $B_{\alpha\beta}$ alloy is obtained near the superplastic temperature of ∿ 600°C. Now, since grain boundary sliding is the predominant mode of deformation in a superplastic alloy and sliding occurs predominantly at α/β interfaces, this value of Q could be referred to as the 'activation energy for interphase diffusion' in this alloy and is similar to the activation energy of deformation of β phase, the latter being 22 Kcal/mole. At 600°C, the β phase is in a disordered state and interdiffusion of Cu and Zn atoms takes place within it. Thus, so far as the diffusion accommodation of interphase boundary sliding is concerned, the major contribution will come from the β phase, whereas the α phase with an activation energy of 42.2 Kcal/mole will remain relatively inactive.

The hardness and σ_f indicates that the plastic deformation of the β phase is easier than α phase whose H and UTS values are relatively a lot higher than that of β phase at 600°C. This is further confirmed by the observation that ductility value exhibited by the β phase is considerably more than that in α phase at the same temperature. Thus, even the dislocation - accommodation of interphase boundary sliding would be easier on the β phase side compared to the α phase side of the α/β interfaces in $B_{\alpha\beta}$ alloy. The low value of Q could also imply that a thermally-activated motion of dislocations will occur more easily in β phase as compared to the α phase which requires higher value of activation energy.

Figure 73 shows that the amount of cavitation in $B_{\alpha\beta}$ decreases with an increase in temperature, in agreement with other workers[128,129]. Now the hardness and UTS of the two phases of this alloy also decreases with increasing temperature. Therefore, during grain-boundary sliding the dislocation and diffusion processes in the deformed region near the grain or phase boundaries would be faster at higher temperatures than at lower temperatures.

The proportion of each phase in $B_{\alpha\beta}$ alloy varies with temperature (see Table 2). At 500°C, the α phase is quite hard

($H_V \approx 22$) and there is a large proportion of it ($\alpha:\beta = 88:12$) in $B_{\alpha\beta}$. At 600°C where the two phases are present in approximately equal proportions, the ratio of the hardness, UTS and ductility of the α and β phases is $H(\alpha)/H(\beta) \approx 7.6$, $UTS(\alpha)/UTS(\beta) \approx 7.2$ and $\frac{1}{\text{Ductility}(\beta)/\text{Ductility}(\alpha)} \approx \frac{1}{3.7}$. The ratio $\frac{H(\alpha)}{UTS(\alpha)} \approx 3.4$ and $\frac{H(\beta)}{UTS(\beta)} \approx 3.2$ at the same temperature. The calculated flow stress values for the in-situ α and β phases of the $B_{\alpha\beta}$ alloy are 5.23×10^3 psi and 0.88×10^3 psi respectively. The in-situ $UTS(\alpha)/UTS(\beta) \approx 5.9$. This large difference in mechanical properties together with different activation energies (Q_α = 42.2 Kcal/mole, Q_β = 22 Kcal/mole) of the two phases leads to extensive cavitation due to unbalanced accommodation of the grain boundary sliding at the α/β interfaces in this alloy. At 700°C the difference in mechanical properties is small and this leads to less cavitation at this temperature. The alloy consists of a larger proportion of β phase and also exhibits lower ductility at this temperature than at 600°C, probably due to rapid grain growth and so a smaller number of α/β boundaries. Both these factors will make for less grain boundary sliding. The individual phases were found to be elongated along the tensile axis (figure 74).

According to Humphries and Ridley[128](1978), if the external stress level reflects the magnitude of the stress concentrations which can develop in the material, the threshold stress for cavity nucleation will be exceeded at more potential nucleation sites as the stress level rises, (ie., as the temperature decreases) therefore, increasing the cavity nucleation rate. On the other hand, if cavity growth was controlled by lack of diffusional accommodation, then decreasing the temperature wouldlead to lower diffusivities. The large number of isolated cavities in Figure 72 shows that the interlinkage of cavities is very slow, but it can be seen from figure 75 that it is the interlinking of cavities which leads to final fracture. From Figures 24 and 32 the hardness of the two phases in $B_{\alpha\beta}$ alloy is seen to be about the same ($\sim$ 95 H_V) at 250°C (0.45 T_m). The alloy was tested at various strain rates at this temperature and gave an optimum elongation of $\sim$ 110 pct. Although the difference in hardness of the two phases was negligible, the alloy still exhibited extensive cavitation at triple points, involving both phases (Figure 76). Thus, in addition to the relative hardness of the phases, the stress level and temperature of the alloy are also important. The individual phases of the alloy were observed to be elongated in the direction of the tensile axis. It was felt that the grain size of the starting material was quite large ($\sim$ 7 μm) in comparison to the Zn-Al eutectoid (grain size $\sim$ 1 μm) which shows superplasticity without any significant cavitation at 250°C (0.7 T_m).

Steels may be made superplastic by obtaining a microduplex structure which consists of either α + Fe_3C or α + γ. The α + Fe_3C[133,134] microduplex structures were produced by spheroidizing plain carbon steels, giving a grain size of $\sim$ 5 μm and an elongation of $\sim$ 130 pct at 700°C. However, the material cavitates extensively at the /Fe_3C interfaces leading to failure. Walser, Kayaki and Sherby[209] have developed a thermal mechanical process to obtain a mixture of cementite in ferrite consisting of ferrite grains finer

than one micron in size and cementite particles finer than one tenth of a micron in size. Such a steel (1.6%C) exhibited elongations up to 750% when deformed at 650°C. They attributed this phenomenon to the presence of strong cementite in the alpha range which mades plastic flow by normal slip processes more difficult, thus extending the scope of superplastic behaviour. The alloy does not show any cavitation during superplastic deformation. For ambient temperature applications the material is of very high strength and its ductility can be improved by heat treatment.

It is, therefore, proposed that some kind of thermomechanical processing should be developed, or a powder metallurgical technique used to make an ultrafine microstructure (grain size $\leq$ 1 μm) in duplex 60/40 brass. Then the deformation processes may be confined mainly to the large grain boundary area available and high ductility may be obtained without significant cavitation occurring at 250°C (0.45 T_m). This assumes that rapid grain growth would not occur at this temperature. For low temperature applications (ie., below 0.3 T_m) a component formed from such an alloy would yield a high tensile strength $\sigma_y \propto \left(\frac{1}{\sqrt{\text{grain size}}}\right)$ and good fatigue resistance. On the other hand, for high temperature applications its creep resistance can be improved by coarsening the microstructure by annealing treatment.

The high temperature ($\geq$ 0.5 T_m) stability of the duplex structure of a superplastic alloy will be greater, the greater the difference in composition of the two phases. It was observed that the microstructure of Zn/Al eutectoid, in which the two phases differ much in composition remains almost unchanged after superplastic deformation. In the case of 60/40 brass, in which the two phases do not differ much in composition, rapid grain growth occurs during superplastic deformation at 600°C (grain size after superplastic deformation was $\sim$ 40 μm) which leads to large strains arising from GBS and makes the alloy more prone to cavitation. The further development of the alloy for commercial applications is being considered by Sagat et al[5], particularly, with regard to restricting grain growth and so cavitation by means of precipitate particles, and possibly decreasing the superplastic temperature.

The importance of cavitation during superplastic forming depends upon the tensile strains involved in making a component, provided the strain rate and temperature are carefully selected. Although superplasticity has been observed in Cu- and Fe- base alloys here cavitation is a serious problem in their commercial exploitation for it drastically limits the elongation to failure and may affect the service properties of superplastically formed components. Dunlop et al[6] defined an acceptable level of cavitation as that which left the subsequent room temperature properties nearly unaffected and determined 'useful' elongation as a function of engineering strain-rate at 1073°K for CDA alloy 619. Smith and Ridley[11] designed an iron K1970 alloy of composition Fe-4%Ni3%Mo-1.6%Ti, size $\sim$ 3 μm, which showed good superplastic behaviour in the temperature range 900-960°C, where it exists as an α/γ structure containing approximately equal proportions of the two phases. The alloy cavitates during superplastic deformation.

In an attempt to reduce the extent of cavitation in this alloy, an addition of boron was made, because boron is known to reduce microcracking[150] during creep of austenitic stainless steels. It was found that trace additions of boron (40 ppm) to the alloy led to a marked decrease in the extent of cavitation. However, the way in which cavitation was inhibited by trace additions of boron, was not understood.

Figures 77 and 78 show the extent of cavitation at 600°C in Bα and Bβ alloys respectively. The Bα alloy consists mainly of α phase with a small proportion of β phase at 600°C. It is clear that Bα shows extensive cavitation whereas there is a small number of cavities present in Bβ alloy. The Bβ alloy is highly ductile (elongation ∿ 170 pct at 600°C) and there is evidence of subgrain formation after deformation (Figure 79). Griffith and Hammond[207] attributed the high ductility of β brass to the formation of a stable subgrain boundary network after a few percent strain in which the subgrain boundaries act as the sources and sinks for a Herring-Nabarro diffusional process. The high rate of diffusion required is provided by the inherent anomalously high diffusivity of the b.c.c β brass. Their study of β brass (47.7 Zn) at 0.8 T_m gave an activation energy of 24 Kcal/mole. Funamizu and Katsuya[208] studied the effect of the order-disorder transformation upon the diffusion behaviour in the Cu-Zn system and showed that the activation energy for interdiffusion in the ordered β' phase (34.2 36.6 Kcal/mole) was about 1.5 times higher than that in the disordered β phase (ie., 23.9 ∿ 21.2 Kcal/mole). From the present study the Q-values obtained were 42 Kcal/mole and 21.2 Kcal/mole in the ordered and disordered region respectively.

The occurrence of cavitation in Bα alloy may be explained on the same basis as in Bαβ alloy. The Bα alloy is not a single α phase but contains a small proportion of β phase at 600°C. Any cavity created at the triple point involving both phases will grow because of unbalanced accommodation to grain boundary sliding by the two phases. The cavitation at α/α boundaries could arise from the action of sliding at these boundaries which produces stress concentrations at any irregularity in the boundary and due to the small amount of accommodation available from either α phase.

Figure 64 shows the in-situ hot hardness data on nominally pure iron (0.014C), cementite of white cast iron, and ferrite and austenite of 0.19C steel from Gove[176]. At 700°C, the hardness of the cementite is about four times the hardness of nominally pure iron. Using the above data and ignoring the effect of modulus variation with temperature, the activation energy values are 83.4 Kcal/mole and 60.2 Kcal/mole for cementite and iron respectively. Thus, the hard cementite contributes little compared to the ferrite in accommodating the grain boundary sliding strains and as a result of unbalanced accommodation cavities will be nucleated at α/Fe_3C interfaces in the (α + Fe_3C) superplastic steel of grain size ∿ 5 μm.

Morrison[10] has studied superplasticity in low carbon steels (grain size ∿ 2 μm), containing alloying elements Al, Si and P to raise the testing temperature in the α + γ region to 900°C. Maximum elongation was ∿ 370 pct and the existence of pores were observed in the

elongated specimens. It was thought that the pores probably originated as a result of incompatible deformation of the materuak on either side of the interface.

Ideally, the two phases of a steel, whose cavitation behaviour is to be studied, should be hot-hardness-tested in-situ at the superplastic temperature and their properties compared. From Figure 64 at 900°C, the hardness of austenite of 0.19C steel and ferrite of pure iron is 20 H_V and 6 H_V respectively. Using the data in Figure 65 and ignoring the effect of temperature on modulus, activation energy values of 28.7 Kcal/mole and 60.2 Kcal/mole were found in the α and γ regions respectively. Thus, if these phases represent the behaviour of α and γ phases in a cavitating (α + γ) steel, then the occurrence of cavitation may be explained on the basis of incomplete accommodation.

The commercial alloy Supral 150 (Al-6%Cu-0.5%Zr) is used superplastically at 450°C and Figure 62 shows that its nardness is minimum at near 450°C above which it rises, probably because of rapid grain growth. It is clear from Figure 62 that the hardness of the alloy in the superplastic condition is lower than the hardness of its individual phases, as was the case in Zn-Al eutectoid. Although the alloy exhibits large elongations (∿ 1000 pct) it cavitates during superplastic deformation. Dynamic recrystallisation[210,211] is thought to be operating during superplastic deformation of this alloy, but Ridley[123] has pointed out that it is difficult to see how the alloy can cavitate without any grain boundary sliding occurring in it during deformation. Using hot hardness data on $CuAl_2$ from Petty[201] an activation energy of 50.8 Kcal/mole was obtained (Figure 63). The present in-situ hot hardness sutdy of the Al-matrix and the alloy itself gave an activation energy of 37.3 Kcal/mole and 21.6 Kcal/mole respectively. These values of the activation energy were obtained without taking into account the effect of temperature on modulus. The activation energy of lattice self-diffusion for Cu and Al is 47 Kcal/mole and 34 Kcal/mole respectively. Assuming that grain boundary diffusion activation energy is half the self-diffusion value (eg., 17 Kcal/mole in Al) it is clear that the rate controlling process in the superplastic deformation of the alloy has an activation energy which is close to the grain boundary diffusion energy.

Dynamic recrystallisation[210,211] is occurring during at least the early stages of deformation in this alloy. It was proposed that the $CuAl_2$ particles disturb the pattern of plastic flow in their vicinity and act as preferential nucleation sites for recrystallisation in the alloy. At the superplastic temperature the hardness of $CuAl_2$ and the Al-matrix is ∿ 80 and ∿ 6 H_V respectively. Thus, during superplastic deformation the high concentration of stress developed at the $CuAl_2$/Al-matrix interfaces may lead to decohesion of the particles because these are both harder and have an activation energy (= 50.8 ± 2 Kcal/mole) higher than that of the Al-matrix (Q = 37.3 ± 2 Kcal/mole) and will relatively contribute less to accommodation than Al-matrix.

6.3 Conclusions

1 The superplastic alloys are very soft at their superplastic temperatures, eg., the hardness of the Zn/Al eutectoid at 250°C is ∿ 2 Hv, 60/40 brass at 600°C is ∿ 3.1 Hv and Supral 150 is ∿ 1.4 Hv.

2 Almost no cavitation occurs during superplastic deformation of fine-grained Zn/Al eutectoid, though some inclusions were present in the as-received alloy. These did not change shape during deformation indicating that they are hard, compared with their surroundings. A few cavities were found to be associated with such inclusions.

3 The microduplex $B_{\alpha\beta}$ alloy cavitates extensively during superplastic deformation at 600°C. The amount of cavitation decreased with increasing temperature at a fixed strain rate. Cavities were situated mainly at α/β boundaries.

4 The fine-grained Zn/Al eutectoid has a minimum hardness between 250 - 270°C, above which it increases and then falls slowly. This is so, because the alloy becomes a single phase α' above 275°C and is no longer a mixture of two very fine phases. At 280°C, the hardness is about five times its value at 270°C.

5 The two phases of the Zn/Al eutectoid have about the same hardness at the superplastic temperature and their ratio $H(\alpha)/H(\beta) = 1.2$.

6a The two phases in-situ of the 60/40 brass have different hardness values at the superplastic temperature and their ratio $H(\alpha)/H(\beta) \simeq 6.3$. The corresponding value of the ratio for separate phases of the alloy is ∿ 7.6.

6b The ratio $H(\alpha)/H(\beta)$ vs $T^{o}K$ plot follows a similar pattern for the in-situ and separate phases of the Bαβ alloy, indicating that the two phases of the alloy are represented fairly accurately by the Bα and Bβ alloys in the present work.

6c At temperatures below 250°C, the β phase of the Bαβ alloy is harder than its α phase, the two phases are about equal in hardness at 250°C and above this the β phase is much softer than the α phase.

7 At the superplastic temperature of the Zn/Al eutectoid, elongations of 30 pct and 33 pct were obtained for its α and β phases respectively. The ratio $UTS(\alpha)/UTS(\beta) \simeq 0.8$ at the same temperature.

8 At the superplastic temperature of the Bαβ alloy, the β phase is highly ductile (172 pct elongation) whereas in the α phase an elongation of only 54 pct could be obtained. The ratio $UTS(\alpha)/UTS(\beta) \simeq 7.2$, $H(\alpha)/UTS(\alpha) \simeq 3.4$ and $H(\beta)/UTS(\beta) \simeq 3.2$ at the same temperature. The calculated flow stress values for the in-situ α and β phases

of the Bαβ alloy are 5.23×10^3 psi and 0.88×10^3 psi respectively. The in-situ UTS(α)/UTS(β) ≃ 5.9.

9 A correlation between hardness and UTS of the alloys can be expressed as, H/UTS = 3 ± 1 in the temperature range 0.4 - 0.84 Tm.

10 A simple empirical relation such as

$$E_{AB} = \frac{x \text{ wt\%A} \times E_A + (100 - x) \text{ wt\%B} \times E_B}{100}$$

cannot be used to predict the modulus of an alloy.

11 The activation energy calculated from hot hardness data for polycrystalline aluminium (Q = 31 ± 2 Kcal/mole) agrees reasonably with the value obtained from other studies (Q = 34 Kcal/mole).

12a The two phases of the Zn/Al eutectoid have similar mechanical properties at the superplastic temperature. Their activation energies imply that the accommodation of GBS may be occurring in the α phase (Q = 29.9 ± 2 Kcal/mole) predominantly by dislocation glide, whereas in the β phase (Q = 19.5 ± 2 Kcal/mole) the diffusion of atoms may be more important. The Q value for the eutectoid is 13.? ± 2 Kcal/mole which is close to the value for grain boundary diffusion in zinc, indicating the important role played by the β phase during deformation.

12b The presence of very hard $FeAl_3$ - type impurities introduces a small amount of cavitation in the otherwise normally non-cavitating Zn/Al eutectoid, becuase of incomplete accommodation at the inclusion/matrix interfaces.

13 The two phases of Bαβ alloy at the superplastic temperature are 'incompatible', that is, they have different activation energies ($Q\alpha$ = 42.2 ± 2 Kcal/mole, $Q\beta$ = 22 ± 2 Kcal/mole) and mechanical properties (H(α) ≃ 12.5 Hv, H(β) ≃ 2 Hv). Their properties suggest that both the dislocation and diffusion accommodation of the interphase boundary sliding would be easier on the β phase side compared to the α phase side of the α/β interfaces in the Bαβ alloy. Thus the alloy cavitates because of unequal contributions made by the two phases to the accommodation of interphase sliding during superplastic deformation. Moreover, there is grain growth occurring during superplastic deformation which leads to large strains arising from GBS.

14a At low temperatures (ie., 120°C and 190°C), the two phases of the eutectoid differ in mechanical properties. However, it does not show any significant amount of cavitation because of its very fine and stable grain size which leads to small strains arising from GBS. Moreover, because of the larger grain boundary area available the contribution to accommodation processes from grain boundary diffusion will be more.

14b At 250°C (0.7 T_m), the lamellar structure of the Zn/Al eutectoid is harder and less ductile (75 pct elongation) than the equiaxed fine-grained structure. It is not superplastic and cavitates extensively, indicating the importance of grain size and shape during deformation.

15 Assuming that the phases of 0.16C steel represent the behaviour of α and Fe_3C or α and γ phases in the α + Fe_3C or α + γ cavitating superplastic steels respectively, then the occurrence of cavitation at the α/Fe_3C or α/γ interfaces in such steels may be explained on the basis of unbalanced accommodation.

16 The $B_{\alpha\beta}$ alloy gives an optimum elongation of ~ 110 pct at 250°C (0.45 T_m) where its two phases are about equal in hardness (~ 95 H_V) but it still exhibits extensive cavitation at triple points involving both phases (Figure 76). It was felt that the grain size of the starting material was quite large (~ 7 μm) in comparison to the Zn/Al eutectoid (grain size ~ 1 μm) which shows superplasticity without any significant cavitation at 250°C (0.7 T_m). Processing which produces a mixture of cementite in ferrite consisting of ferrite grains < 1 μm and cementite particles < 1/10 μm does not cavitate during superplastic deformation. It is, therefore, proposed that some kind of thermomechanical processing should be developed, or a powder metallurgical technique used to made an ultrafine microstructure (grain size ≤ 1 μm) in duplex 60/40 brass. Then, the deformation processes may be confined mainly to the large grain boundary area available and high ductility may be obtained without significant cavitation occurring at 250°C. This assumes that rapid grain growth would not occur at this temperature.

17 The hardness of Supral 150 is lower than the hardness of its individual phases. as is the case with Zn/Al eutectoid. During deformation by dynamic recrystallisation, the high stress concentrations developed at the $CuAl_2$/Al-matrix interface may lead to decohesion of the $CuAl_2$ particles because these are both harder (~ 80 H_V) and have an activation energy (50.8 ± 2KCal/mole) higher than that of the Al matrix (Q = 37.3 ± 2 KCal/mole) and will relatively contribute less to accommodation than the Al matrix.

Thus, it seems that cavitation will not occur during deformation of a superplastic alloy consisting of two phases which are ultrafine (< 1 μm) and stable, whether these are 'compatible' with each other or not. A superplastic alloy (1 μm < grain size < 10 μm) will show cavitation during deformation whenever its two phases are 'incompatible' (ie., they have different mechanical and diffusion properties) at the superplastic temperature. On the other hand, because of the similarity in properties of the two phases of a superplastic alloy (grain size < 10μm), the two phases will make equal contributions to accommodate the strains arising from GBS, as a result cavitation does not occur. This assumes that rapid grain growth does not occur at the superplastic temperature.

REFERENCES

1 E E Underwood, J. Metals, 1962, 14, 914

2 G J Davies, J W Edington, C P Cutler & K A Padmanabhan, J. Mater. Sci., 1970, 5, 1091.

3 R H Johnson, Metallurgical Reviews, 1970, 15, No 146, 115.

4 J W Edington, K N Melton & C P Cutler, Progress Mater. Sci., 1975, 21, 67.

5 S Sagat, P Blenkinsop & D M R Taplin, J. Inst. Metals, 1972, 100, 268

6 G L Dunlop, E Shapiro, D M R Taplin & J Crane, Metallurgical Trans., 1973, 4, 2039

7 K Matukiand & M Yamada, J. Japan Inst. Metals, 1973, 37, 448

8 R H Bricknell, Personal Communication (Ref No 72 in Ref 21).

9 A Karim, D L Holt & W A Backofen, Trans. A.I.M.E., 1969, 245, 1131.

10 W B Morrison, Trans. Quart. ASM, 1968, 61, 423.

11 C I Smith & N Ridley, Metals Tech., 1974, 1, 191.

12 C H M Jenkins, J. Inst. Metals, 1928, 40, 21.

13 C E Pearson, J. Inst. Metals, 1934, 54, 111.

14 A A Bochvar & Z A Sviderskaya, Izv. Akad. Nauk SSSR, Otdel. Tekh. Nauk, 1945, No 9.

15 W A Backofen, I R Turner & D H Avery, Trans. Quart. ASM, 1964, 57, 980.

16 D H Avery & W A Backofen, Trans. Quart. ASM, 1965, 58, 551-62.

17 T H Alden, Acta Met., 1967, 15, 469-80.

18 T H Alden, J. Aust. Inst. Metals, 1969, 14, 207-216

19 D L Holt, Trans. A.I.M.E., 1968, 242, 25-31.

20 M F Ashby & R A Verral, Acta Met., 1973, 21, 149-163

21 J W Edington, Metals Tech., March 1976, Vol 3, No 3, 138-151.

22 T H Alden, Treatise on Materials Science and Technology, Edited by R J Arsenault, Academic Press 1975, Vol 6, p226.

23 K A Padmanabhan, Mat. Sci. & Eng., 1977, 29, 1-18

24 D A Woodford, Trans. Quart. ASM, 1969, 62, 291.

25 C Rossard, Met. Rev., 1966, 63 (3), 225.

26 E W Hart, Acta Met., 1967, 15, 351.

27 P J Wray, J. Appl. Phys., 1970, 41, 3347.

28 R E Smallman , Modern Physical Metallurgy, Bucterworths, 1970.

29 K A Padmanabhan & G J Davies, Phys. Stat. Sol., 1973, A18, 295.

30 P Chaudhari,Acta Met., 1967, 15, 1777.

31 S W Zehr & W A Backofen, Trans. Quart. ASM, 1968, 61, 300.

32 M J Stowell, J L Robertson & B M Watts, Metal Sci. J., 1969, 3, 41.

33 R Raj & M F Ashby, Met. Trans., 1971, 2, 1113.

34 H W Hayden, R C Gibson, H F Merrik & J H Brophy, Trans. ASM, 1967, 60, 3.

35 A Karim, Met. Trans., 1970, 1, 1045.

36 A Karim, Scripta Met., 1969, 3, 887.

37 D L Holt & W A Backofen, Trans. ASM, 1966, 59, 755.

38 W A Backofen, F J Azzarto, G S Murty & S W Zehr, "Ductility", ASM, 1967, p2

39 C M Packer & O D Sherby, Trans. ASM, 1967, 60, 21.

40 N F Mott, Proc. Phys. Soc., 1951, B.64, 729.

41 J Friedel, Dislocations (Pergamon Press, 1964), 279.

42 H W Hayden & J H Brophy, Trans. Quart. ASM, 1968, 61, 542.

43 J Weertman, Trans. ASM, 1968, 61, 681..

44 T H Alden, Acta Met., 1969, 17, 1435.

45 C M Packer, R H Johnson & O D Sherby, Trans. A.I.M.E., 1968, 242, 2485

46 R H Johnson, C M Packer, L Anderson & O D Sherby, Phil. Mag., 1968, 18, 1309.

47 J J Jonas, C M Sellars & W J McG. Tegart, Met. Rev., 1969, No 130.

48 R C Gifkins, J. Inst. Metals, 1967, 95, 373.

49 K D Fike & H J Rack, Trans. ASM, 1969, 62, 537.

50 M J Stowell, B M Watts, D G E Owen & B L Baikie, Inst. Of Metals Meeting on Recrystallisation, London, 1973 (Ref No 198 in Ref 4). R Grimes, M J Stowell & B M Watts, Metals Soc. Meeting on "Alloy Composition and Microstructure Control in Relation to Processing", London, 1975, (Ref No 340 in Ref 4).

51 R N Stevens, Met. Rev., 1966, 11, (108), 129.

52 H E Cline & T H Alden, Trans. A.I.M.E., 1967, 239, 710-714.

53 D Lee & W A Backofen, Trans. A.I.M.E., 1967, 239, 1034-1040.

54 W A Backofen, G S Murty & S W Zehr, Trans. A.I.M.E., 1968, 242, 31.

55 R C Cook & N R Risebrough, Scripta Met., 1968, 2, 487-89.

56 R N Stevens, Phil. Mag., 1971, 23, 265.

57 T S Ke, J. Appl. Phys., 1949, 20, 274.

58 T G Langdon, Phil. Mag., 1970, 22, 689.

59 H Gleiter & B Chalmers, Prog. Mat. Sci., 1973, 16, 1.

60 A Ball & M M Hutchison, Metal Sci. J., 1969, 3, 1-7.

61 F A Mohammed, Shen-Ann Shei & T G Langdon, Acta Met., 1975, 23, 1443-1450.

62 A K Mukherjee, Mater. Sci. Eng., 1971, 8, 83

63 R C Gifkins, to be published (Ref 159 in Ref 4).

64 W A Rachinger, J. Inst. Metals, 1952, 81, 33.

65 H Naziri, R Pearce, M Henderson-Brown & K F Hale, J. Microsc., 1973, 97, 229.

66 A K Mukherjee, J E Bird & J E Dorn, Trans. ASM, 1969, 62, 155.

67 J D Emburry, C M Sergent & R B Nicholson, Acta Met., 1962, 10, 1118.

68 R C Gifkins, Met. Trans., 1976, 7A, 1225-1232.

69 R C Gifkins, Scripta Met., 1973, 7, 27.

70 J H Gittus, Journal of Engineering Materials and Technology, July 1977, 244-251.

71 G Herriott, B Baudelet & J J Jones, submitted for publication 1976, (Ref No 40 in Ref 70).

72(a) F Perinet, CEA-R-4657, "Contribution to the Study of Interfacial Diffusion", Saclay, 1975, Gif sur Yvette, France (Ref No 44 in Ref 70).

72(b) Y G Nakagawa & G C Weatherley, Mater. Sci. & Eng., 1972, 10, 223-228.

73 F Garofalo, "Ductility", ASM, 1967, p87.

74 G W Greenwood, "Interfaces", (Edited by R C Gifkins) Butterworths 1969, p223.

75 A J Perry, J. Mater. Sci., 1974, 9, 1016.

76 R C Gifkins, "Fracture", John Wiley, New York, 1959, p579.

77 D McLean & M H Farmer, J. Inst. Met., 1956-57, 85, 41.

78 D McLean, J. Inst. Met., 1952-53, 81, 293.

79 J N Greenwood, Bull, Inst. Metals, 1952, 1, 104 & 121.

80 J N Greenwood, D R Miller & J W Suiter, Acta Met., 1954, 2, 250.

81 C W Chen & E S Machlin, Trans. Met. Soc. A.I.M.E., 1957, 209, 829.

82 C W Chen & E S Machlin, Acta Met., 1956, 4, 655.

83 R C Gifkins, Acta Met., 1956, 4, 98.

84 A H Cottrell, "Structural Processes in Creep", Iron Steel Inst. and Inst. Met., London, 1961, p1-18.

85 J E Harris, Trans. Met. Soc. A.I.M.E., 1965, 233, 1509.

86 C W Weaver, J. Inst. Metals, 159-60, 88, 296.

87 A E B Presland & R I Hutchinson, J. Inst. Metals, 1961-62, 90, 239.

88 J Intrater & E S Machlin, Acta Met., 1957, 7, 170.

89 B J Nield & A G Quarrell, J. Inst. Metals, 1956-57, 85, 480.

90 R Resnick & L L Siegel, Trans. A.I.M.E., 1957, 209, 87.

91 J P Dennison & B Wilshire, J. Inst. Metals, 1962-63, 91, 343.

92 P W Davies & B Wilshire, Trans. Met. Soc. A.I.M.E., 1961, 221, 1246.

93 B Wilshire, "Mechanisms of Cavity Development during Creep & their Practical Implications", Dept of Metallurgy, University College, Swansea, Paper 13, p123-130.

94 E D Hondros, Proc. Roy. Soc. A., 1965, 286, 479.

95 H R Tipler & D McLean, Metal Sci. J., 1970, 4, 103.

96 P Bowring, P W Davies & B Wilshire, Metal Sci. J., 1968, 2, 168.

97 R C Boettner & W D Robertson, Trans. Met. Soc. A.I.M.E., 1961, 221, 613.

98 R T Ratcliffe & G W Greenwood, Phil. Mag., 1965, 12, 59.

99 R W Balluffi & L L Siegle, Acta Met., 1957, 5. 449.

100 G W Greenwood, Phil. Mag., 1969, 19, 423.

101 J N Greenwood, J. Iron Steel Inst., 1952, 171, 380.

102 D Hull & D E Rimmer, Phil. Mag., 1959, 4, 673.

103 G W Greenwood, Phil. Mag., 1963, 8, 707.

104 R W Balluffi & L L Siegle, Acta Met., 1955, 3, 170.

105 E S Machlin, "Fracture", John Wiley, New York, 1959, 45-46.

106 D Kramer & E S Machlin, Acta Met., 1958, 6, 454.

107 J Intrater & E S Machlin, Acta Met., 1959, 7, 140.

108 A E B Presland & R I Hutchinson, 5th International Conference on Electron Microscopy, Academic Press, New York, 1962, Paper J-15.

109 A E B Presland & R I Hutchinson, J. Inst. Met., 1963-64, 92, 264.

110 J E Harris, V J Haddrell & G A Richards, J. Nuclear Mater., 1962, 6, 144.

111 A Gittins, M. Eng. Sc. Thesis, Melbourne, 1961, (quoted by R C Gifkins, "Fracture", Butterworths, London, 1963, 44-60).

112 D M R Taplin & L J Barker, Acta Met., 1966, 14, 1527.

113 I J Spark & D M R Taplin, J. Aust. Inst. Met., 1969, 14, 298.

114 D M R Taplin, Met. Eng. Quart., 1970, 10, 31.

115 D M R Taplin & A L Wingrove, Acta Met., 1967, 15, 1231.

116 J N Greenwood, J. Iron Steel Inst., 1954, 176, 268.

117 L L Siegle, Acta Met., 1959, 7, 421.

118 H C Rogers, "Fracture", John Wiley, New York, 1959, pp46-49.

119 H C Rogers, "Fracture", John Wiley, New York, 1959, pp559-560.

120 G J Cocks & D M R Taplin, Scripta Met., 1969, 3, 623.

121 R G Fleck, G J Cocks & D M R Taplin, Met. Trans., 1970, 1, 3415.

122 D M R Taplin, J. Aust. Inst. Met., 1965, 10, 336.

123 N Ridley, Metals Tech., March 1976, 3, 169.

124 R Grimes, Metals Tech., March 1976, 3, 169.

125 T Chandra, J J Jonas & D M R Taplin, J. Aust. Inst. Met., 1975, 20, 220.

126 N Ridley, C W Humphries & D Livesey, Proc. 4th International Conference on the Strength of Metals and Alloys, Nancy-France, 30 August - 3 September, 1976, p433.

127 T Chandra, J J Jonas & D M R Taplin, J. Mater. Sci., 1978, 13, 2380.

128 C W Humphries & N Ridley, J. Mater. Sci., 1978, 13, 2477.

129 S Sagat & D M R Taplin, Acta Met., 1976, 24, 307-315.

130 R G Fleck, C J Beavers & D M R Taplin, J. Mater. Sci., 1974, 9, 1737.

131 C I Smith, B Norgate & N Ridley, Metal Sci., 1976, 10, 182.

132 H Naziri, Proc. 3rd Intern. Conf. on High Voltage Electron Microscopy, Edited by P R Swann et al, Academic Press, 1974, p245.

133 G R Yoder & V Weiss, Metall. Trans., 1972, 3, 675.

134 A R Marder, Trans. A.I.M.E., 1969, 245, 1337.

135 C W Humphries & N Ridley, J. Mater. Sci., 1977, 12, 851.

136 D W Livesley & N Ridley, J. Mater. Sci., 1973, 13, 825.

137 A N Stroh, Proc. Roy. Soc. A., 1934, 223, 404.

138 N Ridley & D W Livesley, Fracture 1977, Vol 2, Edited by D M R Taplin, Univ. of Waterloo Press, 1977.

139 G Brinson, Private Communication (Ref No 338 in Ref 4).

140 S Sagat, PhD Thesis, 1974, Univ. of Waterloo.

141 E Smith & J T Barnby, Metal Sci. J., 1967, 1, 1.

142 R G Fleck, C J Beavers & D M R Taplin, Acta Met., 1975, 23, 415.

143 D M R Taplin & R F Smith, Fracture 1977, Vol 2, Edited by D M R Taplin, Univ. of Waterloo Press, 1977.

144 J W Hancock, Met. Sci., 1976, 10, 319.

145 G L Dunlop & D M R Taplin, J. Mater. Sci., 1972, 7, 316.

146 G L Dunlop & D M R Taplin, J. Aust. Inst. Met., 1971, 16, 195.

147 H W Schadler, Trans. Met. Soc. A.I.M.E., 1968, 242, 1281.

148 C W Humphries & N Ridley, J. Mater. Sci., 1974, 9, 1429.

149 H W Hayden, S Floreen & P D Goodell, Met. Trans., 1972, 3, 833.

150 C Crussard et al, Joint Int. Conf. on Creep, London, Inst. of Mech. Eng., 1963, 1, 91.

151 C W Humphries, MSc Thesis, 1973, Univ. of Manchester.

152 C W Humphries, PhD Thesis, 1975, Univ. of Manchester.

153 R G Fleck, C J Beavers & D M R Taplin, Met. Sci., 1975, 9, 49.

154 R G Fleck, C J Beavers & D M R Taplin, J. Mat. Sci., 1974, 9, 241.

155 J W Christian, "The Theory of Transformations in Metals and Alloys", Pergamon Pressm Oxford, 1965, p489.

156 D H Avery & W A Backofen, Trans. ASM, 1968, 61, 300.

157 R G Fleck, PhD Thesis, 1973, Univ of Birmingham.

158 S Sagat & D M R Taplin, Met. Sci., 1976, 10, 94.

159 B W Mott, "Microindentation Hardness Testing", Butterworths, London, 1956.

160 B W Mott, S D Ford & E R W Jones, A.E.R.E., Harwell, Report M/R, 1017, 1952, quoted in Ref 159.

161 D Tabor, "The Hardness of Metals", Clarendon Press, 1951.

162 E R Petty, Metallurgia, 1962, 65, 25.

163 V A Borisenko, Soviet Powder Met., 1965, No 2, 134, quoted in Ref 164.

164 Jorgen Larsen-Badse, Trans. Jap. Inst. Metals, 1968, 9, 312.

165 F P Bens, Trans. ASM, 1947, 38, 505.

166 F Garofalo, P R Malenock & G V Smith, Trans. ASM, 1953, 45, 377.

167 E E Underwood, Mater. Methods, 1957, 45, 127, J. Inst. Metals, 1959-60, 88, 266.

168 E R Petty, J. Inst. Metals, 1960-61, 89, 123; E R Petty & H O'Neill, Metallurgia, 1961, 63, 25.

169 T O Mulhearn & D Tabor, J. Inst. Metals, 1960-61, 89, 7.

170 R K Steele & M J Donachie, Trans. ASM, 1965, 58, 273.

171 A G Atkins, A Silverio & D Tabor, J. Inst. Metals, 1966, 94, 369.

172 J A Marcantonio, L F Mondolfo & V Weiss, Metals and Materials, Oct 1973, p449.

173 J A Belk, Metals and Materials, Sept 1974, p414.

174 A G Atkins, "The Science of Hardness Testing and its Recent Applications", ASM, Ohio, 1973.

175 G A Geach, International Metallurgical Reviews, 1974, 19, 255.

176 K B Gove, PhD Thesis, 1972, Univ. of Cambridge.

177 H O'Neill, "Hardness Measurements of Metals and Alloys", Chapman and Hall, London, 1967.

178 K G Robinson, Metallurgia, May 1947, 45.

179 L Small, "Hardness - Theory and Practice", 1960; Ferndale Mich. (Servia Diamond Tool Co.) quoted in Ref 175.

180 J H Westbrook, Proc. ASTM, 1957, 57, 873.

181 G A Geach & O F Hartree (High Temperature Tester), Fenner, Mech. Testing of Materials, 1965, George Newnes, London. Quoted in Ref 177.

182 K Sumino & H Hasegawa, Trans. Jap. Inst. Met., 1968, 9, (supplement), 749.

183 R L Landingham, Proc. Second Annual Technical Meeting, Int. Metallographic Soc. Inc., 1970, 179.

184 K B Gove & J A Charles, The Metallurgist and Materials Technologist, April 1974, p119.

185 F Hargreaves, J. Inst. Met., 1928, 39, 301. F Hargreaves & R J Hills, J. Inst. Met., 1929, 41, 257.

186 V P Shishokin,Z. anorg. Chem., 1930, 189, 263. V P Shishokin, V A Ageyeva & N A Vikhoreva, Zhur. Tekhn. Fiziki, 1940, 10, 49. V P Shishokin, Zhur. Tekhn. Fiziki, 1930, 8, 1613. Quoted in Ref 175.

187 J Pomey, A Royez & J P Georges, Compt. rend., 1957, 245, 1424; Rev. Met., 1959, 56, 215.

188 N F Mott, Phil. Mag., 1953, 44, 742.

189 H D Merchant, Trans. Met. Soc. A.I.M.E., 1964, 230, 1206.

190 O D Sherby & P E Armstrong, Metall. Trans., 1971, 2, 3479.

191 O D Sherby & J E Dorn, Trans. TMS-A.I.M.E., 1952, 194, 959.

192 W D Klopp, W R Witzke & P L Raffo, Trans. TMS-A.I.M.E., 1965, 233, 1860.

193 C R Barrett, A J Ardell & O D Sherby, Trans. TMS-A.I.M.E., 1964, 230, 200.

194 J Weertman, W V Green & E G Zukas, J. Matl. Sci. Eng., 1970, 6, 199.

195 H D Merchant, G S Murti, S N Bahadur, L T Dwivedi, Y Mehrotra, J. Mater. Sci., 1973, 8, 437-442.

196 M G Lozinskii, "High Temperature Metallography", Pergamon Press, Oxford, 1961.

197 D Bruce & P Hancock, J. Inst. Metals, 1969, 97, 140.

198 M F Fine, Rev. Sci. Instr., 1957, 28, 643.

199 W Köster, Z Metallk., 1948, 39, 1.

200 O D Sherby, "An Atomistic Approach to the Nature and Properties of Materials", Edited by J A Pask, John Wiley, 1967, p370.

201 E R Petty, J. Inst. Metals, 1960-61, 89, 345.

202 J Woodthorpe & R Pearce, Metal Sci., March 1977, 103.

203 H Naziri & R Pearce, J. Inst. Metals, 1973, 101, 197.

204 T S Lundi & J F Murdock, J. Appl. Phys., 1962, 33, p1971.

205 J Weertman, Trans. A.I.M.E., 1960, 218, 207.

206 O D Sherby & P M Burke, Progr. Mater. Sci., 1968, 13, 325.

207 P Griffiths & C Hammond, Acta Met., 1972, 20, 935.

208 Yasuhiro Funamizu & Katsuya Watanabe, J. Jap. Inst. Met., Oct 1975, 39 (10), 1087-92.

209 Bruno Walser, E Sabri Kayali & Oleg D Sherby, Proc. 4th Int. Conf. on the Strength of Metals and Alloys, Nancy-France, 30 Aug-3 Sept, 1976, p456.

210 B M Watts, M J Stowell, B L Baikie & D G E Owen, Metal Sci., June 1976, 198-206.

211 R Grimes, M J Stowell & B M Watts, Metals Tech., March 1976, 3, 154.

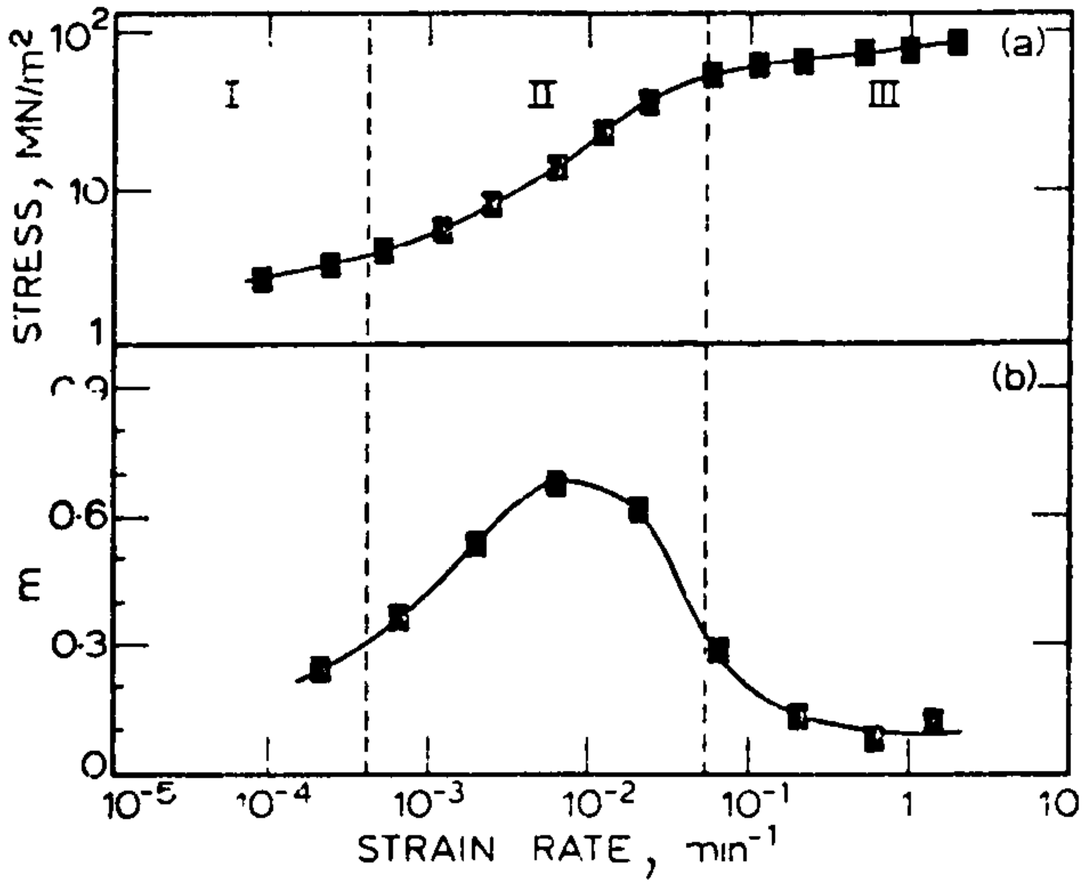


Fig 1. Strain-rate $\dot{\epsilon}$ dependence of (a) flow stress σ and parameter $m = (\frac{\delta \ell n \sigma}{\delta \ell n \dot{\epsilon}})$ for the Mg-Al eutectic alloy. Regions I, II and III are delineated (after D. Lee, Acta. Met. 17 (1969) 1057.

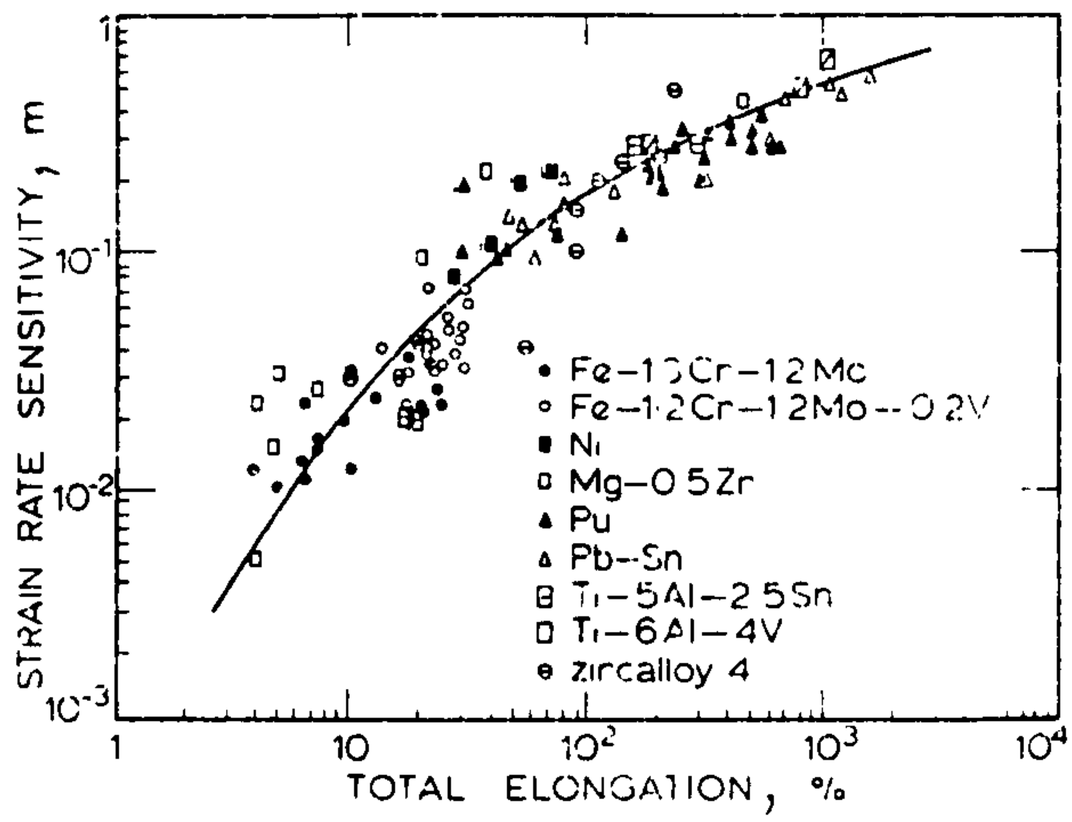


Fig 2. Relationship between tensile elongation and strain-rate sensitivity, m, for a number of materials (after Woodford[24]).

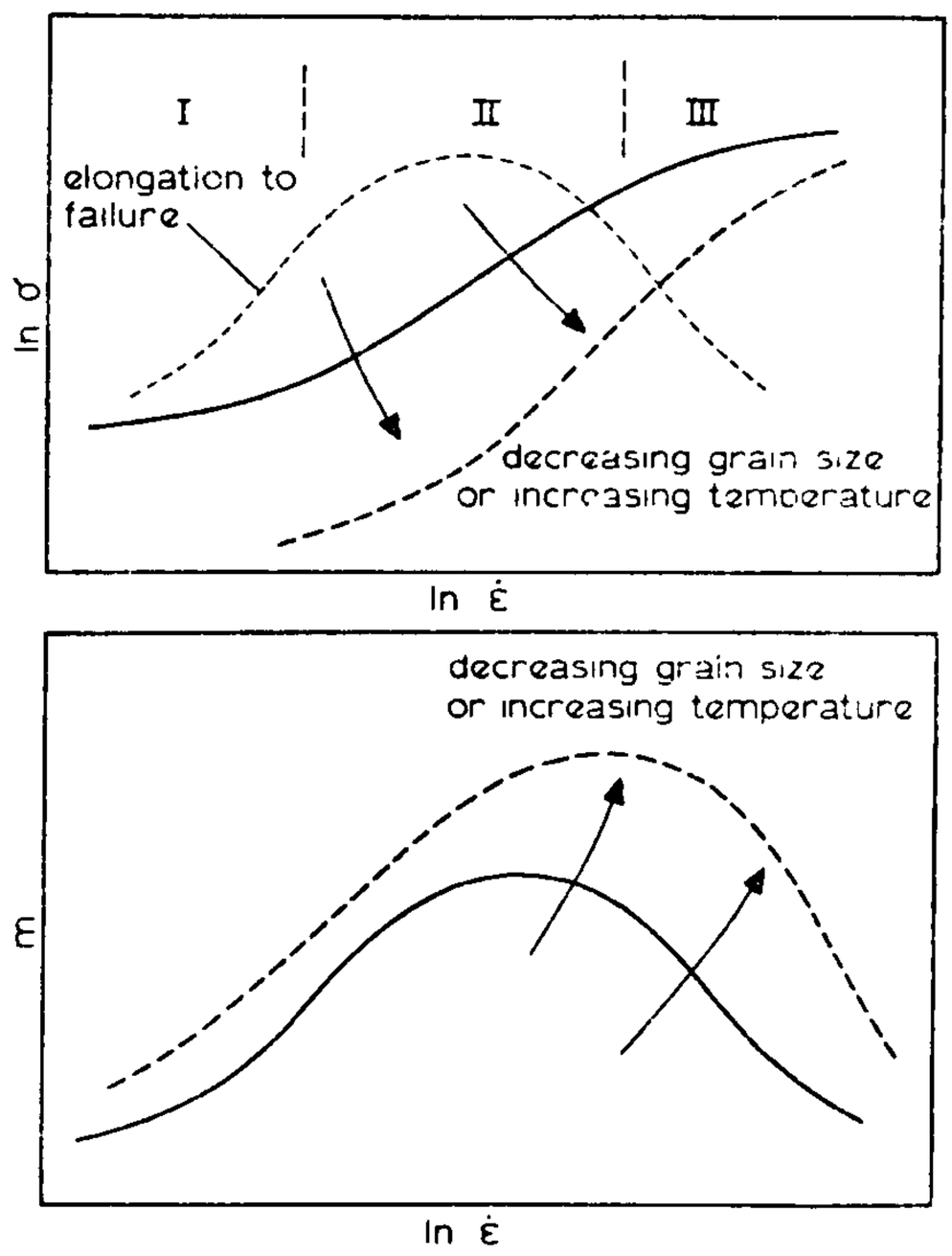


Fig 3. Schematic diagrams summarising the important features of mechanical properties of superplastic materials (after Edington[21]).

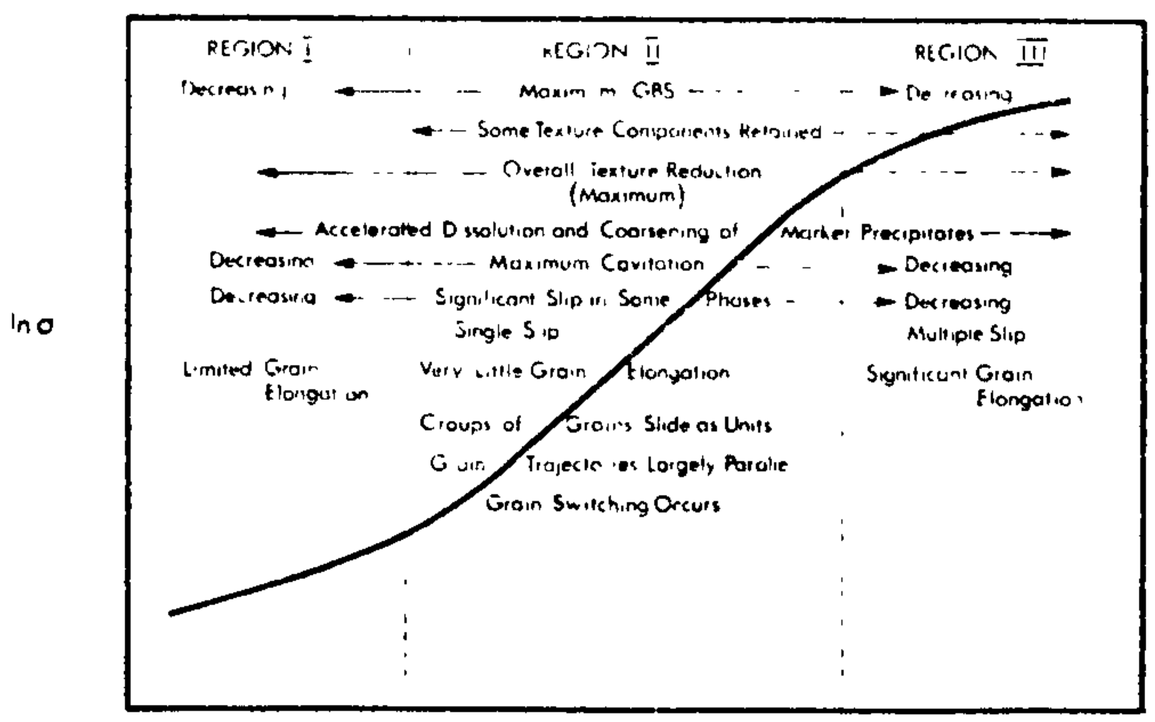


Fig 4. A summary of the important metallographic and texture changes accompanying superplastic deformation in different regions of the $\ell n\sigma$ - $\ell n\dot{\varepsilon}$ curve (after Edington et al[4]).

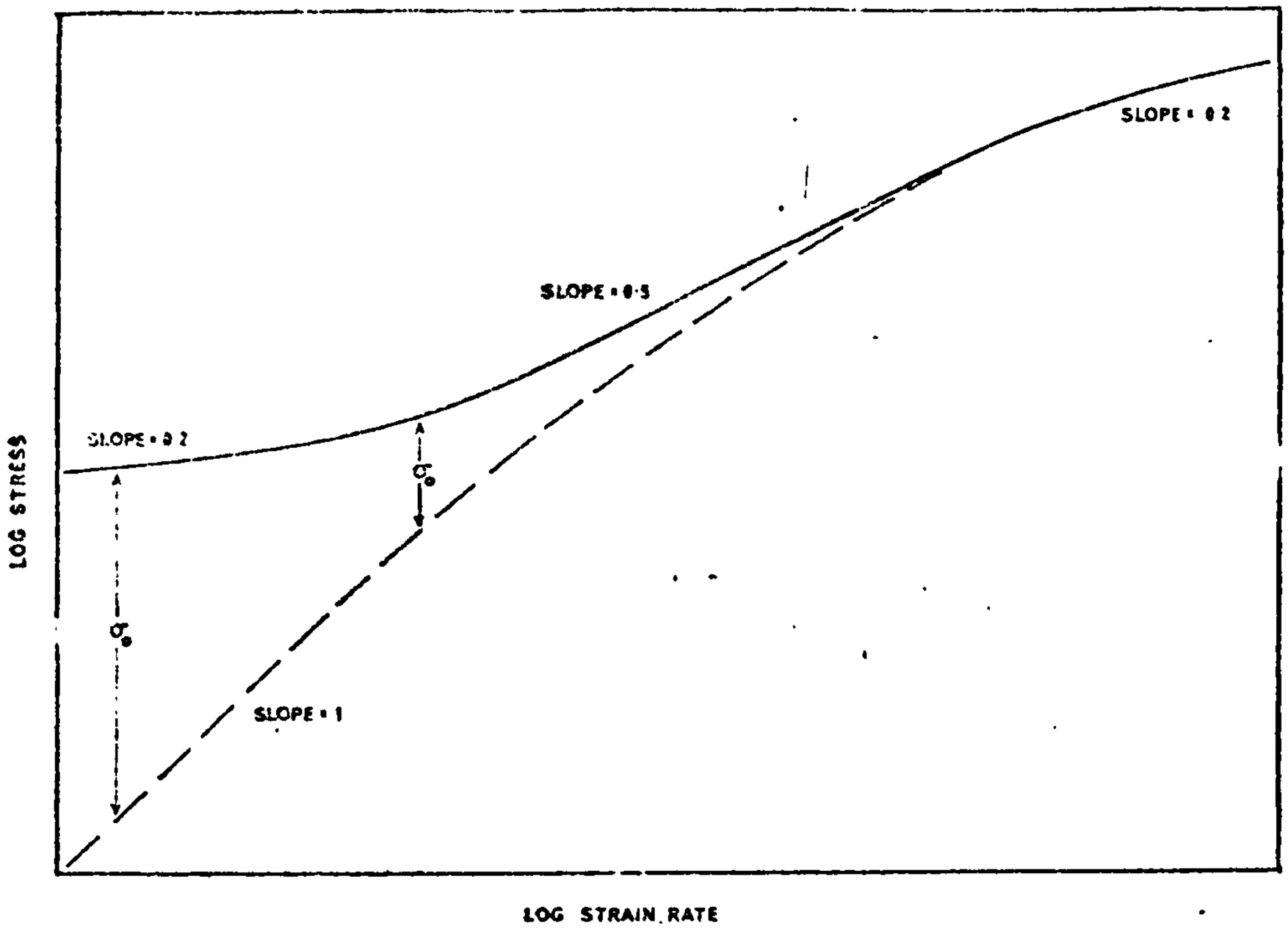


Fig 5. Typical relationship between measured strain rate and applied stress (solid line) for superplastic materials. The effect of subtracting a constant-stress term (σ_o) is shown by the broken line, slope values = stress-rate-sensitivity index m. (after R H Johnson[3]).

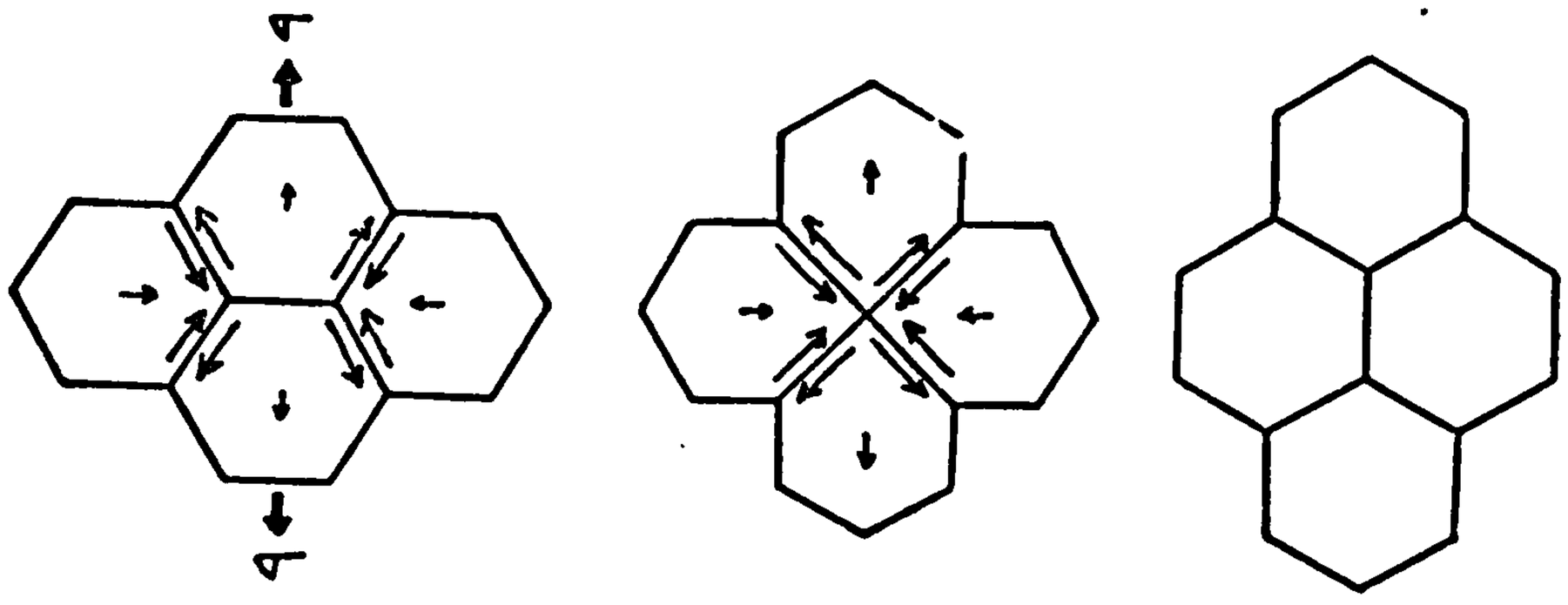


Fig 6. A schematic illustration of the grain-switching mechanism described by Ashby and Verral[20]. A group of four grains moves from the initial, through the intermediate, to the final state. The true strain is 0.55 and the process is achieved if the grains slide past one another in the direction of the arrows, maintaining contact by accommodation strains. (after Ashby and Verral[20]).

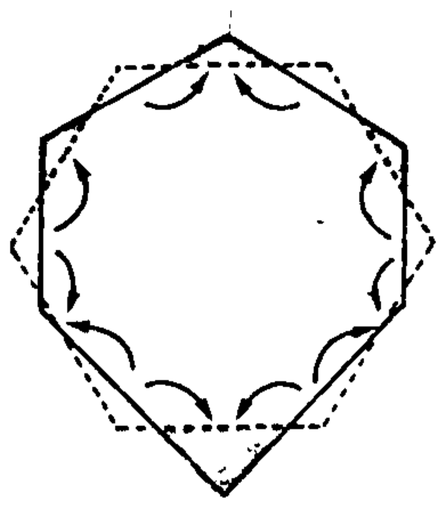


Fig 7. Diffusion accommodation at the intermediate stage of the switching event illustrated in Fig 6. The arrows show the six diffusion paths and the shaded regions represent the volume of material to be moved. (after Ashby and Verral[20]).

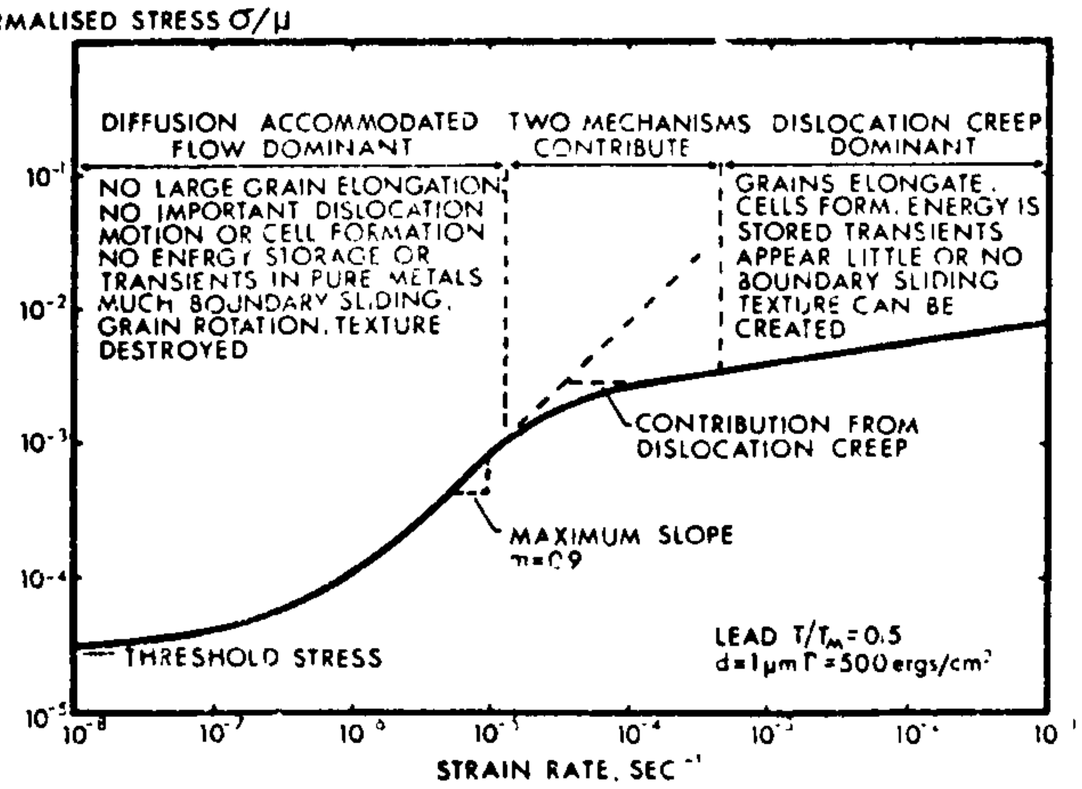


Fig 8. A plot of equation (2 - 36) using the input data for lead. The microstructural and other characteristics of the model are listed. (after Ashby and Verral[20]).

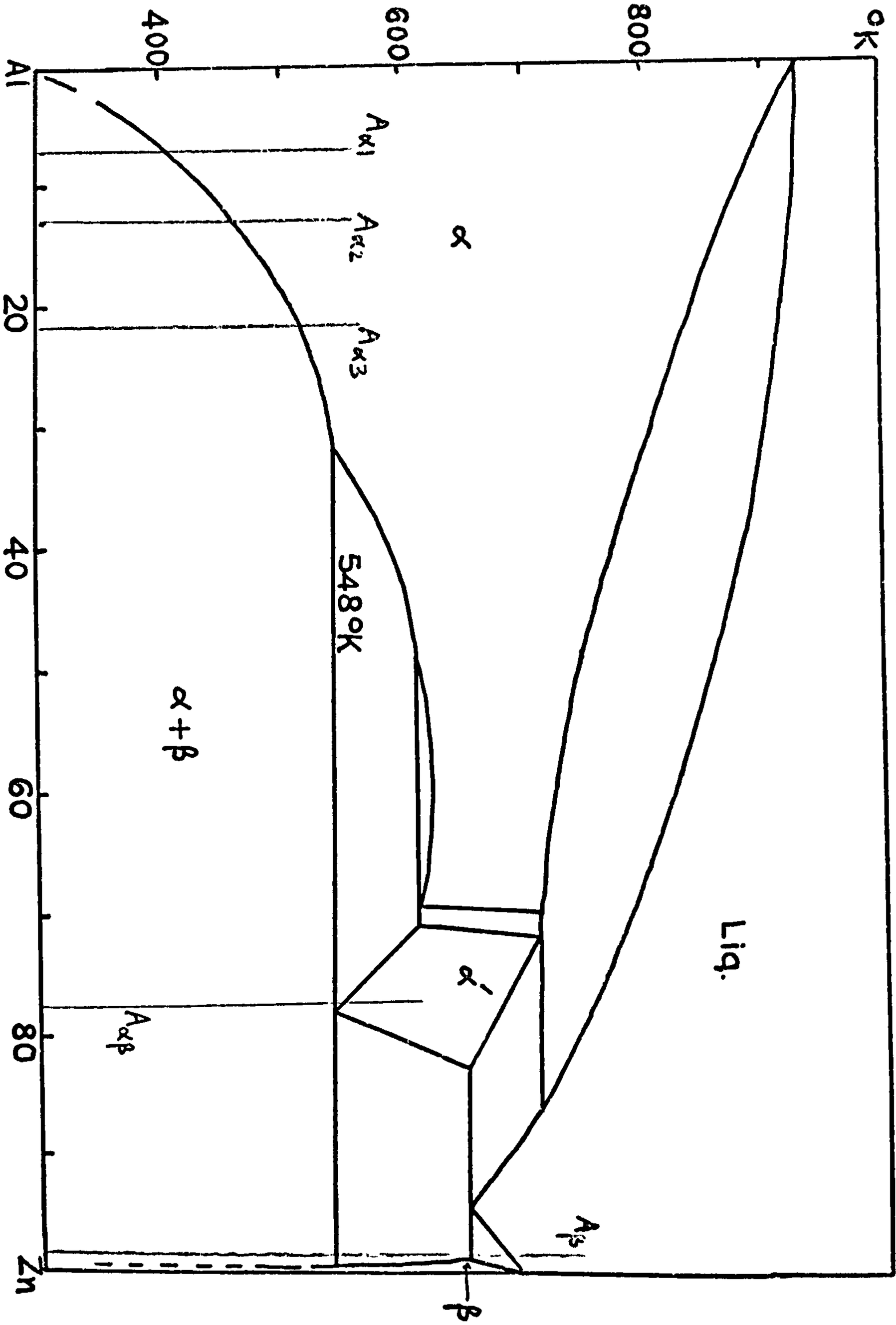

°K
400
600
800
Al
$A_{\alpha 1}$
$A_{\alpha 2}$
$A_{\alpha 3}$
α
548°K
α+β
20
40
60
80
Wt.%Zn
$A_{\alpha\beta}$
α+L
Liq.
A_{β}
Zn
β

Fig. 9.

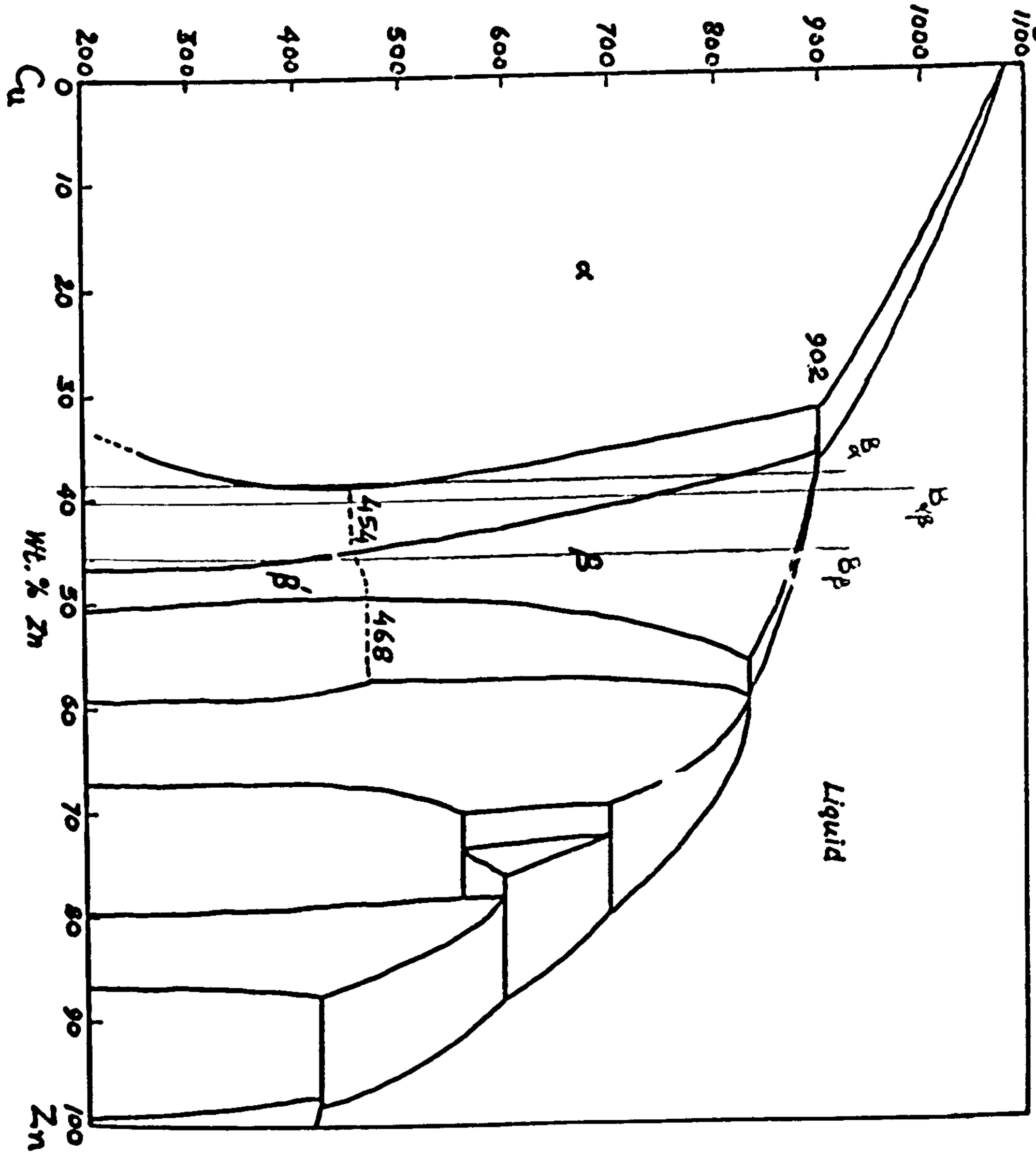
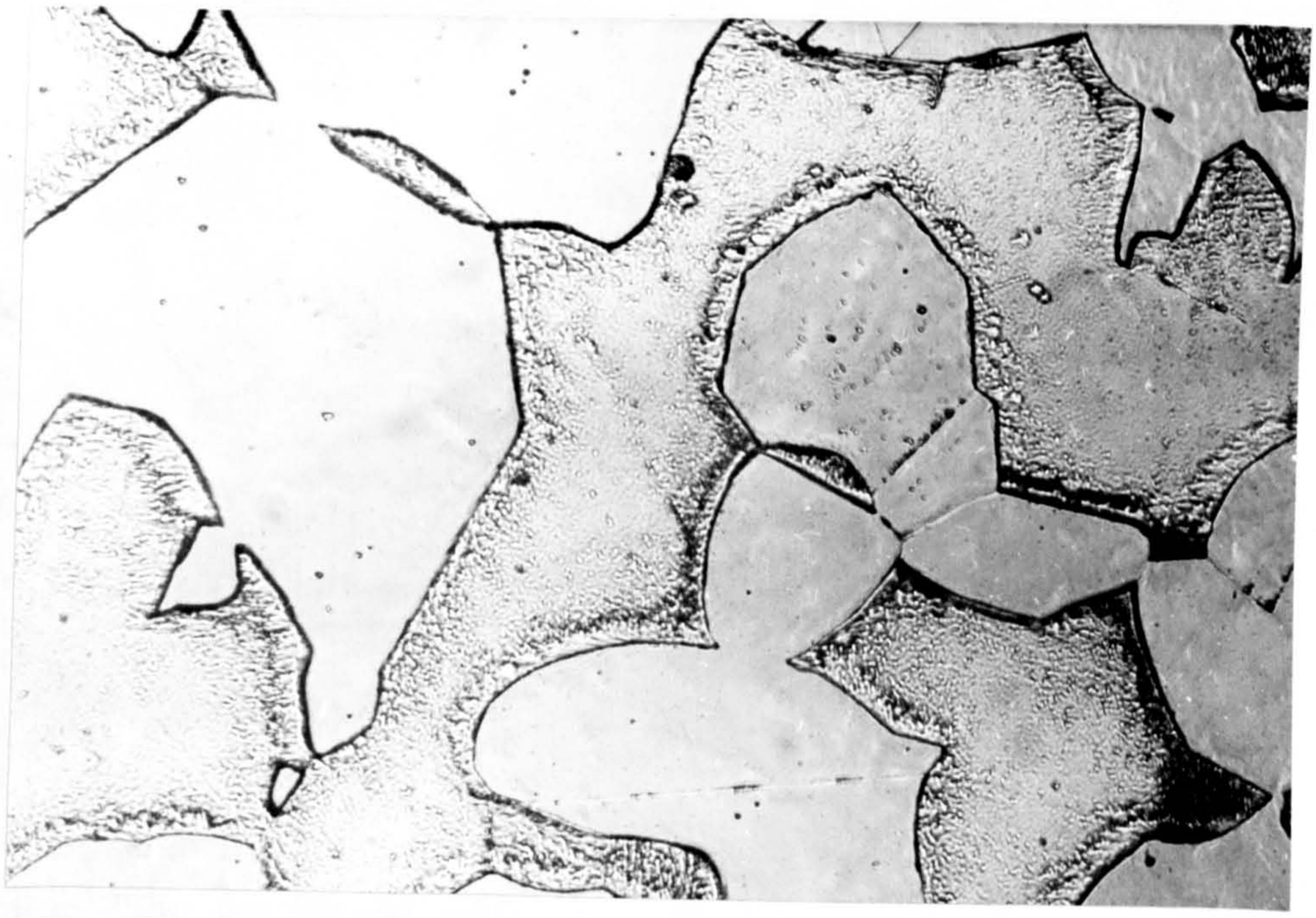
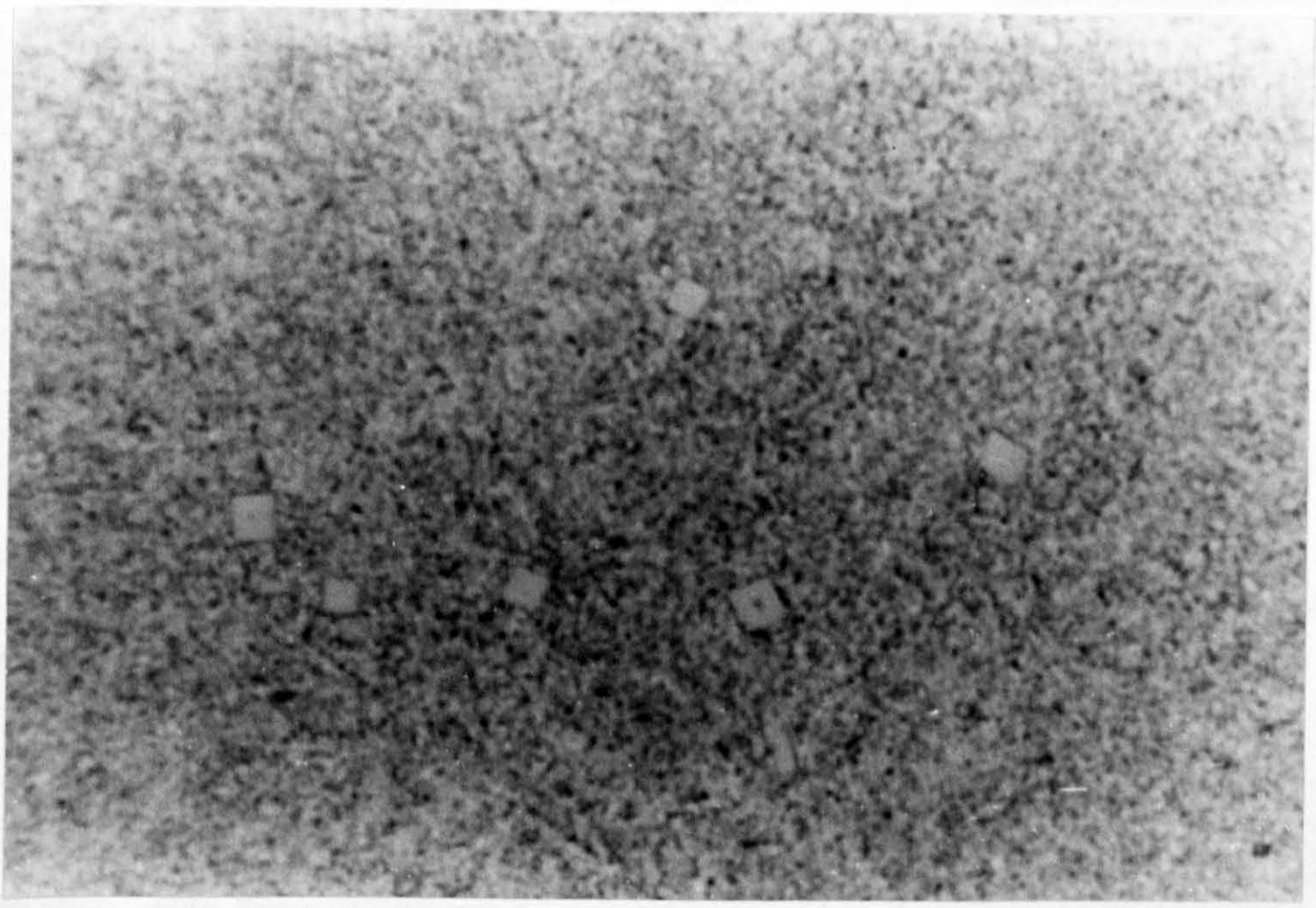

°C
1100
1000
900
800
700
600
500
400
300
200
C_u
0
10
20
30
40
50
60
70
80
90
100
Zn
Wt. % Zn
α
902
α_β
$b_{\gamma\beta}$
β_α
454
468
β
β'
Liquid

Fig. 10.



X240

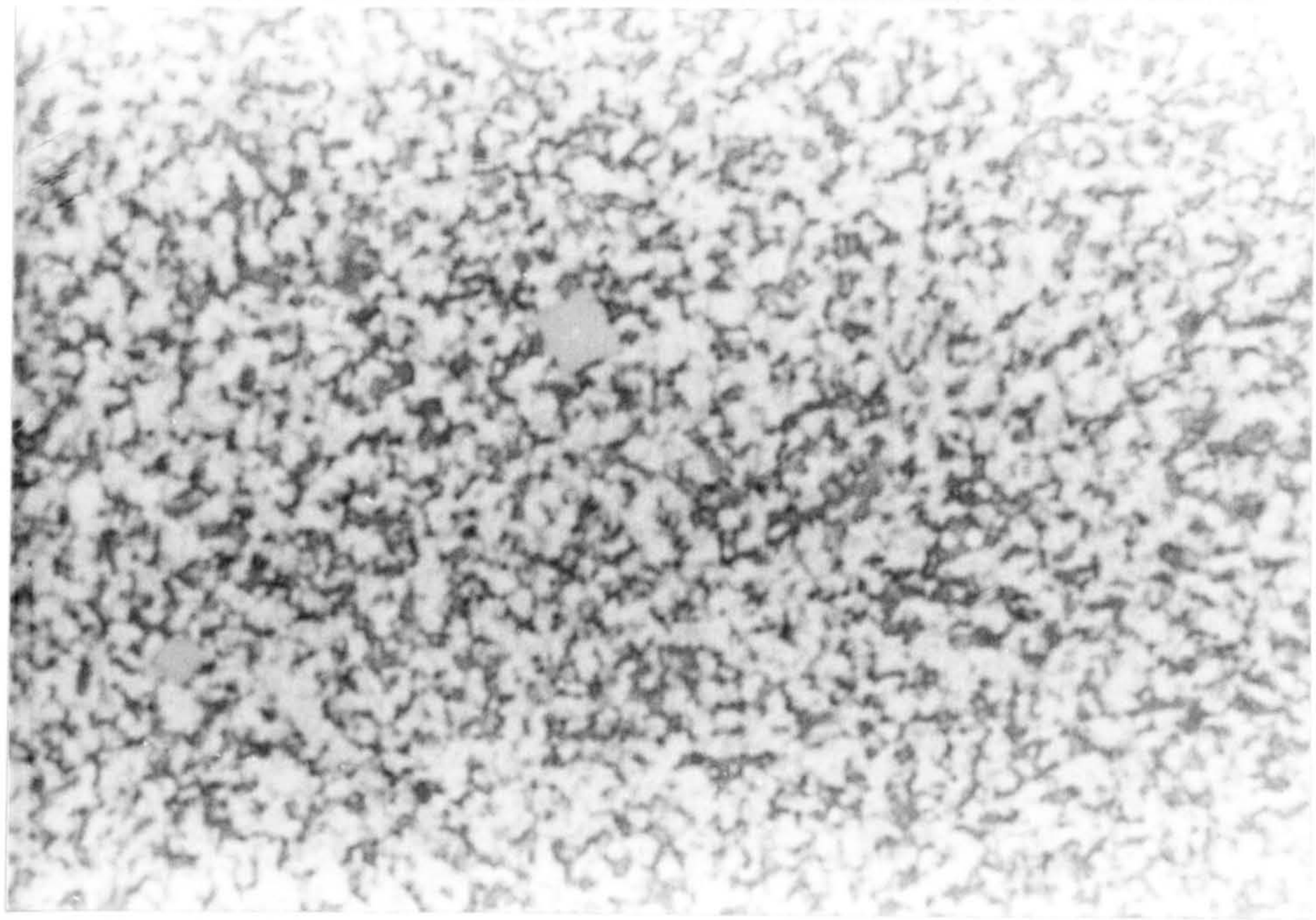
Fig 11. Optical micrograph of 60/40 brass. Annealed at 700°C for 118 hours, quenched water. Grain size ~ 100 μm. The matrix is the β phase.



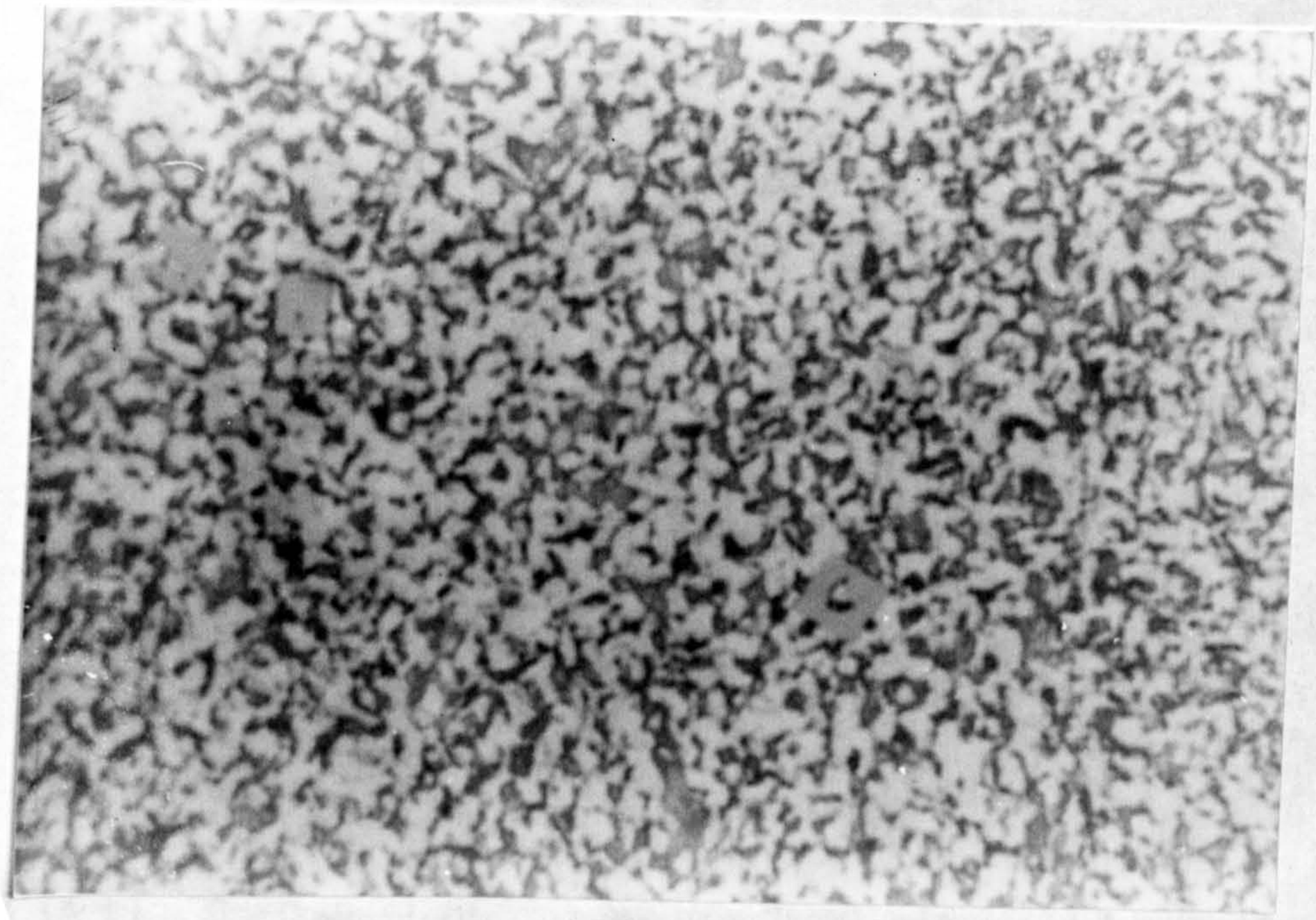
X1600

Fig 12(a). Optical micrograph of Zn/Al eutectoid. Homogenised at 380°C for 25 hours, quenched iced-water. $FeAl_3$ type inclusions are ~ 2 - 3 μm in size. As-quenched.

(b)

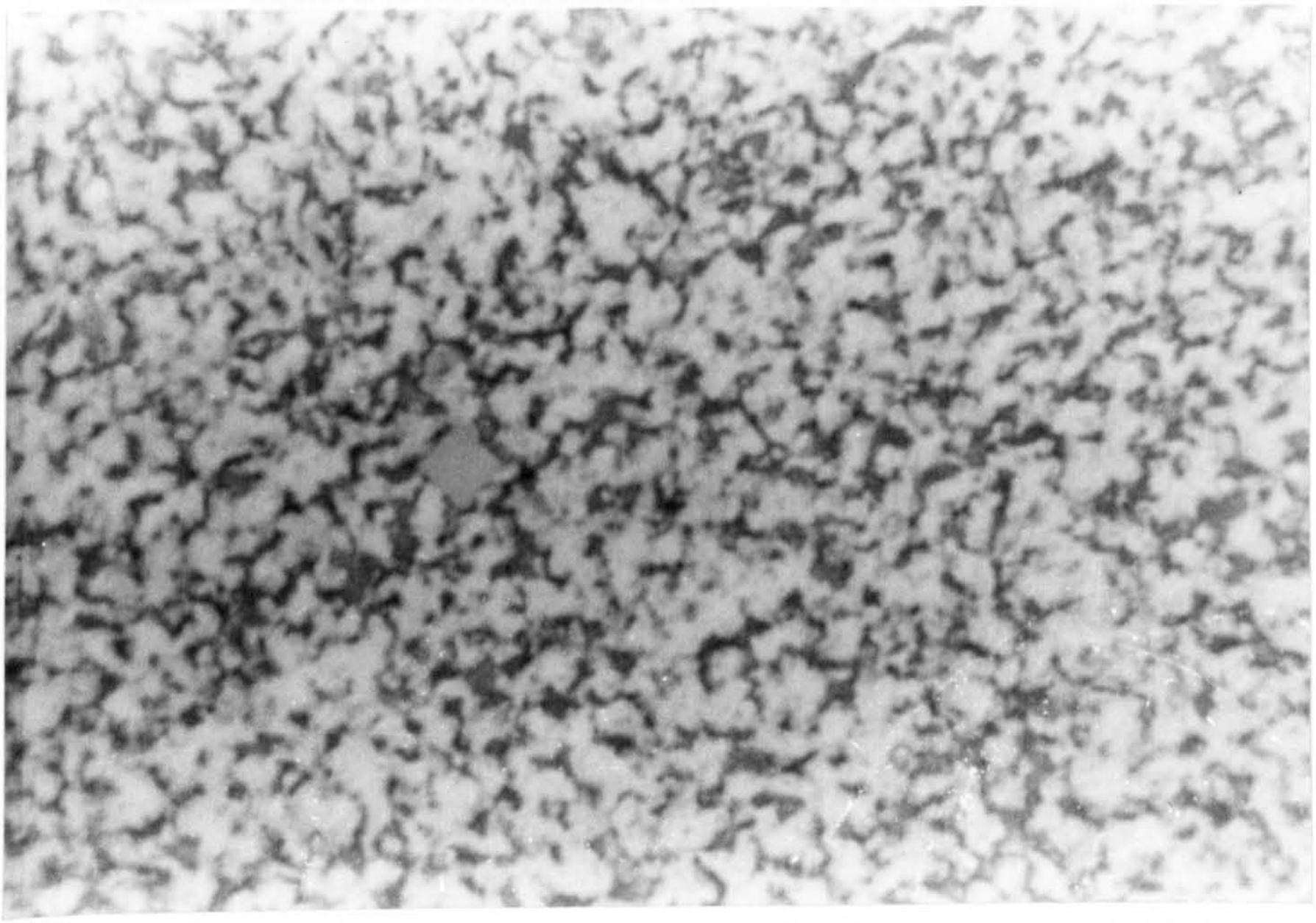


(c)



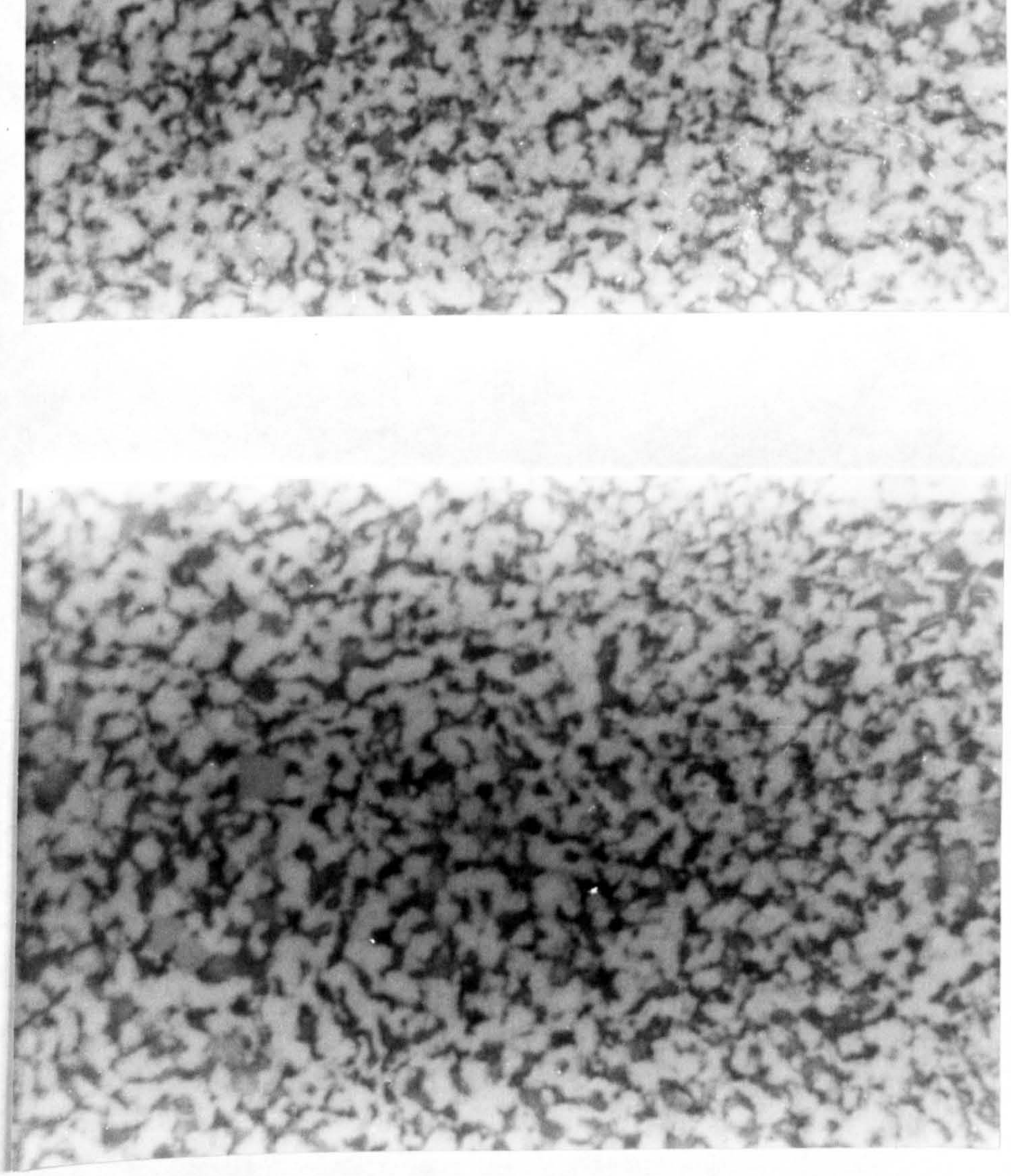
X2500

(d)



X2500

(e)



X2500

Fig 12 (b-e) Optical micrograph of the Zn/Al eutectoid homogenised at 380°C for 25 hours, quenched iced-water. Then annealed at 260°C (0.7 Tm) for (b) 1 hr, (c) 2 hr, (d) 3 hr and (e) 5 hr.

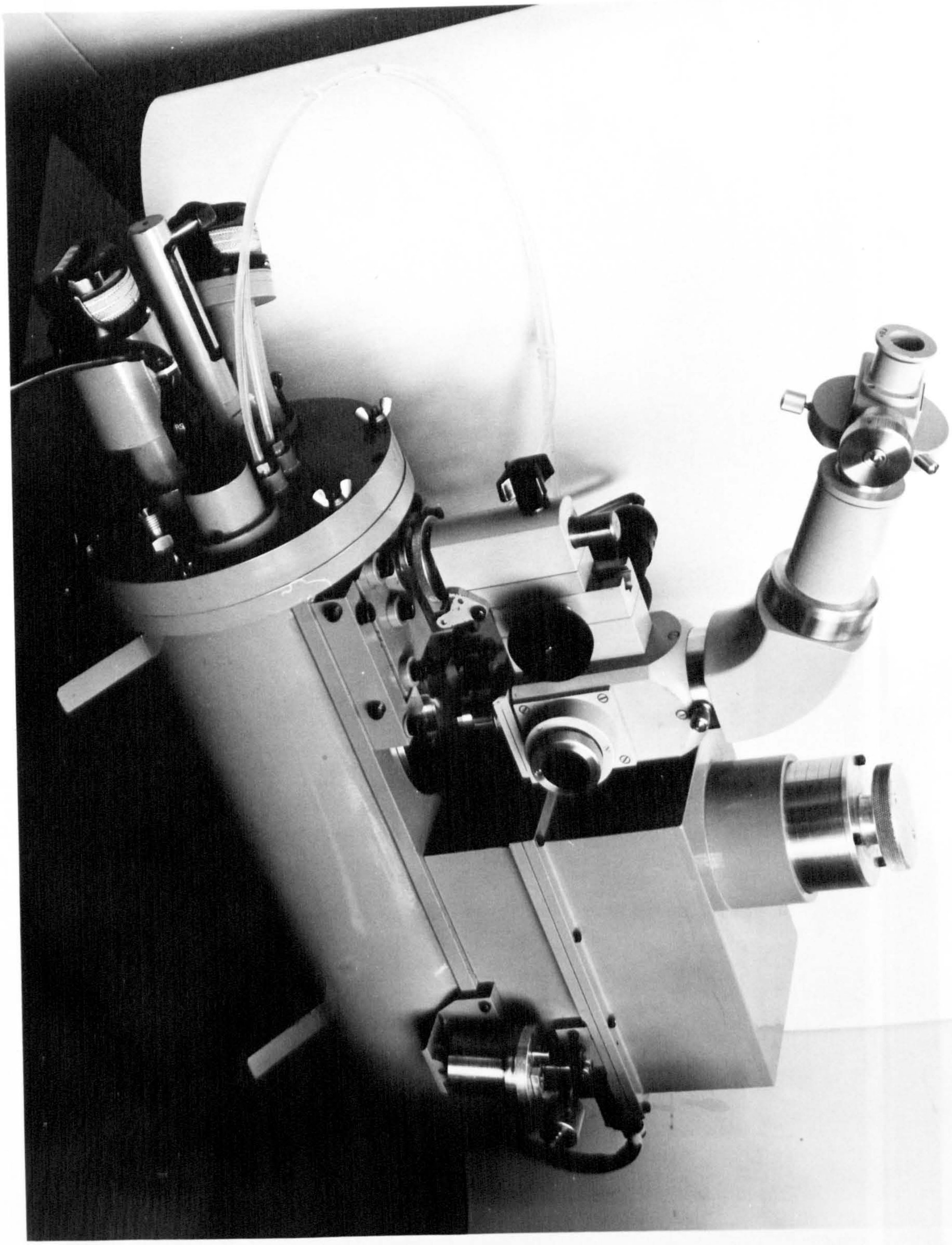


Figure 13(a) High temperature microhardness tester - general view

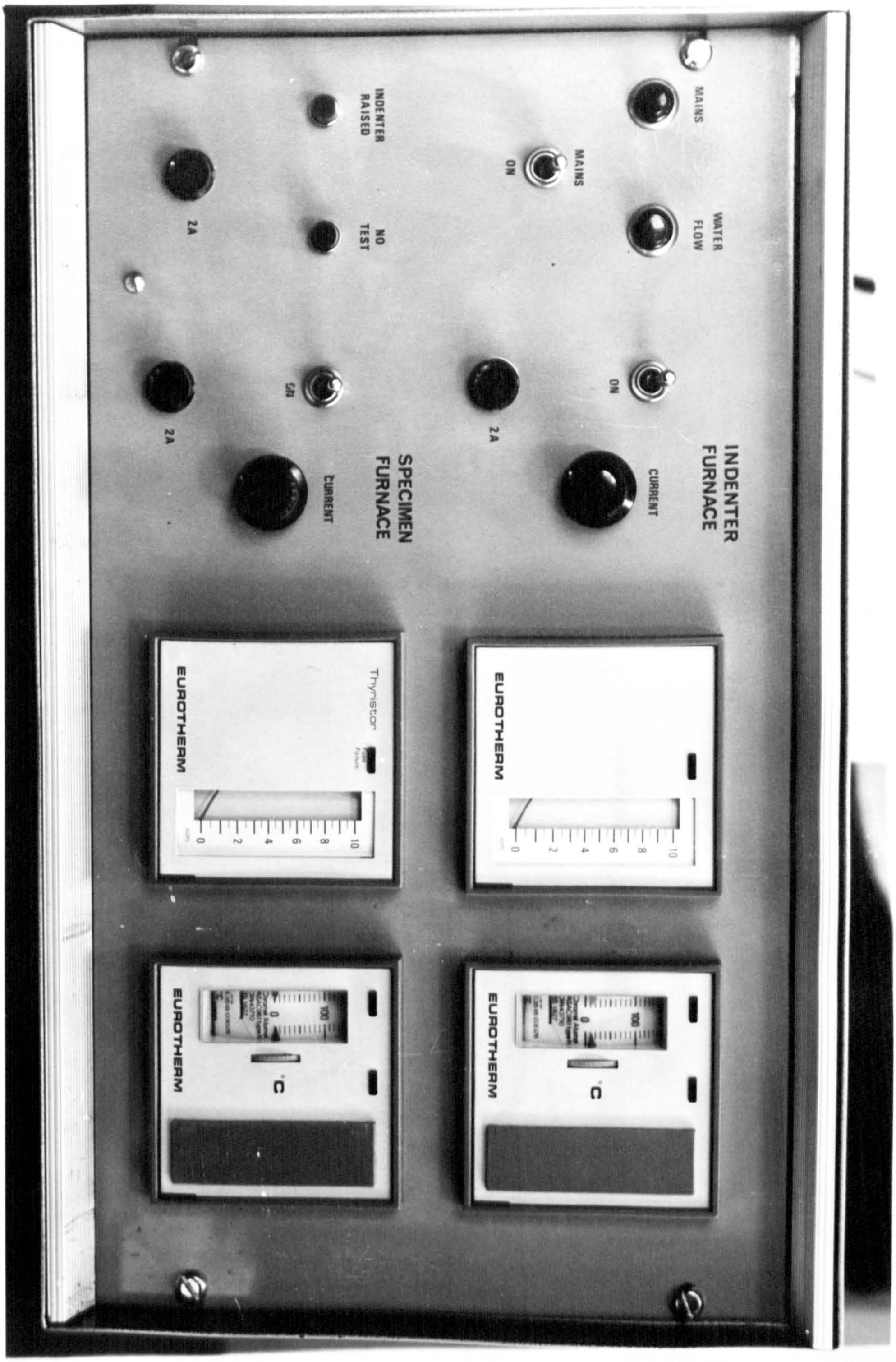


Figure 13(b) Console front

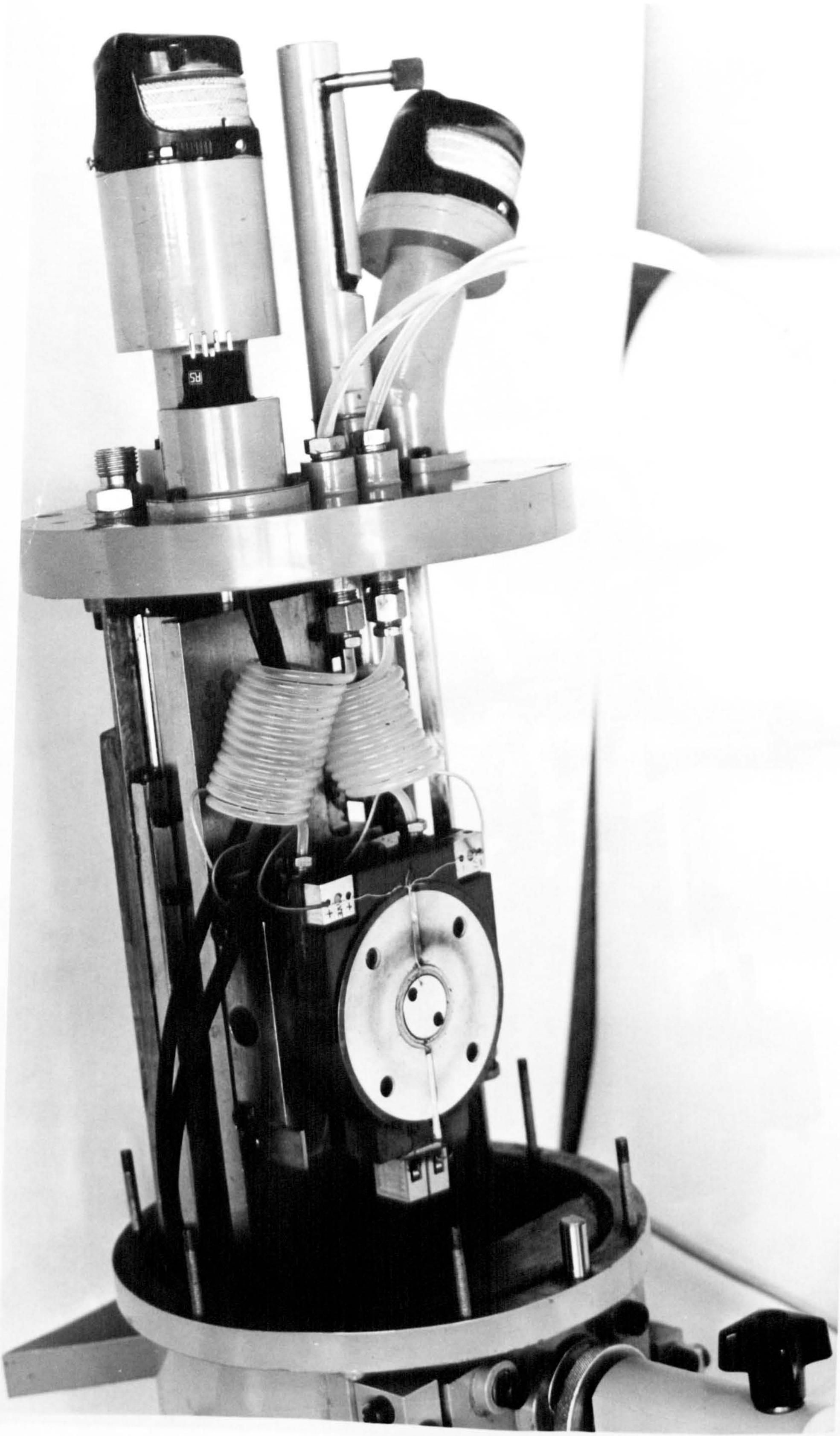


Figure 13(c) Base plate assembly

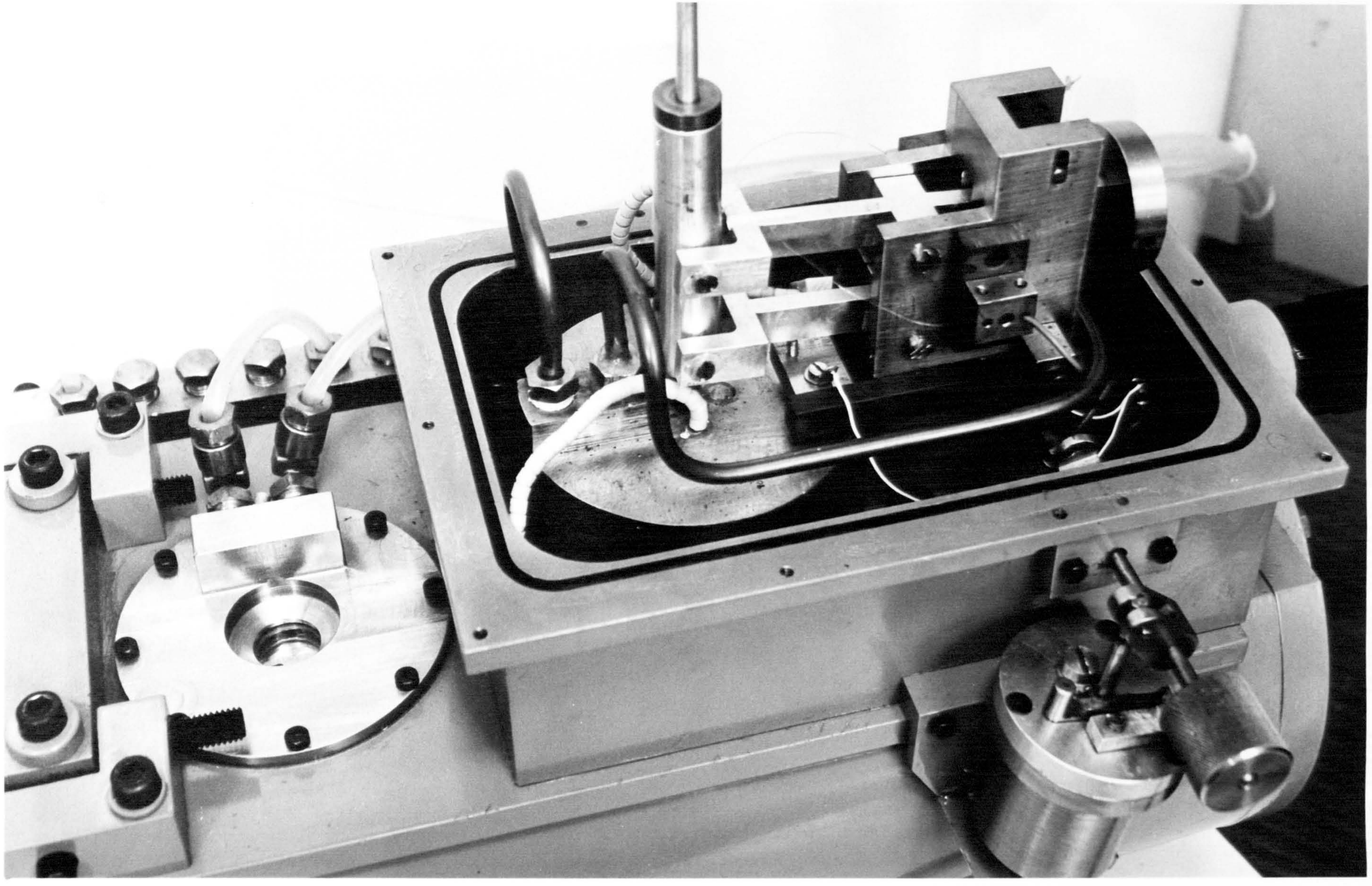


Figure 13(d) Window, indenter beam assembly and dashpot

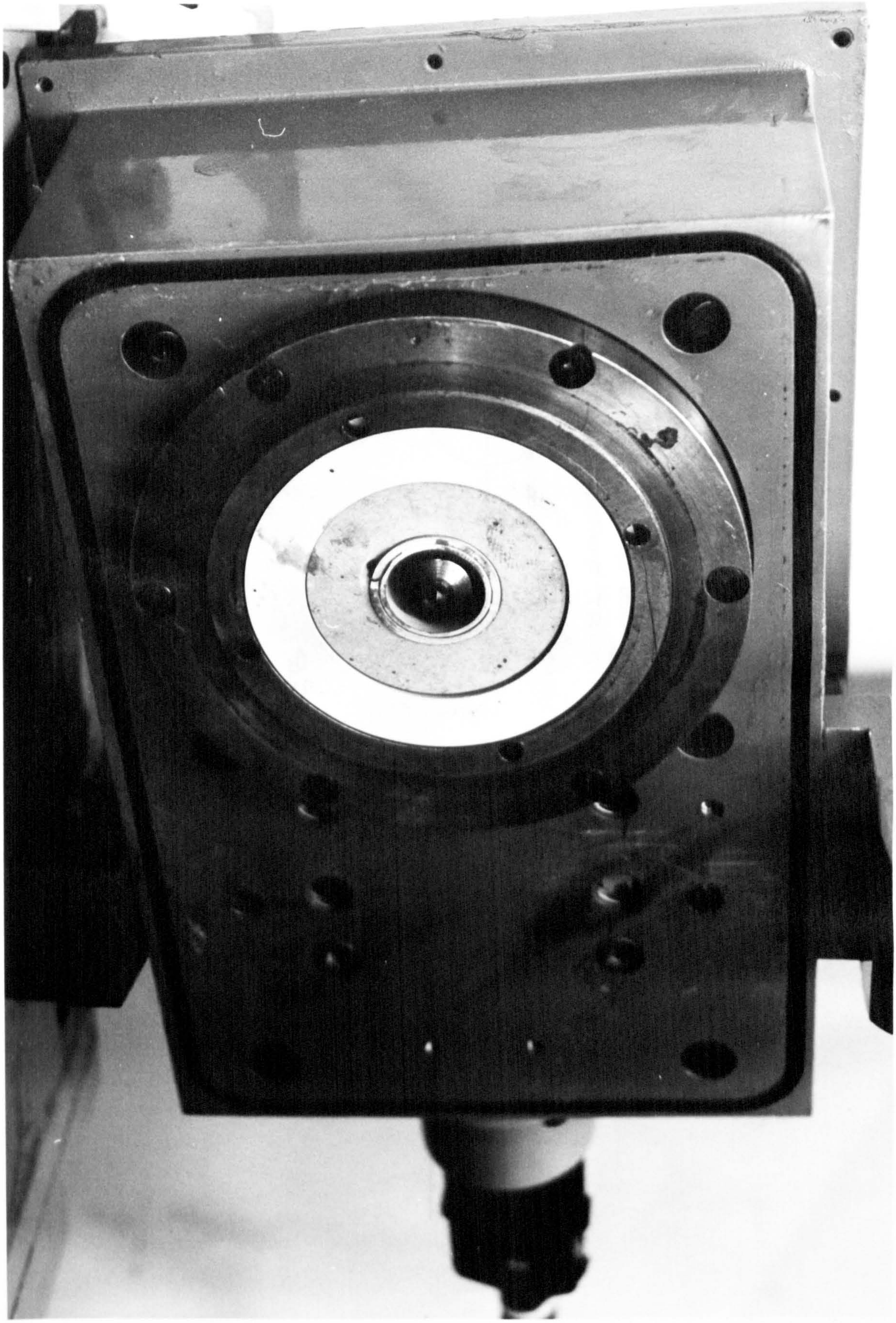


Figure 13(e) Indenter position inside its furnace

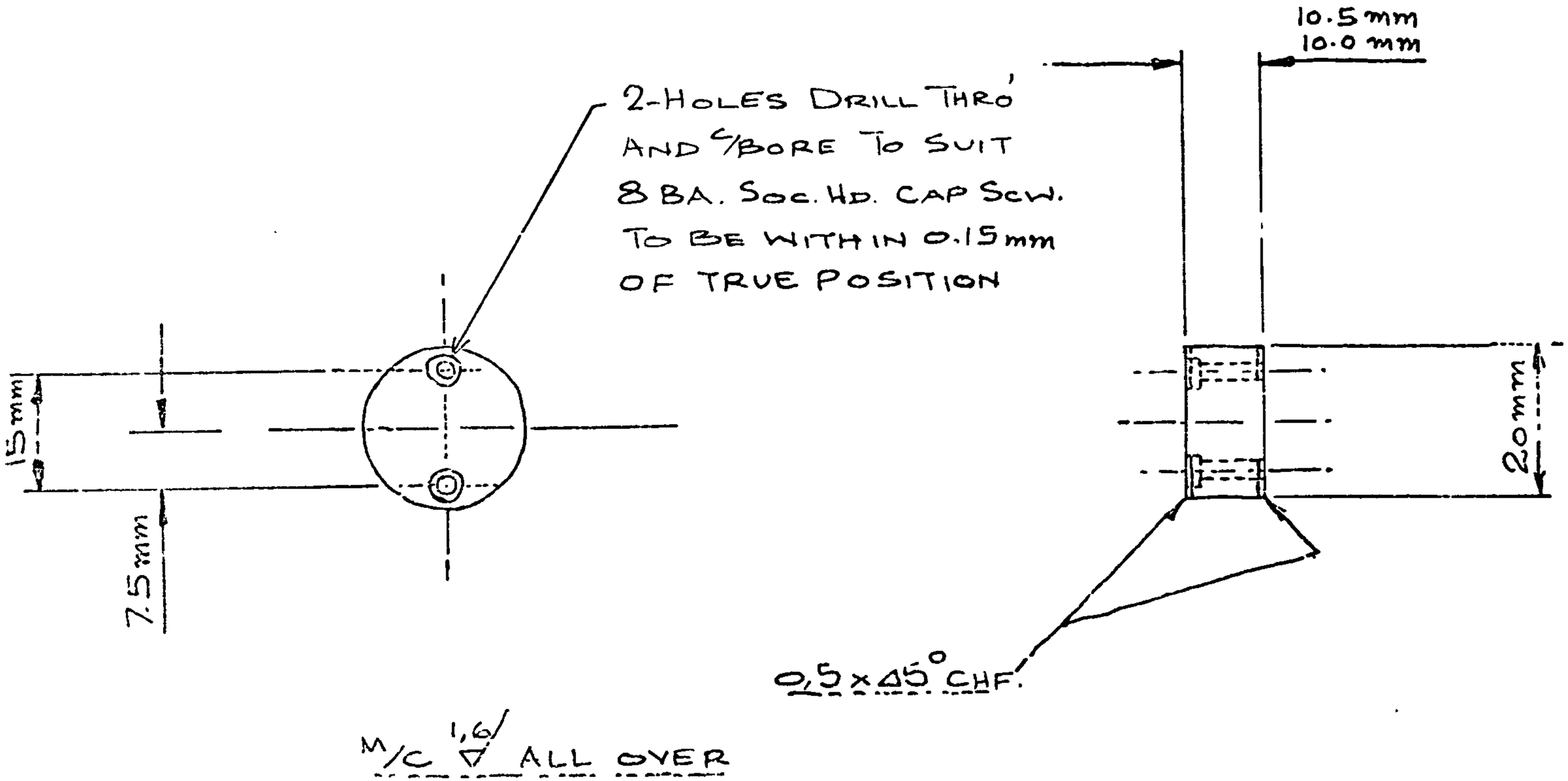


Fig. 14 Specimen drawing.

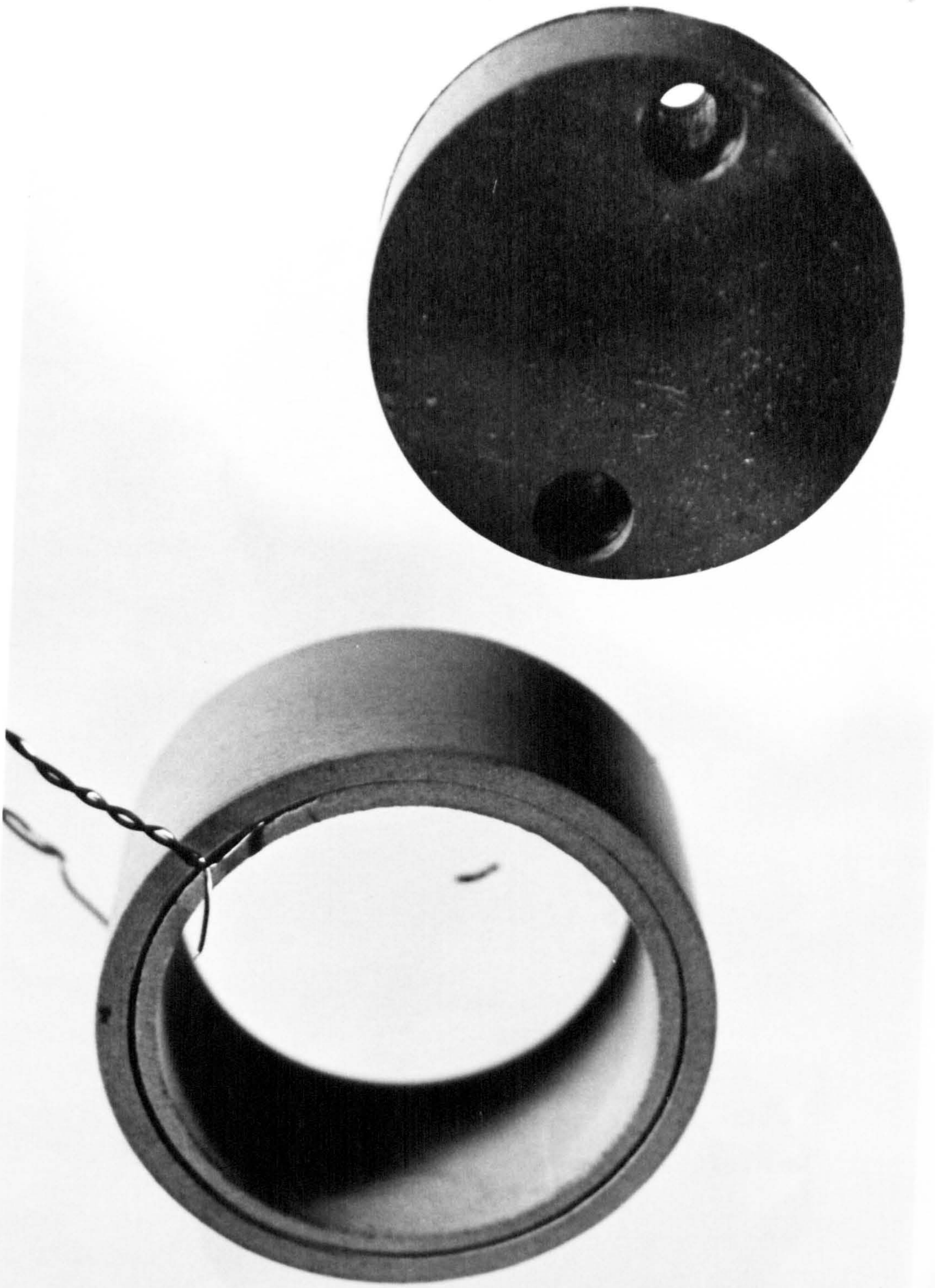


Figure 15 Specimen and its furnace

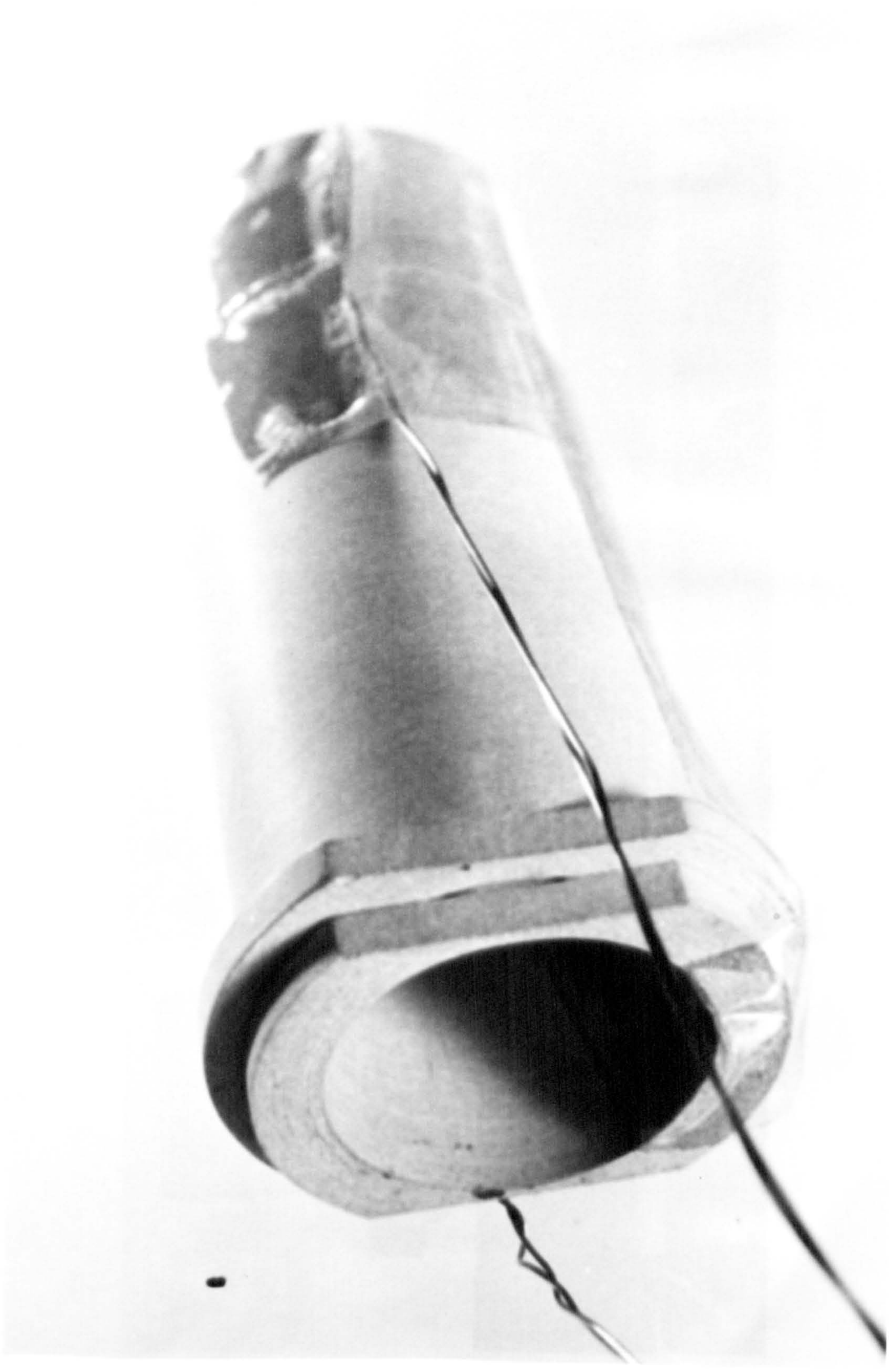


Figure 16 Indenter furnace

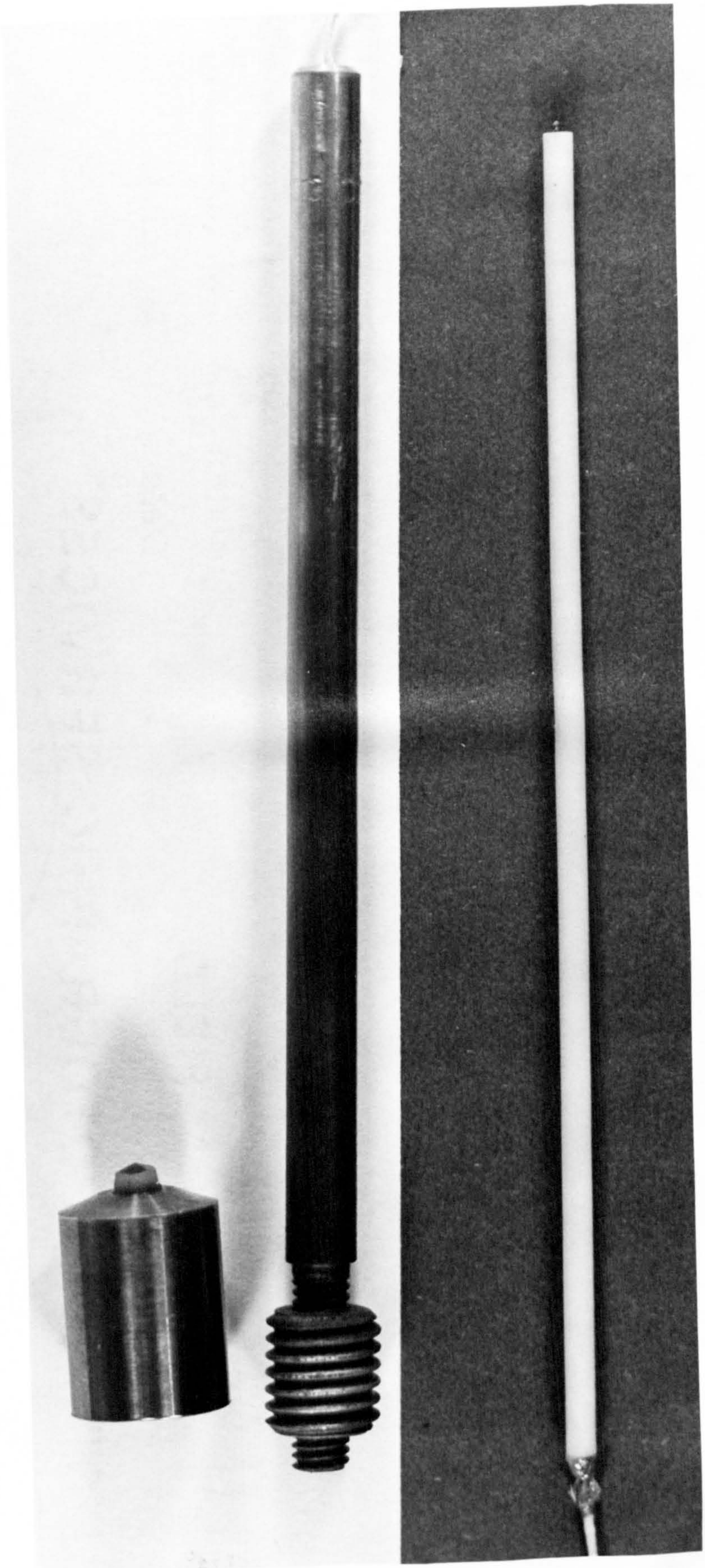


Figure 17 Parts of the indenter assembly

MATERIAL LEADED BRASS

o-----THIS MACHINE

▽-----VICKERS

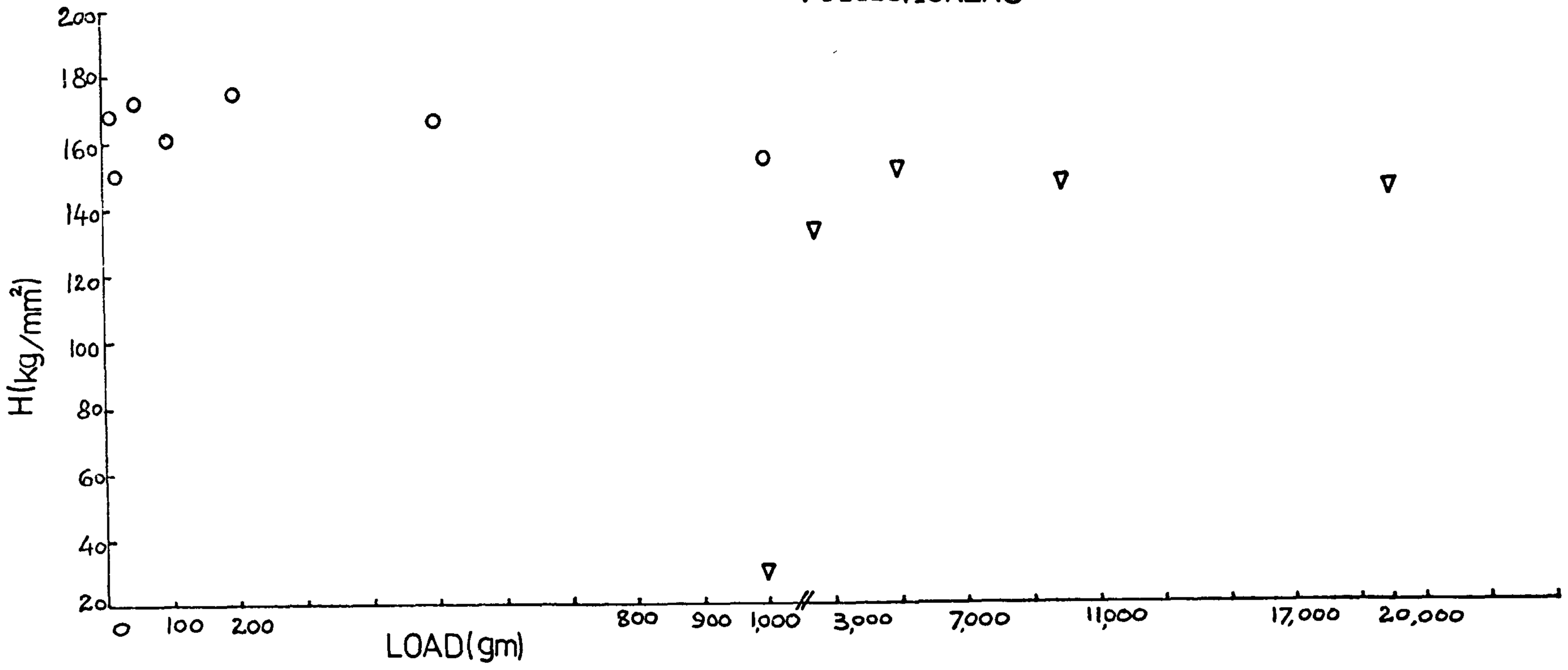


Fig.18

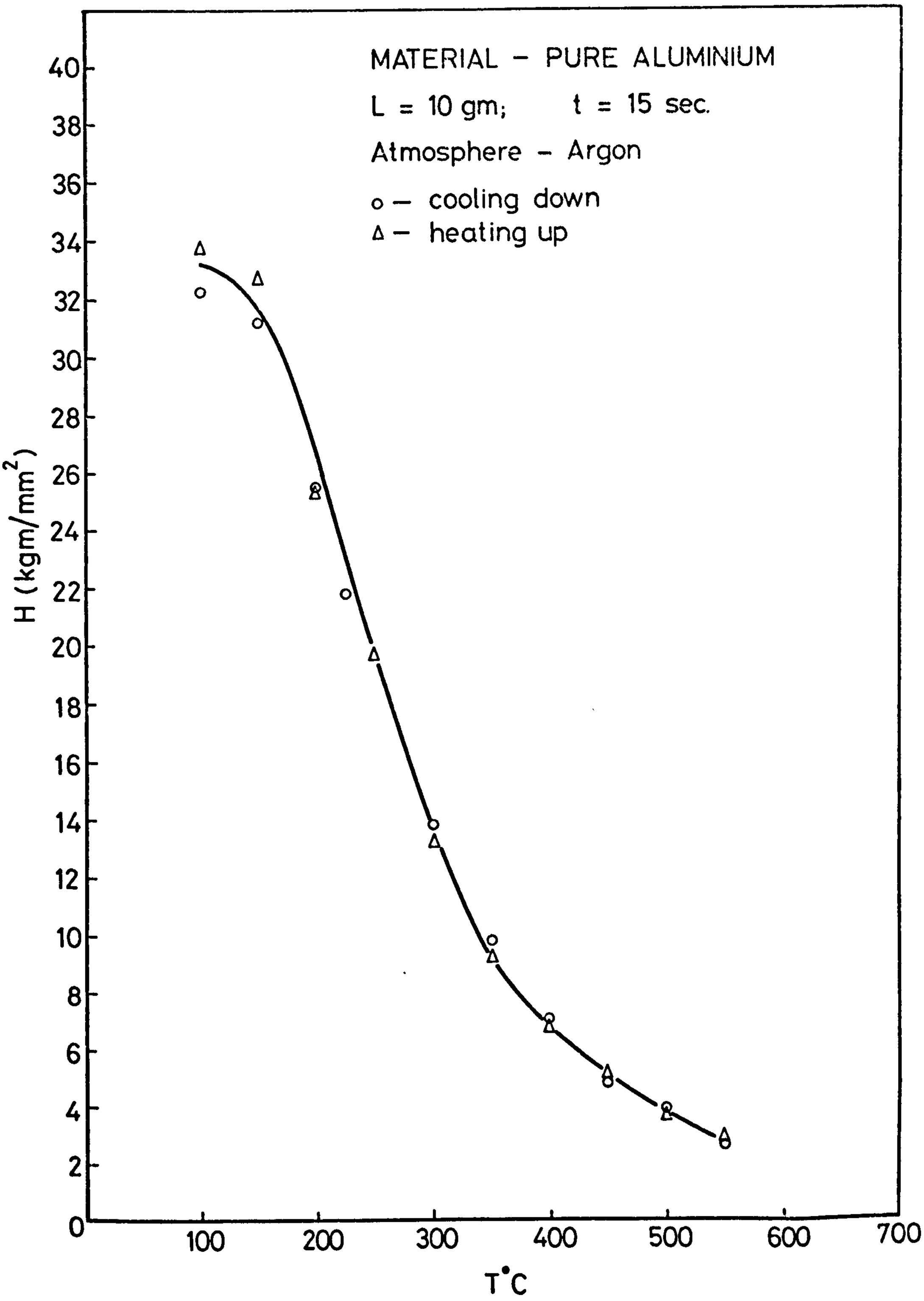

MATERIAL – PURE ALUMINIUM
L = 10 gm; t = 15 sec.
Atmosphere – Argon
o – cooling down
Δ – heating up
H (kgm/mm²)
T°C
0
2
4
6
8
10
12
14
16
18
20
22
24
26
28
30
32
34
36
38
40
100
200
300
400
500
600
700

Fig. 19

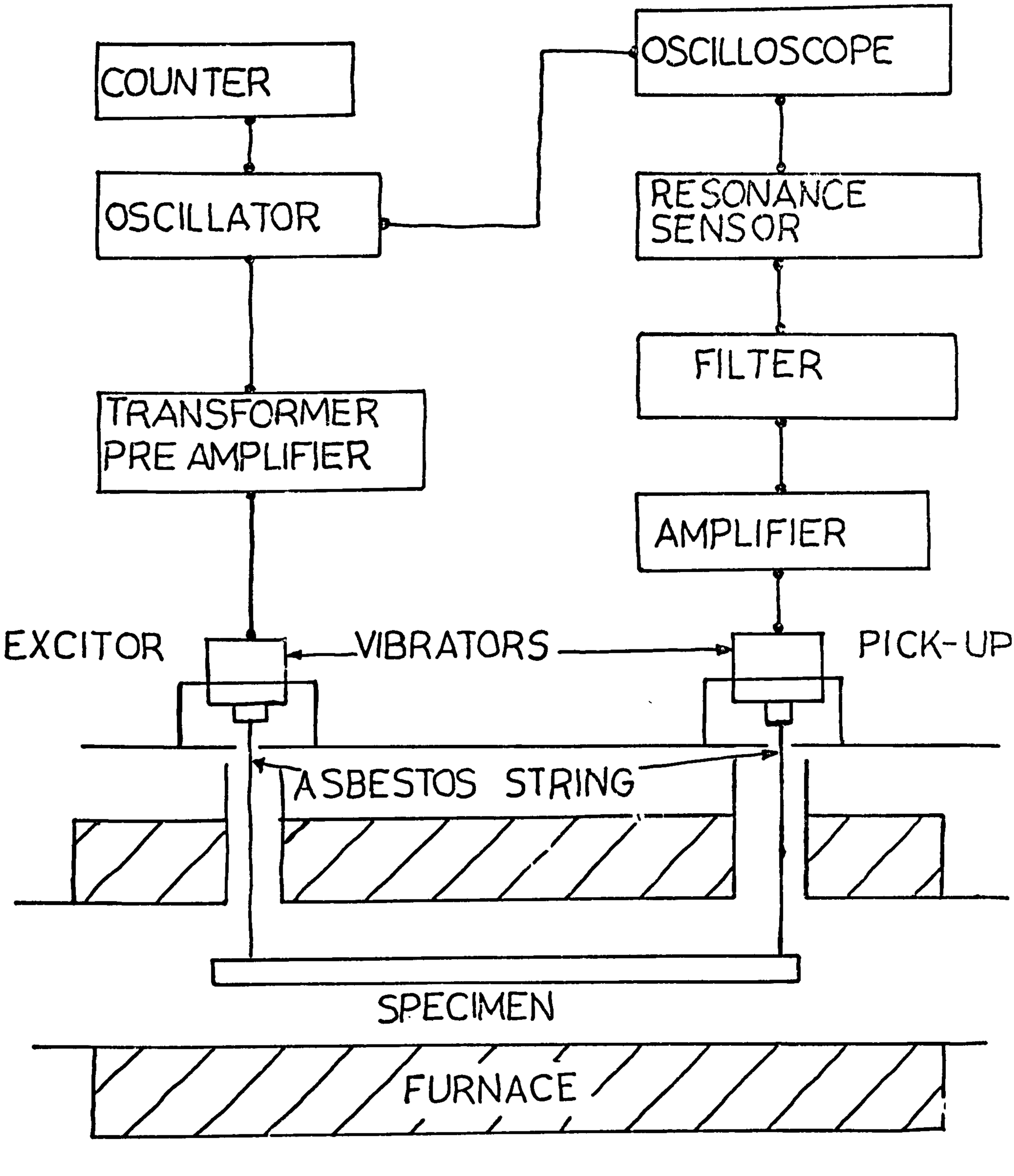


Fig. 20. SCHEMATIC LAYOUT OF A VIBRATION TECHNIQUE

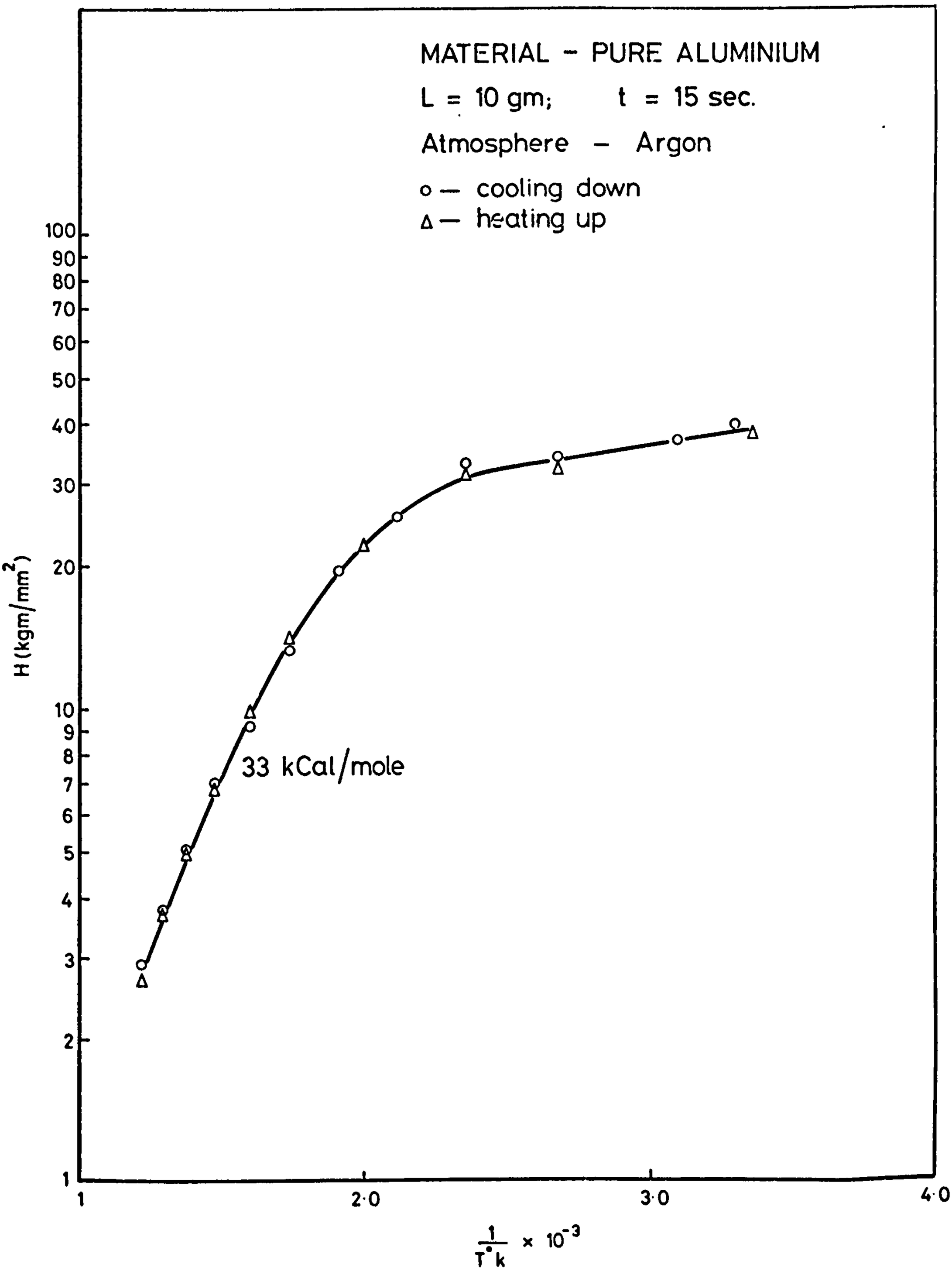

MATERIAL - PURE ALUMINIUM
L = 10 gm; t = 15 sec.
Atmosphere - Argon
o — cooling down
Δ — heating up
33 kCal/mole
H (kgm/mm²)
100
90
80
70
60
50
40
30
20
10
9
8
7
6
5
4
3
2
1
1
2·0
3·0
4·0
1/T°k × 10⁻³

Fig. 21

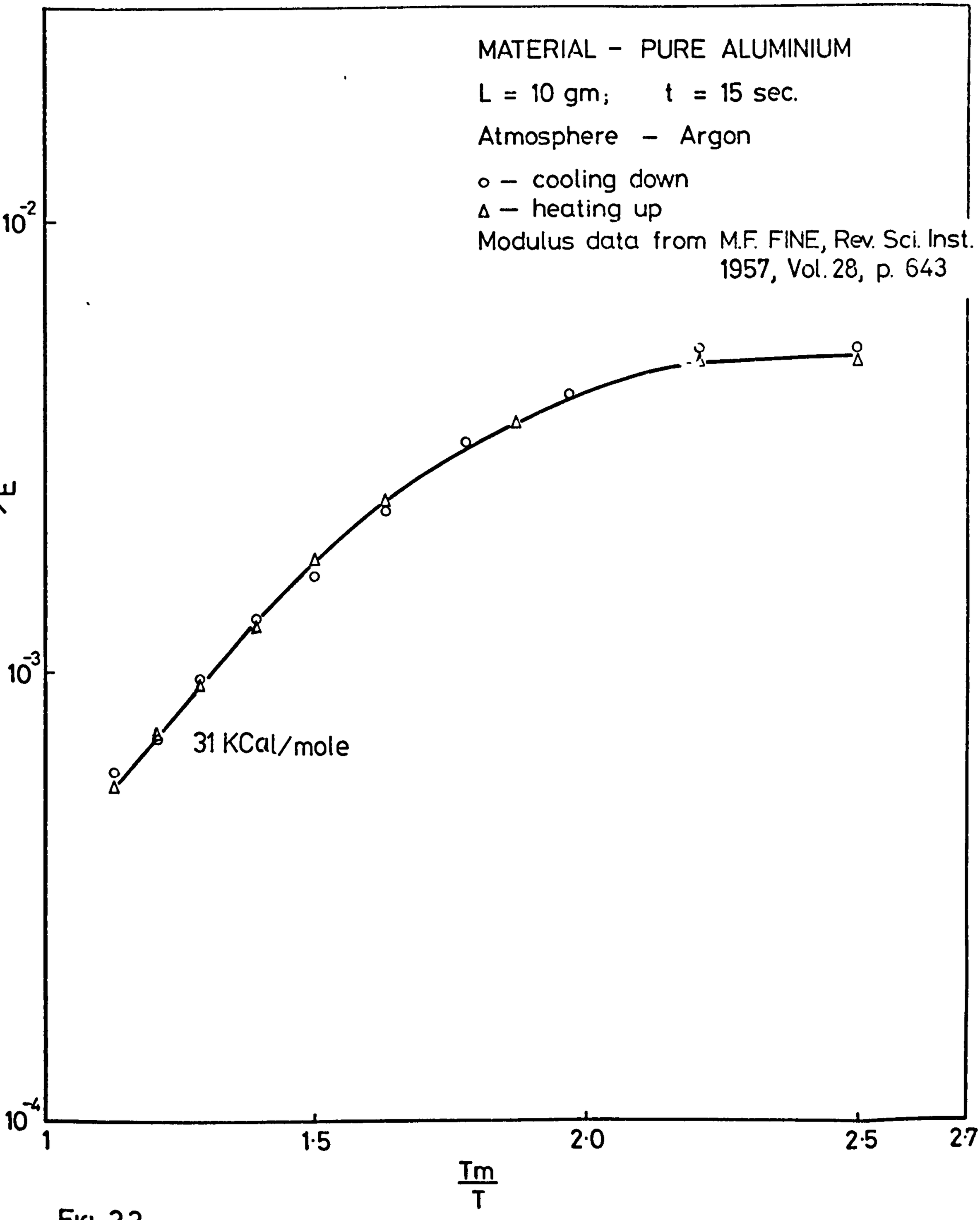

MATERIAL - PURE ALUMINIUM
L = 10 gm; t = 15 sec.
Atmosphere - Argon
o - cooling down
Δ - heating up
Modulus data from M.F. FINE, Rev. Sci. Inst. 1957, Vol. 28, p. 643
H/E
10^-2
10^-3
10^-4
31 KCal/mole
1
1·5
2·0
2·5
2·7
Tm/T

Fig. 22

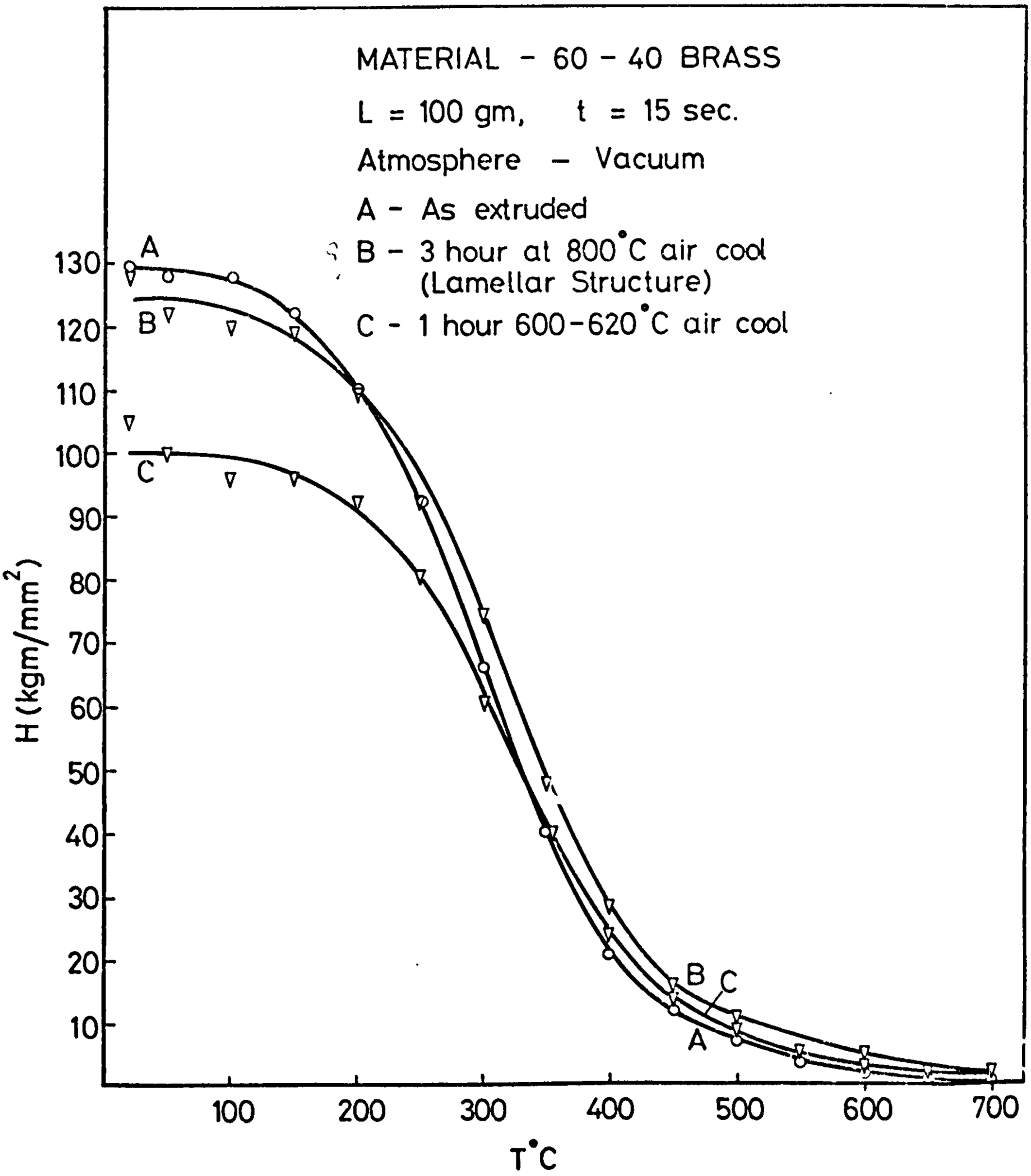

MATERIAL - 60 - 40 BRASS
L = 100 gm, t = 15 sec.
Atmosphere - Vacuum
A - As extruded
B - 3 hour at 800°C air cool
(Lamellar Structure)
C - 1 hour 600-620°C air cool
H (kgm/mm²)
T°C
130
120
110
100
90
80
70
60
50
40
30
20
10
100
200
300
400
500
600
700
A
B
C

Fig. 23

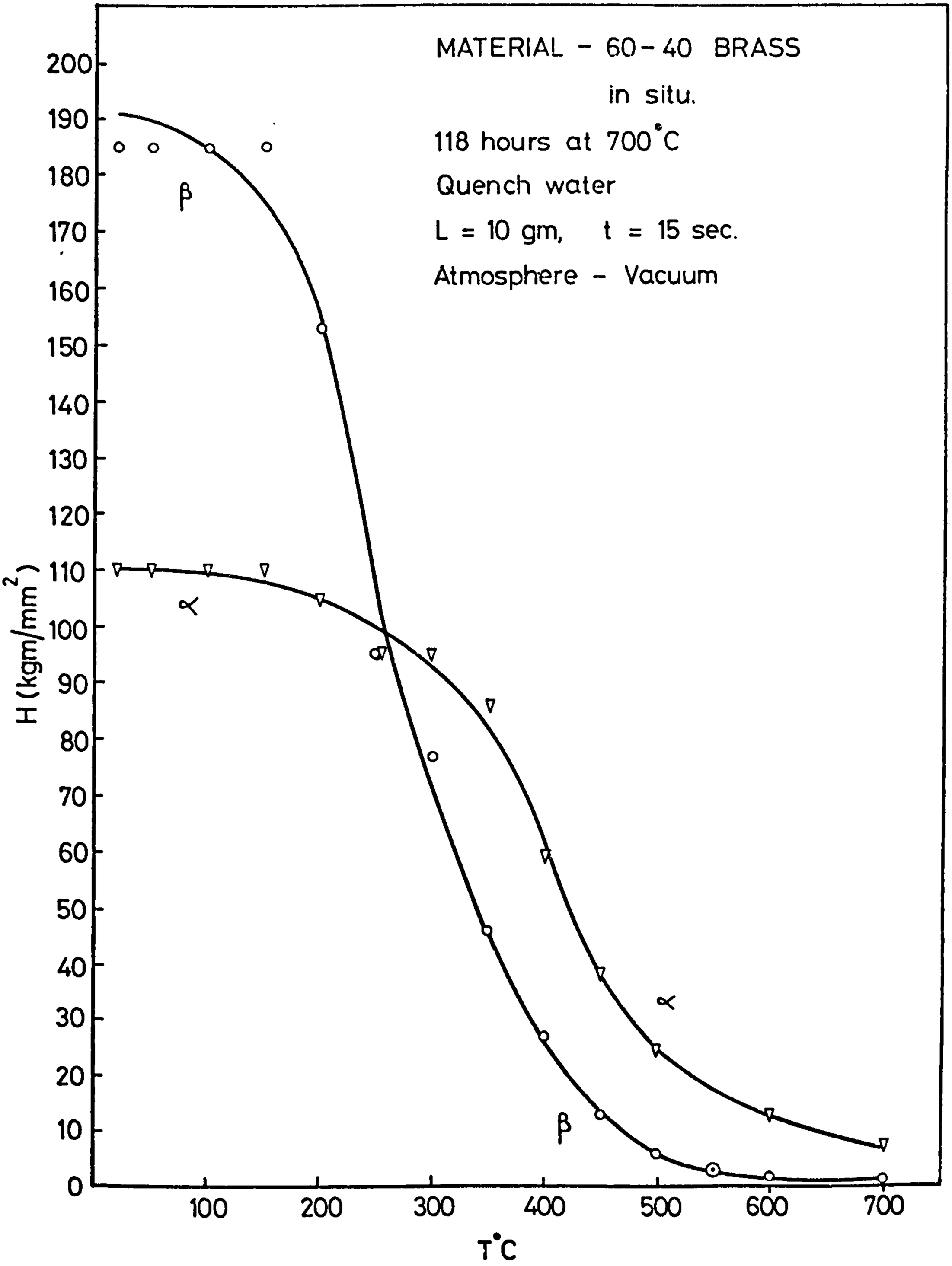

MATERIAL - 60-40 BRASS
in situ.
118 hours at 700°C
Quench water
L = 10 gm, t = 15 sec.
Atmosphere - Vacuum
H (kgm/mm²)
T°C
β
α
200
190
180
170
160
150
140
130
120
110
100
90
80
70
60
50
40
30
20
10
0
100
200
300
400
500
600
700

Fig. 24

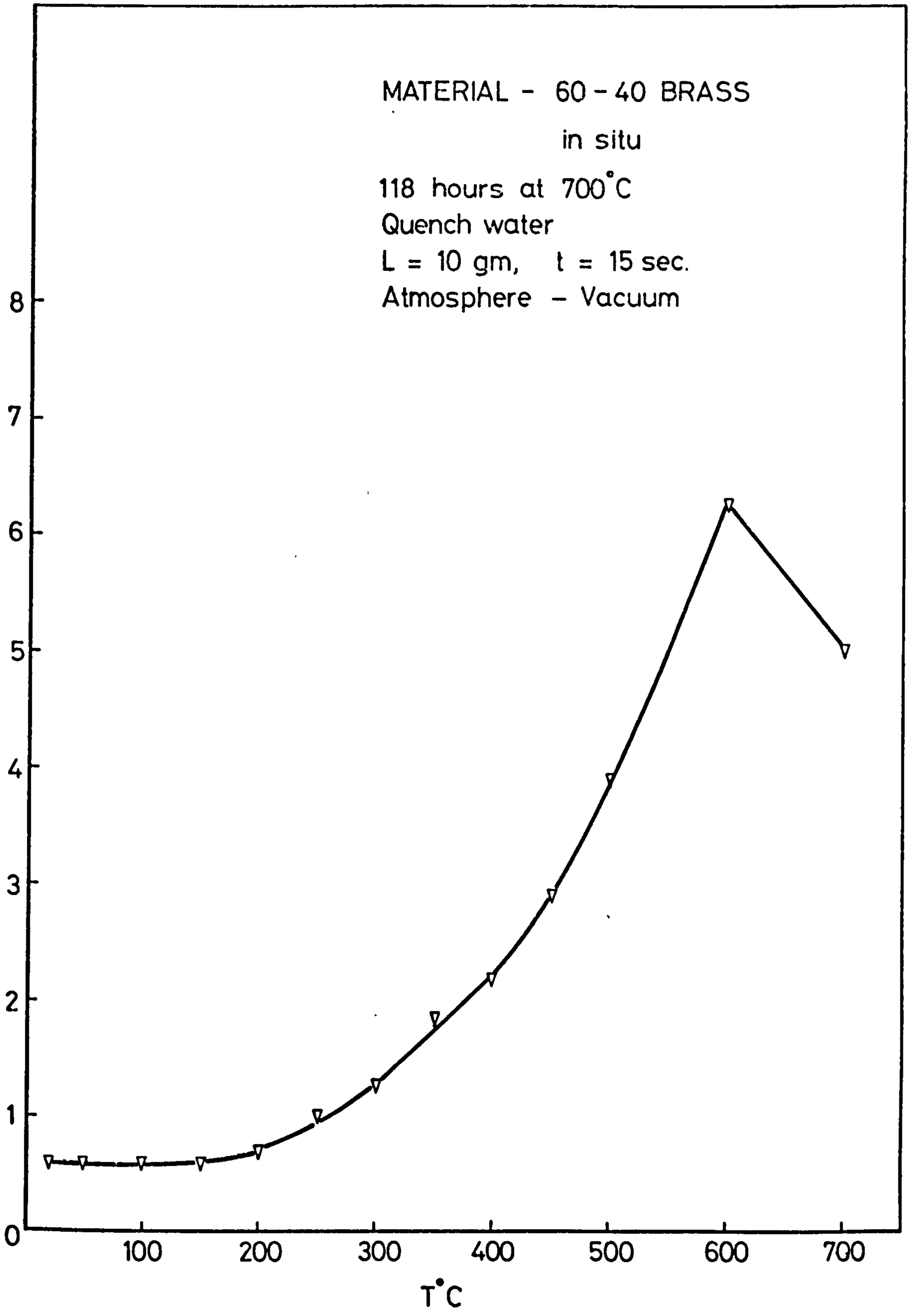

MATERIAL - 60 - 40 BRASS
in situ
118 hours at 700°C
Quench water
L = 10 gm, t = 15 sec.
Atmosphere - Vacuum
Hardness of α phase / Hardness of β phase = Hα / Hβ
0
1
2
3
4
5
6
7
8
100
200
300
400
500
600
700
T°C

Fig. 25

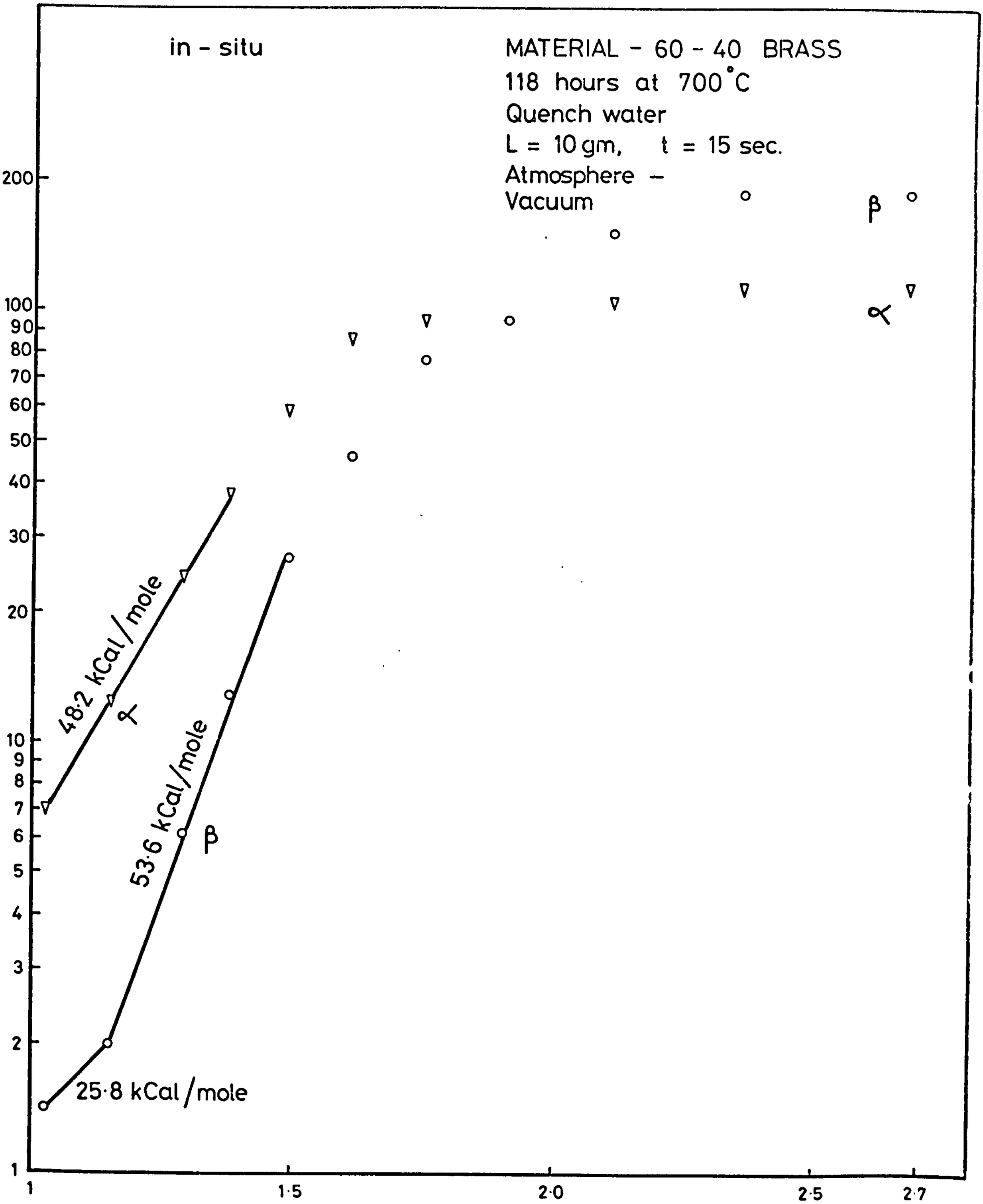

in - situ
MATERIAL - 60 - 40 BRASS
118 hours at 700°C
Quench water
L = 10 gm, t = 15 sec.
Atmosphere - Vacuum
H (kg/mm²)
48·2 kCal/mole
53·6 kCal/mole
25·8 kCal/mole
α
β
200
100
90
80
70
60
50
40
30
20
10
9
8
7
6
5
4
3
2
1
1
1·5
2·0
2·5
2·7
1/T°K × 10⁻³

Fig. 26

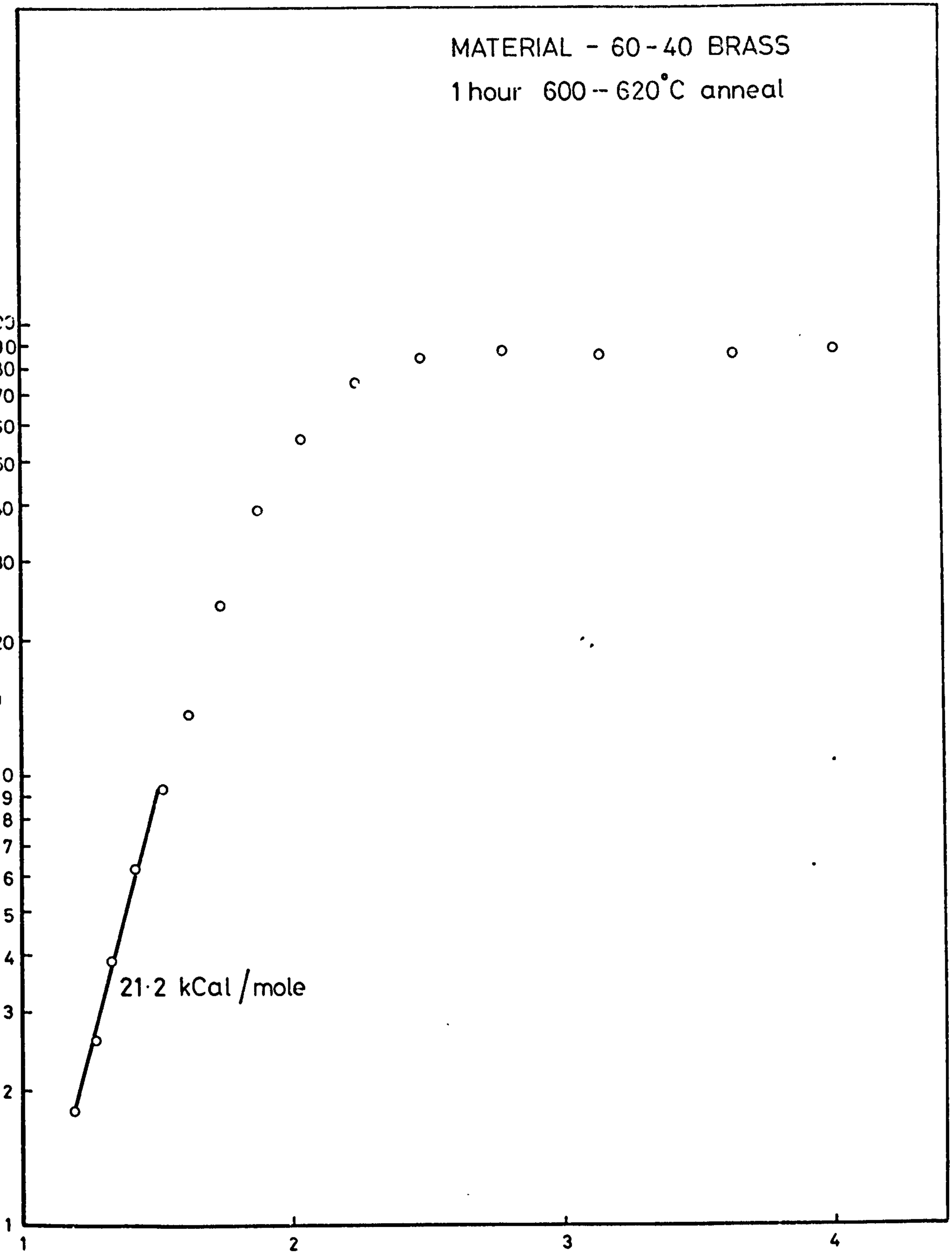

MATERIAL - 60-40 BRASS
1 hour 600 -- 620°C anneal
100
90
80
70
60
50
40
30
20
10
9
8
7
6
5
4
3
2
1
$\times 10^{-4}$, H/E
21·2 kCal / mole
1
2
3
4
Tm/T

Fig. 27

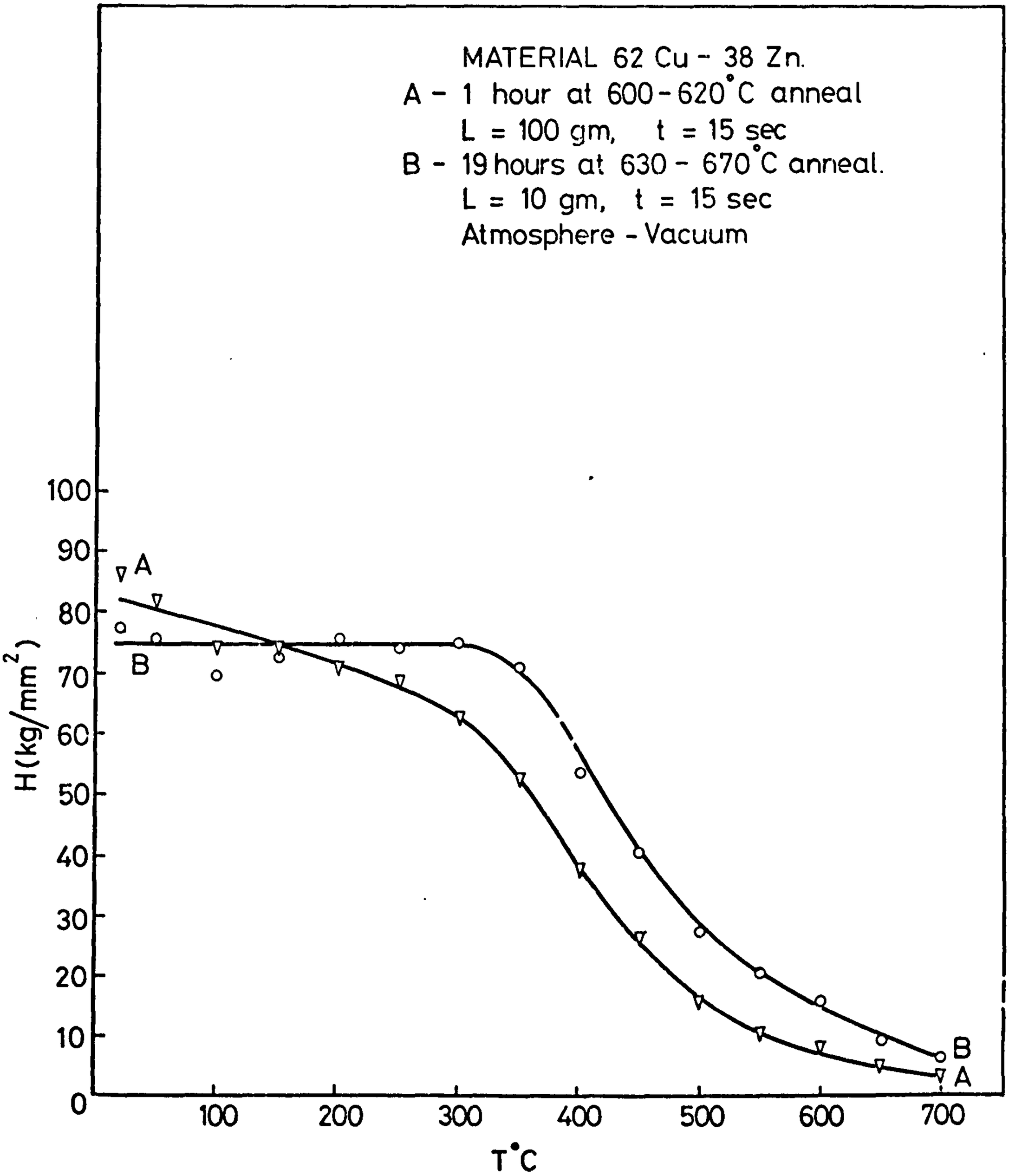

MATERIAL 62 Cu - 38 Zn.
A - 1 hour at 600 - 620°C anneal
L = 100 gm, t = 15 sec
B - 19 hours at 630 - 670°C anneal.
L = 10 gm, t = 15 sec
Atmosphere - Vacuum
H(kg/mm²)
T°C
A
B
0
10
20
30
40
50
60
70
80
90
100
200
300
400
500
600
700

Fig. 28

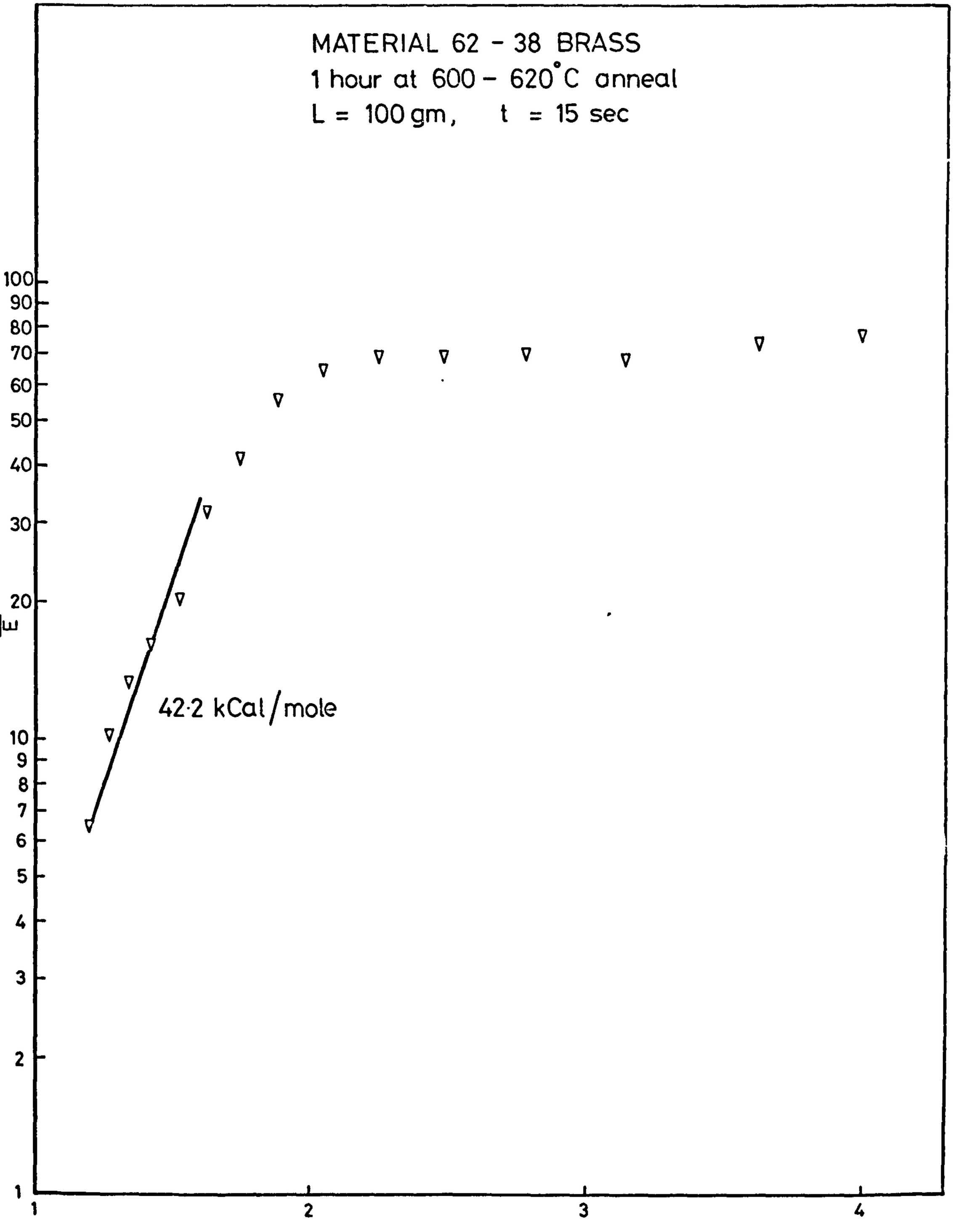

MATERIAL 62 - 38 BRASS
1 hour at 600 - 620°C anneal
L = 100 gm, t = 15 sec
42·2 kCal / mole
$\frac{H}{E} \times 10^{-4}$
$\frac{Tm}{T}$
100
90
80
70
60
50
40
30
20
10
9
8
7
6
5
4
3
2
1
1
2
3
4

Fig. 29

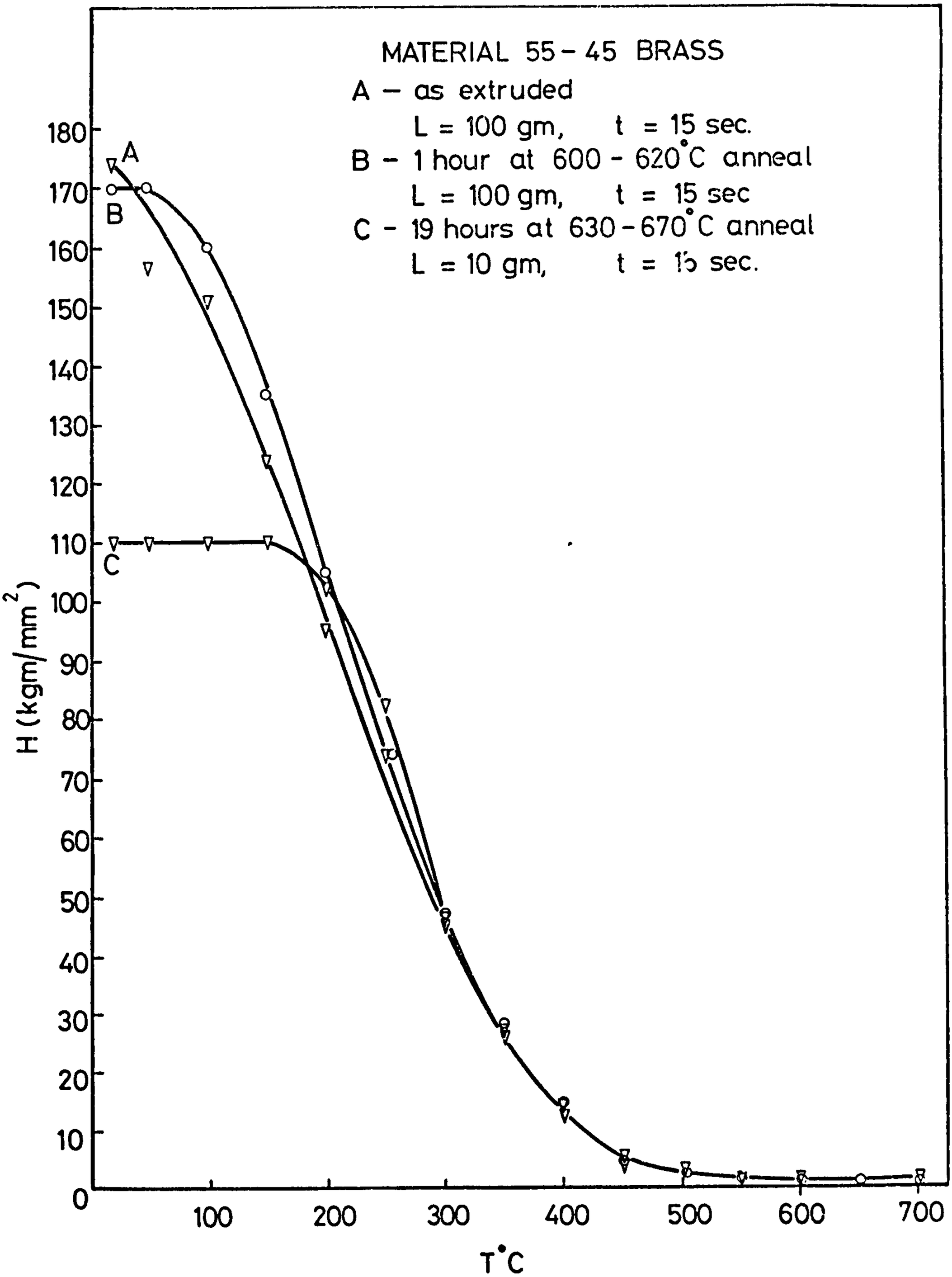

MATERIAL 55 – 45 BRASS
A – as extruded
L = 100 gm, t = 15 sec.
B – 1 hour at 600 - 620°C anneal
L = 100 gm, t = 15 sec
C – 19 hours at 630 – 670°C anneal
L = 10 gm, t = 15 sec.
A
B
C
H (kgm/mm²)
180
170
160
150
140
130
120
110
100
90
80
70
60
50
40
30
20
10
0
100
200
300
400
500
600
700
T°C

Fig. 30

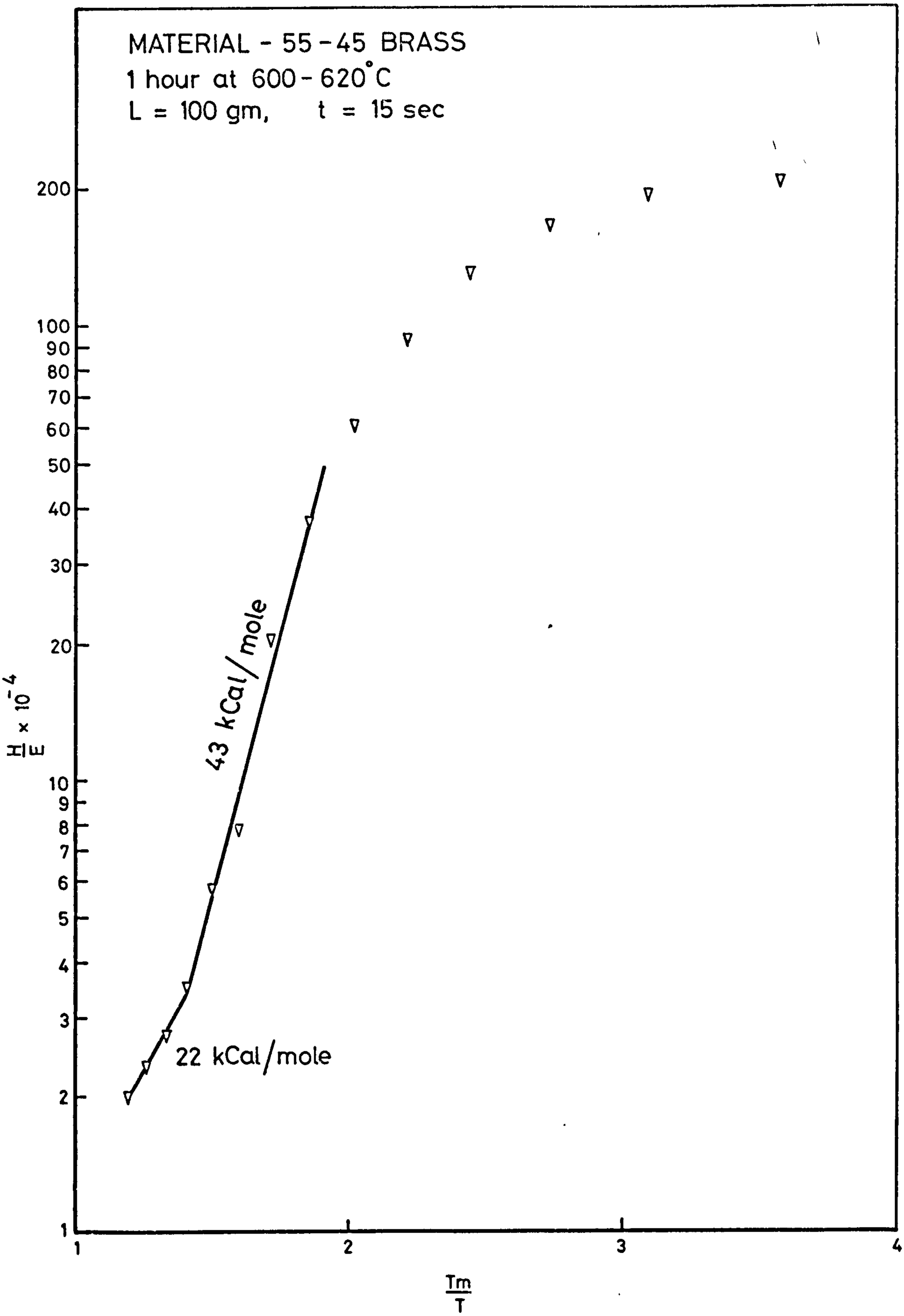

MATERIAL - 55 - 45 BRASS
1 hour at 600 - 620°C
L = 100 gm, t = 15 sec
200
100
90
80
70
60
50
40
30
20
10
9
8
7
6
5
4
3
2
1
$H_E \times 10^{-4}$
43 kCal/mole
22 kCal/mole
1
2
3
4
$\frac{Tm}{T}$

Fig. 31

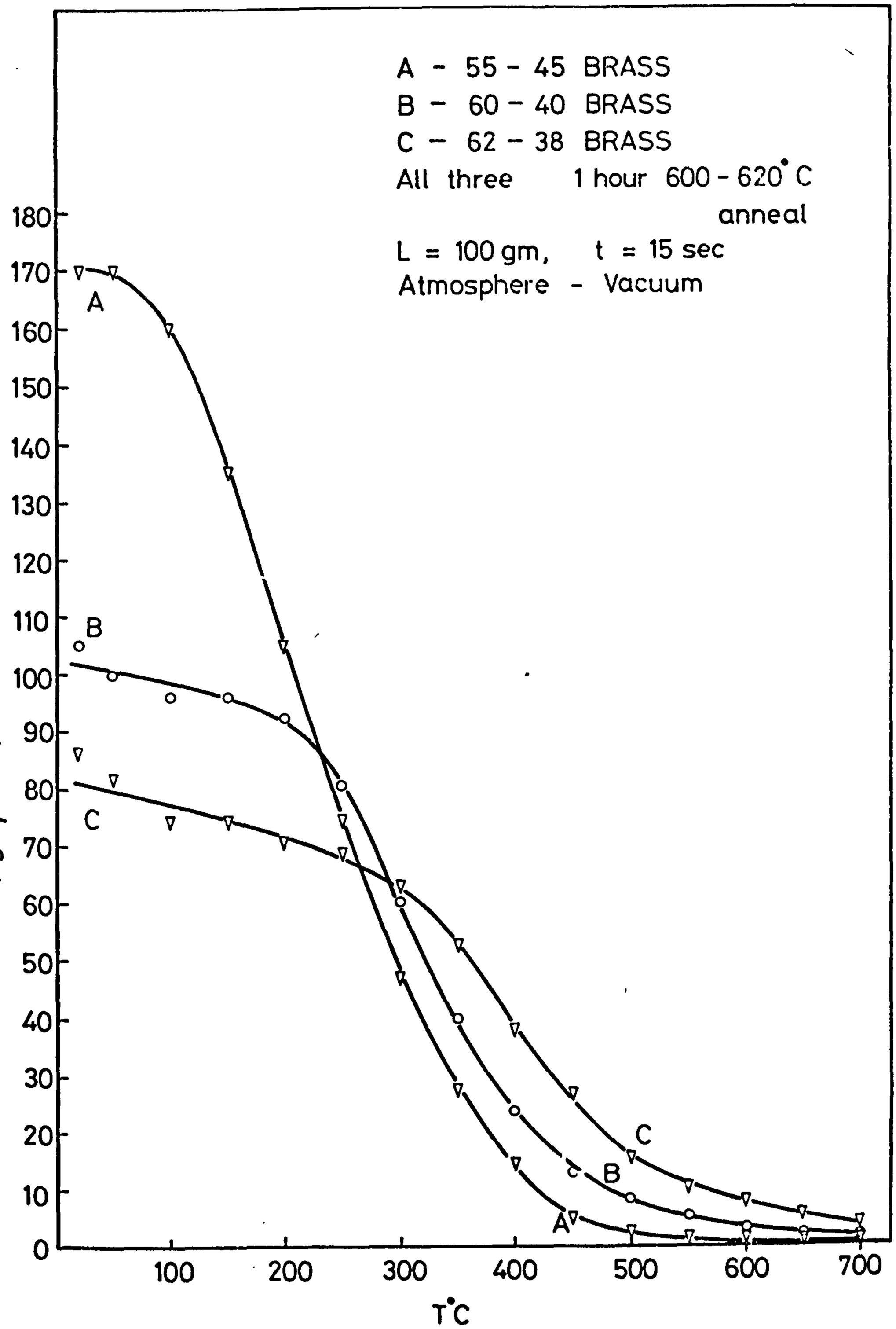

A - 55 - 45 BRASS
B - 60 - 40 BRASS
C - 62 - 38 BRASS
All three 1 hour 600 - 620° C anneal
L = 100 gm, t = 15 sec
Atmosphere - Vacuum
H (kgm/mm²)
T°C
A
B
C
180
170
160
150
140
130
120
110
100
90
80
70
60
50
40
30
20
10
0
100
200
300
400
500
600
700

Fig. 32

MATERIAL 60-40 BRASS
A - 19 hours at 630-670°C
L = 10 gm, t = 15 sec
B - 1 hour at 600-620°C
L = 100 gm, t = 15 sec
C - in-situ
(118 hours at 700°C. Quench water)
In A & B, ∝ and β phases are represented by 62-38 and 55-45 brasses respectively.

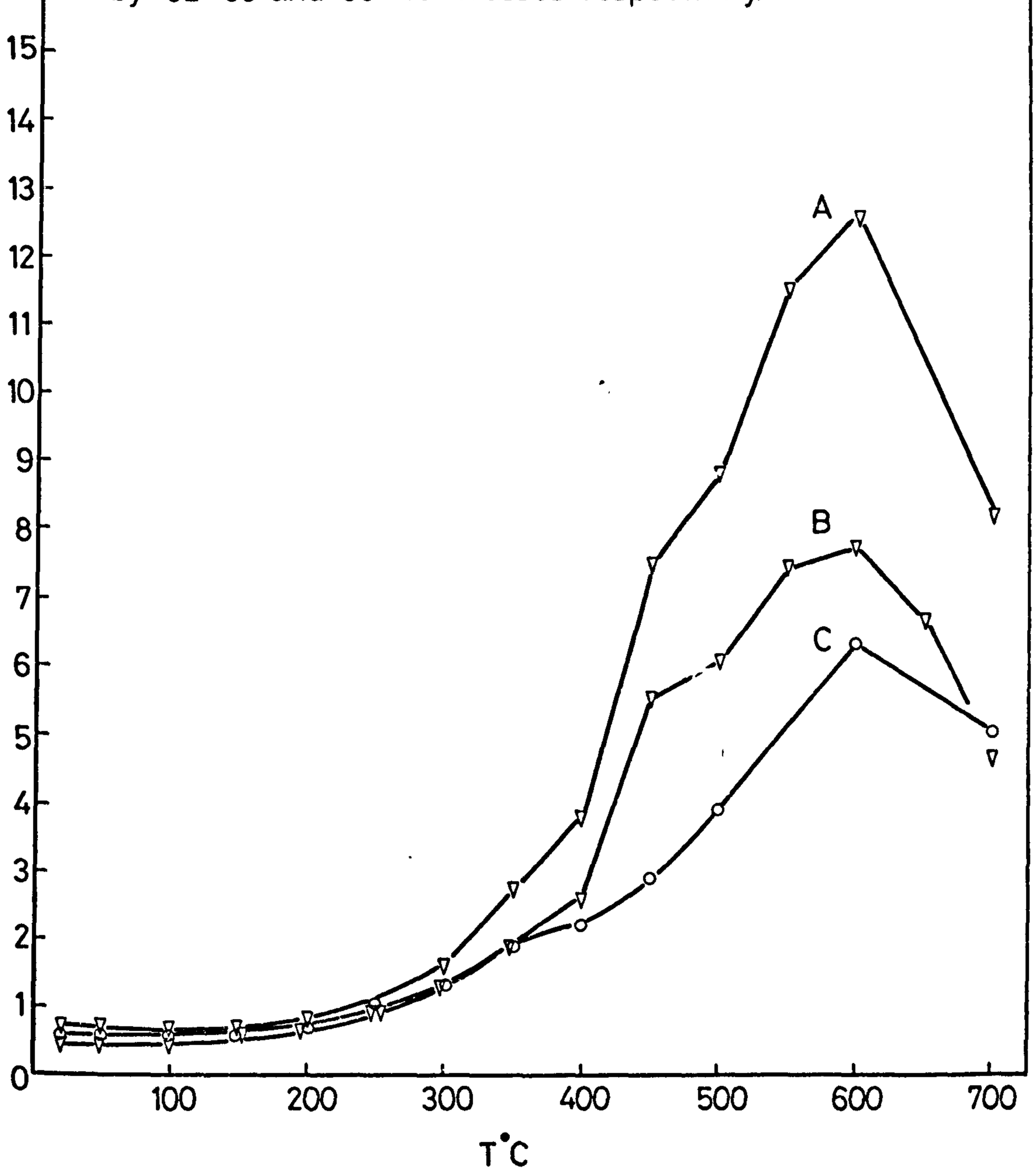


Fig. 33

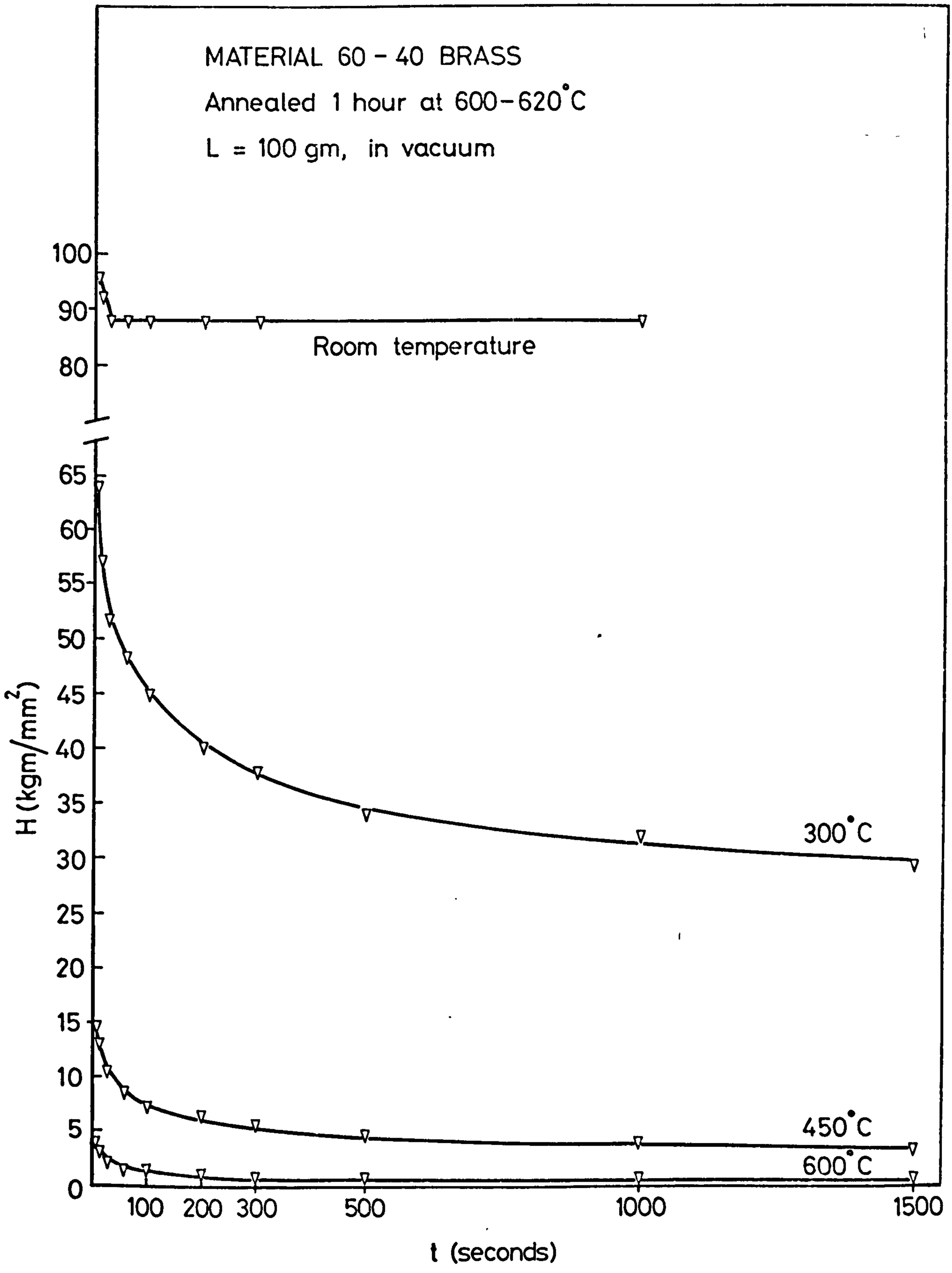

MATERIAL 60 - 40 BRASS
Annealed 1 hour at 600-620°C
L = 100 gm, in vacuum
Room temperature
300°C
450°C
600°C
H (kgm/mm²)
t (seconds)
100
90
80
65
60
55
50
45
40
35
30
25
20
15
10
5
0
100
200
300
500
1000
1500

Fig. 34

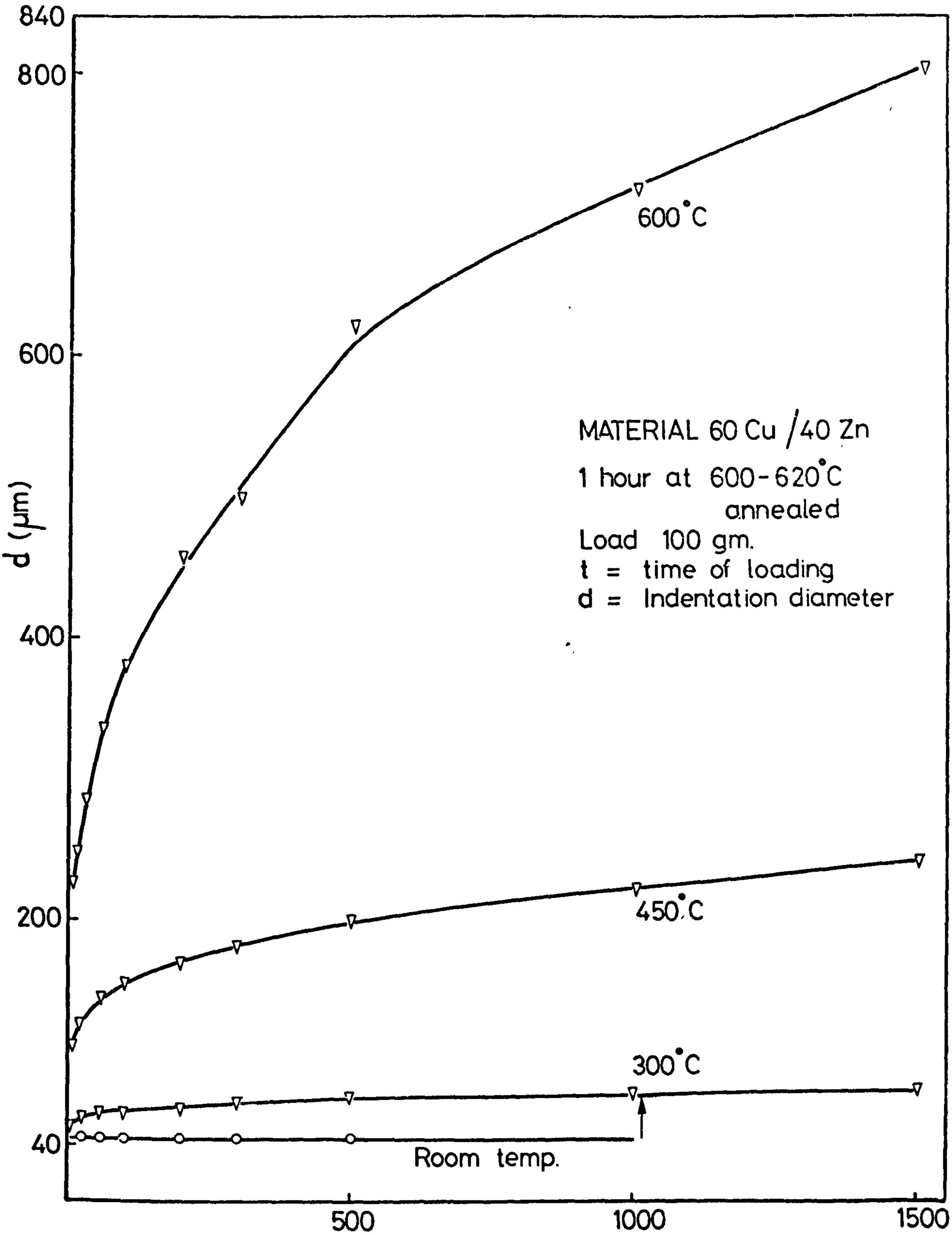
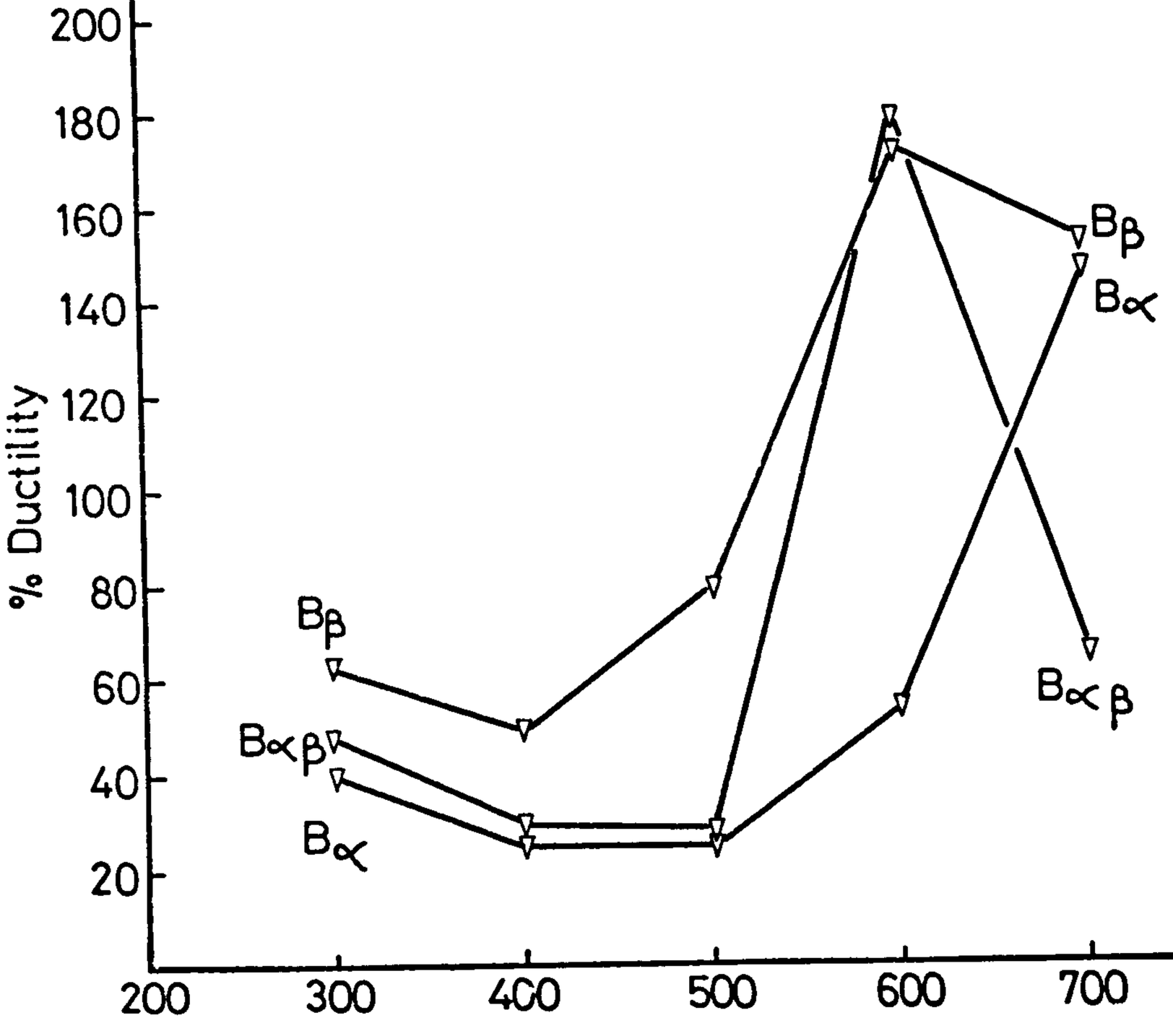

840
800
600
400
200
40
d (μm)
600°C
450°C
300°C
Room temp.
500
1000
1500
t (sec)
MATERIAL 60 Cu /40 Zn
1 hour at 600-620°C
annealed
Load 100 gm.
t = time of loading
d = Indentation diameter

Fig. 35

MATERIAL 60-40 BRASS

at T = 600°C

$\frac{D(\beta)}{D(\alpha)} = 3.2$



MATERIAL 60-40 BRASS

at T = 600°C

$\frac{U.T.S.(\alpha)}{U.T.S.(\beta)} = 7.2$

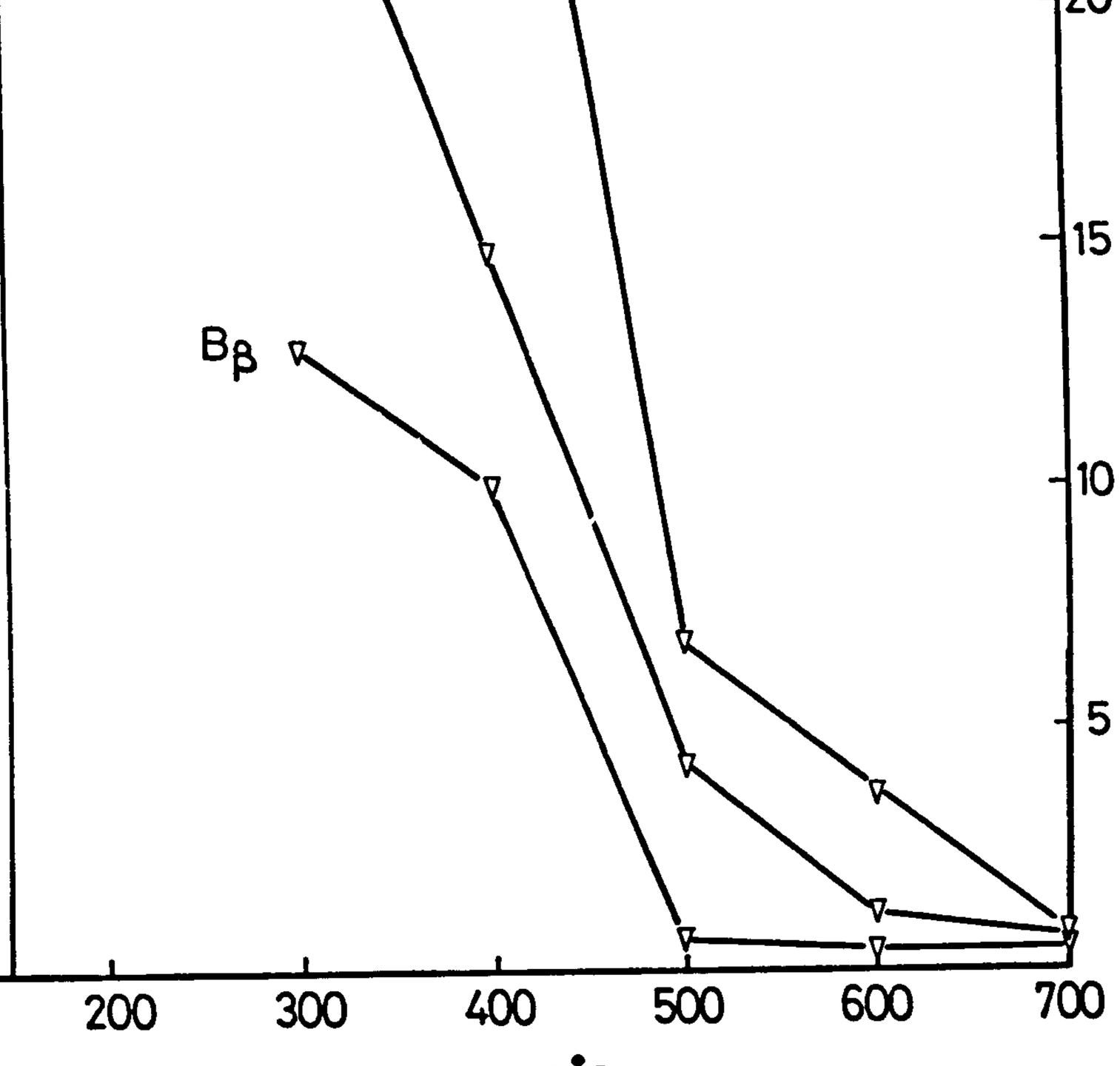
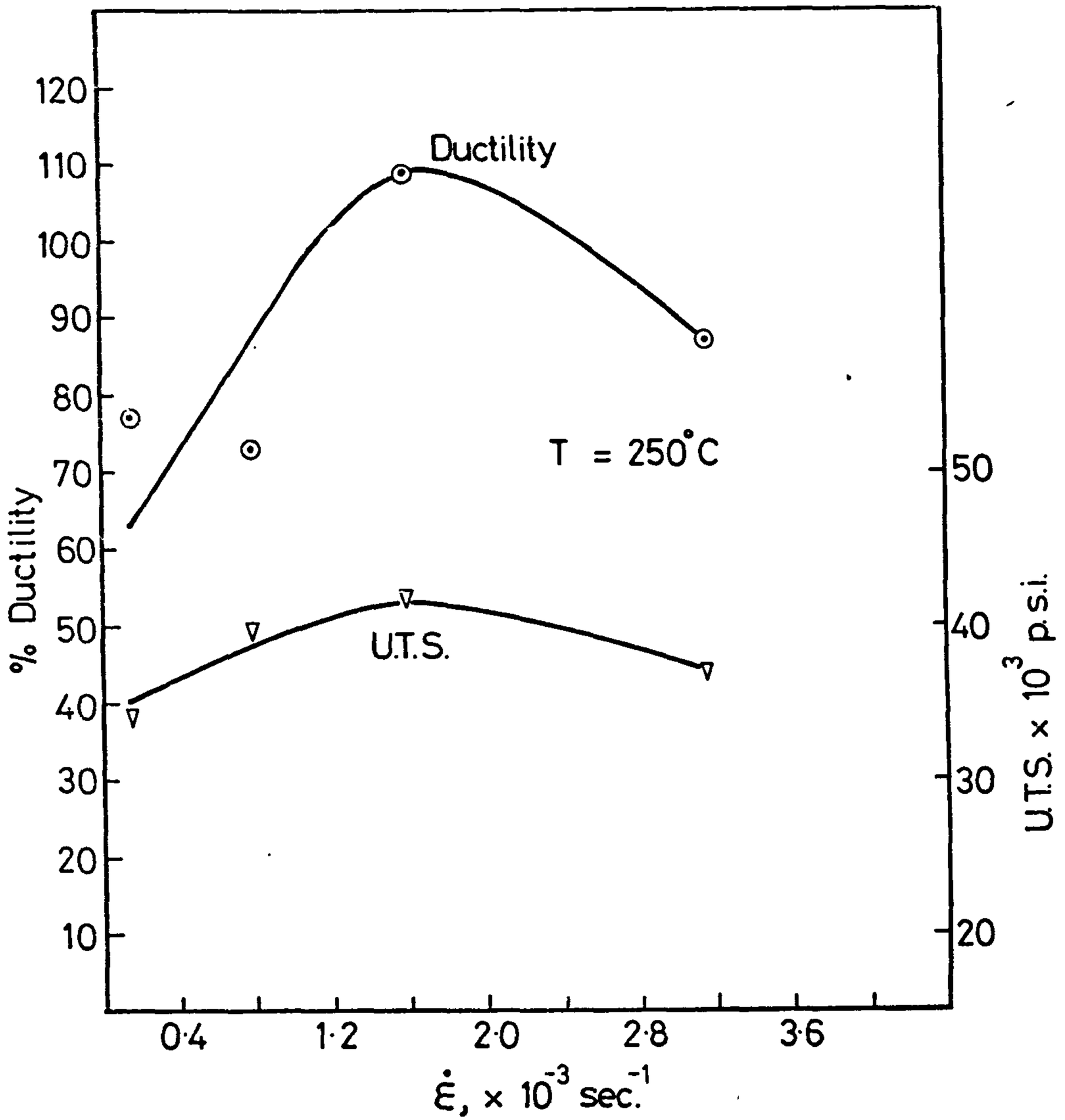


Fig. 36

Fig. 37



60 Cu - 40 Zn

T = 250° C

$\dot{\varepsilon} = 1{\cdot}6 \times 10^{-3}$ sec.$^{-1}$

CONDITION	DUCTILITY	U.T.S. $\times 10^{-3}$ p.s.i.
as extruded	109	41·6
1 hr. 400° C	67	41·2
1 hr. 600° C	67	31·8

Table. 9

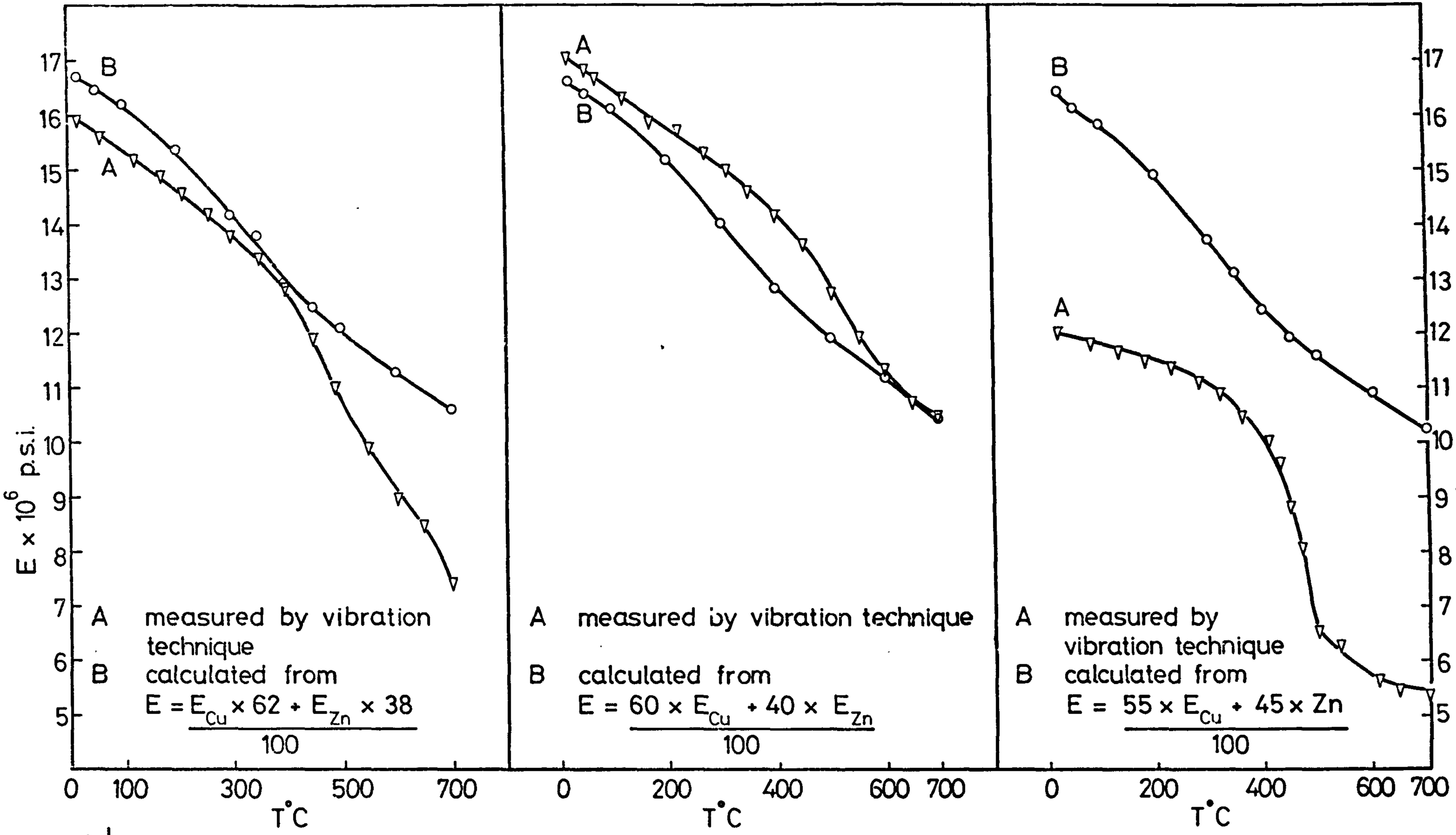


Fig.38

62 Cu – 38 Zn BRASS
Annealed at 400°C
for 2 hrs. in argon

60 Cu – 40 Zn
Annealed at 400°C
for 2 hrs. in argon

55 Cu - 45 Zn
Annealed at 400°C
for 2 hrs. in argon

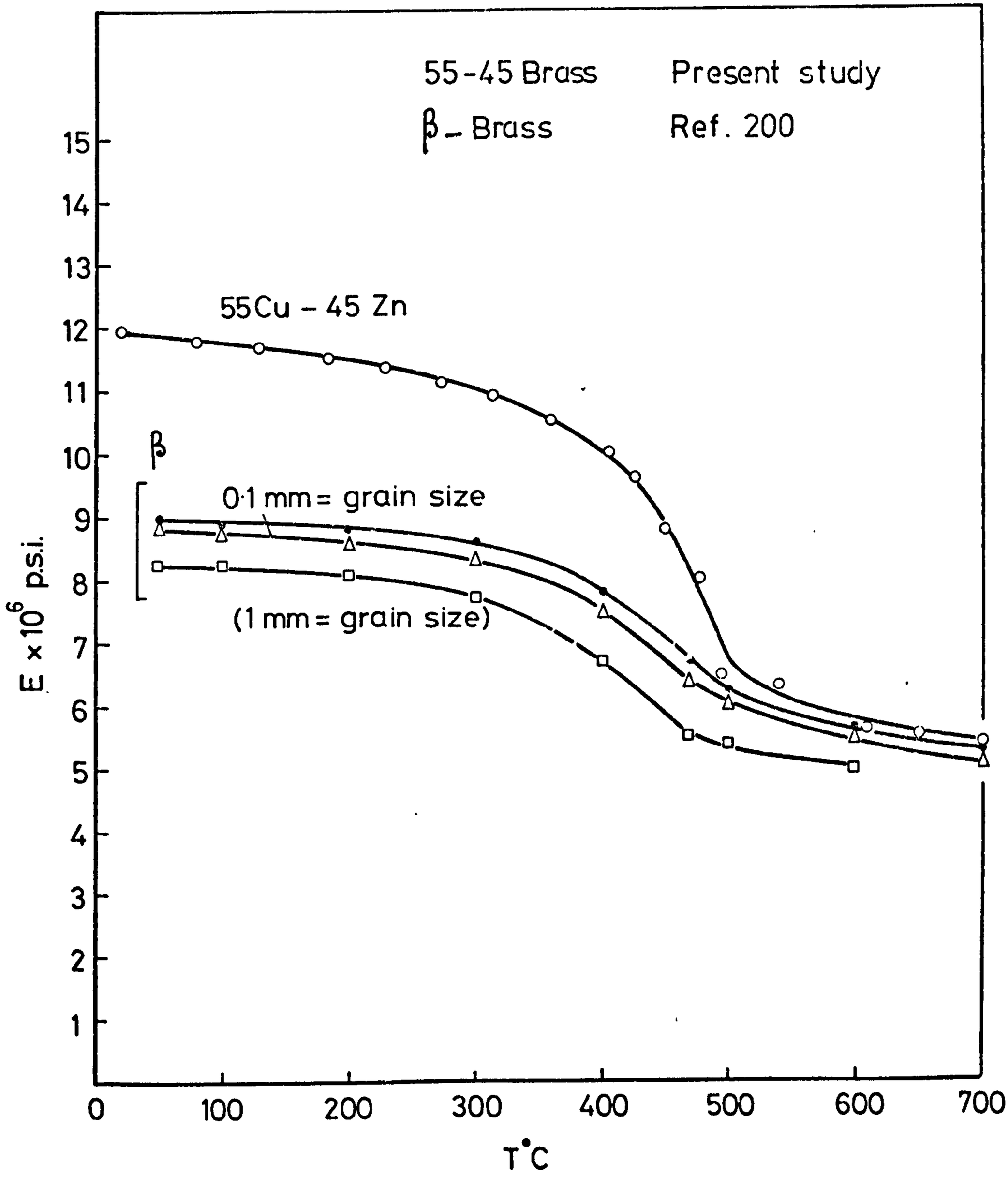

55-45 Brass
Present study
β - Brass
Ref. 200
55Cu - 45 Zn
β
0·1 mm = grain size
(1 mm = grain size)
E x 10^6 p.s.i.
T°C
0
100
200
300
400
500
600
700
1
2
3
4
5
6
7
8
9
10
11
12
13
14
15

Fig. 39

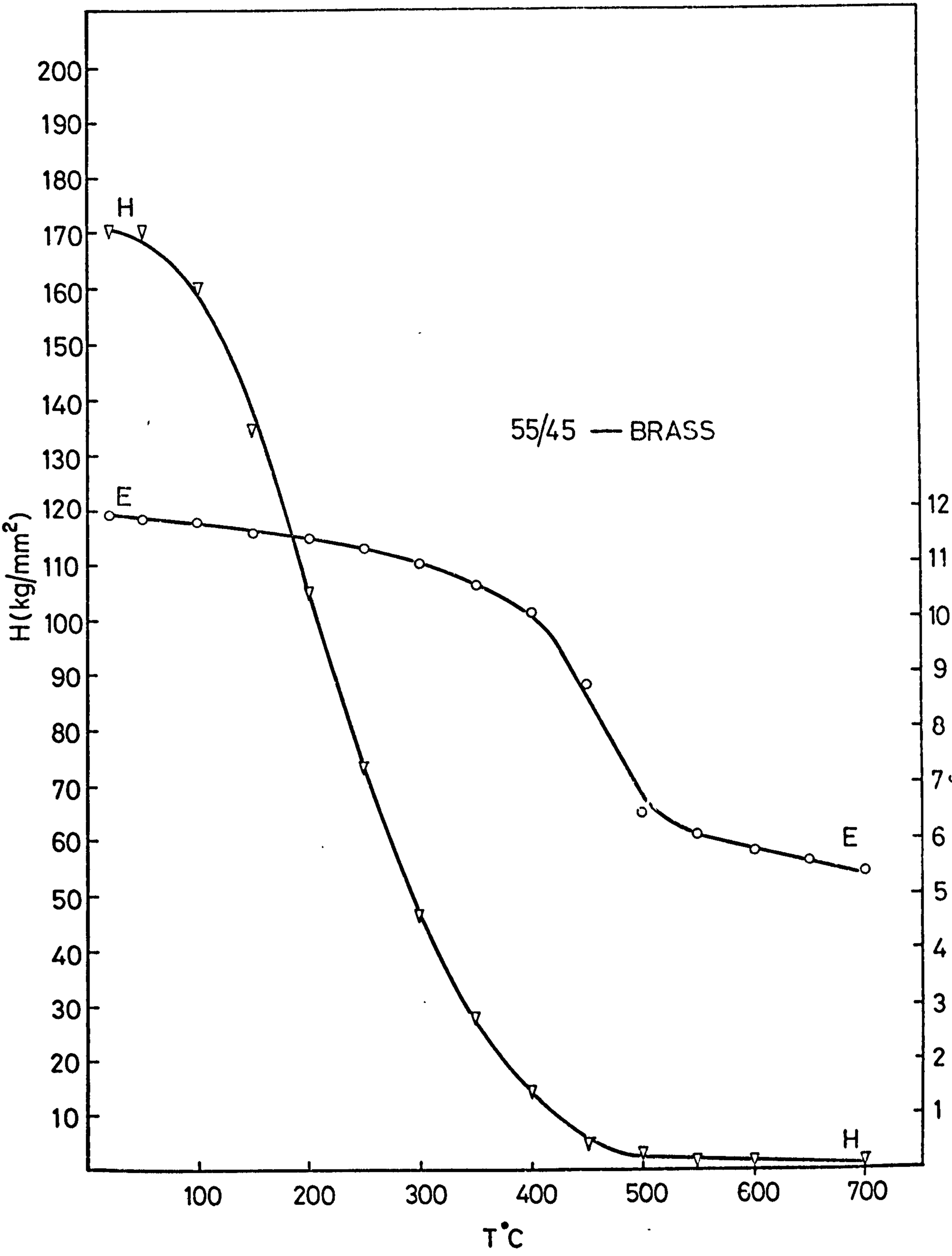

55/45 — BRASS
H
E
H(kg/mm²)
E, x 10⁶ p.s.i.
T°C
200
190
180
170
160
150
140
130
120
110
100
90
80
70
60
50
40
30
20
10
12
11
10
9
8
7
6
5
4
3
2
1
100
200
300
400
500
600
700

Fig. 40

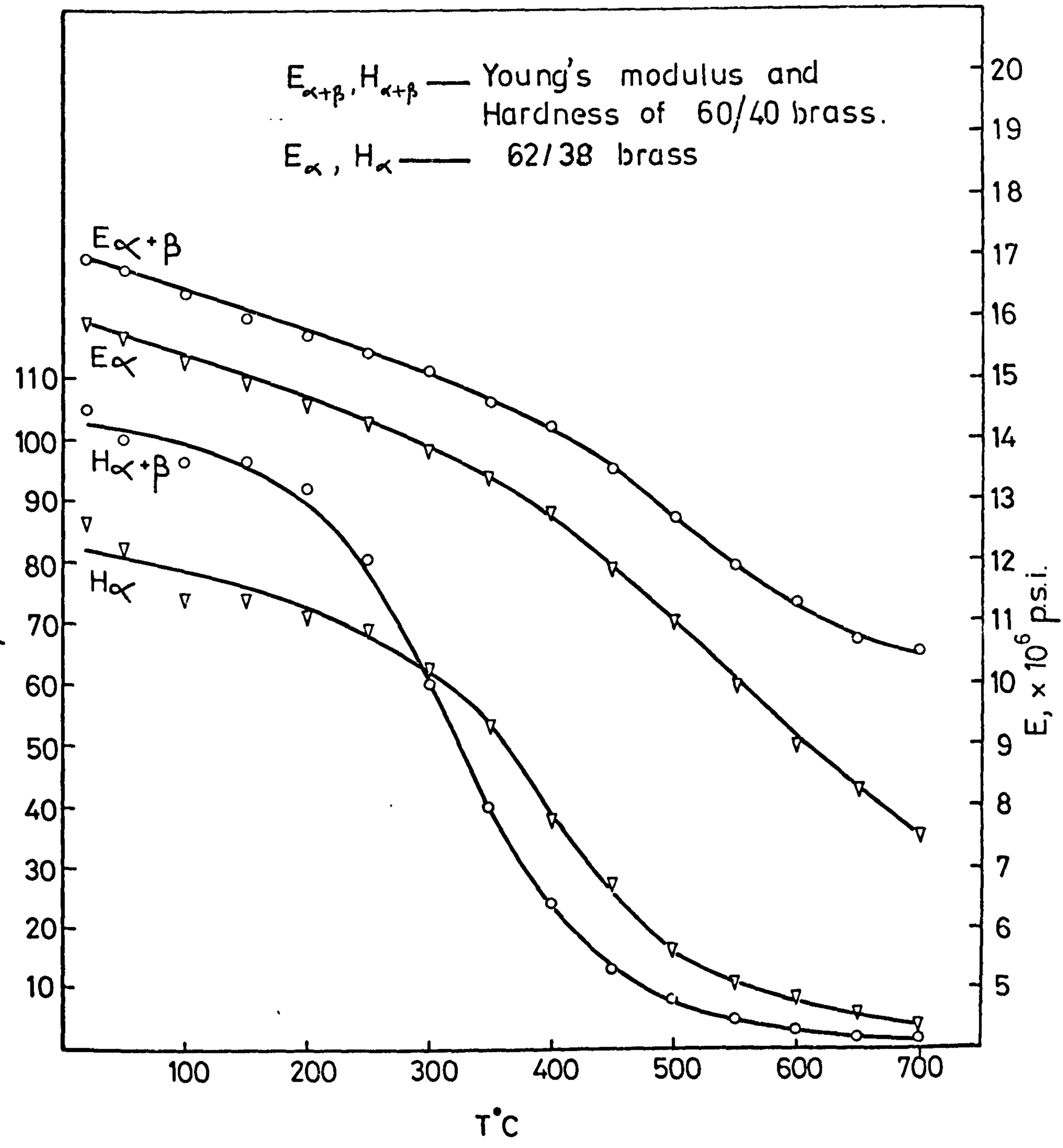
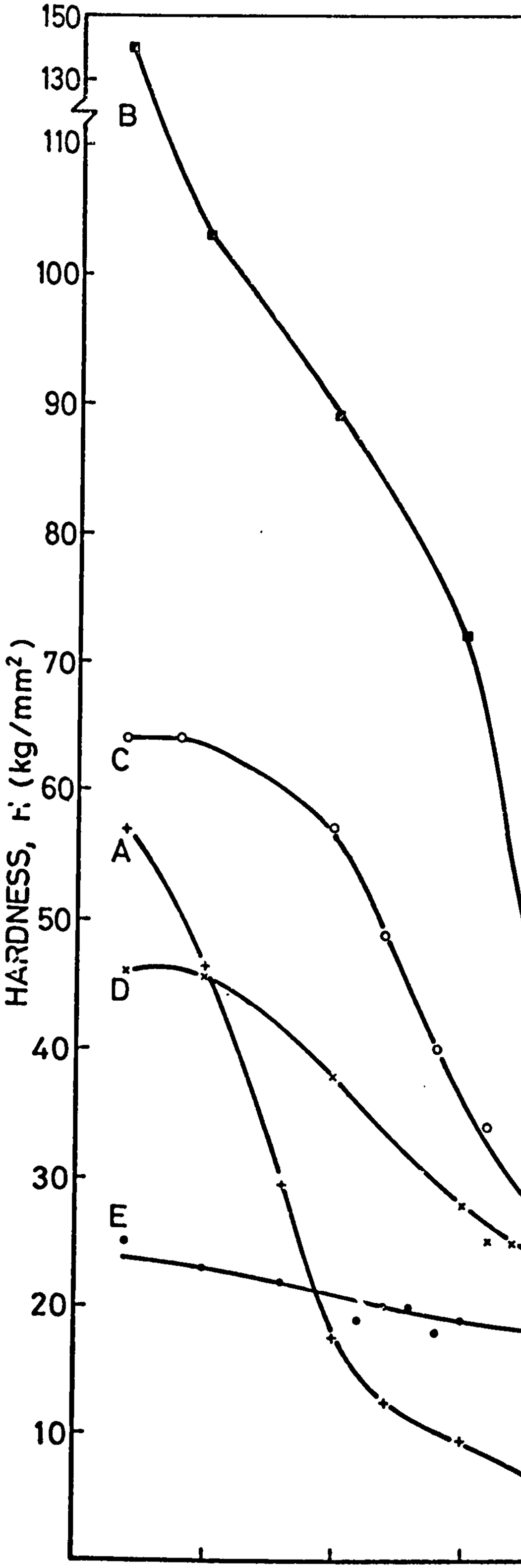

$E_{\alpha+\beta}, H_{\alpha+\beta}$ —— Young's modulus and Hardness of 60/40 brass.
E_{α}, H_{α} —— 62/38 brass
$E_{\alpha+\beta}$
E_{α}
$H_{\alpha+\beta}$
H_{α}
H (kgm/mm²)
E, x 10⁶ p.s.i.
T°C
110
100
90
80
70
60
50
40
30
20
10
20
19
18
17
16
15
14
13
12
11
10
9
8
7
6
5
100
200
300
400
500
600
700

Fig. 41



A = 78 Zn – 22 Al EUTECTOID
3 hours at 370°C. Quenched water (at room temperature)
L = 10 gm, t = 15 sec.

B = 22 Zn – 78 Al
1 hour at 400°C + 1 hour at 500°C.

C = 99·5 Zn – 0·5 Al
1 hour at 350°C

D = 12·4 Zn – 87·6 Al
2 hours at 500°C + 5 min. at 600°C

E = 5·6 Zn – 94 4 Al
2 hours at 500°C + 5 min. at 600°C

In all cases
L = 10 gm, t = 15 sec.
Atmosphere – Vacuum

Fig. 42

ALLOY	PHASE REPRESENTED IN Zn-Al EUTECTOID	TEMP. RANGE, T°C
5·6 Zn - 94·6 Al	α	0-150
12·4 Zn - 87·6 Al	α	160-220
22 Zn - 78 Al	α	230-270
99·5 Zn - 0·5 Al	β	0-270

LOAD = 10 gm, time of loading = 15 sec.

Atmosphere - Vacuum

Fig. 43

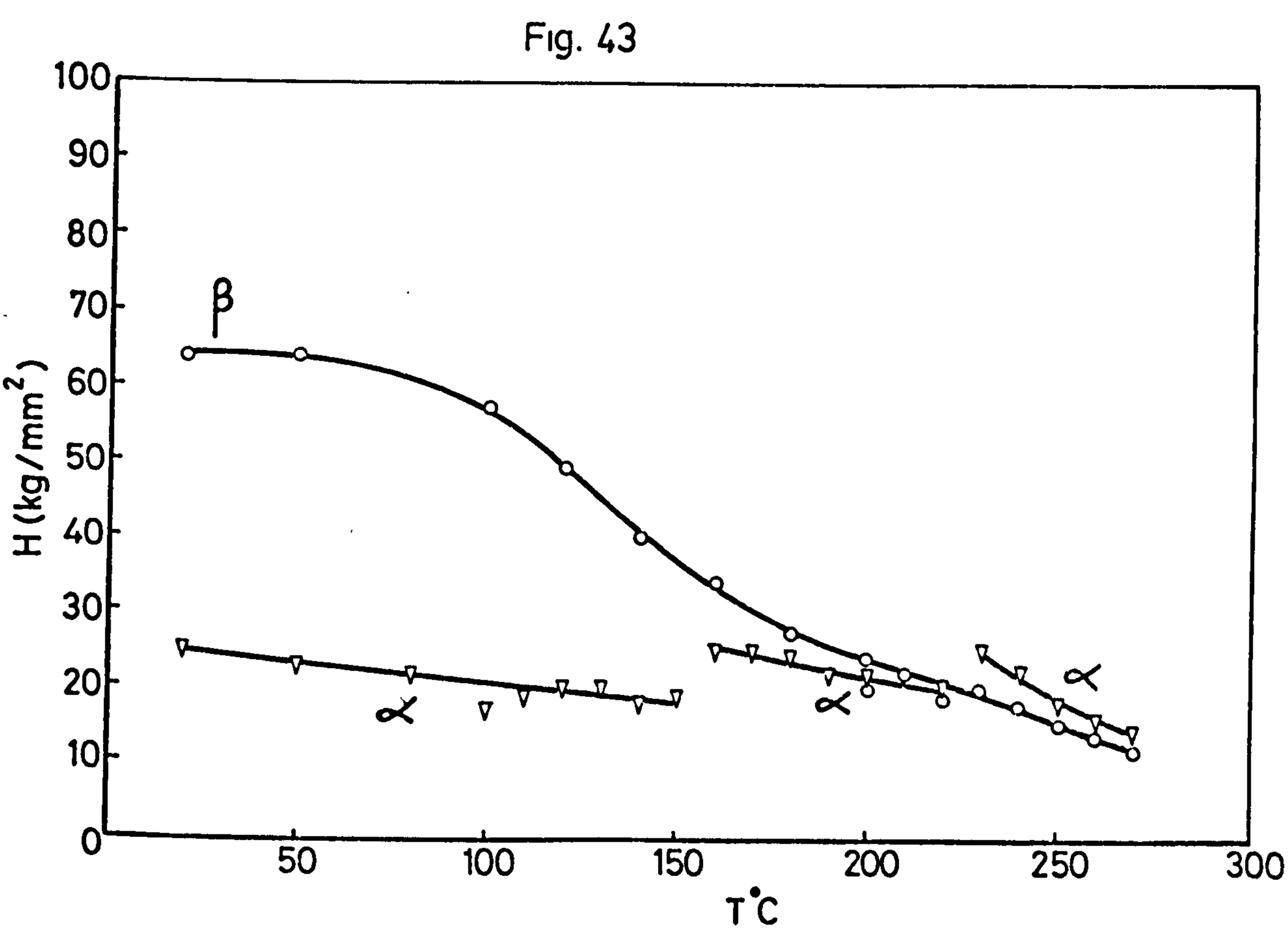
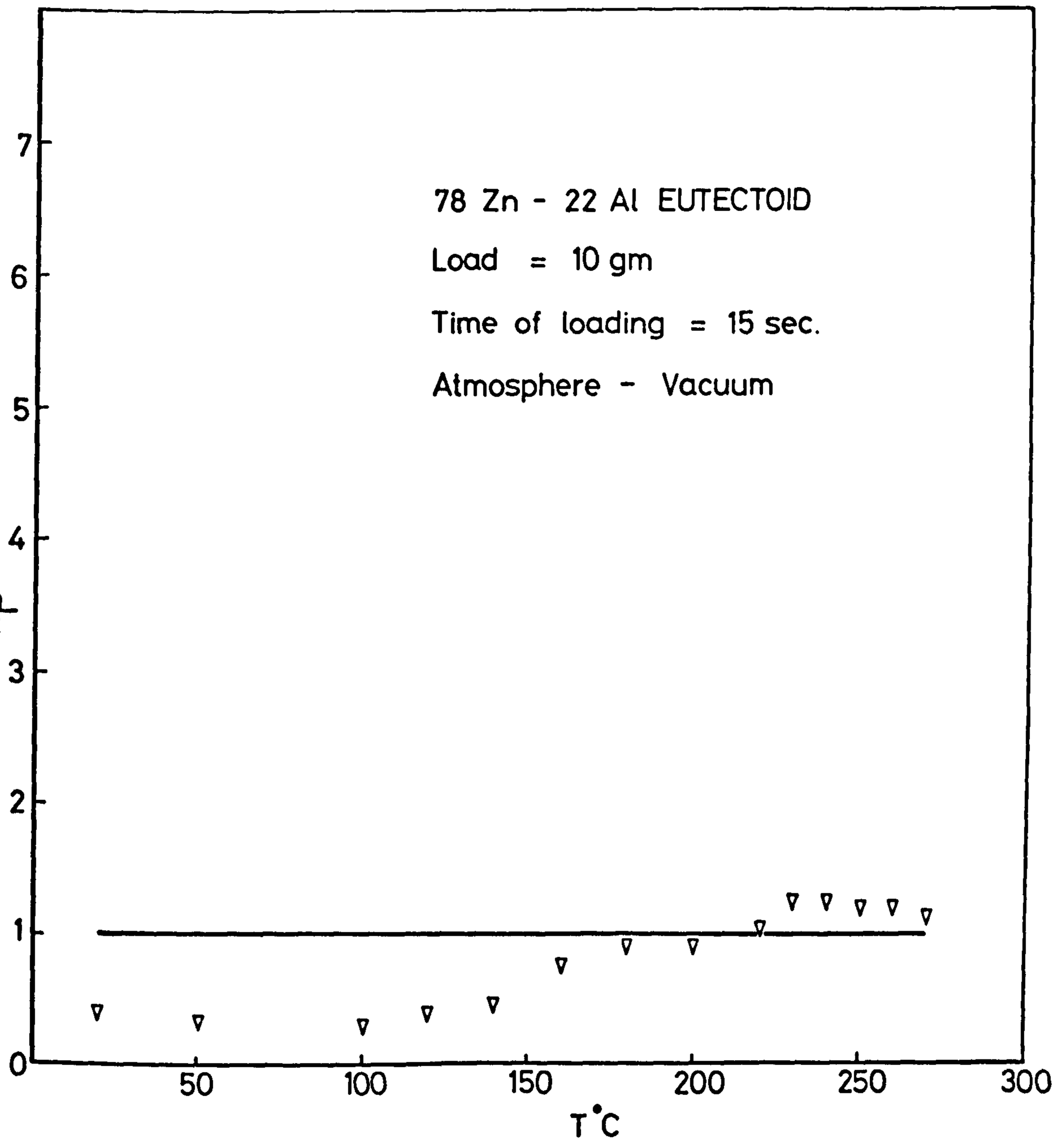


Fig. 44


78 Zn - 22 Al EUTECTOID
Load = 10 gm
Time of loading = 15 sec.
Atmosphere - Vacuum
Hα/Hβ
T°C
0
1
2
3
4
5
6
7
50
100
150
200
250
300

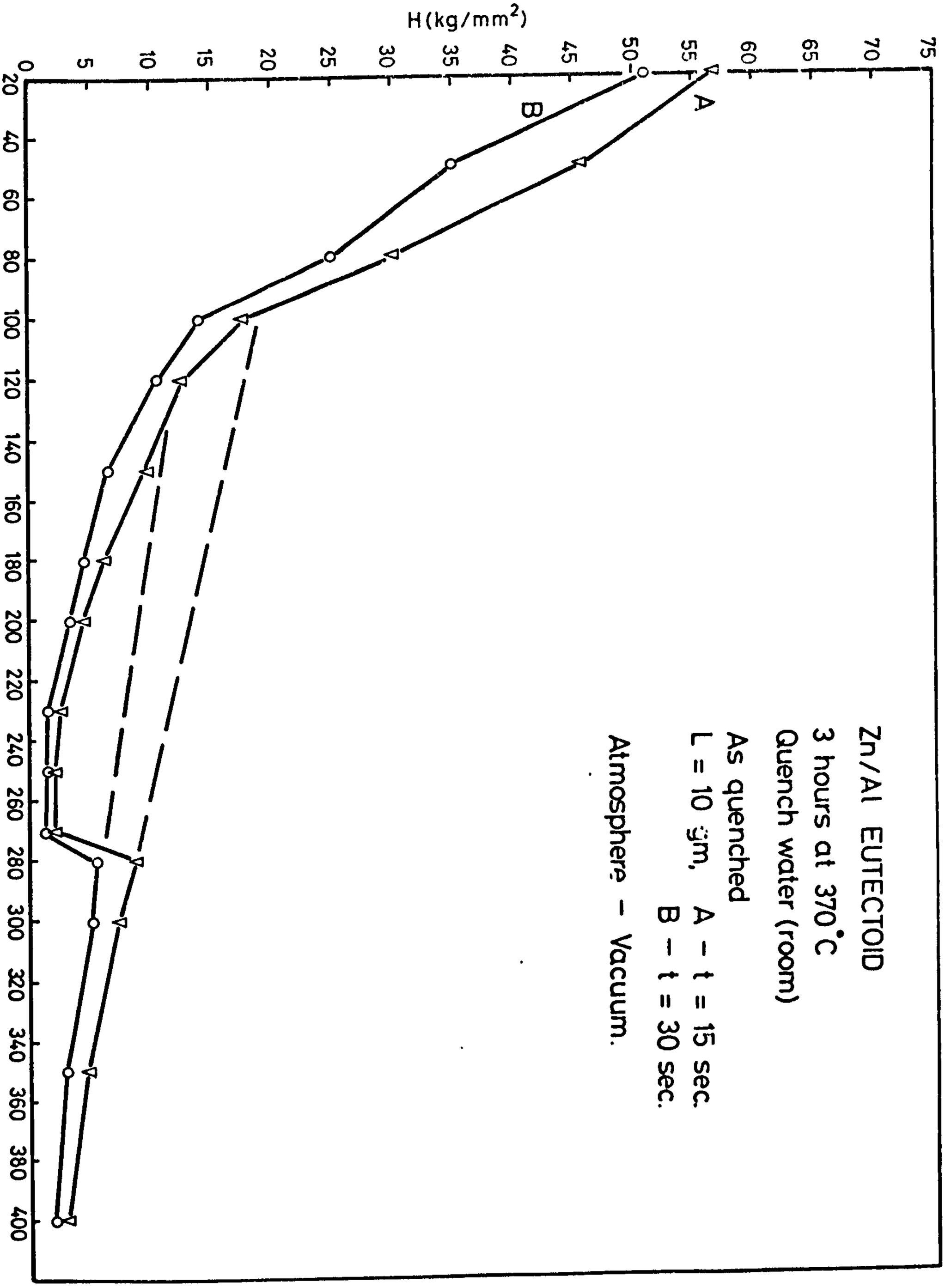
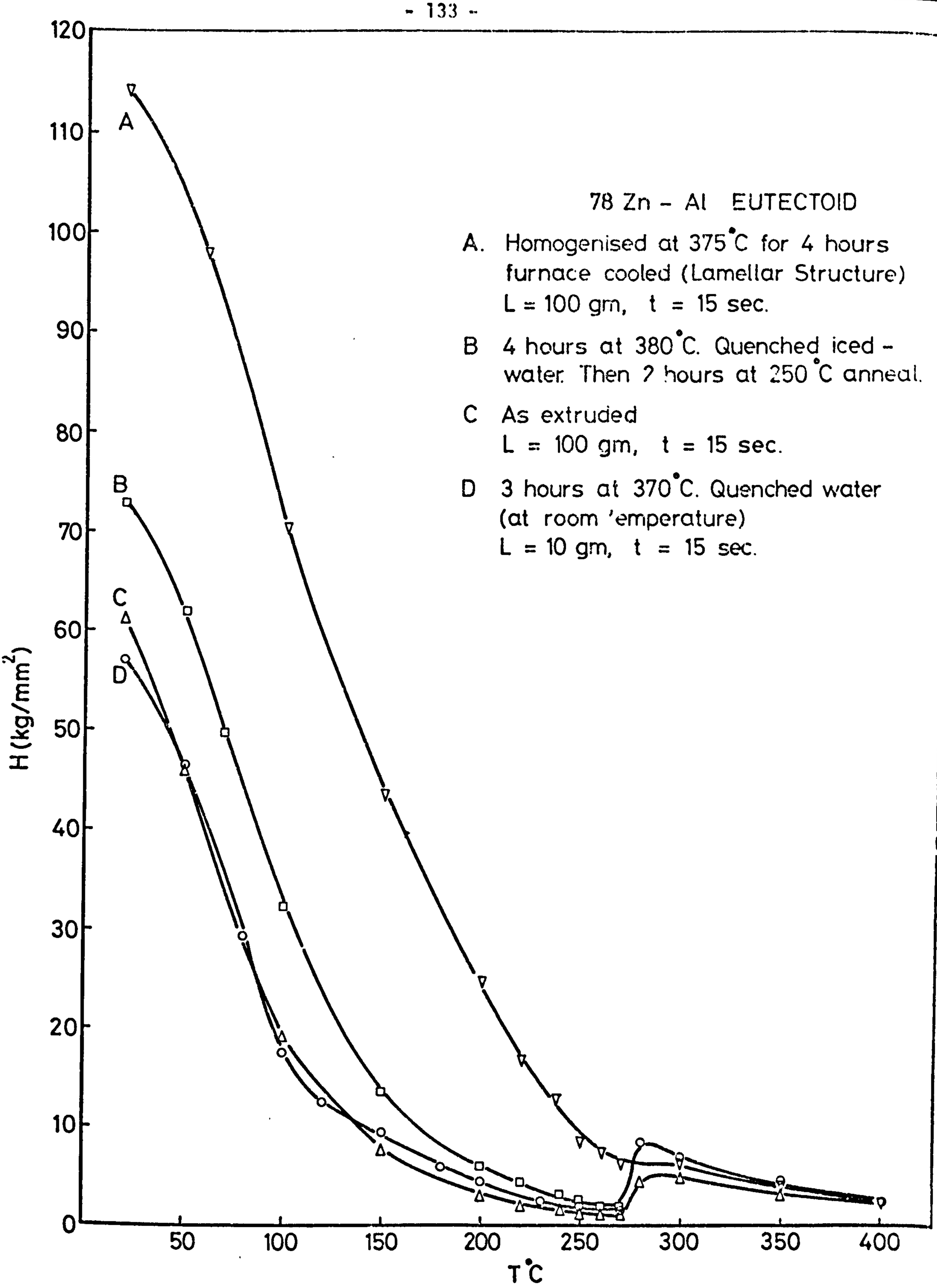

H(kg/mm²)
0
5
10
15
20
25
30
35
40
45
50
55
60
65
70
75
T°C
20
40
60
80
100
120
140
160
180
200
220
240
260
280
300
320
340
360
380
400
A
B
Zn/Al EUTECTOID
3 hours at 370°C
Quench water (room)
As quenched
L = 10 µm, A – t = 15 sec.
B – t = 30 sec.
Atmosphere – Vacuum.

Fig. 45



78 Zn – Al EUTECTOID

A. Homogenised at 375°C for 4 hours furnace cooled (Lamellar Structure) L = 100 gm, t = 15 sec.

B 4 hours at 380°C. Quenched iced – water. Then 2 hours at 250°C anneal.

C As extruded L = 100 gm, t = 15 sec.

D 3 hours at 370°C. Quenched water (at room 'emperature) L = 10 gm, t = 15 sec.

Fig. 46

78 Zn – 22 Al EUTECTOID

3 hours at 380 – 400°C
Quench ice - water
Atmosphere – Vacuum

A – L = 10 gm.
B – L = 100 gm.

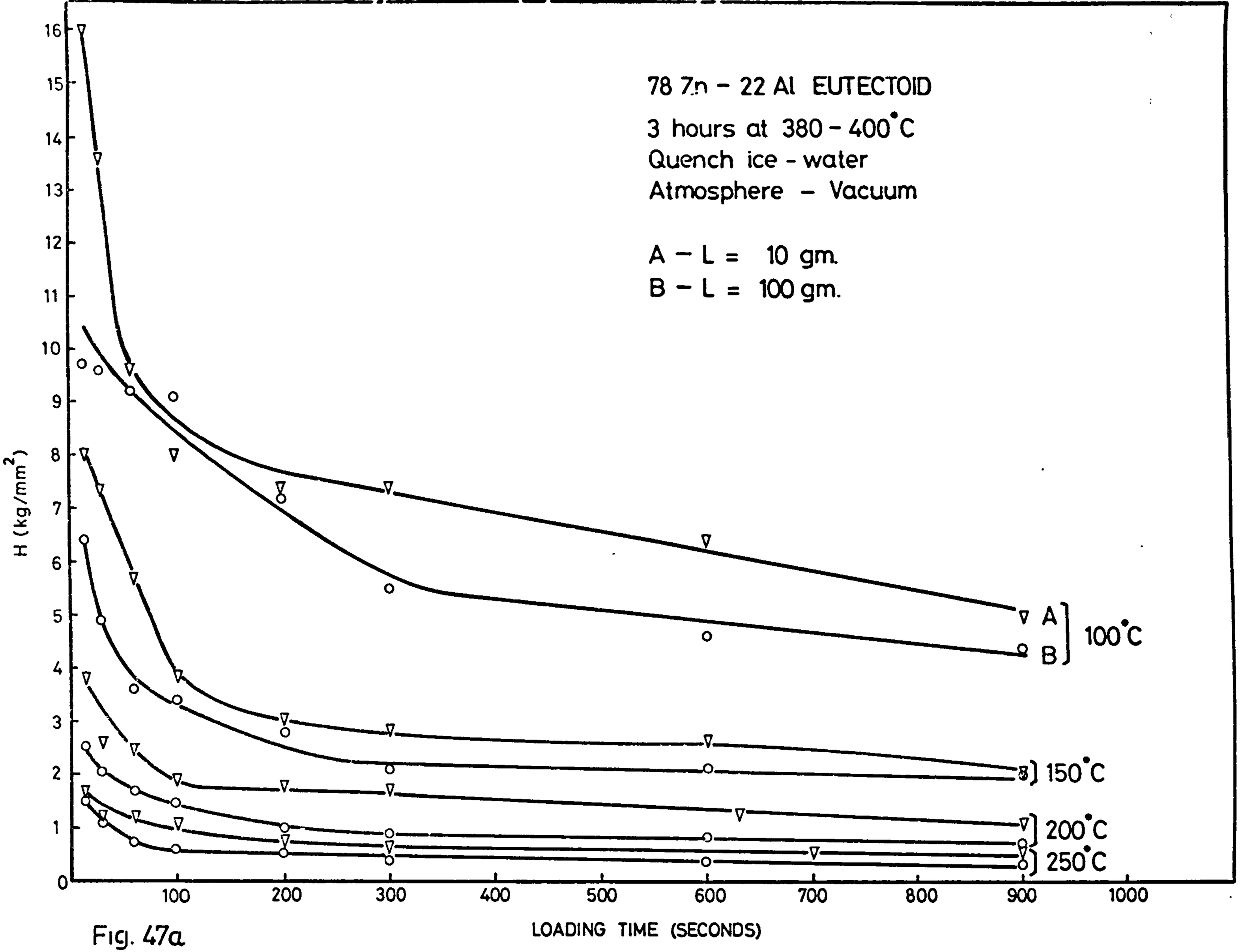


Fig. 47a

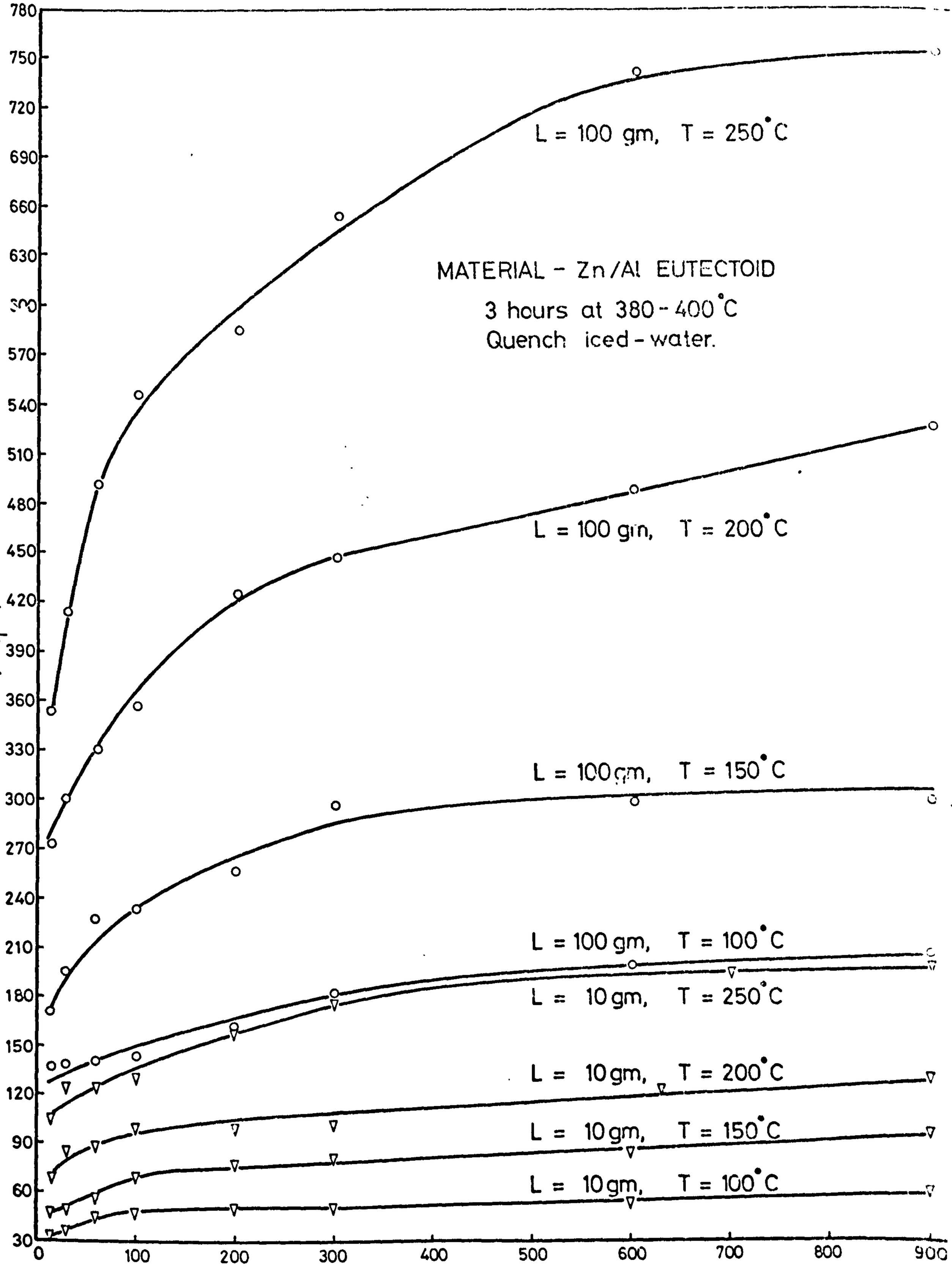

L = 100 gm, T = 250°C
MATERIAL - Zn/Al EUTECTOID
3 hours at 380 - 400°C
Quench iced - water.
L = 100 gm, T = 200°C
L = 100 gm, T = 150°C
L = 100 gm, T = 100°C
L = 10 gm, T = 250°C
L = 10 gm, T = 200°C
L = 10 gm, T = 150°C
L = 10 gm, T = 100°C
INDENTATION DIAMETER, d (μm)
780
750
720
690
660
630
600
570
540
510
480
450
420
390
360
330
300
270
240
210
180
150
120
90
60
30
0
100
200
300
400
500
600
700
800
900
LOADING TIME, t (seconds)

Fig. 47b

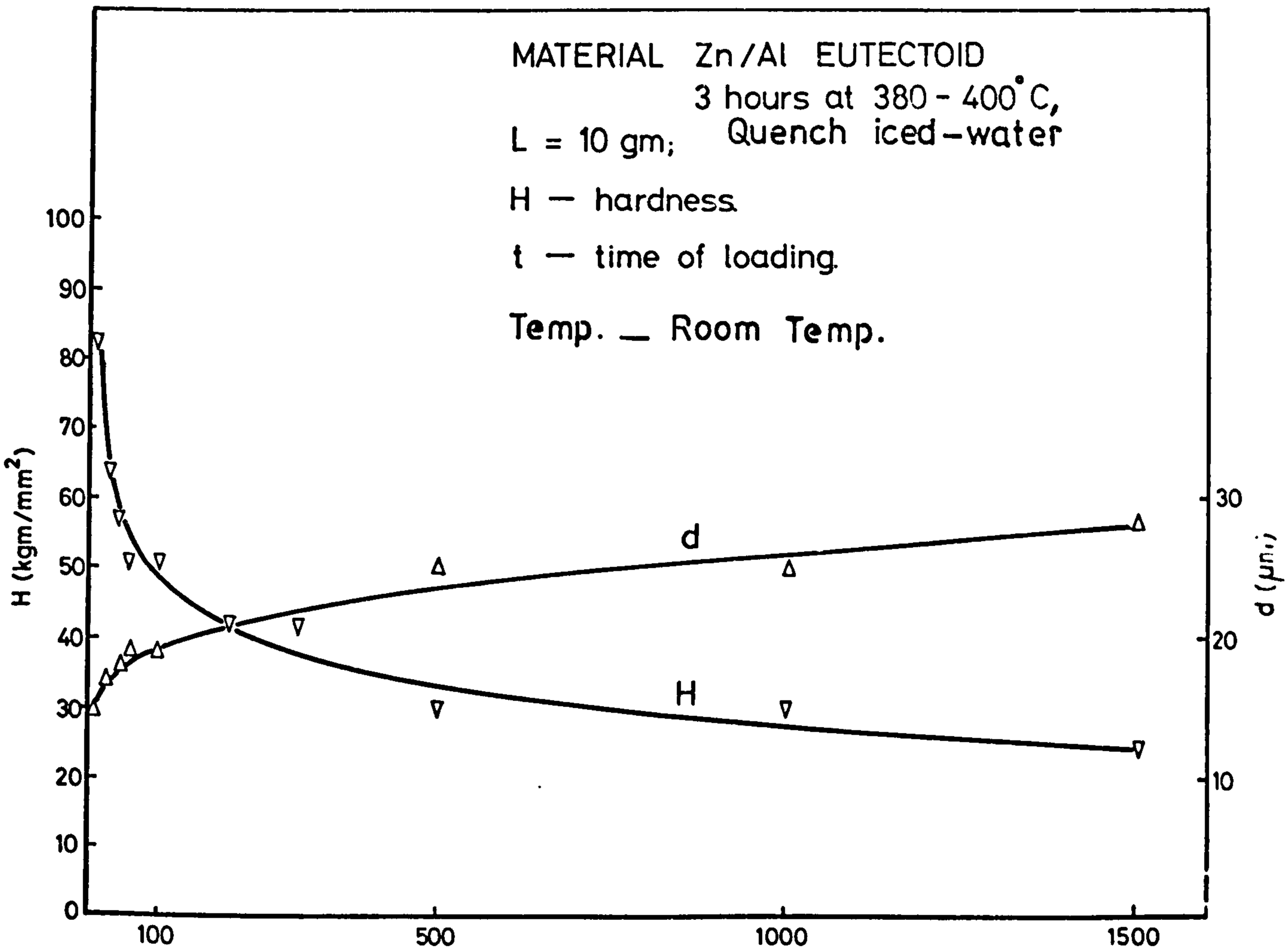

MATERIAL Zn/Al EUTECTOID
3 hours at 380 - 400°C,
L = 10 gm; Quench iced-water
H — hardness
t — time of loading
Temp. — Room Temp.
H (kgm/mm²)
d (μm)
t (sec)
d
H
100
90
80
70
60
50
40
30
20
10
0
30
20
10
100
500
1000
1500

Fig. 48

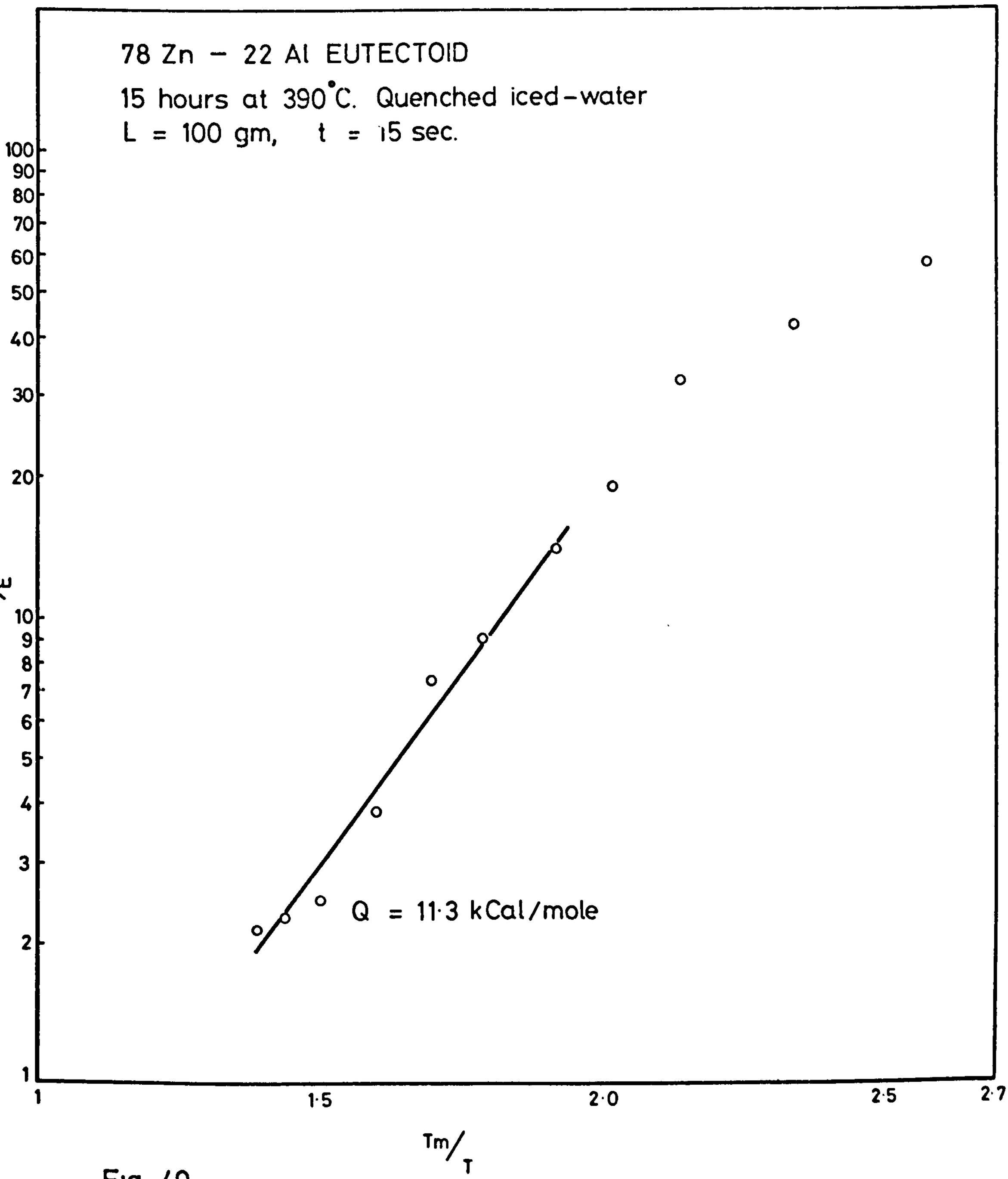

78 Zn – 22 Al EUTECTOID
15 hours at 390°C. Quenched iced-water
L = 100 gm, t = 15 sec.
H/E × 10⁻⁴
100
90
80
70
60
50
40
30
20
10
9
8
7
6
5
4
3
2
1
1
1·5
2·0
2·5
2·7
Tm/T
Q = 11·3 kCal/mole

Fig. 49

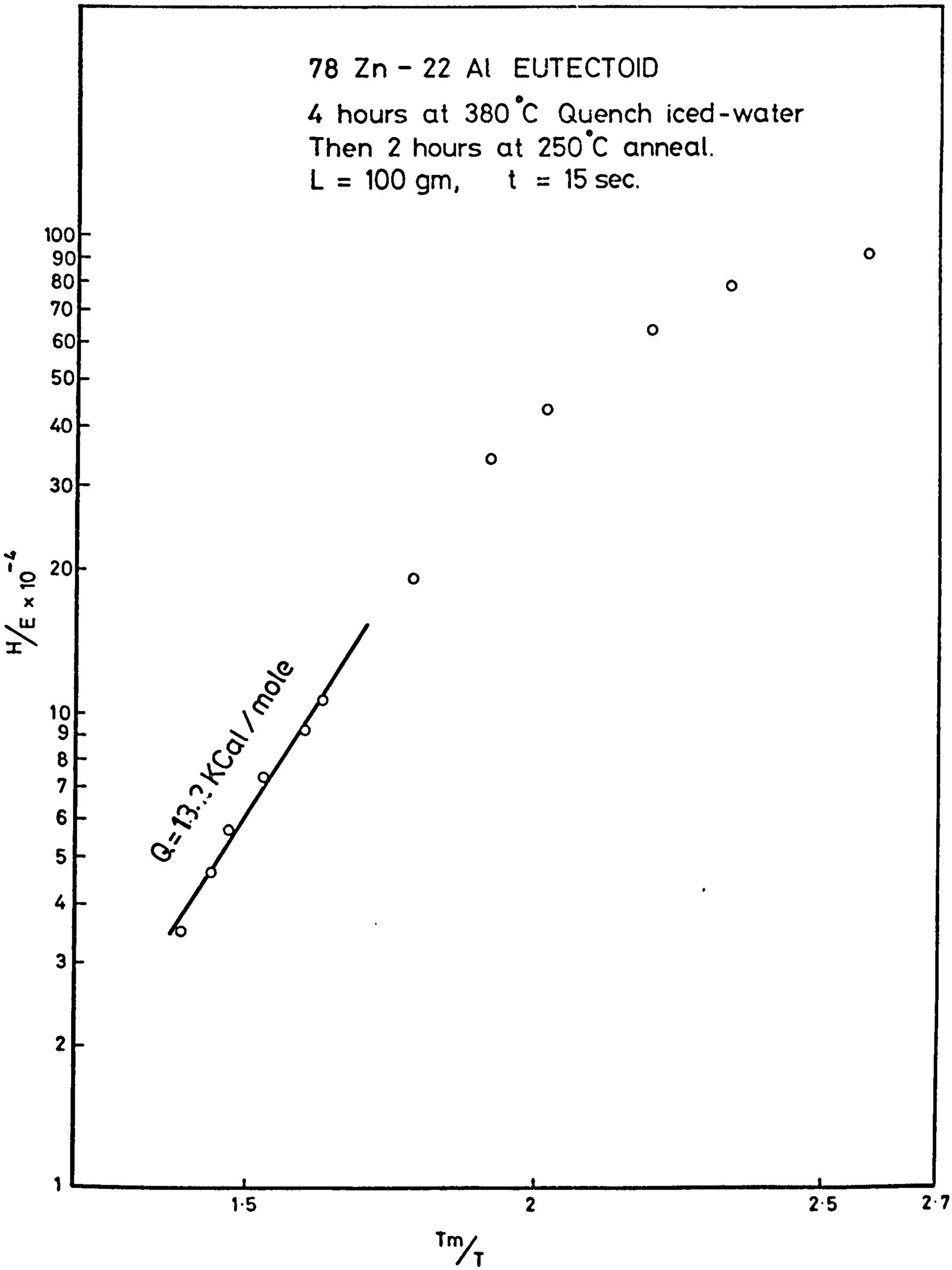

78 Zn - 22 Al EUTECTOID
4 hours at 380°C Quench iced-water
Then 2 hours at 250°C anneal.
L = 100 gm, t = 15 sec.
H/E x 10^-4
100
90
80
70
60
50
40
30
20
10
9
8
7
6
5
4
3
2
1
Q=13.2 KCal/mole
1·5
2
2·5
2·7
Tm/T

Fig. 50

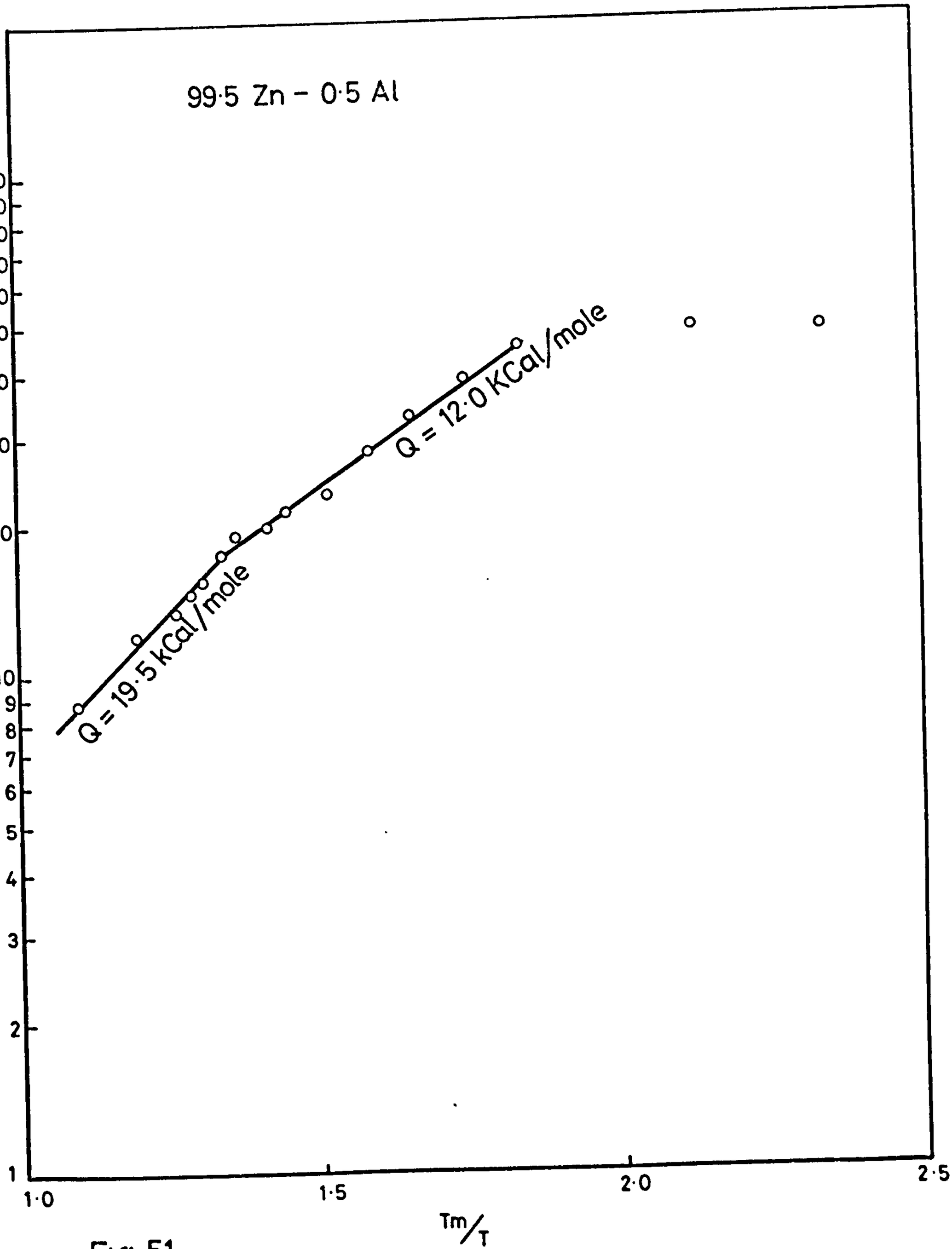

99·5 Zn – 0·5 Al
100
90
80
70
60
50
40
30
20
10
9
8
7
6
5
4
3
2
1
H/E × 10⁻⁴
Q = 12·0 KCal/mole
Q = 19·5 kCal/mole
1·0
1·5
2·0
2·5
Tm/T

Fig. 51

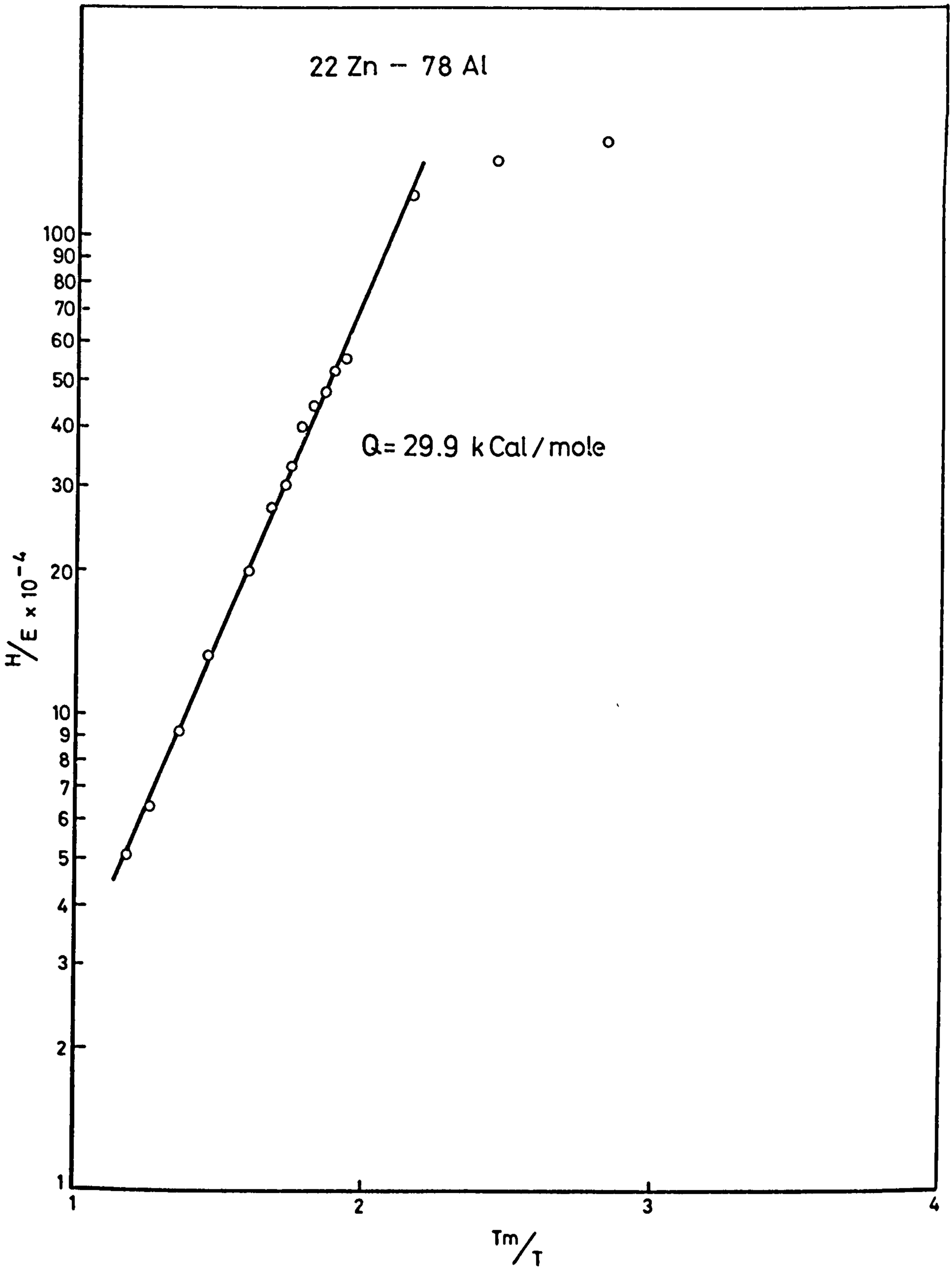

22 Zn – 78 Al
Q= 29.9 k Cal / mole
H/E x 10⁻⁴
100
90
80
70
60
50
40
30
20
10
9
8
7
6
5
4
3
2
1
1
2
3
4
Tm/T

Fig. 52

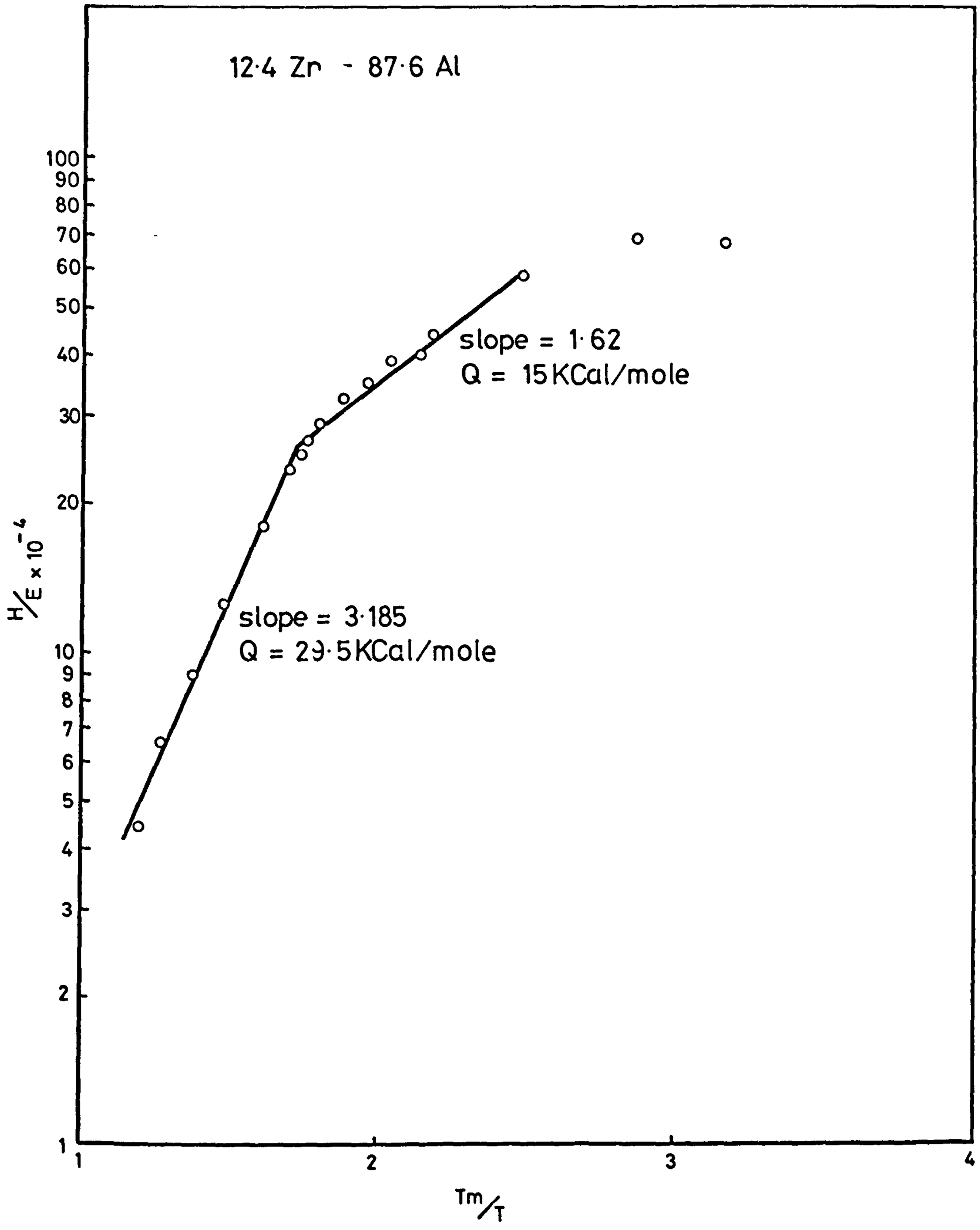

12·4 Zr - 87·6 Al
100
90
80
70
60
50
40
30
20
10
9
8
7
6
5
4
3
2
1
H/E x 10^-4
slope = 1·62
Q = 15 KCal/mole
slope = 3·185
Q = 29·5 KCal/mole
1
2
3
4
Tm/T

Fig. 53

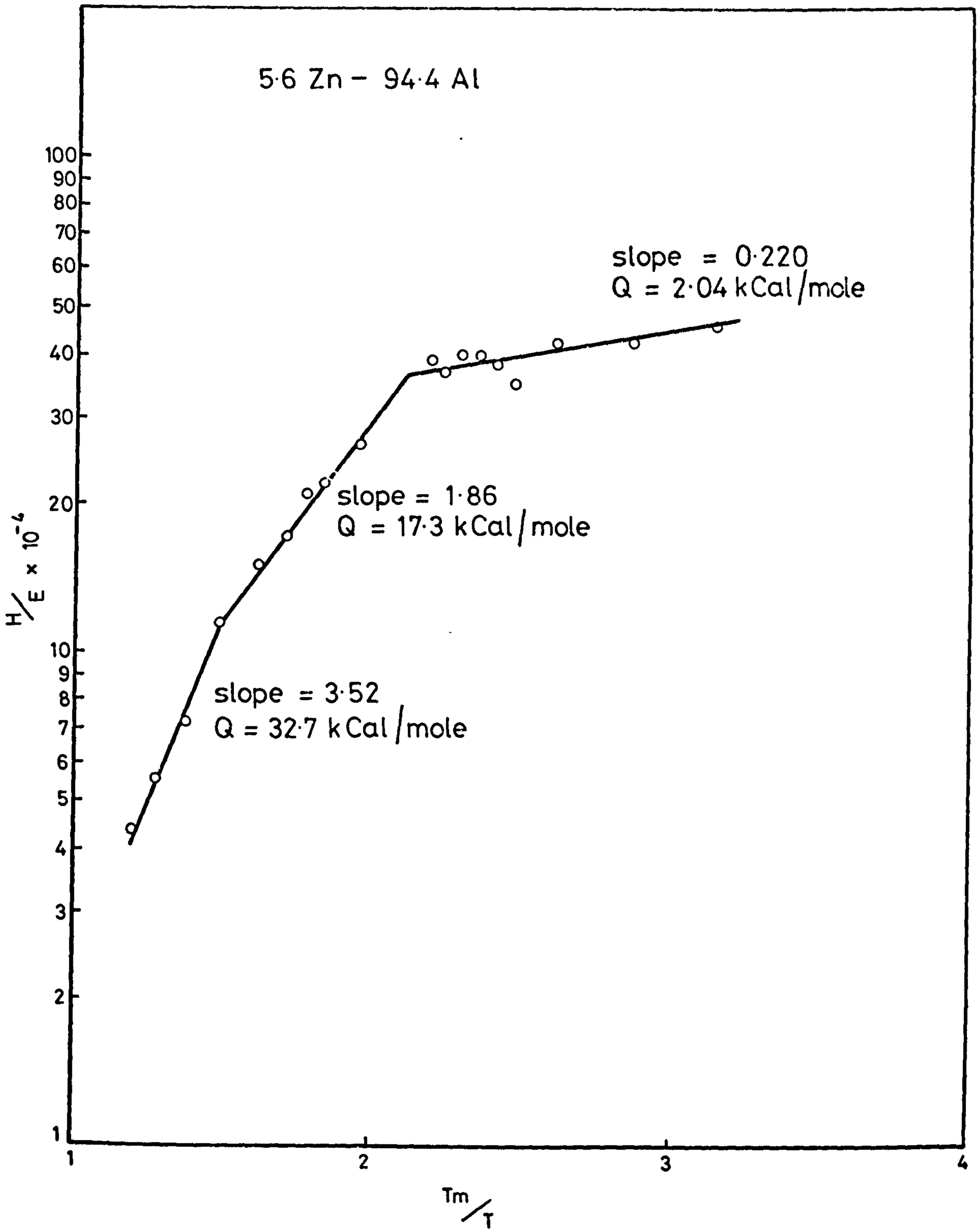

5·6 Zn – 94·4 Al
slope = 0·220
Q = 2·04 kCal/mole
slope = 1·86
Q = 17·3 kCal/mole
slope = 3·52
Q = 32·7 kCal/mole
H/E x 10⁻⁴
Tm/T
100
90
80
70
60
50
40
30
20
10
9
8
7
6
5
4
3
2
1
1
2
3
4

Fig. 54

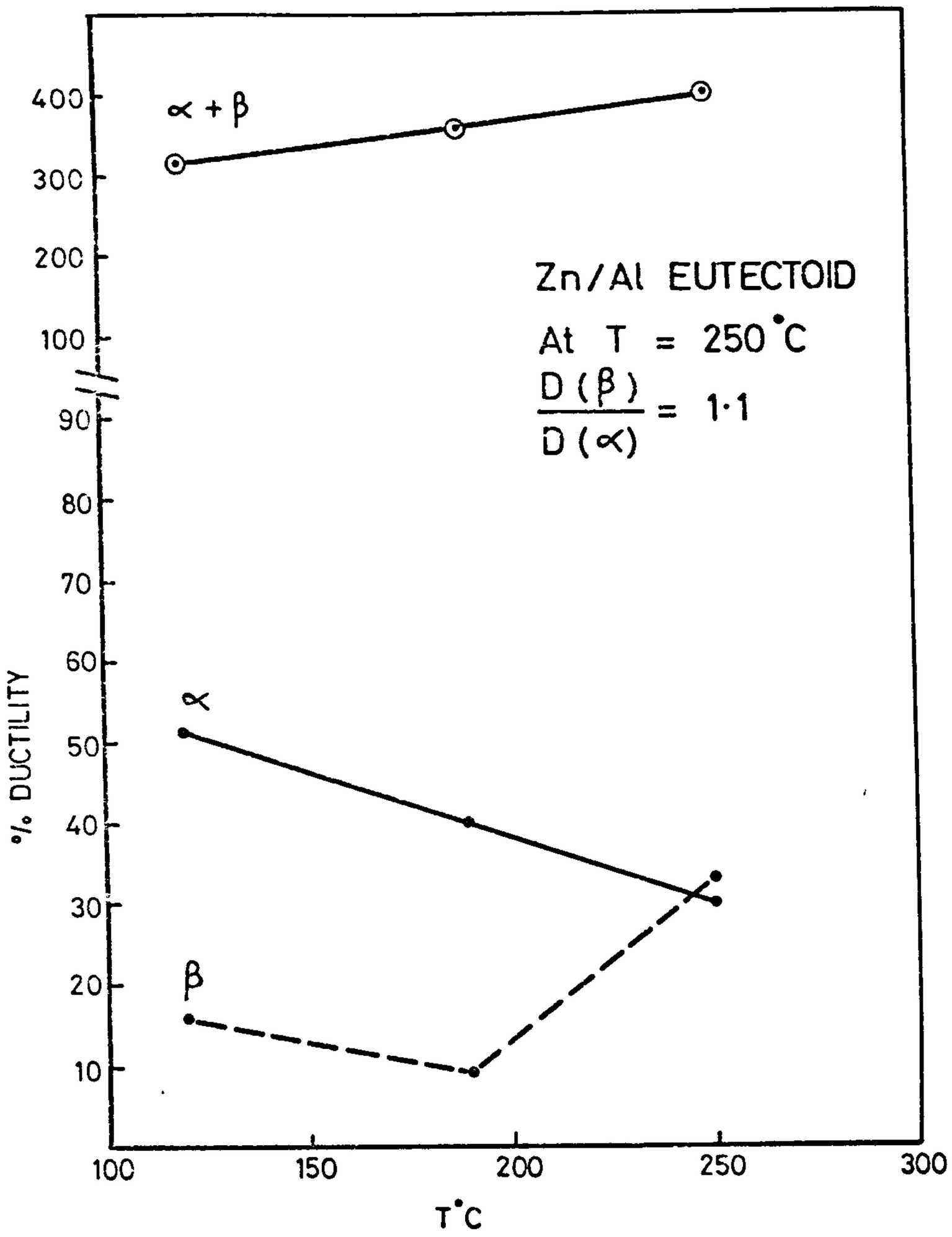


Fig. 55a

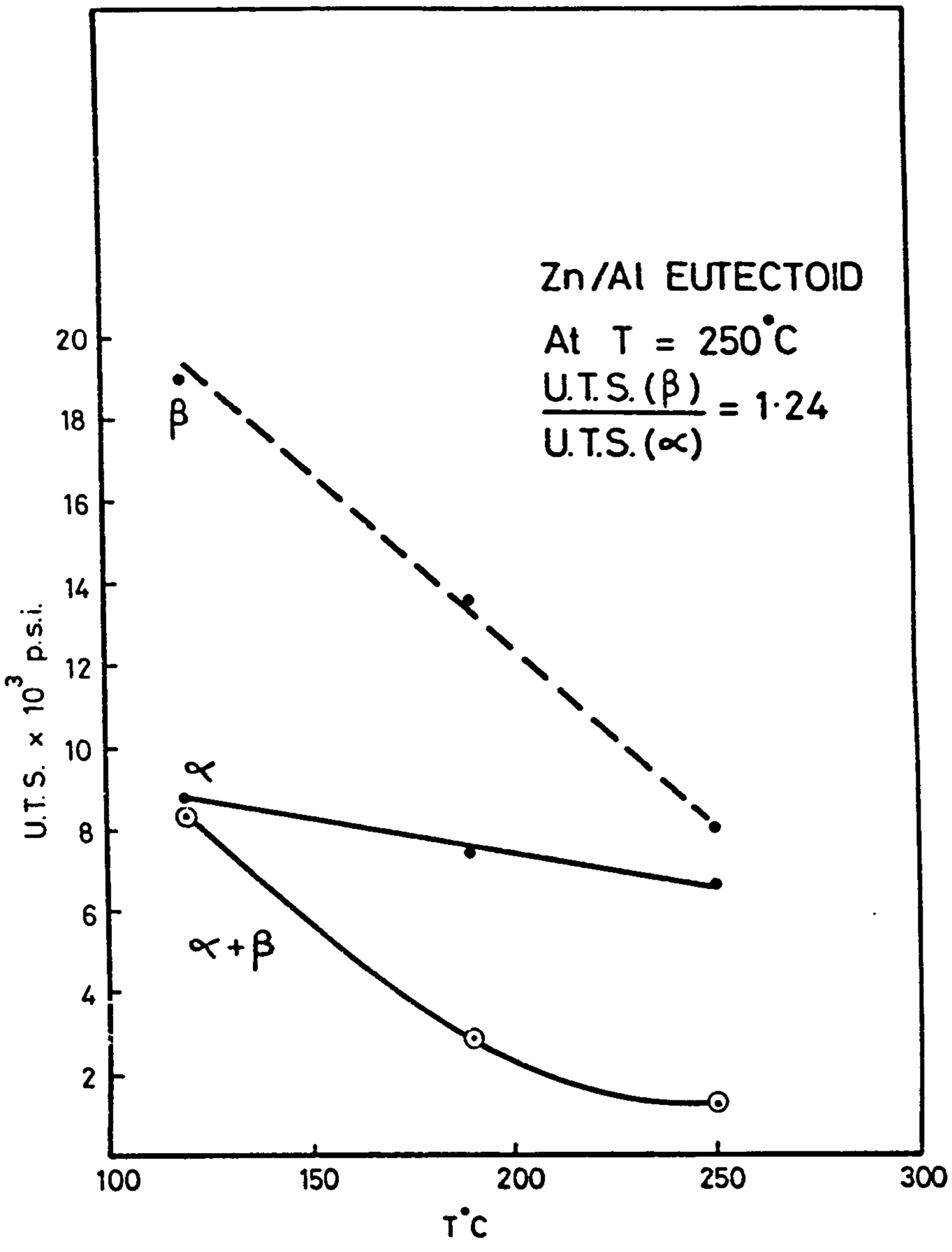


Fig. 55b

A → measured by vibration technique.
B → calculated from :
$E = N_{Al}\ E_{Al} + N_{Zn}\ E_{Zn}$ where N_{Al} and N_{Zn} are the atomic fractions and E_{Al} and E_{Zn} are the values of the Young's modulus for the pure Al and Zn respectively, taken from Köster.[199]

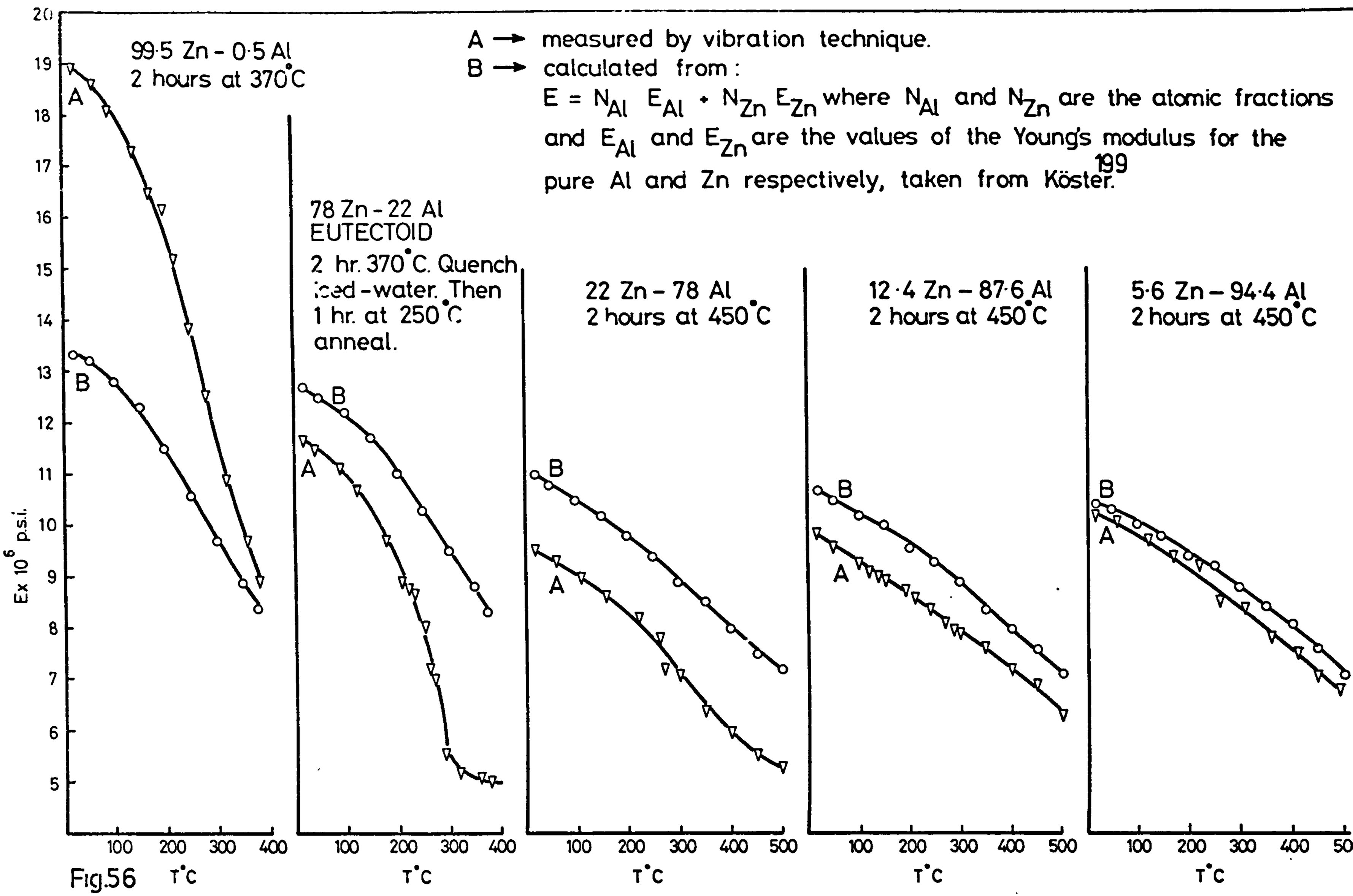


Fig.56

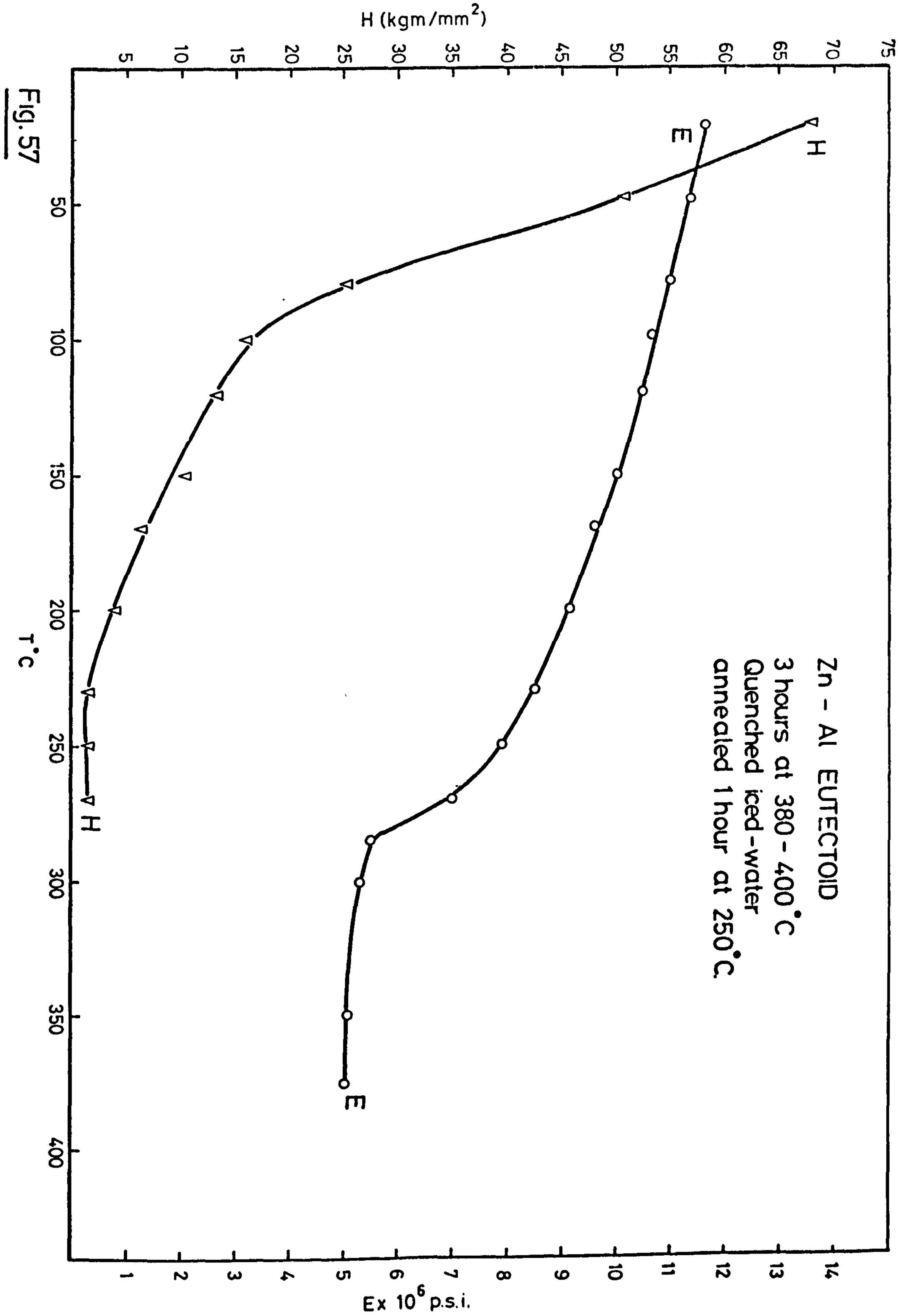

H (kgm/mm²)
5
10
15
20
25
30
35
40
45
50
55
60
65
70
75
T°c
50
100
150
200
250
300
350
400
H
E
H
E
Zn - Al EUTECTOID
3 hours at 380 - 400°C
Quenched iced-water
annealed 1 hour at 250°C.
1
2
3
4
5
6
7
8
9
10
11
12
13
14
Ex 10⁶ p.s.i.

Fig. 57

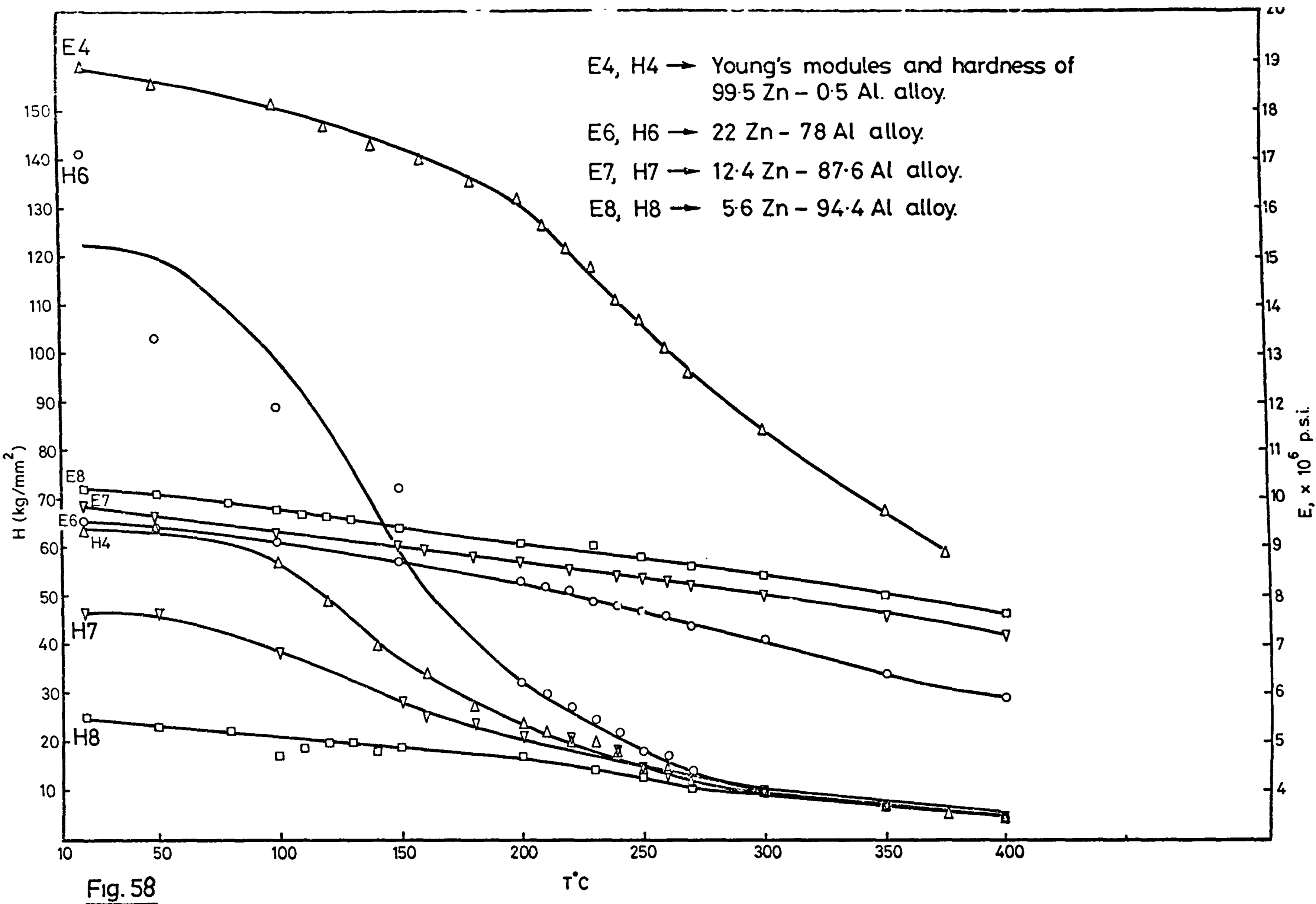

E4, H4 → Young's modules and hardness of 99·5 Zn – 0·5 Al. alloy.
E6, H6 → 22 Zn – 78 Al alloy.
E7, H7 → 12·4 Zn – 87·6 Al alloy.
E8, H8 → 5·6 Zn – 94·4 Al alloy.
E4
H6
E8
E7
E6
H4
H7
H8
H (kg/mm²)
E, x 10⁶ p.s.i.
T°C
10
50
100
150
200
250
300
350
400

Fig. 58

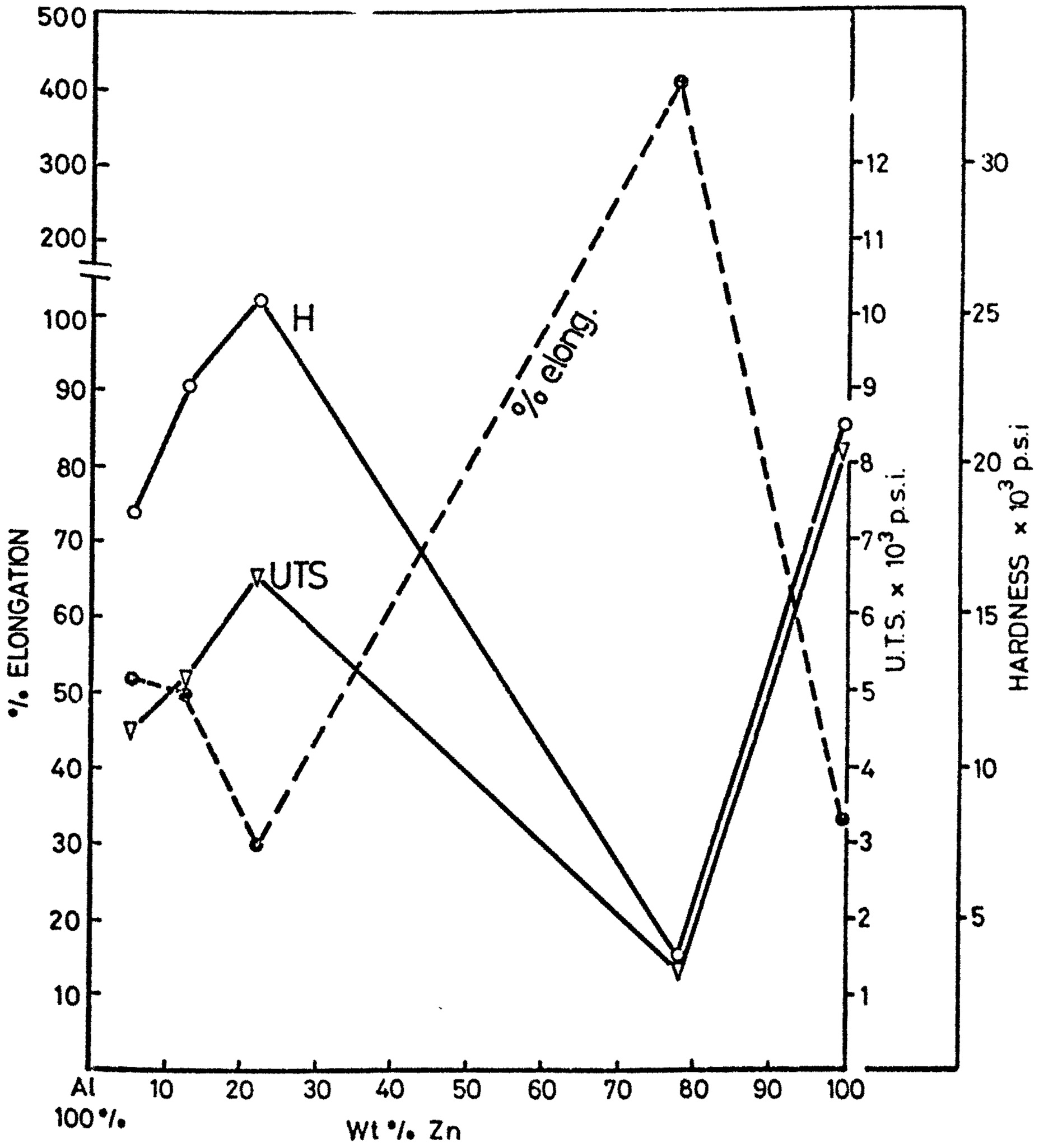

500
400
300
200
100
90
80
70
60
50
40
30
20
10
H
UTS
% elong.
% ELONGATION
12
11
10
9
8
7
6
5
4
3
2
1
U.T.S. × 10³ p.s.i.
30
25
20
15
10
5
HARDNESS × 10³ p.s.i
Al
10
20
30
40
50
60
70
80
90
100
100 %
Wt % Zn

Fig. 59

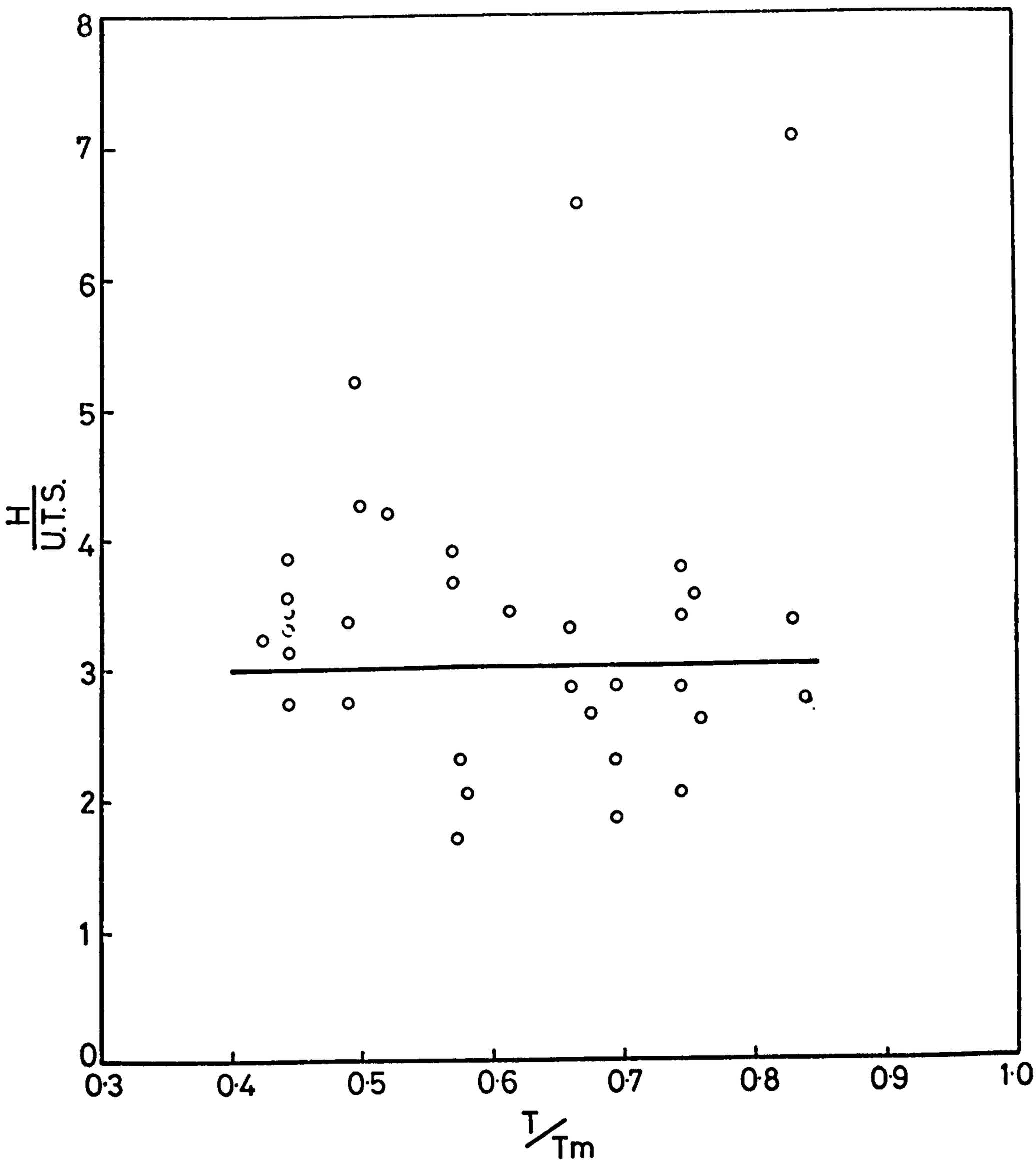


Fig. 60

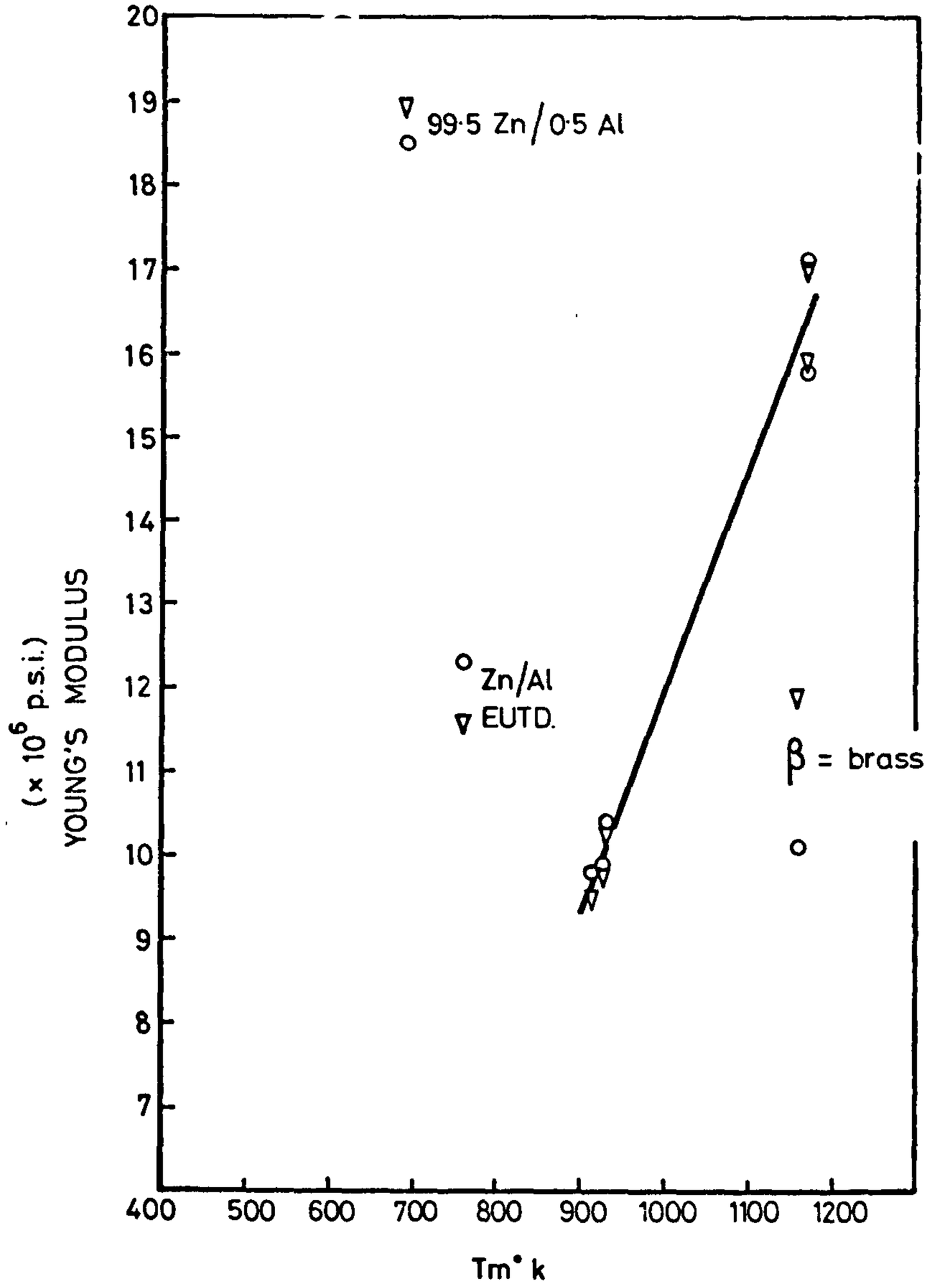

99·5 Zn/0·5 Al
Zn/Al
EUTD.
β = brass
YOUNG'S MODULUS (× 10^6 p.s.i.)
20
19
18
17
16
15
14
13
12
11
10
9
8
7
400
500
600
700
800
900
1000
1100
1200
Tm° k

Fig. 61

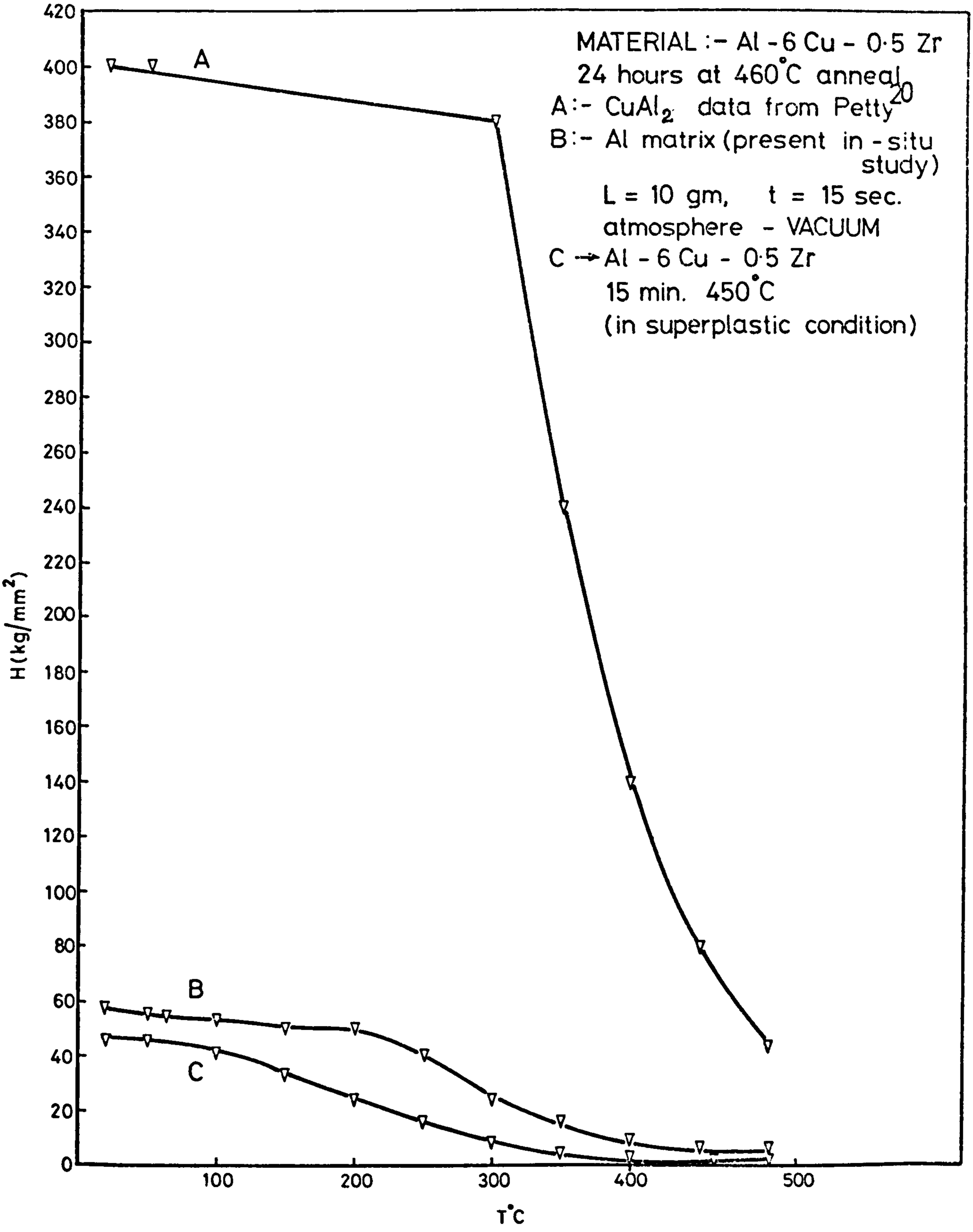

MATERIAL :- Al - 6 Cu - 0·5 Zr
24 hours at 460°C anneal
A :- $CuAl_2$ data from Petty[20]
B :- Al matrix (present in - situ study)
L = 10 gm, t = 15 sec.
atmosphere - VACUUM
C → Al - 6 Cu - 0·5 Zr
15 min. 450°C
(in superplastic condition)
A
B
C
H(kg/mm²)
T°C
420
400
380
360
340
320
300
280
260
240
220
200
180
160
140
120
100
80
60
40
20
0
100
200
300
400
500

Fig. 62

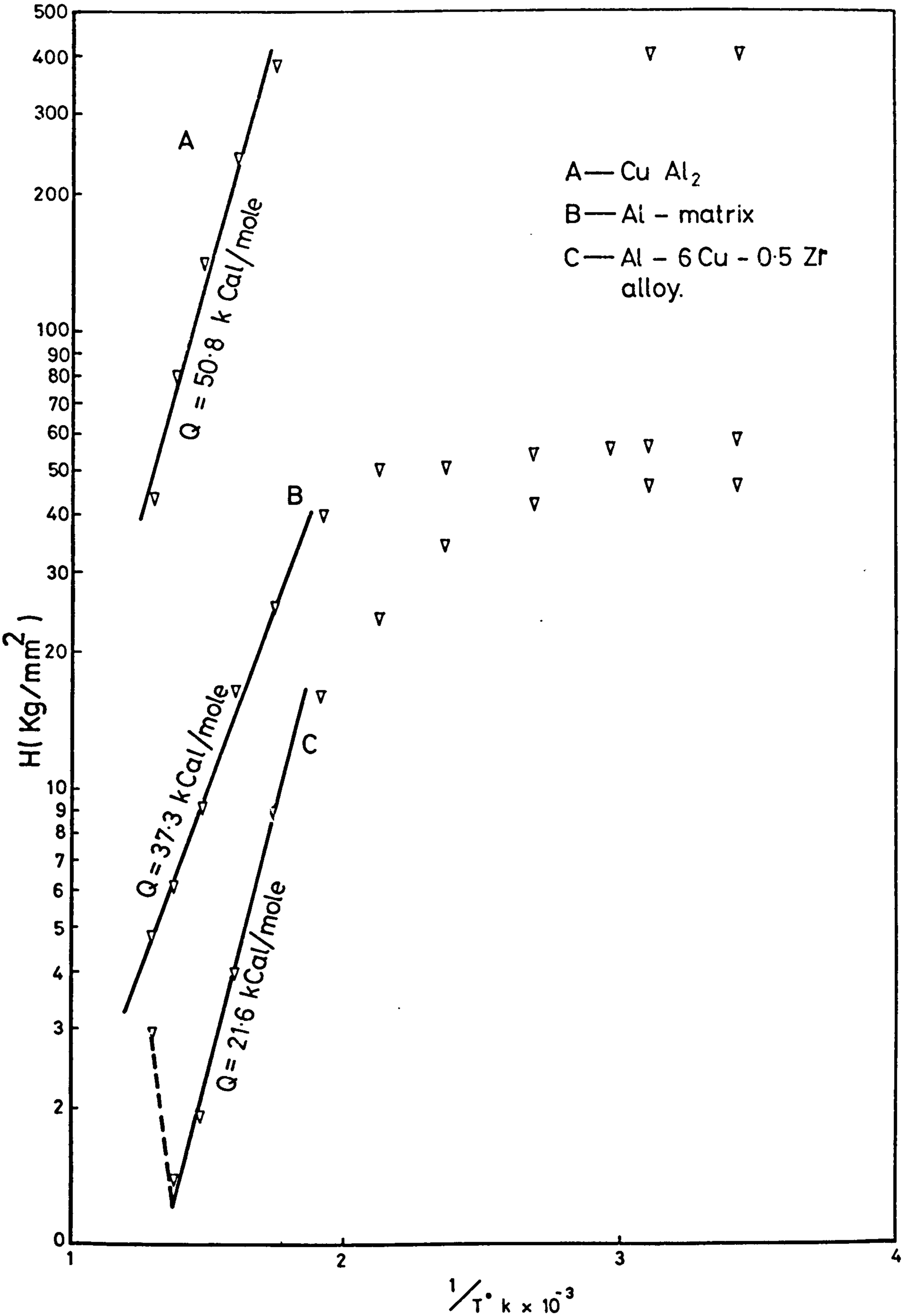
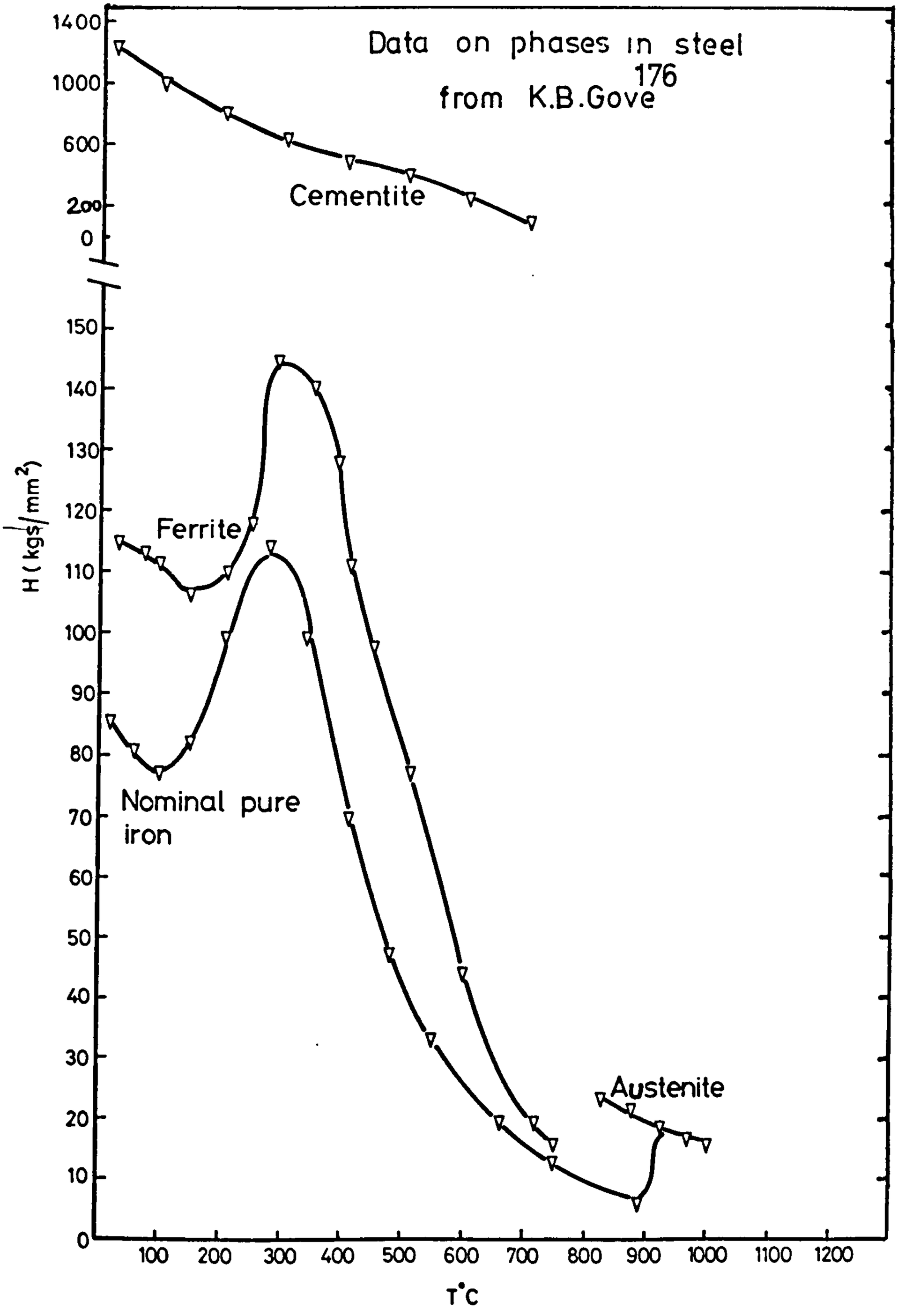

A
B
C
Q = 50.8 k Cal/mole
Q = 37.3 kCal/mole
Q = 21.6 kCal/mole
A— Cu Al2
B— Al – matrix
C— Al – 6 Cu - 0·5 Zr alloy.
H(Kg/mm2)
1/T° k x 10-3
500
400
300
200
100
90
80
70
60
50
40
30
20
10
9
8
7
6
5
4
3
2
0
1
2
3
4

Fig. 63

Fig. 64


Data on phases in steel
176
from K.B.Gove
Cementite
Ferrite
Nominal pure iron
Austenite
H (kgs/mm²)
T°C
1400
1000
600
200
0
150
140
130
120
110
100
90
80
70
60
50
40
30
20
10
0
100
200
300
400
500
600
700
800
900
1000
1100
1200

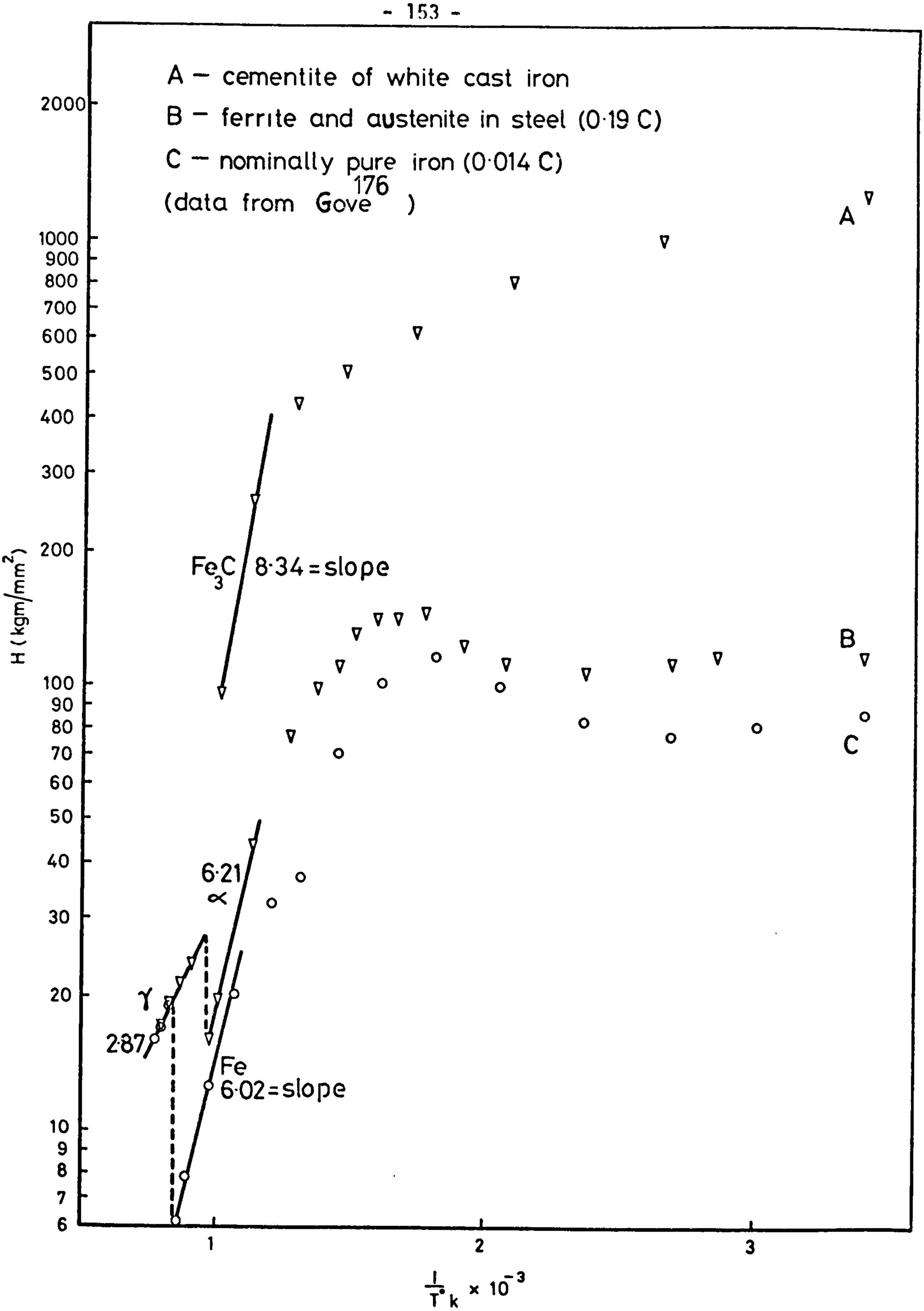
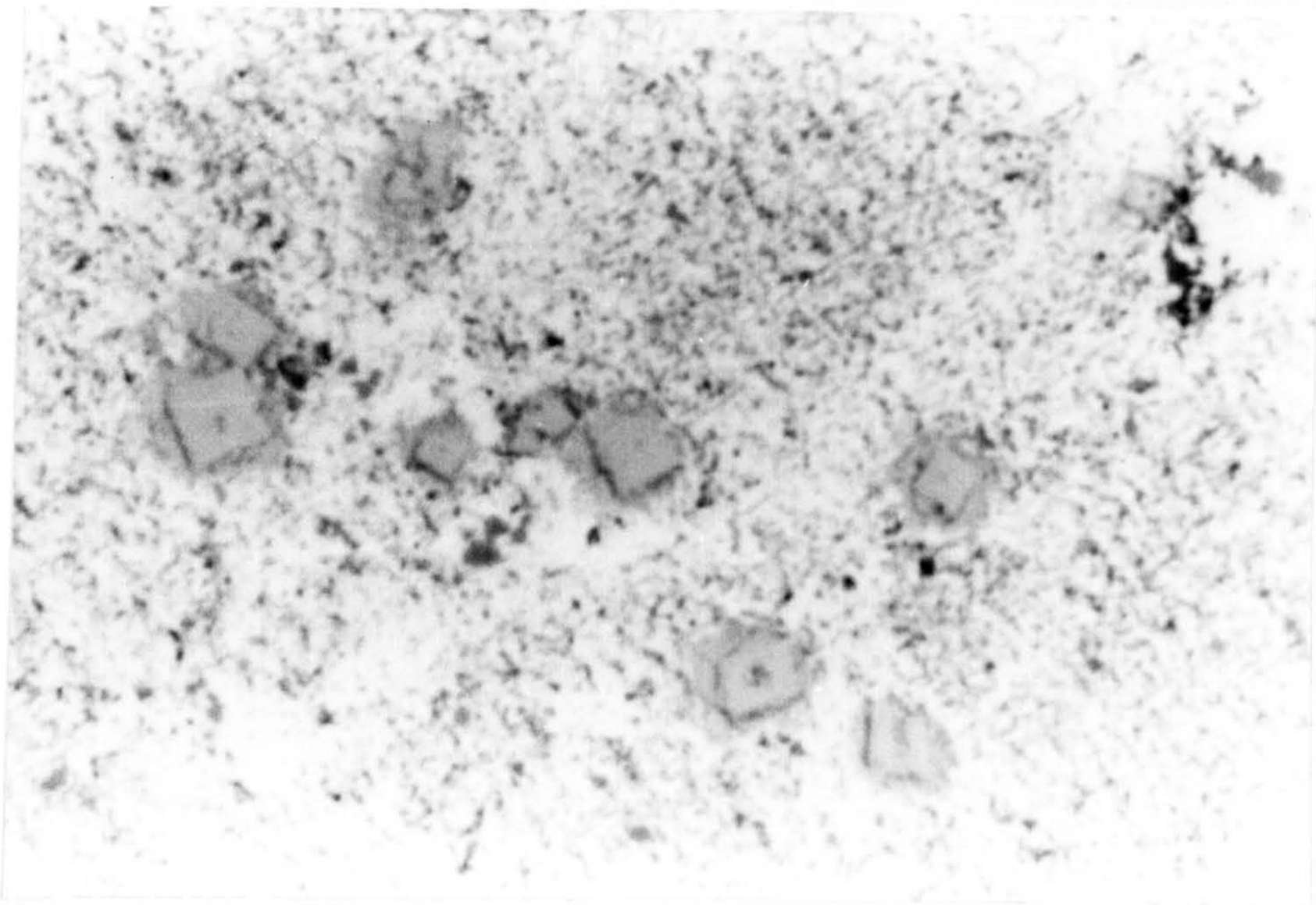

A – cementite of white cast iron
B – ferrite and austenite in steel (0·19 C)
C – nominally pure iron (0·014 C)
(data from Gove[176])
A
B
C
Fe3C 8·34 = slope
6·21
α
γ
2·87
Fe
6·02 = slope
H (kgm/mm²)
2000
1000
900
800
700
600
500
400
300
200
100
90
80
70
60
50
40
30
20
10
9
8
7
6
1
2
3
1/T°k × 10⁻³

Fig. 65

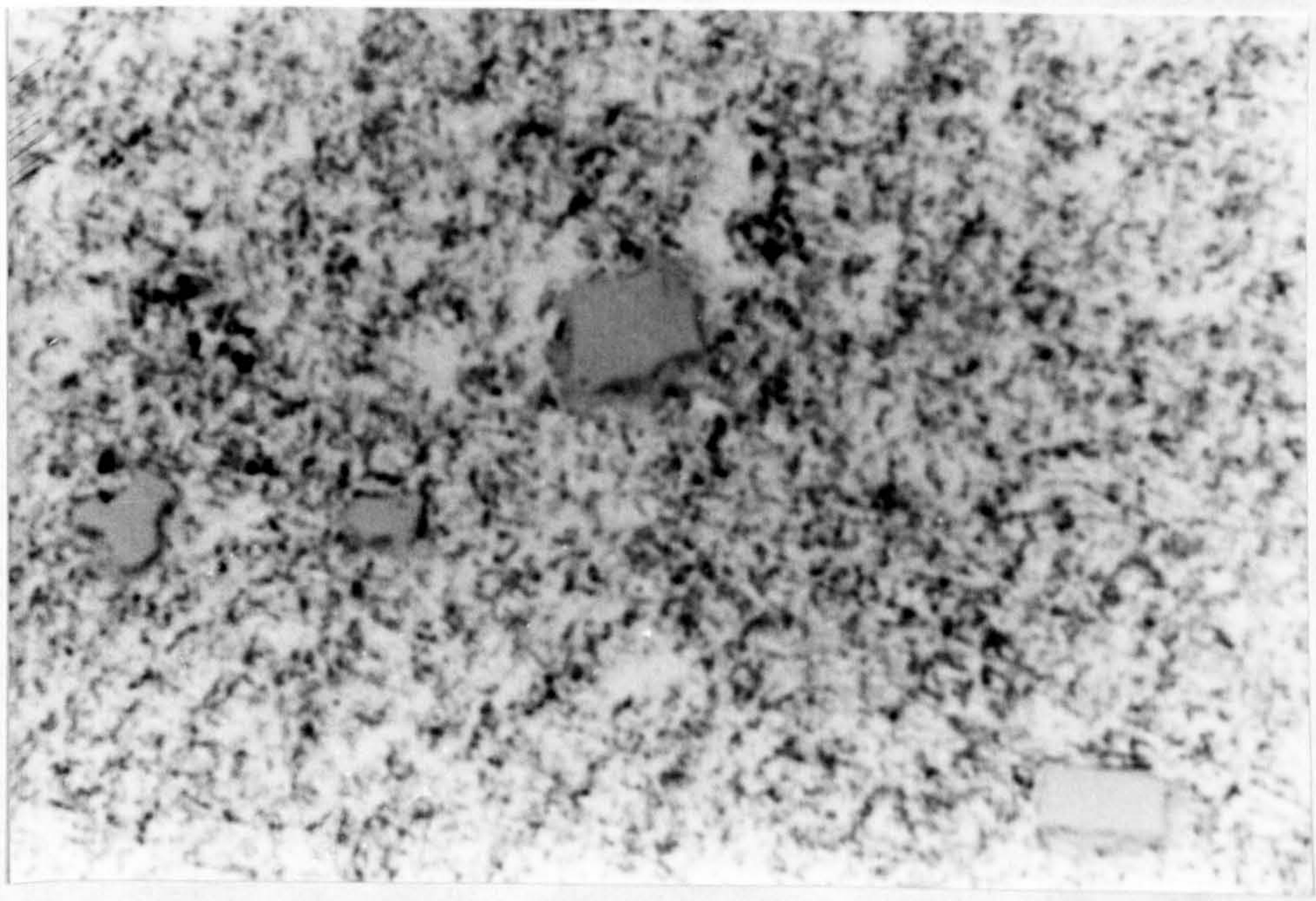


Fig 66. Optical micrograph of Zn/Al eutectoid deformed superplastically to 400% at 250°C (∿ 0.7 Tm), $\dot{\varepsilon} = 1.6 \times 10^{-3} sec^{-1}$. There is little cavitation. The $FeAl_3$ type inclusions are shown. Tensile axis vertical.



X2000

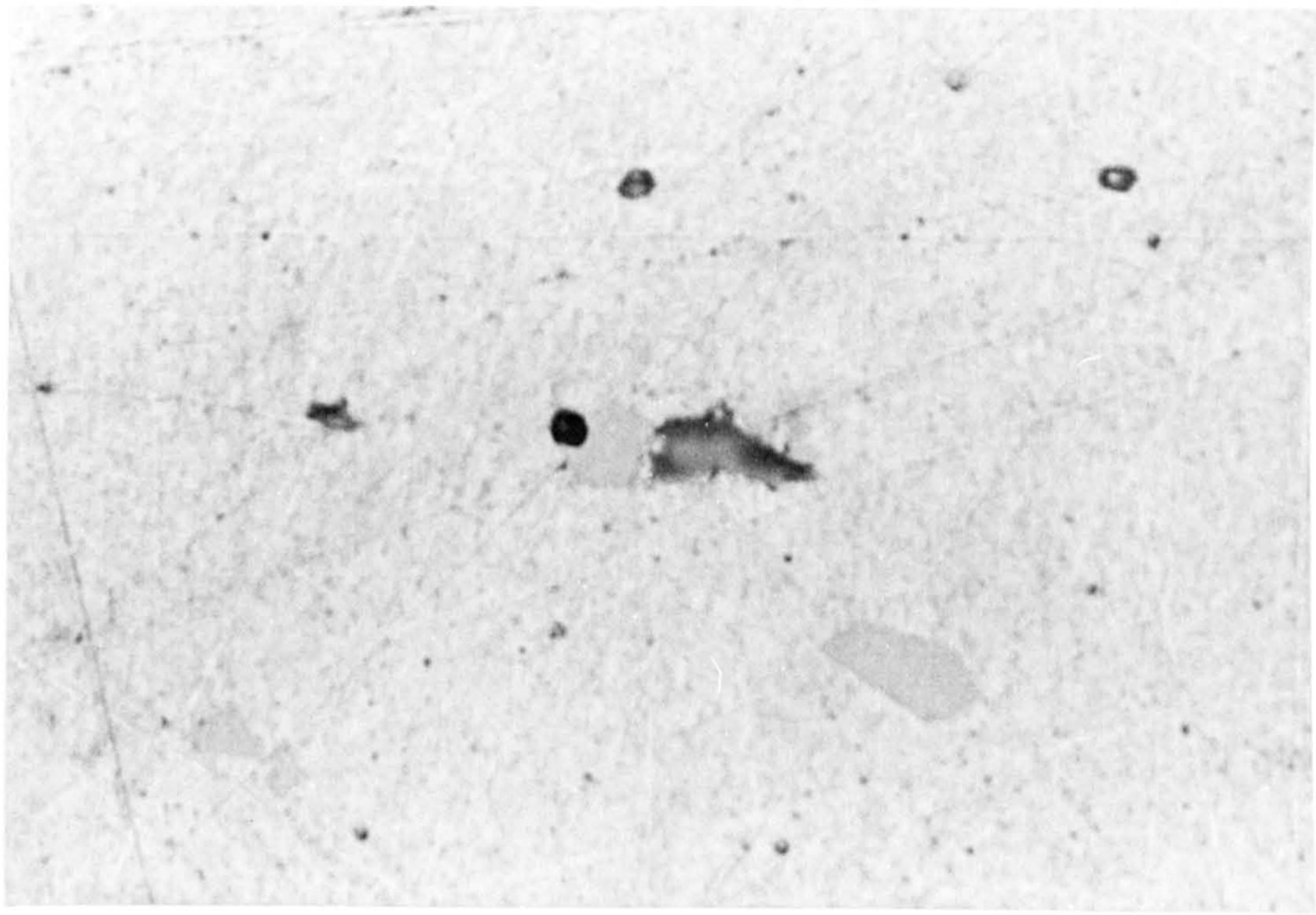
Fig 67. Optical micrograph of Zn/Al eutectoid in the as-received condition, showing the presence of $FeAl_3$ type inclusions.



X2500

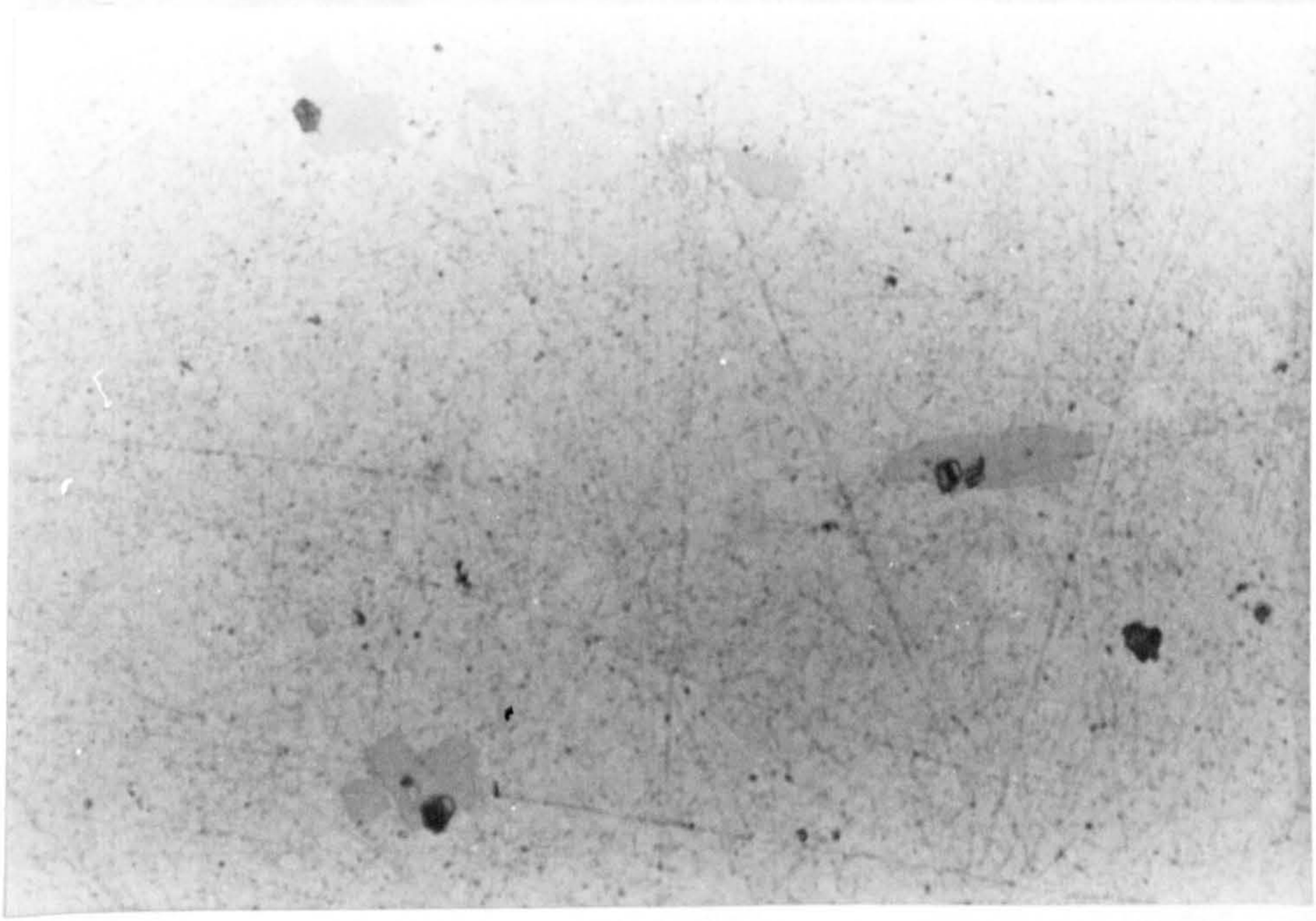
Fig 68. Optical micrograph of Zn/Al eutectoid after 400 pct superplastic deformation at 250°C (∿ 0.7 Tm) showing that the $FeAl_3$ type inclusions neither changed in shape nor cracked during deformation. Tensile axis is horizontal.

(a)



X800

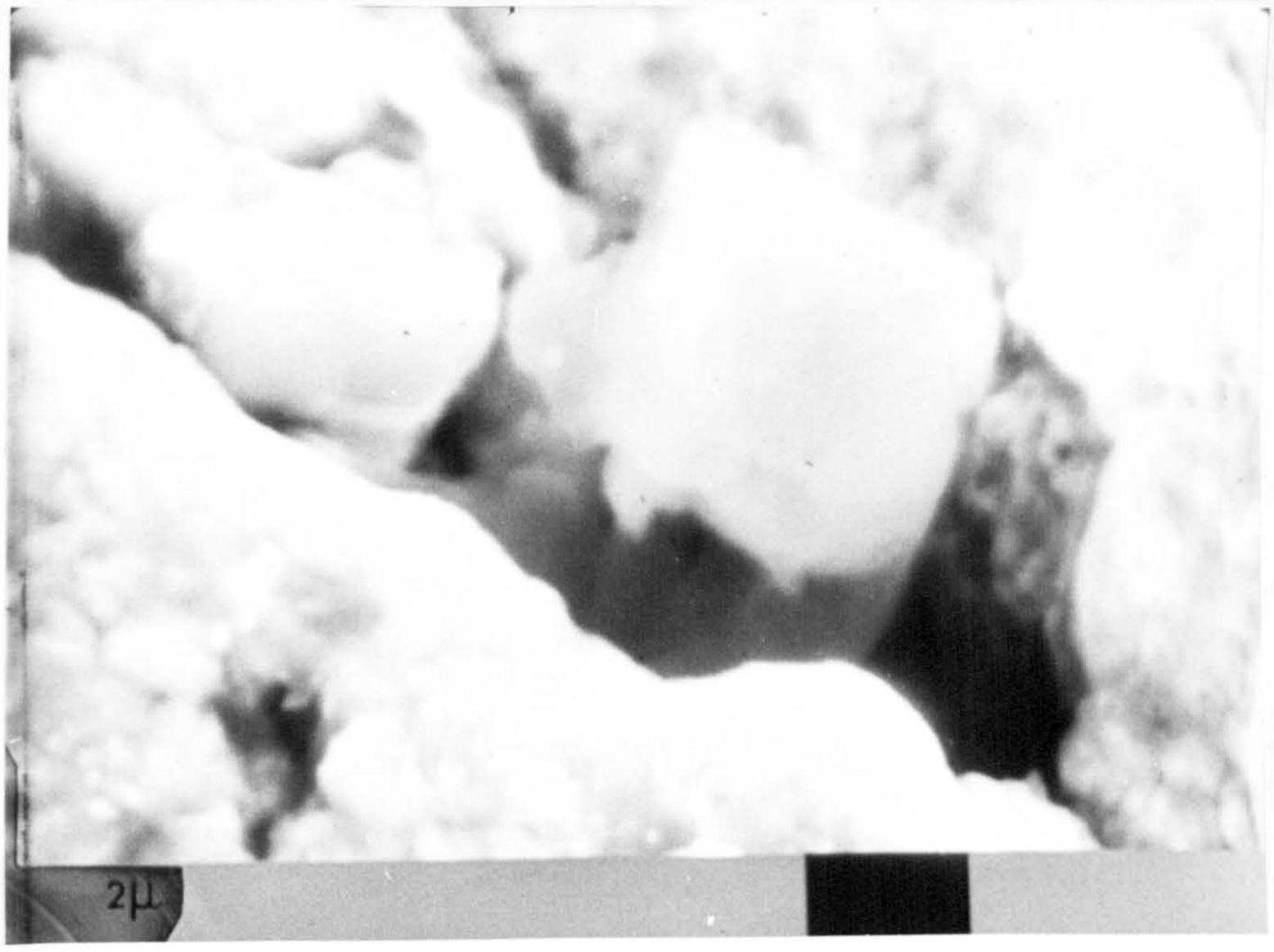
(b)



X1280

Fig 69 (a-b) Optical micrographs of Zn/Al eutectoid after 400% superplastic deformation at 250°C (∿ 0.7 Tm) showing that some of the cavities are associated with inclusions. Tensile axis horizontal.

(a)



(b)

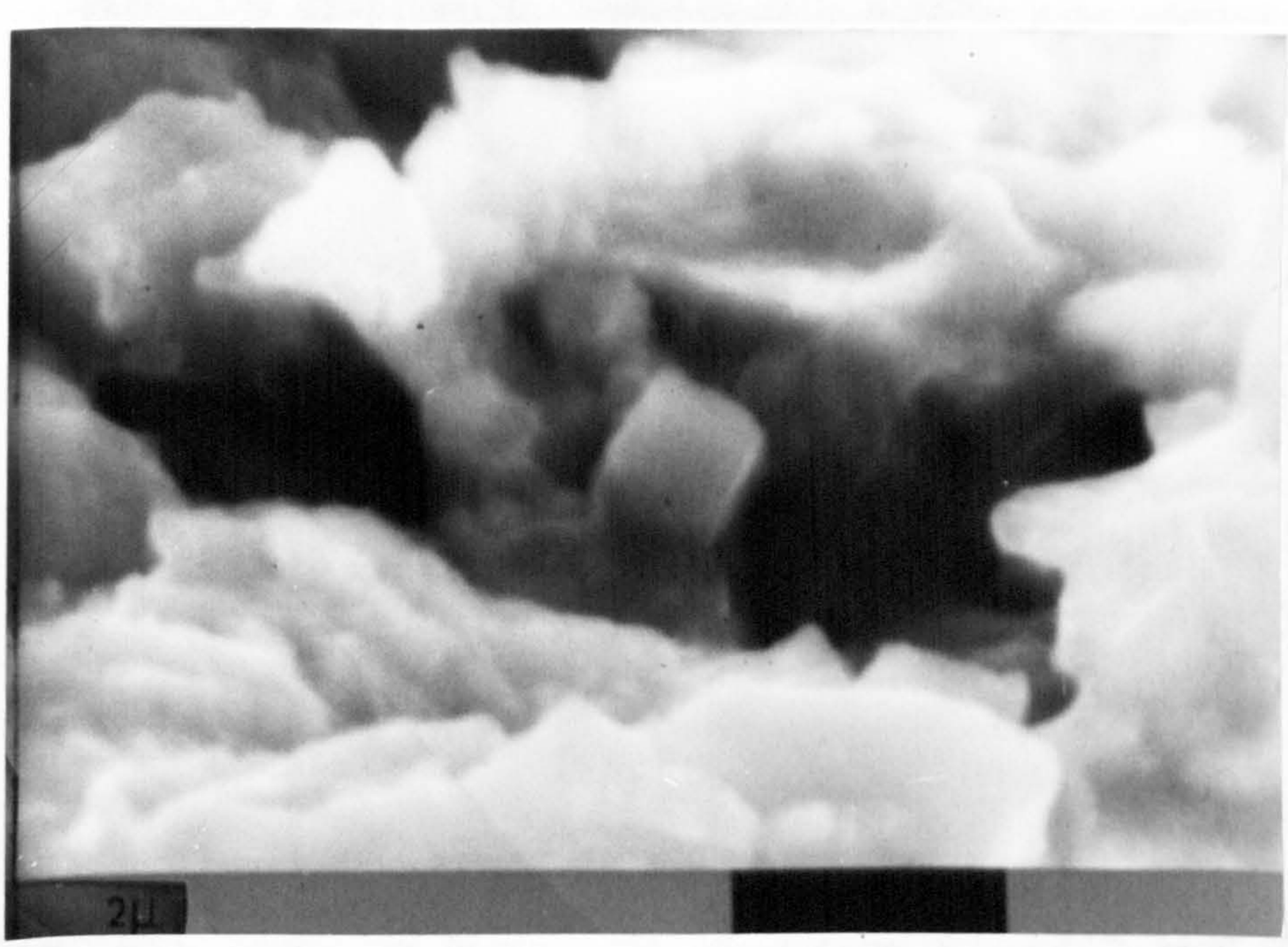
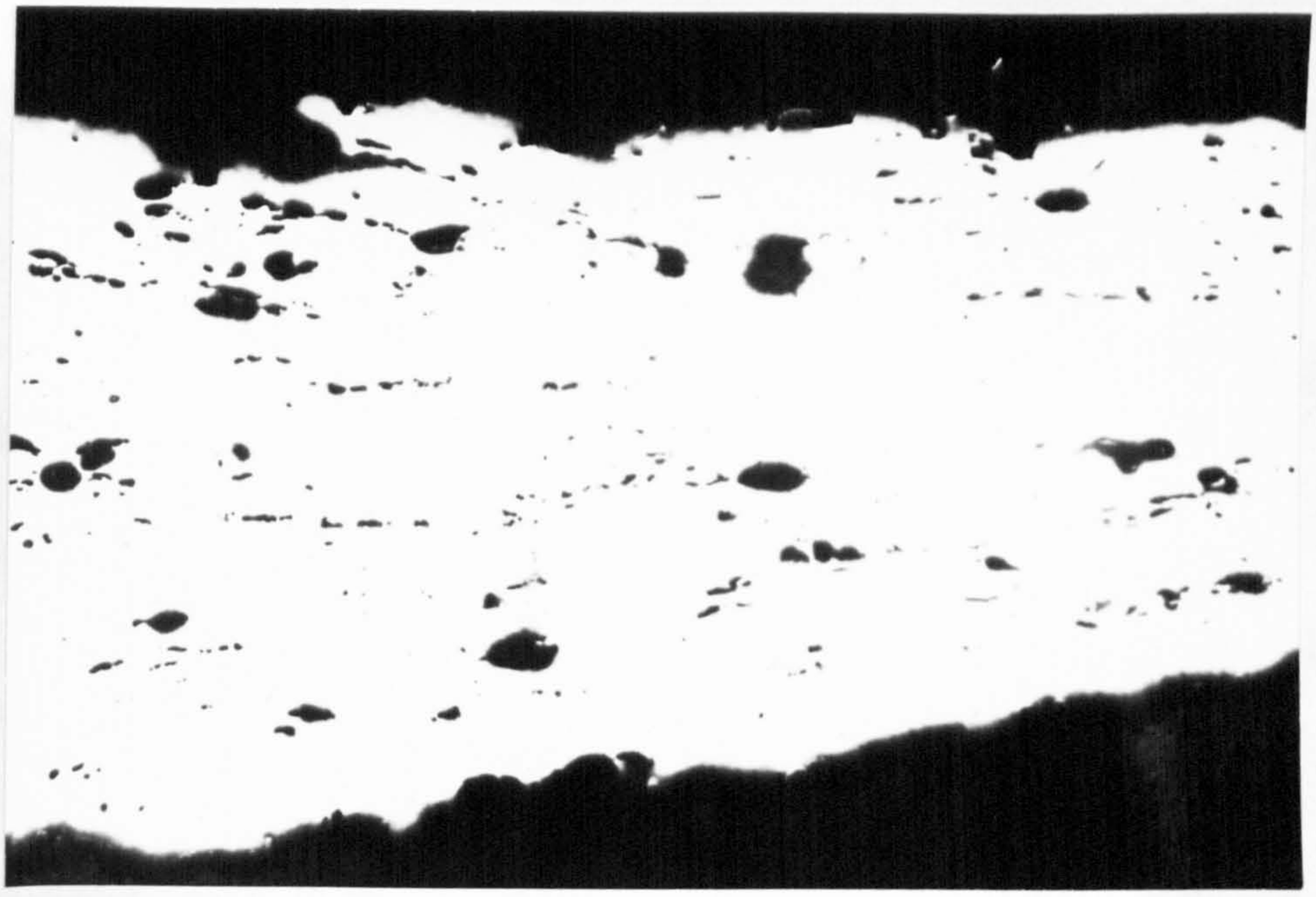
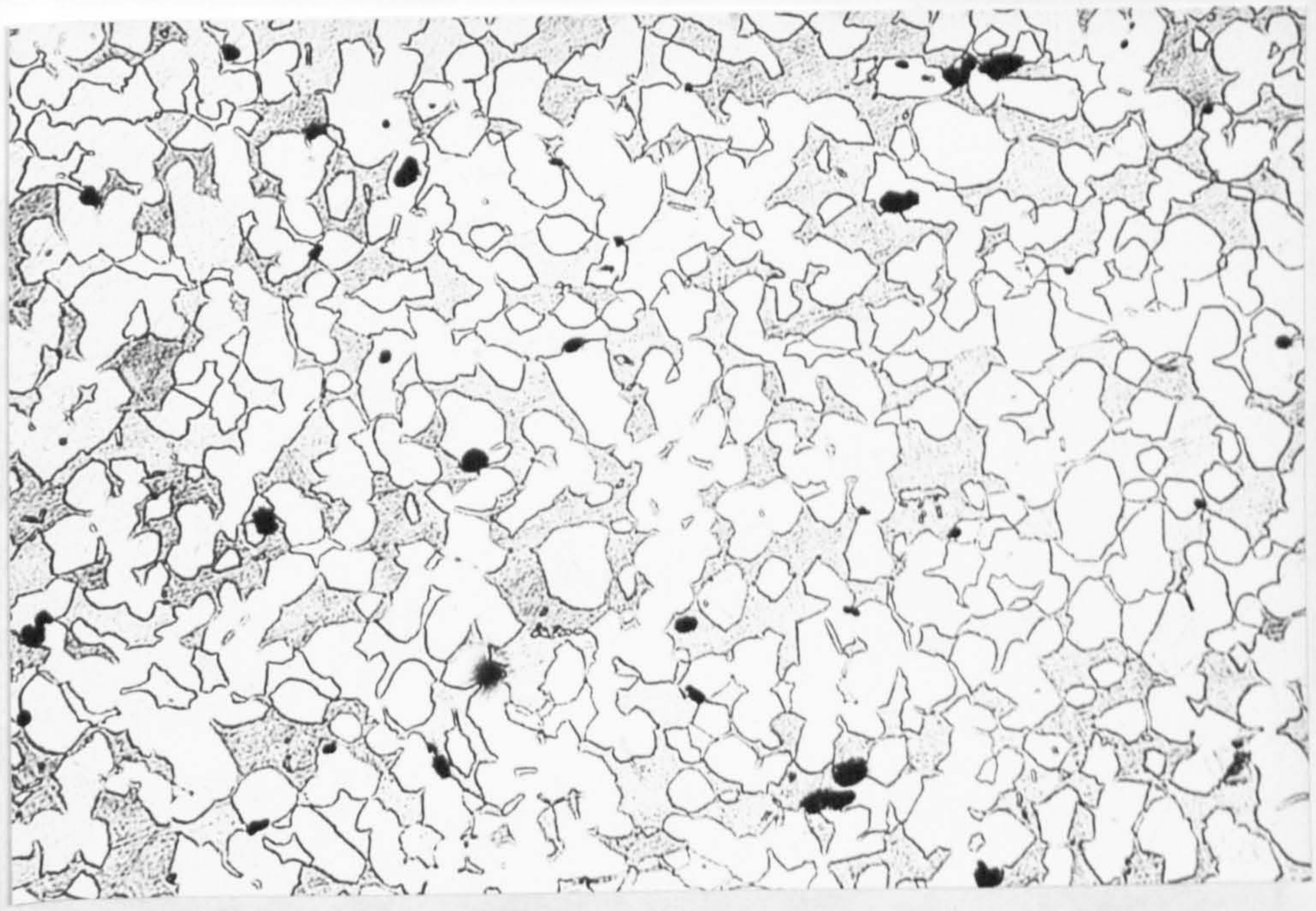


Fig 70. Scanning electron micrographs of fracture surfaces of specimens of Zn/Al eutectoid deformed at (a) 250°C (∿ 0.7 Tm), (b) 190°C (∿ 0.6 Tm) showing decohesion of $FeAl_3$ type particles to form cavities.



X50

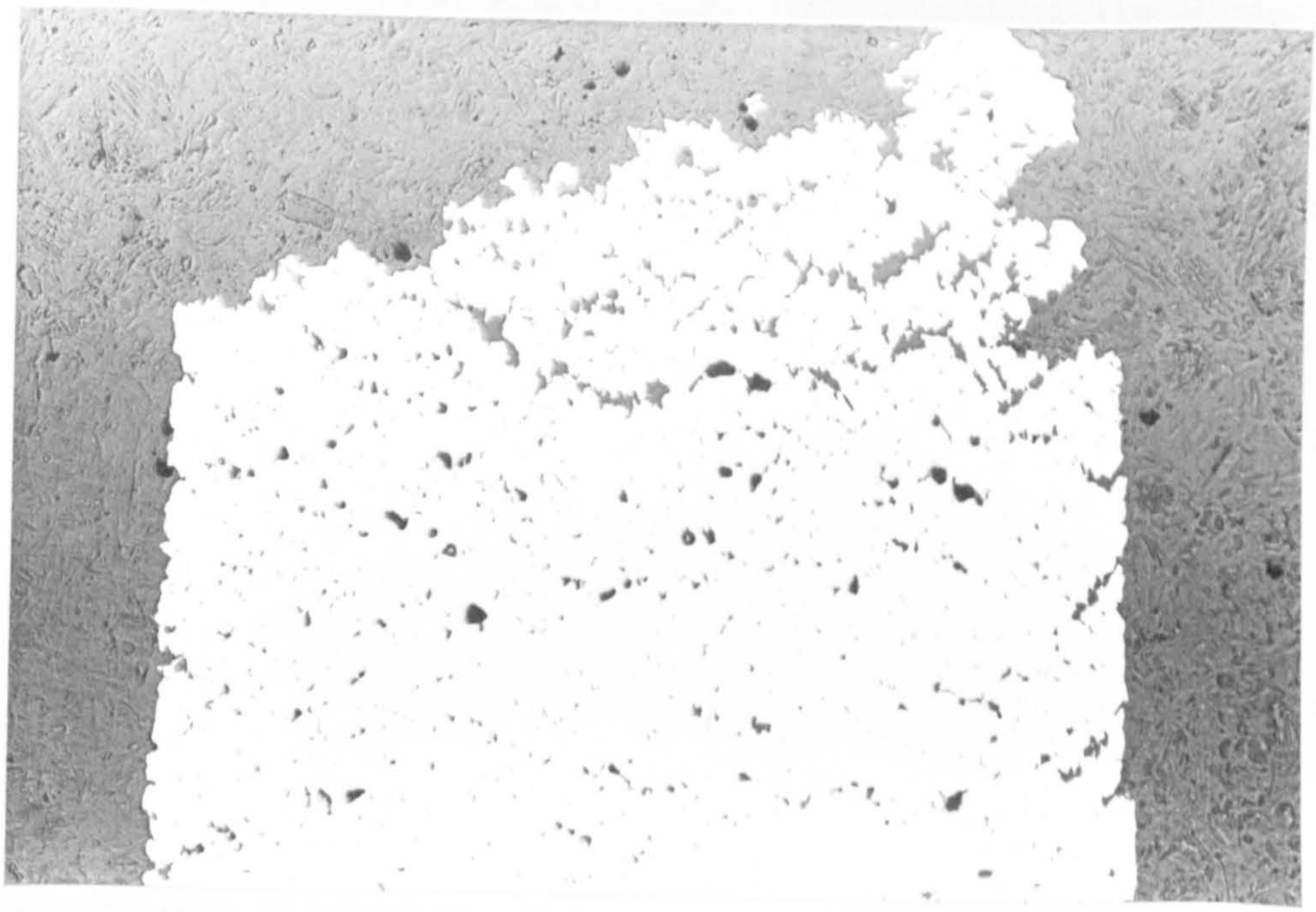
Fig 71. Optical micrograph of lamellar Zn/Al eutectoid (not superplastic) after 70% deformation at 250°C (∿ 0.7 Tm) showing extensive cavitation. Tensile axis horizontal.



X120

Fig 72. Optical micrograph of duplex 60/40 brass after 170% superplastic deformation at 600°C (0.74 Tm), $\dot{\varepsilon} = 1.6 \times 10^{-3} sec^{-1}$ showing cavitation mainly at the α/β boundaries. Tensile axis horizontal. Grain size ∿ 40 μm, initial grain size was ∿ 7 μm.

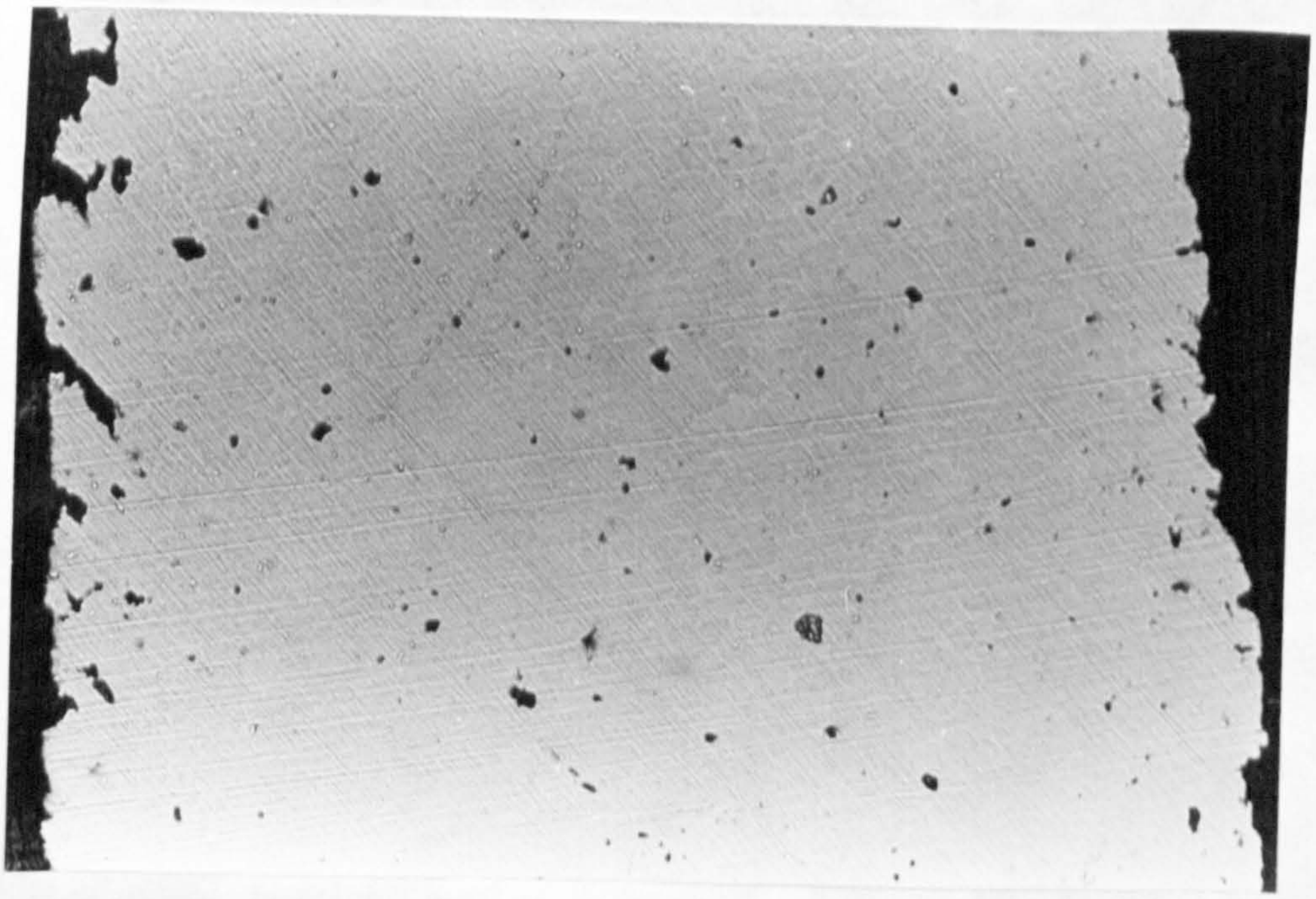
(a)



X50

Tensile Axis

(b)



X80

Tensile Axis

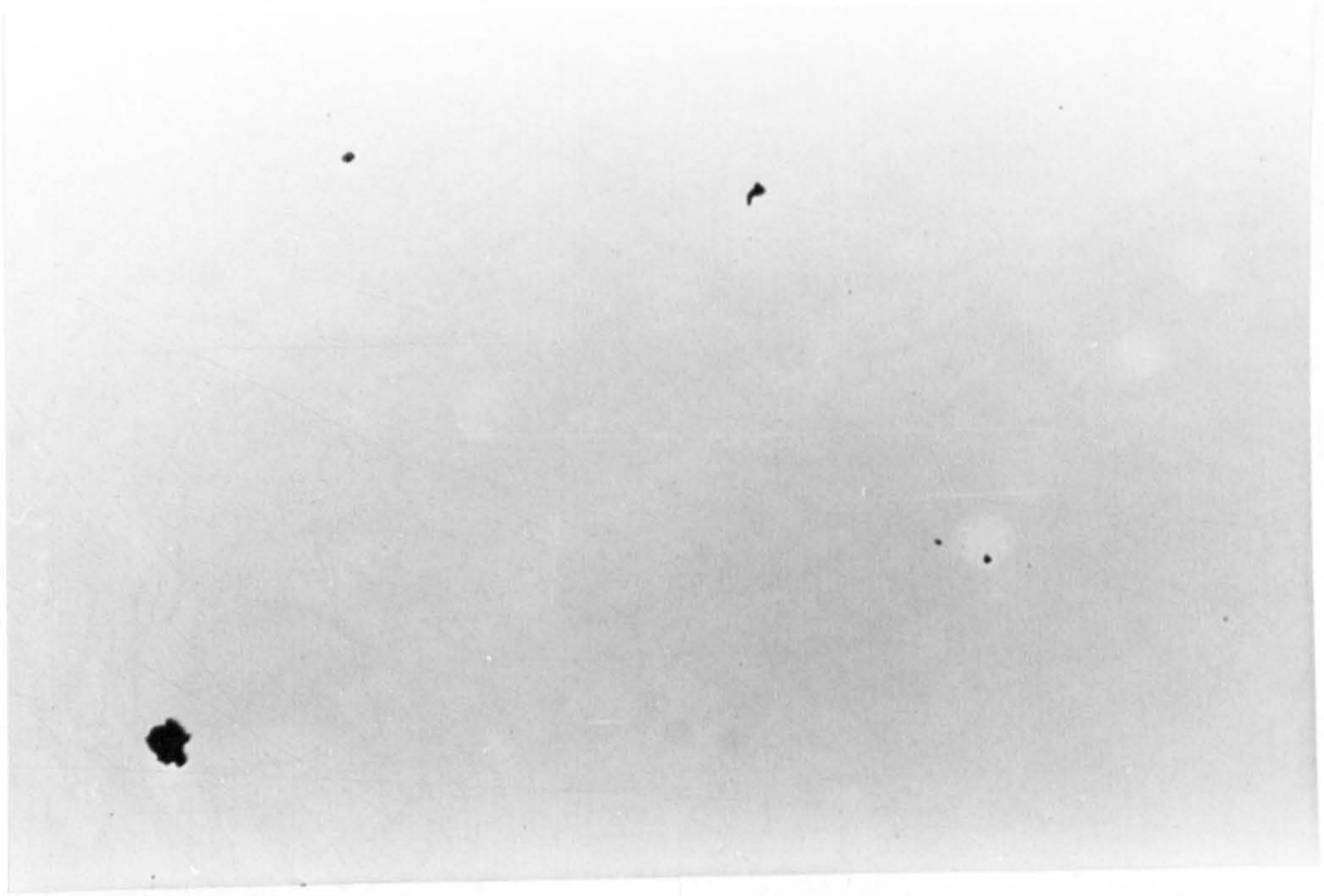


Fig 73. Optical micrographs of 60/40 brass deformed at (a) 500°C (0.66 Tm), (b) 600°C (0.74 Tm) and (c) 700°C (0.83 Tm), $\dot{\varepsilon} = 1.6 \times 10^{-3} sec^{-1}$ showing that the amount of cavitation decreases with an increase in temperature.

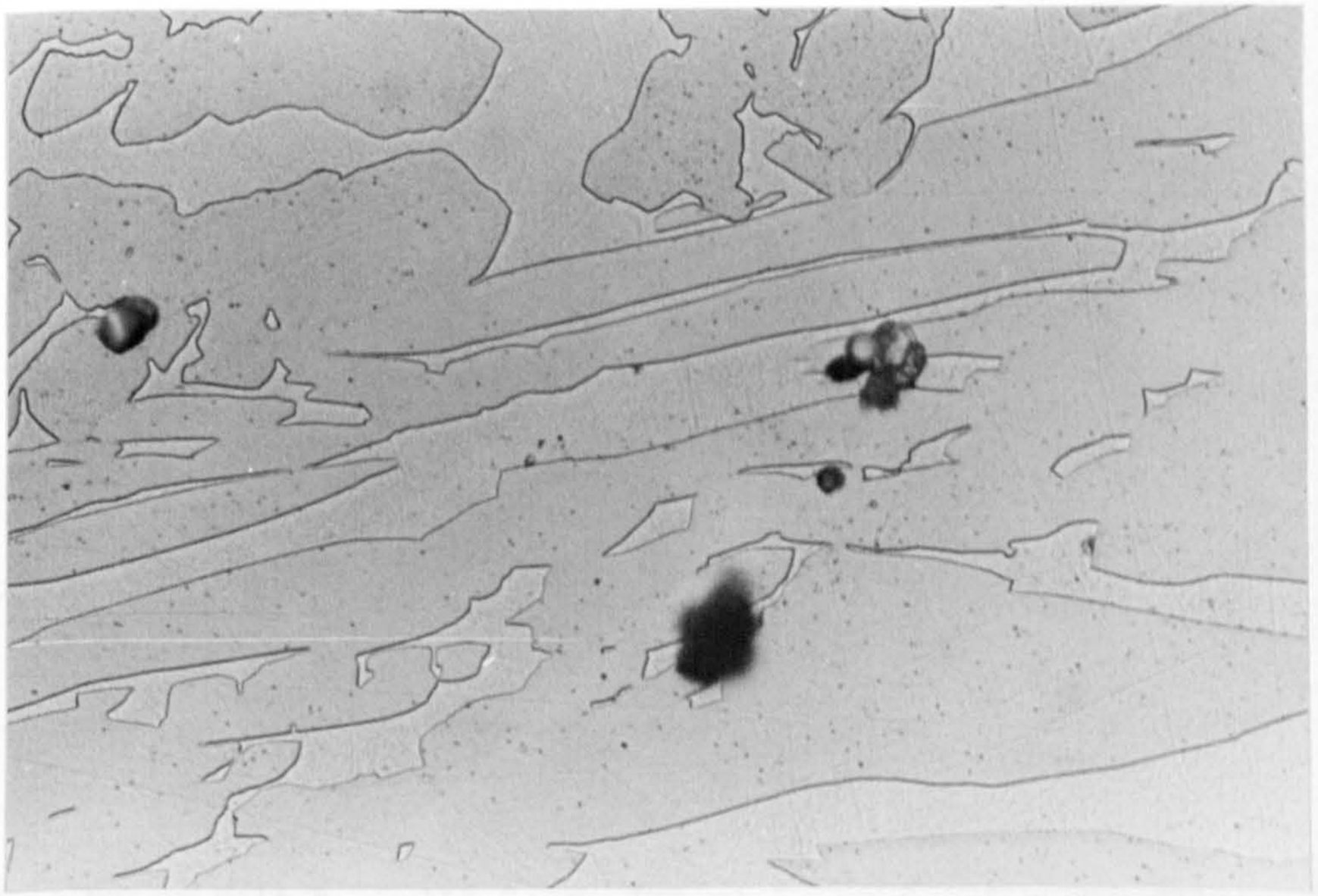
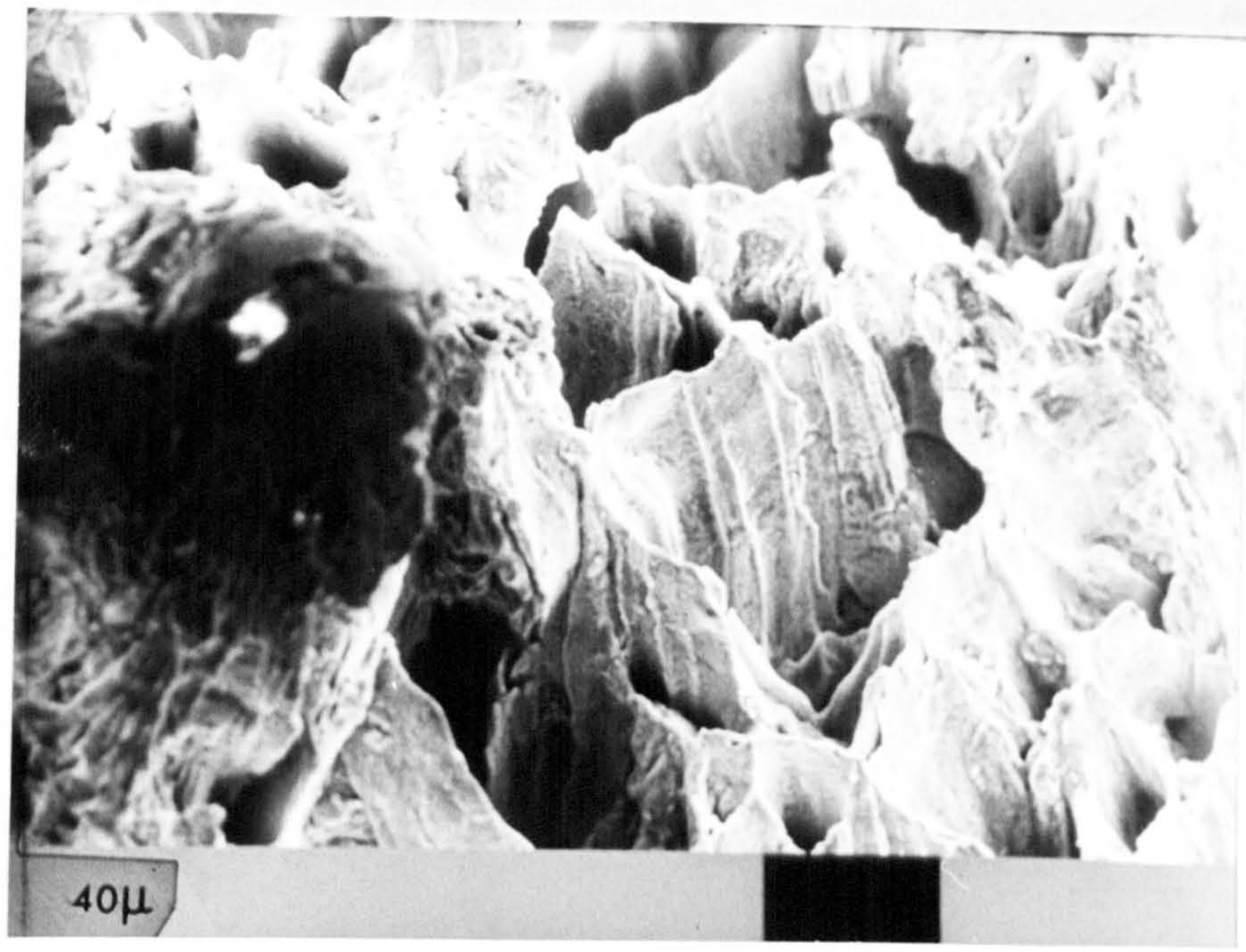


Fig 74. Optical micrograph of 60/40 brass deformed at 700°C, $\dot{\varepsilon} = 1.6 \times 10^{-3} sec^{-1}$, showing elongation of individual phases in the direction of the tensile axis.

(a)



(b)

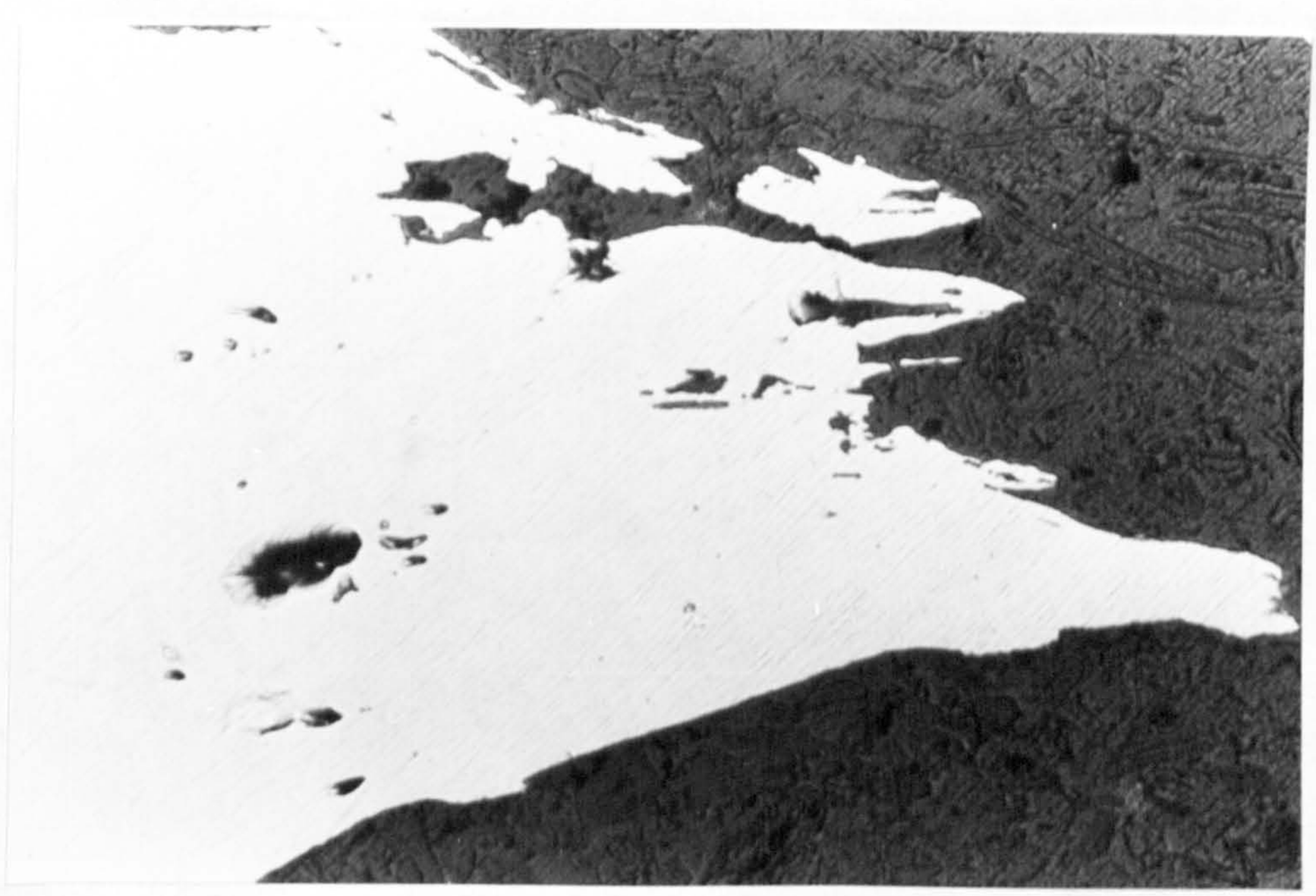


Fig 75. (a) Scanning electron micrograph of the fracture surface and (b) optical micrograph of the 60/40 brass deformed at 600°C (0.74 Tm), $\dot{\varepsilon} = 1.6 \times 10^{-3} sec^{-1}$, showing interlinking of the cavities to cause final failure of the alloy.

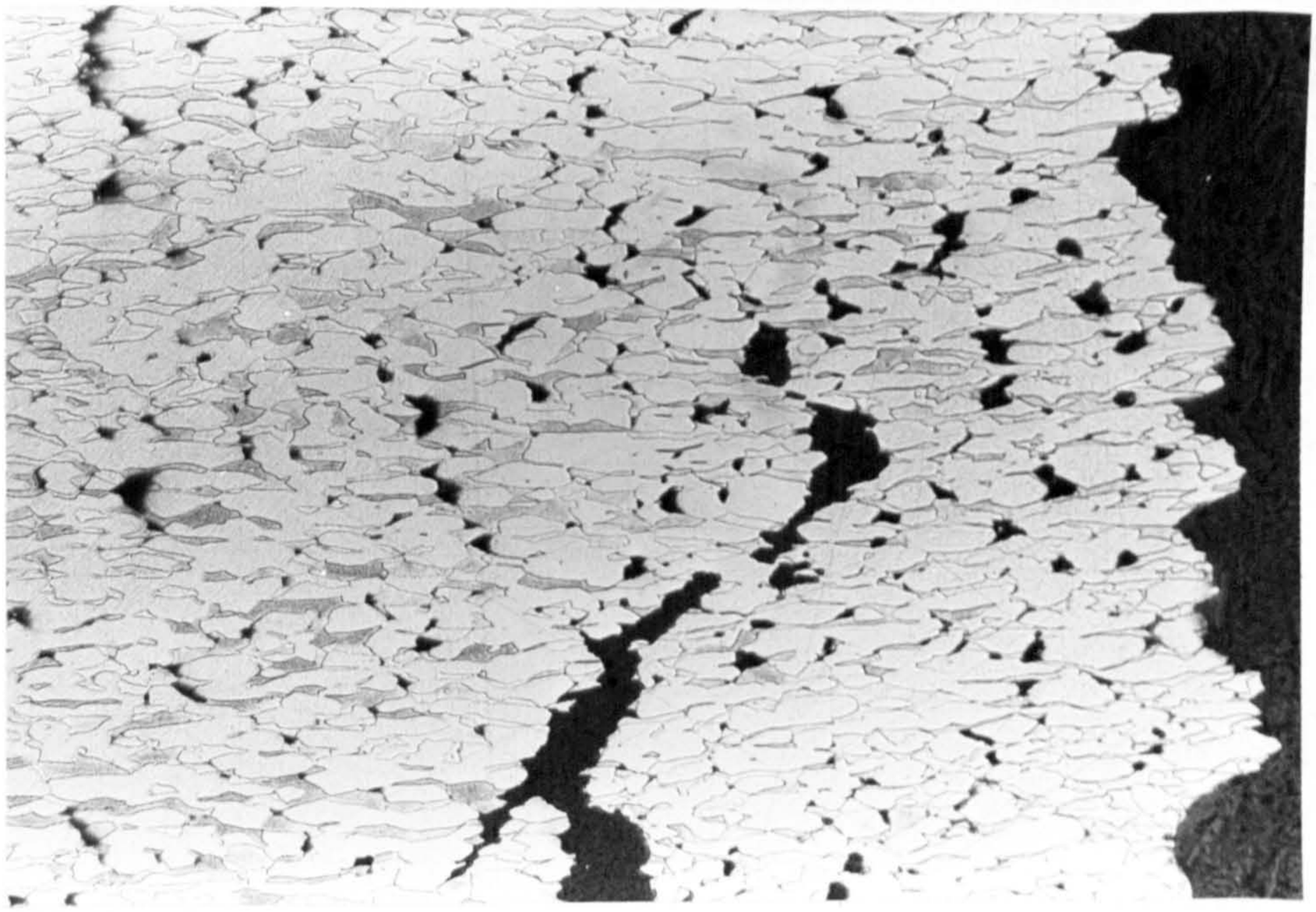


Fig 76. Optical micrograph of 60/40 brass deformed at 250°C (0.45 Tm), $\dot{\varepsilon} = 1.6 \times 10^{-3} sec^{-1}$, showing cavitation at triple points. The individual phases are elongated in the direction of the tensile axis.

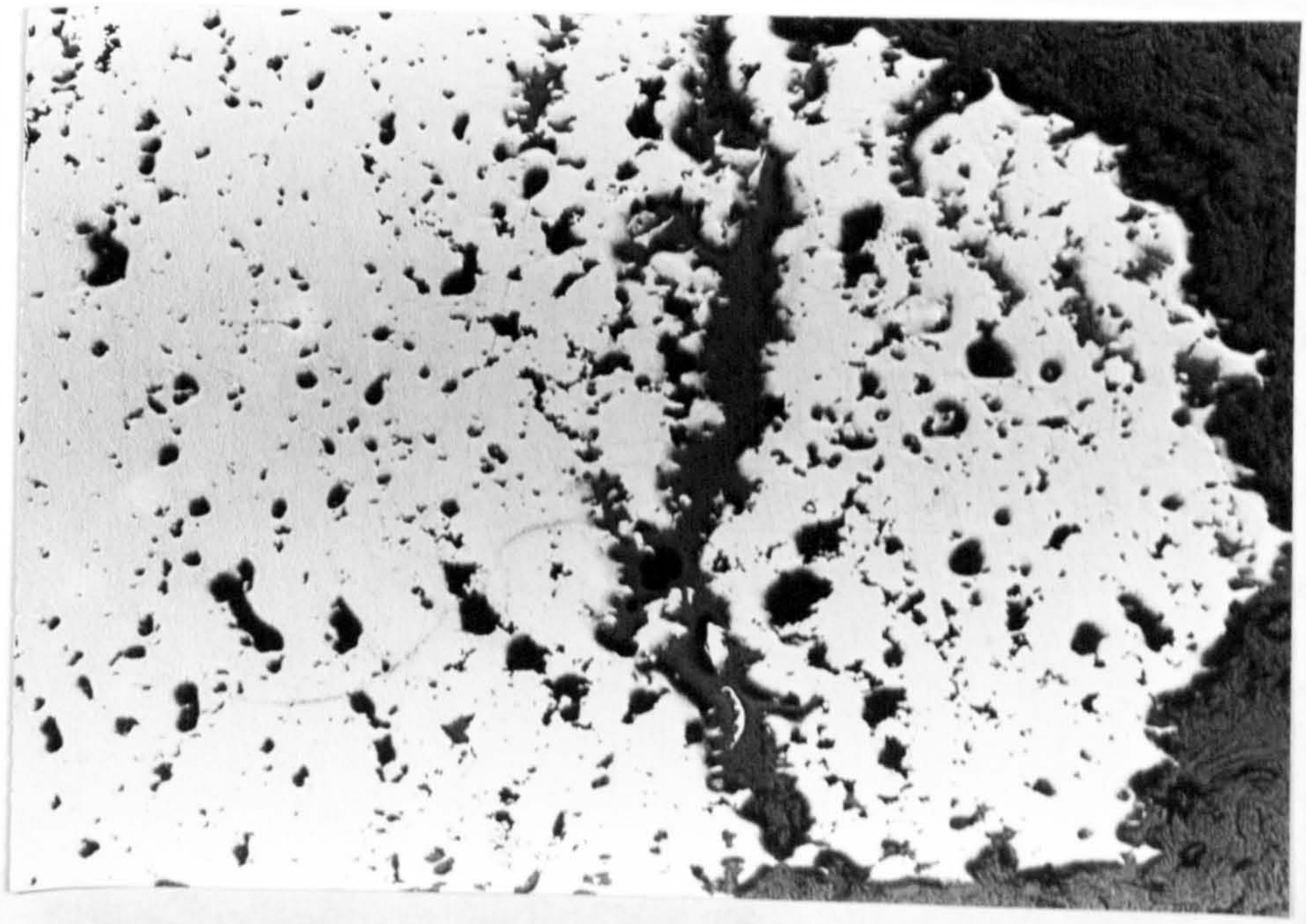
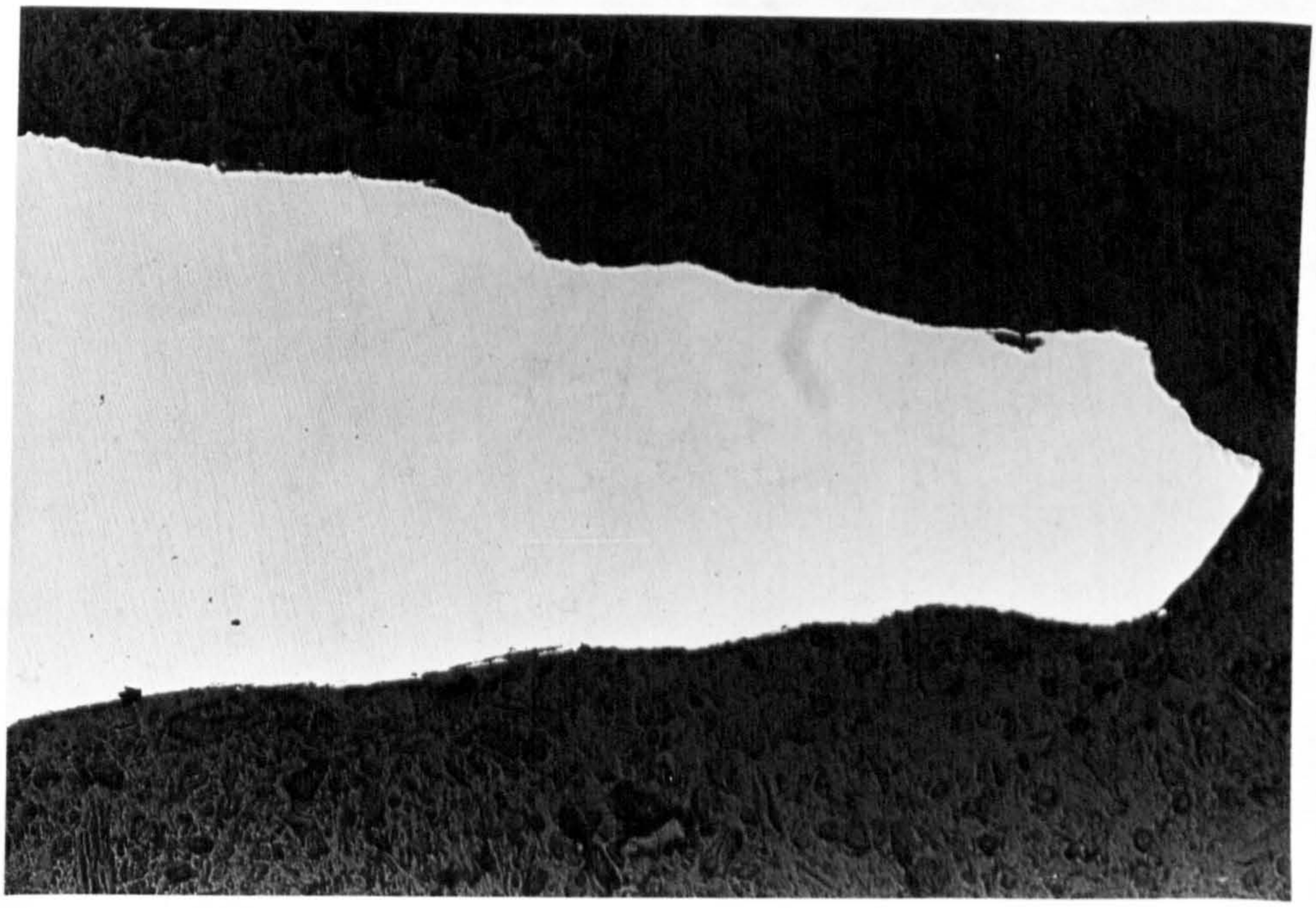
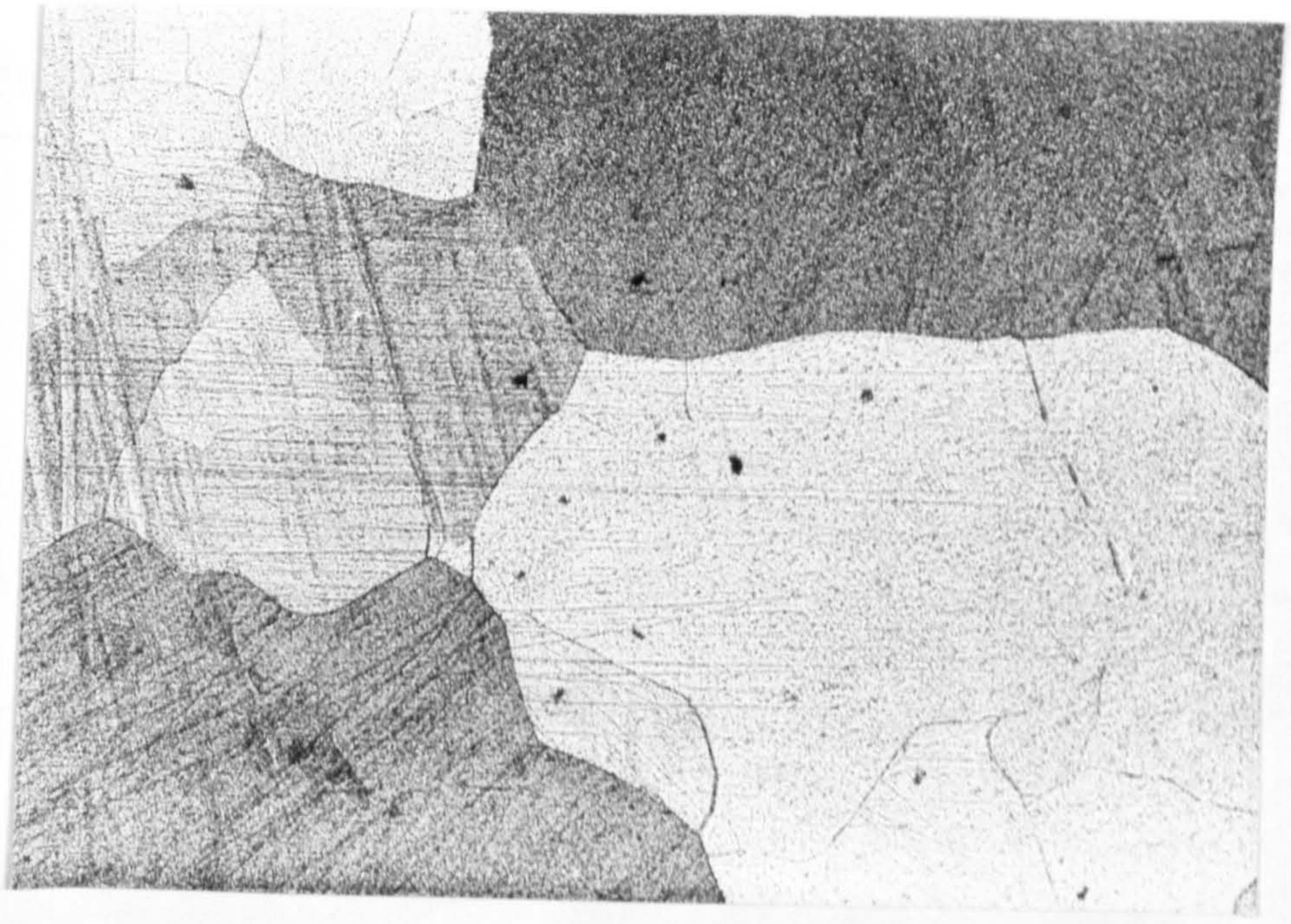


Fig 77. Optical micrograph of 62/38 brass deformed at 600°C (0.74 Tm), $\dot{\varepsilon} = 1.6 \times 10^{-3} sec^{-1}$, showing extensive amount of cavitation in the vicinity of the fractured tip.



X50

Fig 78. Optical micrograph of 55/45 brass deformed at 600°C (0.75 Tm), $\dot{\varepsilon} = 1.6 \times 10^{-3} sec^{-1}$, showing very little cavitation in the vicinity of the fractured tip. Tensile axis horizontal.



X50

Fig 79. Optical micrograph of 55/45 brass deformed to 170% at 600°C (0.75 Tm) $\dot{\varepsilon} = 1.6 \times 10^{-3} sec^{-1}$, showing small grains apparently forming within larger ones. Tensile axis is horizontal.

Table 1 - Composition and proportion of α and β phases in the Zn/Al eutectoid at different temperatures

78 Zn - 22 Al eutectoid ($A_{\alpha\beta}$)

Temp °C	Composition (wt%)		Proportion α : β
	α phase	β phase	
	Zn Al	Zn Al	
120	5.6 - 94.4	99.5 - 0.5	23 : 77
190	12.4 - 87.6	99.5 - 0.5	25 : 75
250	22 - 78	99.5 - 0.5	28 : 72

Table 2 Composition and proportion of α and β phases in the 60 Cu - 40 Zn alloy at different temperatures

60 Cu - 40 Zn alloy ($B_{\alpha\beta}$)

Temp °C	Composition (wt%)		Proportion α : β
	α phase	β phase	
	Cu Zn	Cu Zn	
300	63 - 37	53.5 - 46.5	68 : 38
400	61 - 39	54 - 46	86 : 14
500	61 - 39	55.5 - 44.5	88 : 12
600	62.5 - 37.5	57 - 43	55 : 45
700	64 - 36	59 - 41	20 : 80

Table 3 Composition and room temperature hardness of all the alloys

Alloy		Actual Composition (wt%)	Hardness (Hv = kg/mm^2)	
			As-received	Annealed
Al - 78Zn	($A_{\alpha\beta}$)	Al - 77.4Zn - 0.09Fe	76	49
Al - 5.6Zn	($A_{\alpha 1}$)	Al - 7.3Zn	33	23
Al - 12.4Zn	($A_{\alpha 2}$)	Al - 13Zn	65	55
Al - 22Zn	($A_{\alpha 3}$)	Al - 21.8Zn	119	103
Al - 99.5Zn	(A_{β})	Al - 98.5Zn	60	59
60Cu - Zn	($B_{\alpha\beta}$)	59.6Cu - Zn	136	95
62Cu - Zn	(B_{α})	61.4Cu - Zn	90	61
55Cu - Zn	(B_{β})	54.6Cu - Zn	137	118

Table 4 Alloys that represent the two phases of $A_{\alpha\beta}$ alloy

Alloy	Temperature Range (^{o}C)	Phase represented in $A_{\alpha\beta}$ alloy
$A_{\alpha 1}$	R.T - 150	α
$A_{\alpha 2}$	160 - 220	α
$A_{\alpha 3}$	230 - 270	α
A_{β}	R.T - 270	β

Table 5 Alloys that represent the two phases of $B_{\alpha\beta}$ alloy

Alloy	Temperature Range (^{o}C)	Phase represented in $B_{\alpha\beta}$ alloy
B_{α}	300 - 700	α
B_{β}	300 - 700	β

Table 6 Composition and proportion of phases in $A_{\alpha 1}$, $A_{\alpha 2}$, $A_{\alpha 3}$ and A_{β} alloys

Temp °C	$A_{\alpha 1}$			$A_{\alpha 2}$			$A_{\alpha 3}$			A_{β}		
	Composition wt%Zn/wt%Al		Proportion	Composition wt%Zn/wt%Al		Proportion	Composition wt%Zn/wt%Al		Proportion	Composition wt%Zn/wt%Al		Proportion
	α	β	α:β	α	β	α:β	α	β	α:β	α	β	α:β
120	5.6/94.4	99.5/0.5	99:1	5.6/94.4	99.5/0.5	93:7	5.6/94.4	99.5/0.5	82:18	-	99.5/0.5	β=100%
190	7.3/92.7	-	α=100%	13/87	-	α=100%	13/87	99.5/0.5	89:11	-	99.5/0.5	β=100%
250	7.3/92.7	-	α=100%	13/87	-	α=100%	21.8/78.2	-	α=100%	-	99.5/0.5	β=100%

Table 7 Composition and proportion of phases in B_α and B_β alloys

Temp °C	B_α			B_β		
	Composition wt%Cu/wt%Zn		Proportion	Composition wt%Cu/wt%Zn		Proportion
	α	β	α:β	α	β	α:β
300	63.1/36.9	53.5/46.5	82:18	63.1/36.9	53.5/46.5	11:89
400	61.4/38.6	-	α=100%	61.4/38.6	54.1/45.9	5:95
500	61.4/38.6	-	α=100%	-	54.6/45.4	β=100%
600	62.4/37.6	56.9/43.1	76:24	-	54.6/45.4	β=100%
700	64.1/35.9	58.6/41.4	50:50	-	54.6/45.4	β=100%

Table 8 Hardness of fine-grained Zn/Al eutectoid measured by Reichert and present microhardness tester

Load (gm)	Hardness H_V	
	Reichert	Present Machine
10	44.5 ± 4.5	40.2 ± 1.85
20	45 ± 1.4	41.9 ± 0.7
50	43.3 ± 1.9	45.8
100	45.7 ± 3	46.7 ± 1.4

Table 9 Ductility and UTS values of 60 - 40 brass at 250°C

$\dot{\varepsilon} = 1.6 \times 10^{-3} sec^{-1}$

Condition	% Elongation	UTS x 10^3 psi
as-extruded	109	41.6
1 hr 400°C	67	41.2
1 hr 600°C	67	31.8

Table 10 Ductility and UTS values of 60 - 40 brass at 600°C

$\dot{\varepsilon} = 1.6 \times 10^{-3} sec^{-1}$

Condition	% Elongation	UTS $\times 10^3$ psi
1 hr 600°C	178	1.2
as-extruded	158	1.1
1 hr 750°C (lamellar)	101	3.5

Table 11 Ductility and UTS values of Zn/Al eutectoid at 250°C.

$\dot{\varepsilon} = 1.6 \times 10^{-3} sec^{-1}$

Condition	% Elongation	UTS $\times 10^3$ psi
Homogensied for 2½ hrs at 370°C Quenched iced-water. Annealed 1 hr 250°C	403	1.3
as-extruded	237	0.96
2 hr 370°C air cooled (lamellar)	75	5.4

Table 12 Activation energies for $A_{\alpha 1}$, $A_{\alpha 2}$, $A_{\alpha 3}$ and A_{β} alloys

Alloy	Temperature Range	Activation Energy Q(Kcal/mole)
A_{β}	0.5 - 0.7 Tm	12.9
	0.7 - 0.9 Tm	19.5
$A_{\alpha 3}$	0.5 - 0.8 Tm	29.9
$A_{\alpha 2}$	0.4 - 0.6 Tm	15
	0.6 - 0.8 Tm	29.5
$A_{\alpha 1}$	o.5 - 0.67 Tm	17.3
	0.67 - 0.83 Tm	32.7

(Error in calculating Q-value is ± 2 Kcal/mole)

Table 13 Ductility, hardness and UTS values of Zn/Al eutectoid ($A_{\alpha\beta}$) and its phases

T^oC	% Elongation			Hardness x 10^3 psi			UTS x 10^3 psi		
	α	β	$A_{\alpha\beta}$	α	β	$A_{\alpha\beta}$	α	β	$A_{\alpha\beta}$
120	52	16	319	28.4	69.7	35.5	8.8	19.1	8.4
190	40	9	356	31.3	36.2	10.0	7.4	13.7	2.9
250	30	33	403	25.6	21.3	3.7	6.6	8.1	1.3

Table 14 n values used for the alloys

Alloy	Stress exponent, n	Comment
Zn/Al eutectoid ($A_{\alpha\beta}$)	2	(For most of the super-(plastic alloys:
60/40 brass ($B_{\alpha\beta}$)	2	($\dot{\varepsilon} \alpha \sigma^2$
Supral 150	2	(Ref 4 & 60
B_β brass	3.5	(Ref 4 & 60
B_α brass	5	Ref 206
$A_{\alpha 1}$	5	(data not available.
$A_{\alpha 2}$	5	(It appears that the (creep behaviour of a
$A_{\alpha 3}$	5	(large fraction of (alloys investigated
A_β	5	(is similar to that of (pure metals(Ref 206)

Table 15 Ductility, hardness and UTS values of 60 - 40 brass ($B_{\alpha\beta}$) and its phases

T^oC	% Elongation			Hardness $\times 10^3$ psi					UTS $\times 10^3$ psi		
				in-situ							
	α	β	$B_{\alpha\beta}$	α	β	$\alpha(B_\alpha)$	$\beta(B_\beta)$	$B_{\alpha\beta}$	α	β	$B_{\alpha\beta}$
300	40	63	47	135	109	89.6	66.8	85.3	32.4	12.9	25.3
400	25	50	29	83.8	38.3	54	20.6	34.1	32.2	10.1	14.9
500	25	180	27	34.8	8.8	22.6	3.7	11.9	6.8	0.6	4.2
600	54	172	178	17.8	2.8	12.2	1.6	4.4	3.6	0.5	1.2
700	148	151	65	9.9	2	4.8	1.1	1.9	0.7	0.4	0.6

Table 16

MATERIAL - PURE ALUMINIUM
CONDITION - ANNEALED AT 550^{o}C FOR 1 HOUR
ATMOSPHERE - ARGON (~ 5 Cuft/hr)
L = 10 gm, t = 15 seconds

On Heating Up		On Cooling Down	
T^{o}C	H(kg/mm^2)	T^{o}C	H(kg/mm^2)
25	37.1 ± 4.9	550	2.89 ± 0.39
100	32.2	500	3.66 ± 0.18
150	31.2 ± 1.5	450	5.05 ± 0.23
225	21.8 ± 1.2	400	6.87 ± 0.51
300	13.85 ± 0.3	350	9.16 ± 0.4
350	9.85 ± 0.3	300	13.3 ± 0.4
400	6.86 ± 0.26	250	19.6 ± 0.3
450	4.89 ± 0.22	200	25.5 ± 1.8
500	3.7 ± 0.12	150	32.9 ± 3.2
525	3.13	100	33.9 ± 1.7
550	2.68 ± 0.05	50	37.7 ± 2.6
		30	39.2 ± 4.1

Table 17

Material - 60 Cu/40 Zn ($B_{\alpha\beta}$)
L = 100 gm, t = 15 sec
Atmosphere - vacuum

$T^{o}C$	Hardness (kg/mm^2)	
	As-extruded	Annealed at $800^{o}C$ for 3 hrs. Air cooled to get lamellar micro-structure
20	129	128
50	128	122
100	128	120 ± 4
150	122	119 ± 3
200	110	110
250	92	92 ± 4
300	66	74 ± 5
350	40.1	48 ± 1
400	20.8 ± 0.8	28 ± 0.5
450	11.9	16 ± 0.4
500	7.15 ± 0.05	11 ± 1.8
550	4.15 ± 0.05	-
600	2.2	5 ± 0.3
650	1.28	
700	0.96 ± 0.01	1.5 ± 0.12

Table 18

Material - 60 Cu/40 Zn ($B_{\alpha\beta}$)
Time of loading = 15 sec
Atmosphere - vacuum

$T^{o}C$	Hardness (kg/mm^2)		
	Annealed at 600-620°C for 1hr L = 100 gm	Annealed at 700°C for 118 hrs. Quenched water L = 10 gm	
		α - phase	β - phase
20	105	110	185
50	100 ± 4	110 ± 19	185
100	96	110	185
150	96	110	185
200	92 ± 4	105 ± 10	153
250	80 ± 3	95	95
300	60 ± 1	95	77 ± 5
350	40 ± 1	86 ± 4	46
400	24 ± 0.6	59 ± 2	27 ± 2
450	13 ± 0.1	38	13 ± 1
500	8.4 ± 0.16	24.5 ± 0.5	6.25 ± 0.15
550	5.25 ± 0.11	-	-
600	3.11 ± 0.05	12.5 ± 1	2.0
650	1.96 ± 0.01	-	-
700	1.35 ± 0.01	7.0	1.4

Table 19

Material - 62 Cu/38 Zn (B_α)
Time of loading = 15 seconds
Atmosphere - vacuum

T°C	Hardness (kg/mm^2)	
	Annealed at 600-620°C for 1 hour L = 100 gm	Annealed at 630-670°C for 19 hours L = 10 gm
20	86 ± 5.5	77.5 ± 1.5
50	82 ± 1.5	76
100	74 ± 2.4	70 ± 2
150	74	73 ± 3
200	71	76
250	69	74.5 ± 1.5
300	63 ± 1.7	75.4 ± 2.4
350	53 ± 1.5	71.5 ± 1.5
400	38	53.8 ± 0.8
450	27 ± 1.3	40.7 ± 0.7
500	15.9 ± 0.3	27.7 ± 0.7
550	11.14	21
600	8.55 ± 0.05	16.5 ± 0.5
650	6.0 ± 0.1	10.2 ± 1.8
700	3.42	6.75 ± 0.15

Table 20

Material - 55 Cu/45 Zn (B_β)

Time of loading = 15 sec

Atmosphere - vacuum

T^oC	Hardness (kg/mm^2)		
	As-extruded L = 100 gm	Annealed at 600-620°C for 1 hr L = 100 gm	Annealed at 630-670°C for 19 hrs L = 10 gm
20	174 ± 4	170	110 ± 15
50	157 ± 6	170	110
100	151	160	110 ± 19
150	124 ± 2	135	110 ± 19
200	102 ± 2	105	95 ± 15
250	74 ± 3	74	82
300	45 ± 1	47 ± 2	46 ± 5
350	26 ± 1	28 ± 0.4	27
400	12 ± 0.7	14.5 ± 0.5	14 ± 1
450	4 ± 0.2	4.87 ± 0.1	5.43 ± 0.28
475	-	-	3.58
500	2.44 ± 0.1	2.63 ± 0.01	3.16 ± 0.33
550	-	1.5 ± 0.01	1.82
600	0.9	1.12	1.31 ± 0.02
650		0.91 ± 0.01	-
700		0.75 ± 0.01	0.82

Table 21

Material - 60 Cu/40 Zn ($B_{\alpha\beta}$)

Condition - Annealed at 600-620^{o}C for 1 hr.

Load = 100 gm

Atmosphere - vacuum

d = diameter of indentation (μm); H = Hardness (kg/mm^2)

Time of Loading t(sec)	T = 300^{o}C		T = 450^{o}C		T = 600^{o}C	
	d	H	d	H	d	H
10	54	63.6	112	14.7	229	3.54
15	57	57	120	12.9	248	3.02
30	60	51.5	133	10.5	285	2.28
60	62	48.2	146	8.7	336	1.64
100	64	45.3	156	7.58	380	1.28
200	68	40.1	171	6.34	456	0.89
300	70	37.8	183	5.54	500	0.74
500	74	33.9	199	4.68	620	0.48
1000	76	32.1	222	3.76	716	0.36
1500	80	29	242	3.17	805	0.29

Table 22

Material - 62 Cu/38 Zn (Bα)
Condition - Annealed at 400°C for 2 hours in argon atmosphere. Furnace cooled.
mass of the cylindrical rod = 18.867 gm
length = 11.080 cm, diameter = 0.508 cm
E = Young's modulus, f_o = first natural frequency.

T°C	f_o(KHz)	E(x10^6psi)
21	1.332	15.93
57	1.317	15.57
117	1.300	15.17
168	1.286	14.85
206	1.273	14.55
256	1.257	14.19
304	1.240	13.80
349	1.222	13.41
399	1.195	12.82
450	1.151	11.89
494	1.105	10.96
554	1.050	9.90
600	1.000	8.98
648	0.970	8.45
702	0.910	7.43

Table 23

Material - 60 Cu/40 Zn (Bαβ)

Condition - Annealed at 400°C for 2 hours in argon atmosphere. Furnace cooled.

mass of the cylindrical rod = 18.896 gm
length = 11.020 cm, diameter = 0.508 cm
E = Young's modulus, f_o = first natural frequency.

T°C	f_o(KHz)	E($x10^6$psi)
21	1.387	17.02
50	1.378	16.80
71	1.372	16.65
117	1.358	16.31
172	1.341	15.91
218	1.330	15.65
266	1.3145	15.29
308	1.302	15.00
354	1.286	14.63
400	1.267	14.20
448	1.240	13.60
502	1.200	12.74
548	1.160	11.90
600	1.130	11.30
648	1.100	10.73
701	1.090	10.51

Table 24

Material - 55 Cu/45 Zn (Bβ)
Condition - Annealed at 400°C for 2 hours argon atmosphere. Furnace cooled.
mass of the cylindrical rod = 18.6645 gm
length = 11.118 cm, diameter = 0.508 cm
E = Young's modulus, f_o = first natural frequency.

T°C	f_o(KHz)	E(x10^6psi)
21	1.154	11.95
78	1.148	11.83
130	1.141	11.68
184	1.132	11.50
228	1.125	11.35
275	1.1135	11.13
317	1.101	10.87
362	1.083	10.52
406	1.054	9.965
426	1.034	9.59
452	0.989	8.78
474	0.941	7.95
496	0.851	6.50
542	0.838	6.30
609	0.792	5.63
647	0.786	5.54
702	0.776	5.40

Table 25

Materials - 99.5 Zn/0.5 Al (A_β)
22 Zn/78 Al ($A_{\alpha 3}$)

Load = 10 gm, time of loading (t) = 15 sec
Atmosphere - vacuum

T^oC	Hardness (kg/mm^2)	
	A_β Annealed at 350^oC for 1 hr	$A_{\alpha 3}$ Annealed for 1 hr 400^oC + 1 hr 500^oC
20	64 ± 7	141 ± 12
50	64 ± 7	103 ± 8
100	57	89 ± 7
120	49 ± 3	-
140	40 ± 2	-
150	-	72
160	34 ± 2	-
180	27	-
200	24 ± 2	32 ± 2
210	22 ± 1.4	30
220	19 ± 1	27
230	20 ± 1	24.5 ± 0.5
240	17.5 ± 0.5	22
250	15 ± 1	18 ± 1
260	13.5 ± 0.5	16
270	12 ± 0.4	14
300	9.6	10
350	6.0 ± 0.1	6
400		3.8
450		2.5
500		1.9

Table 26

Materials - 5.6 Zn/94.4 Al ($A_{\alpha 1}$)
12.4 Zn/87.6 Al ($A_{\alpha 2}$)
Condition Both annealed 2 hr 500°C + 5 min 600°C
L = 10 gm, t = 15 sec
Atmosphere - vacuum

T°C	Hardness (kg/mm^2)	
	$A_{\alpha 1}$	$A_{\alpha 2}$
20	25 ± 1	46 ± 4
50	23 ± 1	46 ± 4
80	22	
100	17	38
110	19 ± 1	
120	20 ± 1	
130	20 ± 1	
140	18	
150	19	28 ± 1
160	-	25
170	-	25
180	-	24 ± 2
190	-	22
200	17	21.5 ± 0.5
220	-	19.5 ± 0.5
230	14	
240	-	17 ± 1
250	13 ± 0.8	16 ± 1
260	-	14.5 ± 0.5
270	10.5	13.5 ± 0.5
300	8.7 ± 0.3	10
350	6.5 ± 0.1	6.7 ± 0.3
400	3.9	4.6 ± 0.1
450	2.85 ± 0.05	3.15 ± 0.15
500	2.11 ± 0.26	2.01 ± 0.04

Table 27

MATERIAL - Zn/Al eutectoid ($A_{\alpha\beta}$)
CONDITION - Homogenised at 370°C for 3 hours.
Quenched in water (at room temperature).
L - 10 gm; Atmosphere - Vacuum

T°C	Hardness (kg/mm^2)	
	t = 15 sec	t = 30 sec
20	57.2	51.4
50	46.4	35
80	29.7	25.4
100	17.5 ± 0.5	14.3
120	12.5 ± 0.3	10.5
150	9.4 ± 1.0	6.4
180	6.0 ± 0.1	4.5
200	4.4 ± 0.3	3.3
230	2.45 ± 0.05	1.56
250	1.90 ± 0.05	1.53
270	1.68 ± 0.03	1.29 ± 0.06
280	8.40 ± 0.4	5.5
300	6.90 ± 0.5	5.15
350	4.60 ± 0.9	2.8
400	2.6	1.9

Table 28

MATERIAL - Zn/Al eutectoid
Time of loading (t) = 15 sec
Atmosphere - vacuum

T^oC	Hardness (kg/mm^2)		
	Homogenised at 390^oC for 15 hours. Quenched iced-water.		Homogenised at 380^oC for 4 hours. Quenched iced-water. Then annealed at 250^oC for 2 hours
	L = 10 gm	L = 100 gm	L = 100 gm
20	68 ± 4	47 ± 3	73 ± 2
50	51 ± 5	34 ± 1	62 ± 1
70			49.8 ± 1.6
80	25 ± 3	24.5 ± 0.5	
100	16 ± 1	14.5 ± 0.9	32.7 ± 0.6
120	13.5	10.4 ± 0.8	
150	10.5 ± 0.9	6.3 ± 0.5	13.5 ± 0.2
170	6.4 ± 0.3	5 ± 0.8	
200	3.8 ± 0.2	2.47 ± 0.17	5.92 ± 0.2
220			4.41 ± 0.08
230	1.67 ± 0.02	1.50 ± 0.07	
240			3.25 ± 0.08
250	1.5 ± 0.09	1.28 ± 0.01	2.62 ± 0.19
260			2.13 ± 0.04
270	1.45 ± 0.05	1.05 ± 0.01	1.73 ± 0.03

Table 29

MATERIAL - Zn/Al eutectoid ($A_{\alpha\beta}$)
Load = 100 gm, t = 15 seconds
ATMOSPHERE - vacuum

	As-extruded	Homogenised at 375°C for 4 hours. Furnace cooled to get lamellar microstructure	
T°C	H(kg/mm^2)	T°C	H(kg/mm^2)
20	60.8 ± 1.7	20	114 ± 3.9
50	45.8 ± 0.5	60	98 ± 6.6
100	19.0 ± 0.1	100	70.4 ± 1.8
150	7.5 ± 0.3	150	43.3 ± 0.7
200	3.1 ± 0.06	200	25.1 ± 0.6
220	2.2 ± 0.08	220	16.9 ± 0.1
240	1.35 ± 0.05	240	13 ± 1.7
250	1.26 ± 0.06	250	8.7 ± 0.1
260	1.06 ± 0.10	260	7.5 ± 0.3
270	1.08 ± 0.14	270	6.4 ± 0.1
280	4.47 ± 0.18		
300	5.07 ± 0.34	300	6.5 ± 0.2
350	3.28 ± 0.17	350	4.1 ± 0.7
400	2.5 ± 0.28	400	2.2 ± 0.3

Table 30

MATERIAL - Zn/Al eutectoid ($A_{\alpha\beta}$)
Condition - Homogensied at 380 - 400°C for 3 hours
Quenched iced-water
Atmosphere - Vacuum
d = diameter of indentation (μm), H = Hardness (kg/mm^2)

Time of loading t(sec)	T = 100°C				T = 150°C				T = 200°C				T = 250°C			
	L=10gm		L=100gm		L=10gm		L=100gm		L=10gm		L=100gm		L=10gm		L=100gm	
	d	H	d	H	d	H	d	H	d	H	d	H	d	H	d	H
15	34	16.04	138	9.74	48	8.05	170	6.42	70	3.78	274	2.47	106	1.65	353	1.49
30	37	13.55	139	9.6	50	7.42	194	4.93	85	2.57	301	2.05	122	1.25	415	1.08
60	44	9.58	142	9.2	57	5.71	228	3.57	87	2.45	330	1.70	124	1.21	493	0.76
100	48	8.05	143	9.07	70	3.78	234	3.39	98	1.93	358	1.45	129	1.11	545	0.62
200	50	7.42	161	7.15	73	2.97	259	2.76	100	1.85	425	1.03	158	0.74	585	0.54
300	50	7.42	184	5.48	81	2.83	298	2.09	103	1.75	448	0.92	178	0.59	654	0.43
600	54	6.36	200	4.64	85	2.57	299	2.07	-	-	488	0.78	-	-	740	0.34
630	-	-	-	-	-	-	-	-	124	1.21	-	-	-	-	-	-
700	-	-	-	-	-	-	-	-	-	-	-	-	196	0.48	-	-
900	61	4.98	206	4.37	95	2.05	301	2.05	128	1.13	525	0.67	198	0.47	752	0.33

Table 31

Material - 99.5 Zn/0.5 Al (Aβ)
Condition - Annealed at 370°C for 2 hours
Furnace cooled.
mass of the cylindrical rod = 15.5948 gm
length = 10.864 cm, diameter = 0.509 cm
E = Young's modulus, f_o = first natural frequency.

T^oC	f_o(KHz)	E($x10^6$psi)
21	1.652	18.94
56	1.636	18.58
94	1.616	18.12
140	1.578	17.28
170	1.543	16.52
198	1.526	16.16
222	1.480	15.20
246	1.410	13.80
276	1.342	12.50
318	1.255	10.93
355	1.180	9.66
376	1.135	8.94

Table 32

Material - Zn/Al eutectoid (Aαβ)
Condition - Homogenised at 370°C for 2 hours
Quenched iced-water. Then
annealed at 250°C for 1 hour
mass of the cylindrical rod = 11.0990 gm
length = 10.846 cm, diameter = 0.513 cm
E = Young's modulus, f_o = first natural frequency.

T°C	f_o(KHz)	E(x10^{6}psi)
21	1.563	11.64
41	1.554	11.50
86	1.527	11.11
119	1.495	10.65
144	1.430	9.74
175	1.424	9.66
206	1.370	8.94
216	1.360	8.81
232	1.350	8.68
246	1.296	8.00
260	1.230	7.21
268	1.210	6.98
287	1.072	5.48
315	1.040	5.15
364	1.030	5.05
376	1.020	4.96

Table 33

Material - 22 Zn/78 Al ($A\alpha_3$)
Condition - Annealed at 450°C for 2 hours
Furnace cooled.
mass of the cylindrical rod = 6.950 gm
length = 11.13 cm, diameter = 0.508 cm
E = Young's modulus, f_o = first natural frequency.

T°C	f_o(KHz)	E($\times 10^6$psi)
21	1.683	9.50
56	1.668	9.33
106	1.642	9.04
160	1.603	8.61
217	1.565	8.21
259	1.525	7.80
270	1.464	7.19
304	1.450	7.05
350	1.380	6.38
397	1.336	5.98
452	1.280	5.49
504	1.258	5.31

Table 34

Material - 12.4 Zn/87.6 Al ($A\alpha_2$)
Condition - Annealed at 450°C for 2 hours
Furnace cooled.
mass of the cylindrical rod = 6.50 gm
length = 10.98, diameter = 0.5085 cm
E = Young's modulus, f_o = first natural frequency.

T°C	f_o(KHz)	E(x10^6psi)
21	1.808	9.80
54	1.786	9.56
100	1.7565	9.25
120	1.744	9.12
138	1.734	9.02
150	1.7285	8.96
188	1.705	8.72
212	1.691	8.57
238	1.674	8.40
266	1.648	8.14
292	1.633	8.00
299	1.630	7.97
349	1.589	7.57
396	1.552	7.22
449	1.514	6.87
500	1.452	6.32

Table 35

Material - 5.6 Zn/94.4 Al ($A_{\alpha 1}$)
Condition - Annealed at 450°C for 2 hours
Furnace cooled.
mass of the cylindrical rod = 6.3154 gm
length = 11.132, diameter = 0.508 cm
E = Young's modulus, f_o = first natural frequency.

T°C	f_o(KHz)	E(x10^6psi)
21	1.832	10.23
55	1.816	10.05
116	1.787	9.73
170	1.758	9.42
220	1.733	9.15
261	1.670	8.50
313	1.660	8.40
360	1.600	7.80
406	1.570	7.51
451	1.530	7.13
492	1.497	6.83
552	1.444	6.35
595	1.395	5.93

Table 36

Material - Supral 150
(Al - 6 Cu - 0.5 Zr)
L = 10 gm, t = 15 sec
Atmosphere - vacuum

T^oC	Hardness (kg/mm^2)	
	Annealed 15 min at 460°C (superplastic)	Annealed 24 hours at 460°C
	Alloy	Al-matrix
50	46.4	56 ± 2
65	-	55 ± 2
100	42.1	54 ± 2.5
150	33.7 ± 1.5	51 ± 2.5
200	23.6	50 ± 3
250	16	40 ± 1
300	8.9 ± 0.1	25 ± 2
350	4.0 ± 0.1	16.5 ± 0.5
400	1.88 ± 0.03	9.1 ± 0.5
450	-	6.2 ± 0.2
460	1.38 ± 0.05	-
500	2.93 ± 0.03	4.8 ± 0.2